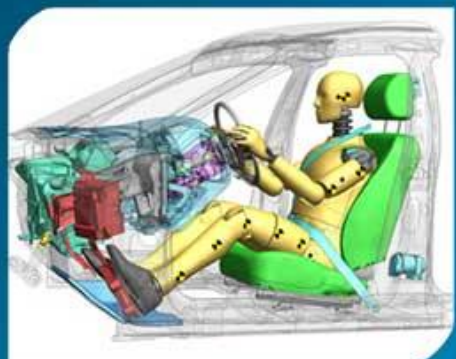
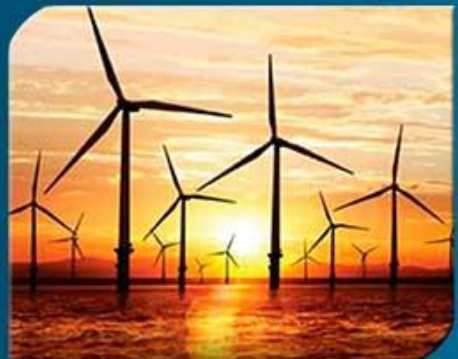


**#5
2016**

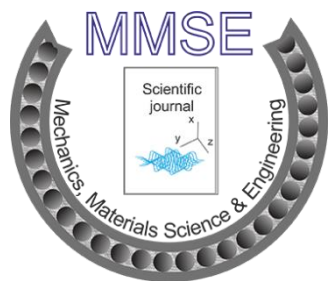
SCIENTIFIC PERIODICALS

**MECHANICS,
MATERIALS SCIENCE &
ENGINEERING**



Sankt Lorenzen 36, 8715, Sankt Lorenzen, Austria

Mechanics, Materials Science & Engineering Journal



July 2016

Mechanics, Materials Science & Engineering Journal (MMSE Journal) is journal that deals in peer-reviewed, open access publishing, focusing on wide range of subject areas, including economics, business, social sciences, engineering etc.

MMSE Journal is dedicated to knowledge-based products and services for the academic, scientific, professional, research and student communities worldwide.

Open Access model of the publications promotes research by allowing unrestricted availability of high quality articles.

All authors bear the personal responsibility for the material they published in the Journal.

The Journal Policy declares the acceptance of the scientific papers worldwide, if they passed the peer-review procedure.

Editor-in-Chief Mr. Peter Zisser

Dr. Zheng Li, University of Bridgeport, USA

Prof. Kravets Victor, Ukraine

Ph.D., Shuming Chen, College of Automotive Engineering, China

Dr. Yang Yu, University of Technology Sydney, Australia

Prof. Amelia Carolina Sparavigna, Politecnico di Torino, Italy

ISSN 2412-5954

e-ISSN 2414-6935

Design and layout. Mechanics, Materials Science & Engineering Journal, www.mmse.xyz

Technical support: hotmail@mmse.xyz

©2016, Magnolithe GmbH

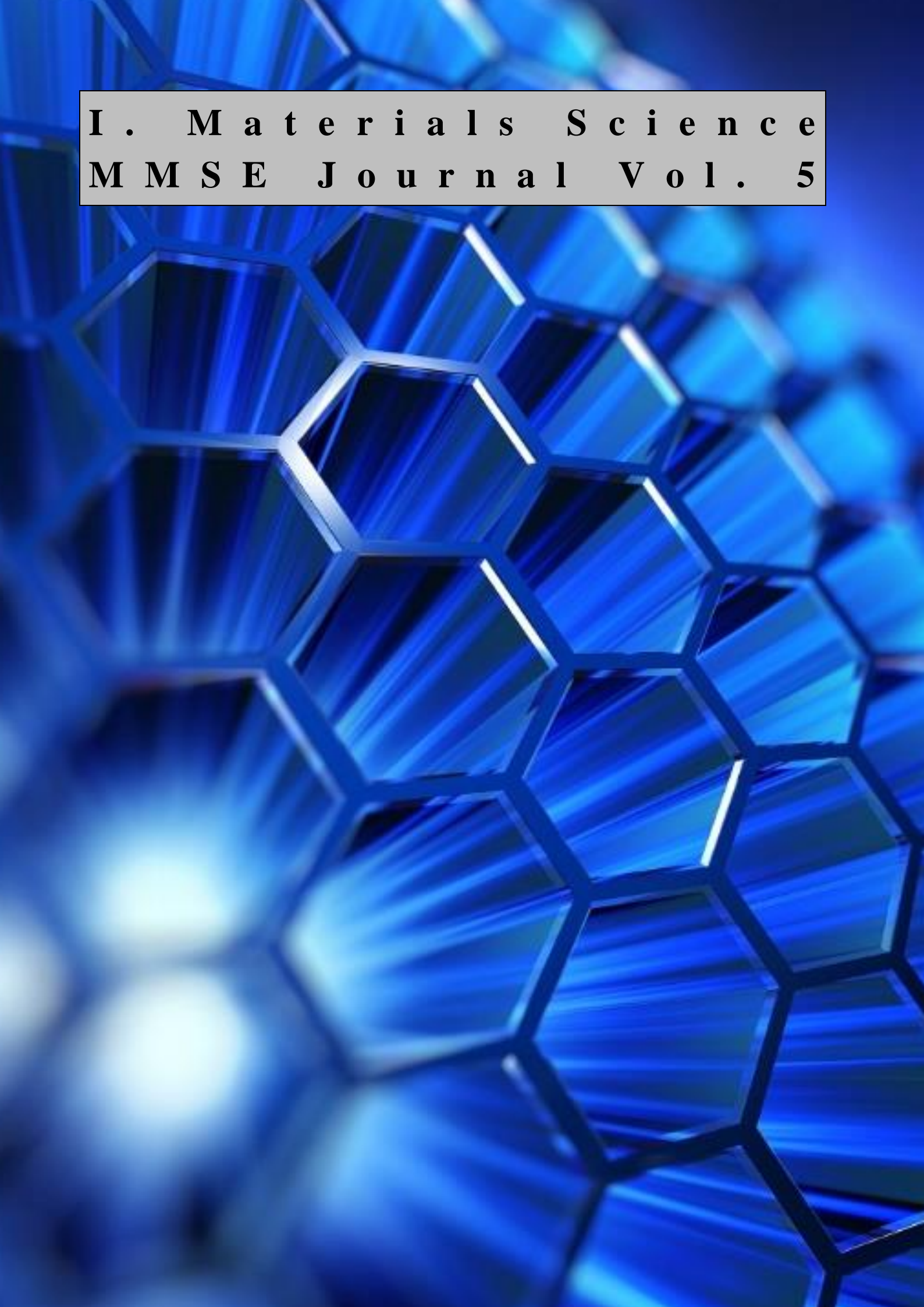
© Copyright, by the authors

CONTENT

I. Materials Science MMSE Journal Vol. 5	6
Detection of Iron Oxide Layer in Quenched and Tempered Gear Steel Using Magnetic Barkhausen Noise. M. M. Blao, M. M. Sawalem	7
Development and Determination of the Age Hardening Characteristics of Al-2.00Mg-2.66Si Wrought Alloy. Ihom A.P., Aniekan Offiong.....	13
Effect of Textures on Tensile Properties of Extruded Ti64/VGCF Composite by Powder Metallurgy Route. Patchara Pripapapong, Shu-feng Li, Junko Umeda, Katsuyoshi Kondoh	22
II. MECHANICAL ENGINEERING & PHYSICS MMSE JOURNAL VOL. 5	33
Strength Analysis of Flat Spring of the Resonant Vibro-Impact Module. Volodymyr Gursky, Igor Kuzio	34
Modelling of Station of Pumping by Variable Speed. Benretem A.	49
A Thermal Force Drifting Particles along a Temperature Gradient. Amelia Carolina Sparavigna	58
Error Analysis of Method for Calculation of Non-Contact Impact on Space Debris from Ion Thruster. Alpatov A.P., Fokov A.A., Khoroshyllov S.V., Savchuk A.P.	64
Increased Wear Resistance of Surfaces of Rotation Bearings Methods Strengthening-Smoothing Processing. A.A. Tkachuk, V.U. Zablotskyi, T.V.Terletskyi, O.L. Kaidyk, S.A. Moroz.....	77
Kinetostatics of Wheel Vehicle in the Category of Spiral-Screw Routes. Kravets V.V., Bas K.M., Kravets T.V., Zubarev M.S., Tokar L.A.	86
An Instrumented Macro-Indentation Method for Determining the Mechanical Properties of Coconut Shell (Coco Nucifera of Cameroon). E. Njeugna, M.B.K. Ganou, D. Ndapeu, J.N.T. Foba, N.R.T. Sikame, P.W.M. Huisken	99
Macroscopic Geometrical Modelling of Oil Palm Mesocarp Fibers of Three Varieties of Palm Nut. E. Njeugna, P. W. M. Huisken, D. Ndapeu, N. R. T. Sikame, J. Y. Dréan.....	107
Comparison of Assemblies of Four-Link Structural Groups of 3rd Class on the Transmission Angle . Matsyuk I.N., Morozova T.I., Shlyakhov E.M.	124
The Mechanics of a Cantilever Beam with an Embedded Horizontal Crack Subjected to an End Transverse Force, Part A: Modelling. Panos G. Charalambides, Xiaomin Fang	131
The Mechanics of a Cantilever Beam with an Embedded Horizontal Crack Subjected to an End Transverse Force, Part B: Results and Discussion. Panos G. Charalambides, Xiaomin Fang...	157
Lagrangian Representations and Solutions of Modified Emden-Type Equations. Aparna Saha, Benoy Talukdar	176
Improvement of Fourier Series Convergence on the Basis of Splines and Its Application for Numerical Inversion of Laplace Transform. Tanya Solyar	188
On the Boltzmann Equation of Thermal Transport for Interacting Phonons and Electrons. Amelia Carolina Sparavigna	203
Dynamical Analyses of Piston Machines Used in Oil Industry. V.I. Bakhshaliev.....	216
VII. ENVIRONMENTAL SAFETY MMSE JOURNAL VOL. 5	223
Study of Ground Treatment on Improvement of Pile Foundation Response in Liquefiable Soils. Chen Yulong	224

Noise-Induced Hearing Loss in Relation With Vibration Disease and Exposure to Vibration Among Employees in Latvia. Kristina Karganova, Jelena Reste	234
IX. ECONOMICS & MANAGEMENT MMSE JOURNAL VOL. 5.....	246
ANFIS and Multi Linear Regression to Estimate the LTLF for the Kingdom of Bahrain. Mohamed Y. Al-Hamad, Isa S. Qamber.....	247
Taxation of Public Owned Land for Real Estate Reconstruction in Kiev, Ukraine. M.A. Malashevskyy, I.M. Ciobanu	262
The Benchmark Survey Methods of the Lecturers and Chairs Work in the Higher Educational Establishments, with Using the Cumulative Ranking Index. Protsiv I.V., Shevchenko O.V., Protsiv V.V.	270

I . M a t e r i a l s S c i e n c e
M M S E J o u r n a l V o l . 5



Detection of Iron Oxide Layer in Quenched and Tempered Gear Steel Using Magnetic Barkhausen Noise

M. M. Blaow ^{1, a} and M. M. Sawalem ^{2, b}

1 – Department of Materials Science and Engineering, Faculty of Engineering, University of Misurata, Aljazera Street, Misurata, Libya

2 – Department of Mechanical Engineering, Faculty of Engineering, University of Misurata, The Coase Road, Misurata, Libya

a – mblaow@yahoo.co.uk

b – ferretti355@gmail.com



DOI **10.13140/RG.2.1.1027.5444**

Keywords: magnetic Barkhausen noise profile, tempering, oxidation, hysteresis.

ABSTRACT. This paper deals with the non-destructive evaluation of surface oxidation of gear steel using magnetic Barkhausen noise profiles analysis. Martensitic specimens are subjected to tempering at various temperatures in a muffle furnace. Tempering induced changes result in Barkhausen profile height increase and peak centers shift to lower fields. Single peak profiles are associated with specimens tempered up to 500 °C. Double peak profiles are seen with specimens tempered at 600 °C and 700 °C. Single peak profiles are observed after removing the oxide layer. The utilization of MBN method for this purpose is based on the difference in the inherent magnetic properties between the degraded surface layer and the sub-surface unaffected bulk. The observations are discussed in the light of established models of Barkhausen noise.

Introduction. The manufacturing processes for gear components include heat treatment operations to achieve surface characteristics for components to increase wear resistance. Heat treatments include carburizing and induction hardening which introduce a hard layer at the surface and maintain a soft interior. Recently Ovako 667 steel was developed for low cost manufacture of wear-resistant elements. This type of steel could be fully hardened by air-cooling from the austenite region. Another feature is that the material is resistant to over-tempering.

When a ferromagnetic material is magnetized by a varying magnetic field, the local changes in the magnetization induces voltage pulses in a search coil placed on the surface which are known as magnetic Barkhausen noise [1]. Magnetic Barkhausen noise (MBN) is mainly associated with the irreversible domain wall movement and refers to the abrupt discontinuous changes in the magnetization rate that result from domain walls overcoming various types of obstacles in their path. Obstacles include grain boundaries, voids and precipitates [2]. The sensitivity of MBN to microstructural inhomogeneities makes it potentially useful as a non-destructive testing technique. Also, the assessment of microstructure and mechanical properties after initial heat treatment as a quality control measurement and their subsequent degradation during service such as exposure to high temperature [3]. In steels, microstructural defects like grain boundaries, inclusions and dislocations promote both mechanical and magnetic hardening, increasing the area of hysteresis curve and reducing permeability. This happens because the same defects which pin dislocations also may “pin” domain walls while moving under the effect of a time varying excitation field [4].

In case carburized and decarburized steels a hardness gradient is present [5-9]. This can cause two MBN intensity peaks to appear at different field strengths. The reason is that each peak originates in a material layer of different hardness. The variation in ferromagnetic material properties can be correlated to different parameters derived from the MBN signal profile generated during the magnetization cycle [10]. The aim of the study is to investigate the magnetic Barkhausen noise response from iron oxide layer formed at the surface of martensite tempered at elevated temperatures as a function of weeping magnetic field.

Materials and Method. The composition of the stock material is shown in Table 1. In the present work, bars ($10 \times 10 \times 120$ mm) machined from the stock were austenitized in vacuum to prevent surface oxidation and decarburization of the specimens. Martensitic specimens were tempered in a muffle furnace at 500, 600 and 700° C for 1 hour to produce different degrees of oxidation. The details of the MBN apparatus is shown elsewhere [13]. In this experiment, the magnetizing frequency used was 1 Hz to enhance the MBN signal to noise ration and maintain a low magnetization rate.

Table 1. Composition of Ovako 677 steel

Element	C	Mn	Ni	Cr	Mo	Si	S	P
Wt %	0.67	1.48	0.11	1.03	0.25	1.46	0.007	0.016

Results. Figure 1 shows half-cycles MBN profiles of a quenched specimen and quenched and tempered at 500°C specimen.

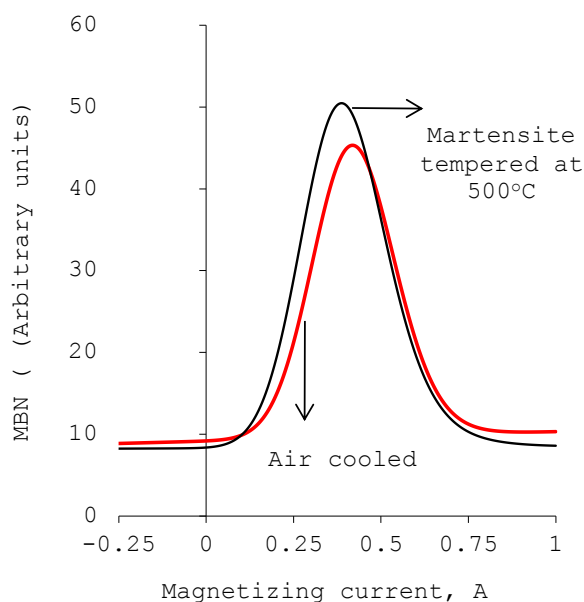


Fig. 1. Half-magnetizing cycle Barkhausen profile from specimen tempered at 500 ° C.

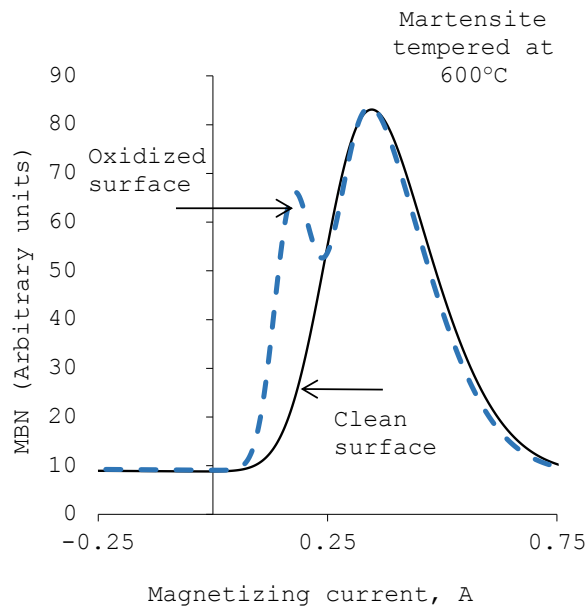


Fig. 2. Half-magnetizing Barkhausen profile from the specimen tempered at 600° C.

The specimens oxidized at 600 and 700 °C show MBN profiles appear to consist of two overlapping peaks (Figs. 2 and 3). It seems reasonable to assume that the MBN profiles reflect the composition gradient at the skin depth of the specimens, which are the iron oxide at the surface and the steel at the subsurface. Figure 4 shows that the second peak at higher field from the oxidized specimen fits with MBN profile of the cleaned specimen which implies that the oxide layer is thin and does not attenuate the Barkhausen emission from the bulk material. After removal of the oxide layer, the specimen tempered at 700 °C shows a remarkable increase in the MBN emission (Fig. 3) compared to that from the oxidized surface.

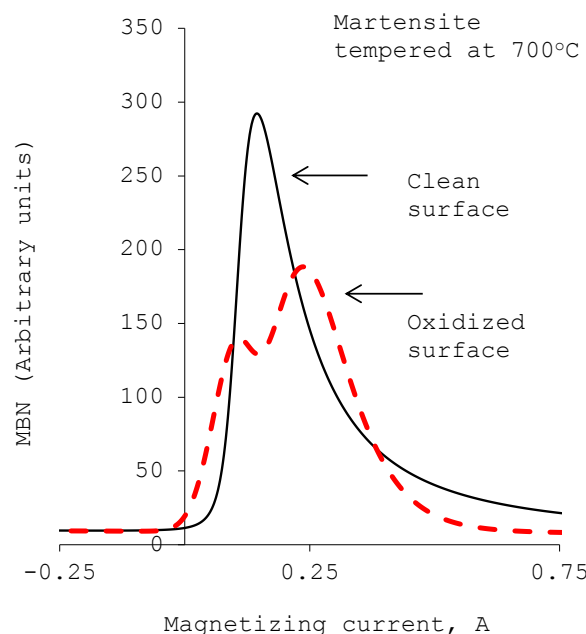


Fig. 3. Half-magnetizing Barkhausen profile from the specimen tempered at 700° C.

This indicates that the oxide layer is able to attenuate the MBN signals from the bulk material. Barkhausen profiles of the quenched and tempered specimens without oxides are shown in Fig. 4.

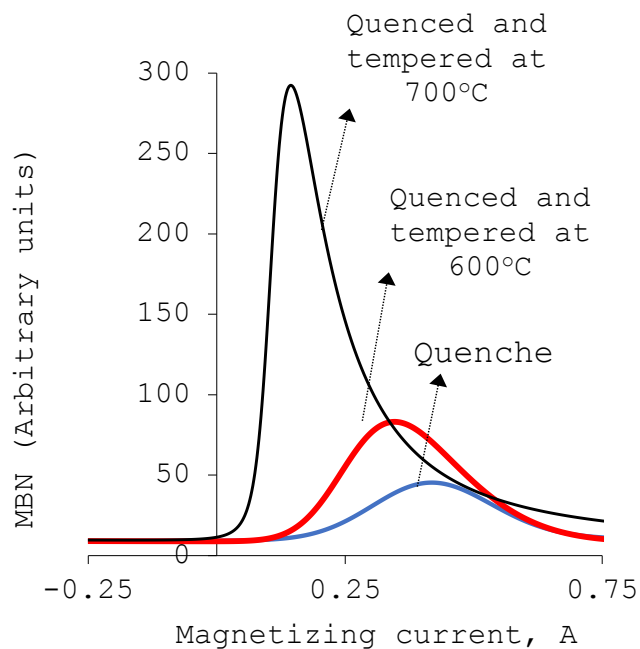


Fig. 4. MBN profiles showing tempering induced changes.

Discussion. Although MBN has been attributed to a number of mechanisms, most current thinking associates it with the irreversible movement of domain walls. Theoretical models highlighting the connection MBN and the irreversible component of magnetisation M_{irr} have been reviewed by Jiles¹⁴. A basic assumption is that the intensity of emission is proportional to the differential susceptibility $\chi_{\text{irr}} = dM_{\text{irr}}/dH$, where H is the magnetic field. This is illustrated schematically in Fig. 5, where the $M_{\text{irr}}-H$ hysteresis loop is shown in relation to MBN emission for a complete magnetisation cycle. The amplitude of emission is greatest when the slope of the $M_{\text{irr}}-H$ curve is a maximum, and smallest at points approaching saturation. The MBN characteristics observed for the different microstructures (Fig. 4) are consistent with the theory. If the hysteresis loop becomes narrower, with steeper sides, the peak intensity of emission will increase and the position of the peak will shift towards zero field. The converse will occur if the hysteresis loop becomes broader with a smaller maximum slope. In the experiments, peak position (Fig. 4) shifted to lower values as the microstructure changes from martensite to ferrite-cementite microstructure.

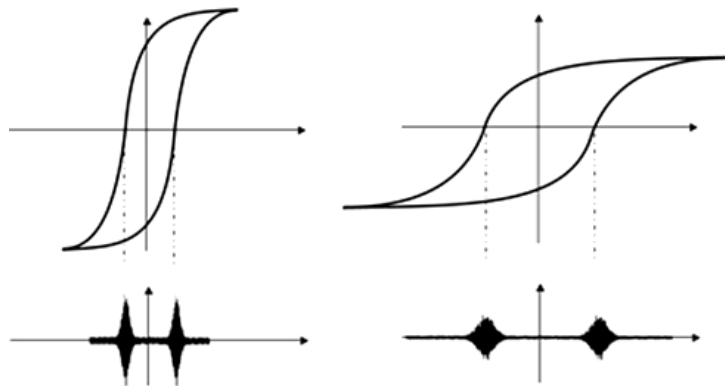


Fig. 5. Magnetic hysteresis loops and the corresponding MBN signals [14].

It is widely accepted that the Barkhausen noise signal is strongly dependent on the number of pinning obstacles met by domain walls during the magnetization process. The peak amplitude is thus strongly sensitive to the phase proportion, whereas the position of the peak is usually linked to the nature and the strength of the obstacles. The discontinuous jumps of Bloch walls are due to their local pinning by different obstacles such as inclusions, precipitates, grain boundaries, and dislocation tangles. The MBN increases with the number of these pinning obstacles. A shift of the peak to the high value of the magnetic field is also observed when the influence of these obstacles on Bloch walls increases. Because the magnetic structure is directly linked to the nature of metallurgical state and hence its differential susceptibility, each phase has its inherent magnetisation saturation and hence a distinctive MBN response [15, 16]. This is consistent with the present observations on the oxidized and non oxidized specimens. The differential susceptibility of iron oxide layer is different from that of ferrite and cementite structure and hence this results in two magnetization responses (MBN) relative to the applied sweeping field .

Summary

1. Iron oxide layer results in a split of the profile into two peak's profiles revealing the iron oxide and the bulk material.
2. Iron oxide layer at the surface of the specimens attenuates the MBN signals.
3. Magnetic Barkhausen noise technique is very sensitive to microstructural gradient at the surface and the subsurface bulk.

References

- [1] E. Gorknov, Yu. Dragoshanskii, and M. Mikhovki. Barkhausen noise and its utilization in structural analysis of ferromagnetic materials (review article v) 5. Effects of volume and surface thermal processing, Russian Journal of Nondestructive Testing, 36 (6) 389 (2000).
- [2] D.C. Jiles, The influence size and morphology of eutectoid carbides on the magnetic properties of carbon steels, Journal of Applied Physics, 63, 2980, 1988.
- [3] D. D'Amato, C. Verdu, X. Kleber, G. Regheere, and A. Vicent, Characterization of Austempered Ductile Iron Through Barkhausen Noise Measurements Journal of Nondestructive Evaluation, Vol 22 (4), pp 127-139, 2004, doi: 10.1023/B:JONE.0000022032.66648.c5.
- [4] D. C. Jiles, "Dynamics of domain magnetization and the Barkhausen effect, Czechoslovak Journal of Physics, 50, 893, 2000.

[5] J. Alessandra, , L. Gunther, and F. Gerhardt, Magnetic Barkhausen Noise Profile Analysis: Effect of Excitation Field Strength and Detection Coil Sensitivity in Case Carburized Steel, Materials Sciences and Applications, Vol. 16, pp.1015-1019, 2013, doi: 10.1590/S1516-14392013005000095.

[6] Hao, X. J., Yin, W., Strangwood, M., Peyton, A. J., Morris, P. F., & Davis, C. L. (2008). Off-line measurement of decarburization of steels using a multifrequency electromagnetic sensor. *Scripta Materialia*, 58(11), 1033-1036. DOI:10.1016/j.scriptamat.2008.01.042.

[7] Lo, C.C.H., Kinser, E.R. and Jiles, D.C. Analysis of Barkhausen Effect Signals in Surface Modified Magnetic Materials Using a Hysteretic Stochastic Model. *Journal of Applied Physics*, 2006.

[8] M. Blaow, J. Evans and B. Shaw, Magnetic Barkhausen noise: the influence of microstructure and deformation in bending, *Acta Materialia*, Vol 53, pp. 279-287, 2005, doi:10.1016/j.actamat.2004.09.021.

[9] X. Kleber, A. Hug-Amalric, and J. Merlin, Evaluation of the Proportion of Phases and Mechanical Strength of Two-Phase Steels Using Barkhausen Noise Measurements: Application to Commercial Dual-Phase Steel, *Metallurgical and Materials Transactions A*, Vol. 39, pp.1308-1318, 2008, doi: 10.1007/s11661-008-9508-3.

[10] D. C. Jiles, L. B. Sipahi, and G. J. Williams, *J. App. Phys* Vol. 73, p. 5830, 1993.

[11] M. Kaplan C. Gür and M. Erdogan, J, Characterization of Dual-Phase Steels Using Magnetic Barkhausen Noise Technique, *Journal of Nondestructive Evaluation*, Vol. 26, pp.79-87, 2007, doi: 10.1007/s10921-007-0022-0.

[12] M. J. Sablik, *J Appl Phys*, Vol. 74, pp.5898, 1993

[13] M. M. Blaow, J. T. Evans and B. A. Shaw, *J. Magn. Magn. Mat.*, Vol.303, pp.153, 2006.

[14] D.C. Jiles, *Czechoslovak J. Phy.* Vol. 50, 893 (2000).

[15]O. Saquet, J. Chicois, and A. Vincent, *Mat. Sci. Eng. A*, Vol. 269, pp. 73-82, 1999.

[16] M. M. Blaow and B.A. Shaw, Magnetic Barkhausen Noise Profile Analysis: Effect of Excitation Field Strength and Detection Coil Sensitivity in Case Carburized Steel, *Materials Sciences and Applications*, Vol. 5 pp.258-266, 2014, doi: 10.4236/msa.2014.55030.

Development and Determination of the Age Hardening Characteristics of Al-2.00Mg-2.66Si Wrought Alloy

Ihom A.P.^{1, a} and Aniekan Offiong¹

1 – Department of Mechanical Engineering, University of Uyo, Uyo , PMB 1017 Uyo-Nigeria

a – ihomeondona@gmail.com, ihomeondona@uniuyo.edu.ng



DOI **10.13140/RG.2.1.1965.7207**

Keywords: precipitation hardening, characterization, solutionising, wrought alloy, development, determination.

ABSTRACT. The study, was carried out by developing the alloy using the foundry route of melting, alloying, and casting. The produced test samples were machined to produce test specimens which were subjected to precipitation hardening treatment. The test specimens were for impact and hardness test to inference the response of the developed alloy to age hardening treatment. The ageing temperature was 190°C, and the ageing time was from 1 -5 hrs. The control specimen was not age hardened and when compared with the age hardened specimens, the tested mechanical properties of the age hardened specimens were better than the control specimen. The hardness was seen to increase, with ageing time peaking at 3hrs of ageing to a value of 38.34 HRB, dropped and rose after 4hrs of ageing and continued to increase, thereby prompting curiosity. The toughness had a steady increase as the ageing time was increased, which clearly showed that the developed alloy responded to age hardening treatment.

Introduction. A lot of aluminium-based alloys have been developed and characterized as can be seen in B.S. Aerospace Series, section L (aluminium and light alloys). Specification of the aluminium-based alloys is clearly stated unfortunately the specification for this research work could not be sighted however, close compositions were seen. According to the wrought aluminum alloy designation system, alloys of these series (Al-Si-Mg) are designated 6xxx. Aluminum – Magnesium – Silicon alloys are heat treatable [2, 5, 11]. Solution treatment followed by either artificial or natural ageing allows considerable increase in yield-strength (3-5 times). Ductility of the alloy decreases as a result of the heat treatment. Hardening of the alloys from this group is achieved due to precipitation of the phase Mg-Si occurring during ageing [5]. The phase has a fixed ratio between the elements content (valence compound), therefore amount of magnesium and silicon in 6xxx alloys is balance according to this ratio or with an excess of silicon. Alloys of this series possess high mechanical strength combined with good formability and corrosion resistance. Excess of silicon enhances effect of precipitation of the alloys but decreases their ductility because of segregation of silicon in the regions of grain boundaries. This adverse effect of silicon may be diminished by addition of chromium and manganese depressing recrystallization during solution treatment. Temperature of artificial ageing of 6xxx alloys is 320 – 360°F (160 – 182°C). Aluminum – Magnesium - Silicon alloys (6xxx series) are used in aircraft and automotive applications, in architectural applications and as structural materials [2].

Aluminium alloys used in both cast and wrought forms may be precipitation hardened if of suitable composition. Age-hardening as it was then called, was infact discovered in some aluminium-based alloys at the beginning of the century and subsequently developed for use in military aircraft during the First World War. The extent of the formation of coherent precipitates at ordinary temperatures is limited so that strength attains a fairly low maximum value in a few days and this process used to be called ‘age-hardening’. At higher temperatures the formation of coherent precipitates proceeds further and so the strength continues to increase. However, a point is reached where the thermal activation is such that tiny non-coherent particles of θ begin to form in accordance with phase equilibrium. Other wrought aluminium alloys which can be precipitation hardened are those

containing small amounts of magnesium and silicon. These form the compound Mg_2Si the solubility of which, like that of $CuAl_2$, increases considerably with temperature [11].

Pure aluminium is relatively soft and weak, it has a tensile strength of no more than $90N/mm^2$ in the annealed condition-and for most engineering purposes is used in the alloyed form. The strengths of many aluminium-base alloys can be further increased by precipitation hardening to produce a strength / mass ratio of the same order as for high-tensile steels. The greater relative volume of aluminium alloy involved for a specific force-bearing capacity means that greater flexibility in design is possible. The objective of this research is to develop another aluminium alloy from the 6xxx series (Al-Mg-Si) and determine its ageing characteristics in terms of effects on its hardness and toughness properties. It's already established that there is a relationship between hardness and tensile strength for most metallic materials although it may not be a direct proportional relationship [1, 11]. In like manner there is a relationship between tensile strength and toughness of a material, this can be observed in stress-strain curve where the area under the curve is proportional to the energy required to fail the metal. This energy is equal to the energy required to fail the same material under toughness or impact test. By implication the toughness of a material can be inferred from the area under the curve of its stress-strain plot [5].

Materials and Method.

Materials. The materials used for this project included the following: aluminium cables which were procured from an electrical company in Uyo, pure silicon and magnesium were acquired from Zaria and other materials like, salt (NaCl), sand, clay and water were locally sourced in the University of Uyo and Uyo town.

Equipment. The equipment used during the research included; melting furnace, round metal mould, impact tester, Hardness tester, centre lathe, hack saw, Bench vice, crucible pot, electric furnace with $1200^{\circ}C$ peak capacity, furnace pan and tong, vernier caliper, electronic measuring scale, and stop watch.

Method. Aluminum cables known to possess 99.8% purity, silicon powder, industrial salt (NaCl), and magnesium were used to produce Al-2.00Mg-2.66Si wrought alloy. The Foundry route was used for the production. Metal moulds, charge preparation and calculation were all carried out before melting in the crucible furnace where it was possible to stir the melt for homogeneity. The melt was poured to produce four test samples of $20.6\text{ mm dia} \times 302\text{ mm}$. These were used to produce test specimens for solutionising and ageing treatments before they were subjected to hardness and toughness tests. Details of the work procedure is as presented below:

Charge Calculations. Total quantity of the developed alloy required for characterisation = 1.4kg (1400g).

But percentage of the alloying element required for the production of the wrought alloy was calculated as follows:

$$\text{The percentage of silicon} = \frac{37.2}{1400} \times 100 = 2.66\%$$

$$\text{The percentage of Mg used} = \frac{28}{1400} \times 100 = 2.0\%$$

The total weight of the cast samples was 1400g and the amount of Si and Mg, used were 37.2g and 28g respectively.

Therefore $37.2+28.0 = 65.2\text{g}$

Subtracting 65.2g from total cast material the balance will be 1334.8 g i.e $(1400-65.2)$

Total amount in grammes of Al used = 1334.8g .

Preparation of the mould:

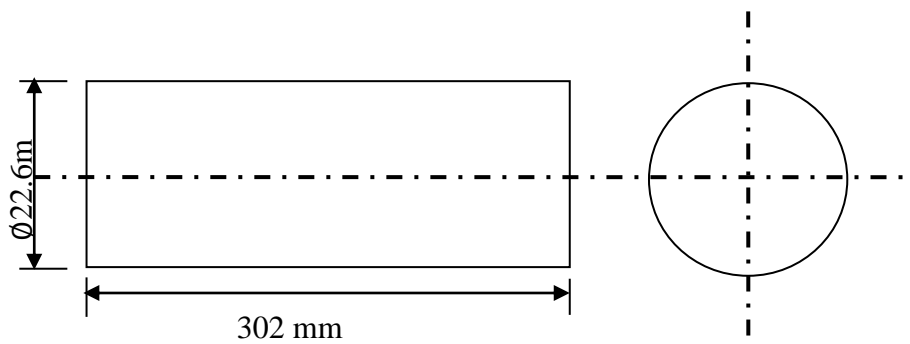


Fig. 1. Side view and bottom view of the steel pipe used in the construction of the metal moulds.

Fig. 1 shows a 302 mm length x 22.6 mm diameter pipe before the pipe was divided into half. Round and flat file was used to remove built up and sharp edges from the surface of the cut to maintain a smooth surface. This pipe was divided in this manner so as to enable the easy removal of the solidified alloy after pouring. Flat sheet metal was welded to each half of the pipe using electric welding. The two halves were brought together again to make one piece, binding wire was used to hold it together and clay was used to seal the opening at the joint. The moulds prepared in this way were dried and ready for use.

Melting and Casting.

The charge as calculated above was transferred to the crucible furnace, where the aluminium was first charged and allowed to melt before the addition of the magnesium and silicon alloying elements. Industrial salt (NaCl) was sprinkled to the melt and vigorously stirred to obtain a homogeneous melt before pouring into the already prepared moulds. The castings were allowed to cool before they were removed from the moulds.

Specimen Preparation.

The sample test bars were as shown in Plate 1, they were machined to produce standard test specimens for hardness test and toughness test. The hardness test specimens were 20mm x20mm while the toughness test specimens were prepared according to ISO Standard for V-Charpy impact test. Plate II shows the prepared specimens.



Plate I. Sample test bars of Al-2.00Mg-2.66Si Alloy.



Plate II. Impact and hardness test specimens before being subjected to ageing process.

Ageing Treatment. The test specimens shown in Plate II were subjected to ageing treatment with the exception of the control specimens. The specimens for ageing treatment were first solutionised at 500°C using the furnace shown in plate III. The test specimens were then quenched in warm water. The quenched specimens were removed and dried before precipitation treatment at 190°C in the same furnace shown in plate III. The ageing time of the test specimens ranged from 1 hr to 5 hrs in steps of 1hr. After the ageing treatment the test specimens were ready for mechanical properties testing.



Plate III. The furnace used for precipitation treatment.



Plate IV. Removal of specimen after each hour of ageing time.

Hardness Testing Procedure. In this experiment test pieces were in round shape as shown in the plate IV below:



Plate V. Hardness specimen before undergoing hardness test.

The test pieces were placed on the table of the testing machine, the wheel was rolled to bring into contact the test piece and the indenter under a minor load of 9.8 kg, which took up the “slack” in the system while the dial indicator was set to zero. The major load was then applied; the indicator made about 2 revolutions before becoming steady, and the hardness value was directly read on the indicator. The machine used had an indenter steel ball (1.6 mm) and Rockwell Hardness B-Scale with minor load 98N (9.8kgf) and major load 980N (100kgf) were selected. The hardness machine identity was Karl Frank 6MBH, WEINHEM BIRKENAH, type – 38506 and werk-Nr-21289.

Impact Testing Procedure. A Notch-bar test piece of standard geometry was mounted horizontally on the anvil of the machine which was struck by a fast moving weighted pendulum with a velocity of 5.24 m/s, while the energy absorbed in breaking the specimen was measured in joules and read directly from a dial indicator. It measured the relative toughness of the material, which indicated the material capacity to absorb energy and deform plastically before fracture. The machine capacity was 300J scale-Charpy with test temperature being room temperature; velocity of pendulum was 5.24 m/s, and the equipment was made by Avery-Denison, England.

Results and Discussion.

Results. The results of the research are displayed in Tables 1-3 below. The variation of the hardness and toughness of the material with ageing time is also shown in figs. 2-3.

Table 1. Result of the hardness test.

Ageing Time	Average Hardness Value
0 hr (unaged)	36.50
1 hr (aged)	36.00
2 hrs (aged)	35.95
3 hrs (aged)	38.34
4 hrs (aged)	34.00
5 hrs (aged)	39.33

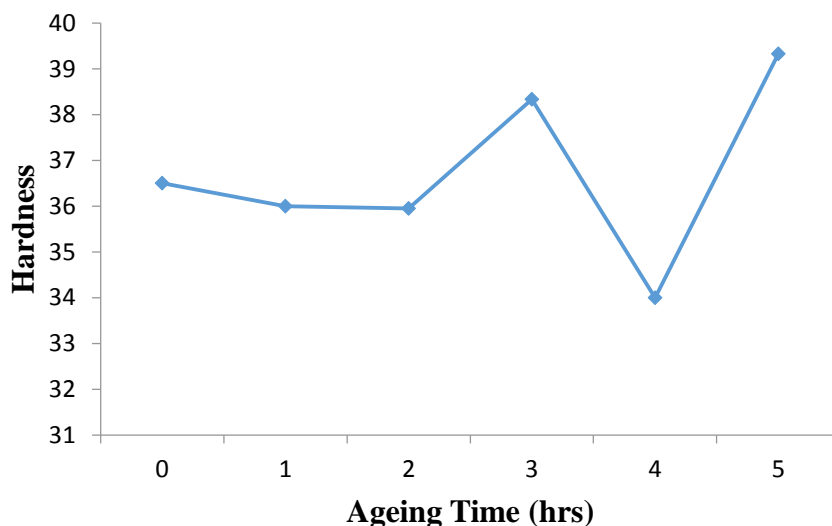


Fig. 2. Hardness variation of the developed Al-2Mg-2.66Si alloy with ageing time.

Table 2. Result of impact test.

Ageing Time	Energy absorbed (J)	Type of specimen
1hr	8j note: blow hole noticed in the sample	Standard v- note (square shape)
2 hrs	28j	Standard v- note (square shape)
3 hrs	21j	Standard v- note (square shape)
4 hrs	28j	Standard v- note (square shape)
5 hrs	38j	Standard v- note (square shape)
Control (Unaged specimen)	9.5j	Standard v- note (square shape)

Table 3. Ageing time versus toughness.

Ageing Time	Toughness
0 hr (unaged)	9.5j
1 hr (aged)	8j
2 hrs (aged)	20j
3 hrs (aged)	21j
4 hrs (aged)	28j
5 hrs (aged)	38j

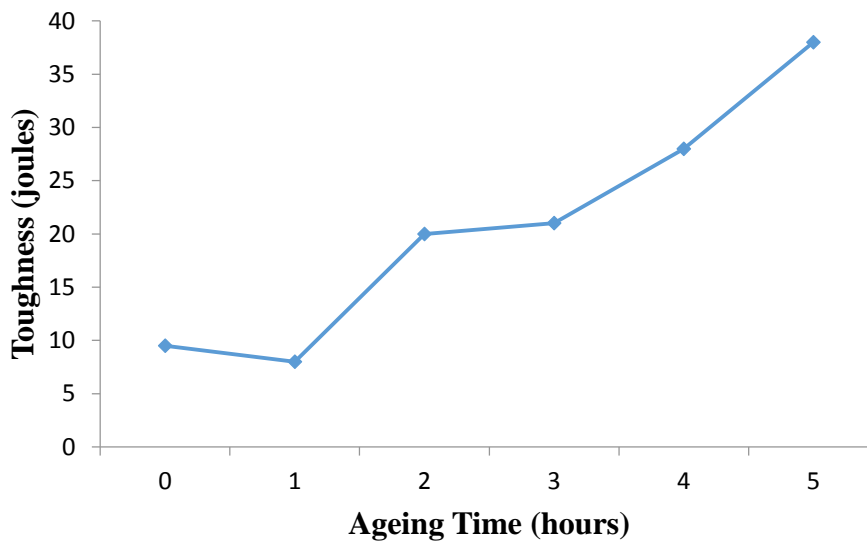


Fig. 3. Toughness variation of the developed Al-2Mg-2.66Si alloy with ageing time.

Discussion. The objective of this research is to develop a wrought aluminium alloy of the composition Al-2Mg-2.66Si and to determine whether it has ageing characteristics. This objective has been implemented and the burden of proof lies with the results generated from the mechanical tests carried out on the developed alloy. The results are interesting as discussed below and should elicit more research work on the alloy from the materials science and engineering research world.

Analysis of Hardness Test Result. Table 1 shows the result of the hardness test and Fig.2 shows a graphical representation of the variation of hardness and the ageing time at constant temperature (190 ^0C). The hardness value of the unaged specimen was 36.50HRB this value dropped gradually to 35.95HRB at 2hrs of ageing. This softening is normal because of the precipitates being formed and rearrangement of atoms. Immediately after 2 hrs of ageing the hardness started increasing and peaked at 38.34HRB this pattern fits in with previous works which showed the curve peaking at 3hrs and then the hardness dropping with further ageing. The hardness in this case actually dropped to 34.00HRB at 4hrs of ageing but suddenly started rising and rose to 39.33 at 5hrs of ageing. It is possible that the hardness will continue to increase beyond the 5hrs of ageing. Unfortunately the work terminated at 5hrs it is suggested that further research work should be carriedout which should go beyond the 5hrs used in this work to actually establish the ageing time relationship with the hardness of the developed alloy. The line trend of hardness-ageing time relationship is very interesting and could mean that at longer ageing time; higher hardness values may be obtained. Essien and Udo [2] have observed that the behaviour of the hardness-ageing time curve to rise, fall and start rising again is not uncommon with ageing, it is possible for the hardness to decrease, and is normally linked to the nature of precipitate that has been formed at a particular time. The

formation of Mg_2Si precipitates is normally associated with the alloy system under consideration. Coherent and non-coherent precipitates will exhibit different hardness values. Non-coherent precipitates are normally associated with discontinuities at the interface with the matrix [9]. Their formation therefore normally results in decrease of hardness of the material. Ihom, et al. [7] agreed with the above explanation but further added that the ageing process is a diffusion controlled process and is controlled by this equation.

$$D = D_0 e^{Q/RT} \quad (1)$$

Where D is the diffusion rate;

D_0 is the diffusion co-efficient;

Q is the activation energy required to move an atom;

R is the gas constant and T is the temperature in Kelvin.

At higher temperatures, the movement of solutes is faster because the activation energy required is met quickly. Also time is required for the atoms to diffuse to new position X ; that is why the distance travelled by the atoms is a function of diffusion coefficient and resident time of the aged alloy ($X = \sqrt{D_0 t}$). According to the equation the extent of interdiffusion X increases with the square root of time t . Therefore if a longer ageing time is applied it may lead to over-ageing, which means the hardness cannot continue to increase indefinitely but must reduce after some time [7, 9, 10].

Impact Test. The essence of the impact test was to determine the effect of age hardening on the developed alloy as would manifest in the toughness of the material with increased energy absorption of the specimens before failure (fracture). The result and the pattern as the ageing time is increased is shown in Tables 2-3. Fig. 3 shows the toughness variation of the developed Al-2Mg-2.66Si alloy with ageing time. The graph clearly shows that as the ageing time was increasing the material toughness was also increasing. There was a drop in toughness value at 1hr of ageing and the reason was as explained in Table 2. There was a blowhole in the test specimen which reduced the true value of the toughness of the material, because of the presence of the blowhole underneath the specimen the energy absorbed before fracture was drastically reduced. The other specimens were defect free and so gave more realistic results. The toughness kept increasing with ageing time, however, previous works have shown that there comes a time when over ageing occurs and thereafter both the hardness and toughness reduces [5, 8]. It therefore means that toughness cannot continue to increase indefinitely with ageing time. The developed alloy from the toughness-ageing time curve has clearly demonstrated that it has responded to precipitation hardening treatment, and it is therefore an age hardening alloy. longer ageing periods may be employed to see the extent of improvement of this property. There is a correlation between toughness of a material and its tensile strength that is why the area under a stress-strain curve can be used to inference the toughness of a material. When the area is small it means the toughness of the material is low the energy absorbed by the material before failure is low, if however, the area under the curve is large it means the material is a tough material and must absorb a substantial amount of energy before failure [5, 8]. From the preceding it therefore means that the tensile strength of the developed material was improved alongside with the toughness of the material as the material was aged at different time intervals.

Summary. The research work titled “Development and Determination of the Age Hardening Characteristics of Al-2Mg-2.66Si Wrought Alloy” has been extensively considered and the following conclusions drawn from the work:

- i) the work developed an alloy of the composition Al-2Mg-2.66Si a wrought alloy that was precipitation hardened at various intervals

- ii) the hardness test results of the age hardened alloy at various periods revealed that the developed alloy responded to age hardening
- iii) the impact results of the age hardened alloy specimens clearly showed that the developed alloy responded to age hardening, as the ageing time was increasing the toughness of the developed alloy was also increasing, and
- iv) the developed alloy exhibited an interesting characteristics as the tested mechanical properties kept increasing with increase in ageing time necessitating the suggestion that further work should be carried out on the developed alloy with ageing treatment covering twelve hours.

Acknowledgement. The authors of this work wish to sincerely acknowledge the contributions of our undergraduate students Mr Essien, E.V., and Mr Udo, U.E. We do hope that the exposure they had during the course of this work will broaden their horizon and help them to appreciate metallurgical engineering.

References

- [1] Alo O.A., Umolu L.E., Ajao J.A. and Oluwasegun K.M. (2012) Thermal, Hardness and Microstructural Characterisation of Al-Si-SiC_p Composites, JMMCE, 11(2), 159-168, doi: 10.4236/jmmce.2012.112013.
- [2] Essien E.V and Udo U.E. (2016) Development and Determination of the Age Hardening Characteristics of Al-Mg-Si based Alloy, B.Eng. Degree project submitted to the Department of mechanical Engineering University of Uyo, Uyo-Nigeria.
- [3] Hassan S.B., Aponbiede O. and Aigbodion V.S. (2008) Precipitation Hardening Characteristics of Al-Si-Fe/- SiC Particulate Composite, Journal of Alloys and Compounds, 466(1-2), 268-222.
- [4] Hassan S.B. and Aigbodion V.S. (2009) The Effect of Thermal Ageing on Microstructure and Mechanical Properties of Al-Si-Fe/Mg Alloys, Journal of Alloys and Compounds, 486 (1-2), 309-314.
- [5] Higgins R.A. (1985) Properties of Engineering Materials, 6th Edition: Great Britain, Hodder and Stoughton Educational.
- [6] Ihom A.P., Nyior G.B., and Zamanni I.G. (2012) The Effect of Thermal Ageing on Microstructure and some Mechanical Properties of Al/2.0% Glass Reinforced Composite, IJRRAS 12(3), 1-6.
- [7] Ihom A.P., Nyior G.B., Nor, I.J., Ogbodo N.J. (2013) Investigation of Egg Shell Waste as an Enhancer in the Carburization of Mild Steel, AJMSE, 1(2), 29-33, doi: 10.12691/ajmse-1-2-3.
- [8] Markson I.E. (2016) The Effects of Pressure on Squeeze Cast Aluminium Alloys, PhD Degree Project Submitted to the Department of Mechanical Engineering, University of Uyo, Uyo-Nigeria.
- [9] Martins J.W. (1998), Precipitation Hardening, 2nd Edition, Butterworth Heinemann, Oxford, pp. 1-20.
- [10] Matthews F.L. and Rawlings R.D. (2005) Composite Materials: Engineering and Science, 4th Edition, England: Woodhead Publishing Limited, pp. 80-90.
- [11] Shragger A.M. (2008), Elementary Metallurgy and Metallography, Second Revised Edition Reprinted, Dover Publications Inc, Newyork, pp. 136-140.

Effect of Textures on Tensile Properties of Extruded Ti64/VGCF Composite by Powder Metallurgy Route

Patchara Pripanapong¹, Shu-feng Li², Junko Umeda², Katsuyoshi Kondoh²

1 – Graduated School of Engineering, Osaka University, 2-1, Yamadaoka, Suita, Osaka, Japan

2 – Joining and Welding Research Institute, Osaka University, 11-1 Mihogaoka, Ibaraki, Osaka, Japan



DOI [10.13140/RG.2.1.1120.1525](https://doi.org/10.13140/RG.2.1.1120.1525)

Keywords: Ti-6Al-4V, VGCFs, composite materials, hot extrusion, dynamic recrystallization.

ABSTRACT. Monolithic Ti-6Al-4V and Ti-6Al-4V composited with vapor grown carbon fibers (VGCFs) were fabricated by powder metallurgy (P/M) route in this research. Spark plasma sintering (SPS) subsequent by hot extrusion was applied in order to fabricate a full-density and high strength composite materials. A severe plastic deformation during hot extrusion resulted in a dynamic recrystallization (DRX) in α -Ti grains. Dynamic recrystallization was observed in a low deformation temperature region, which yield point of material was also observed in the stress-strain curve. Furthermore, the addition of VGCFs encouraged the dynamic recrystallization during hot extrusion. Ti64+0.4 wt-% VGCFs shows the highest tensile strength of 1192 MPa at the end part of the extruded rod where the temperature of material was lower compared to the tip and middle part during extrusion. Additionally, the improvement in tensile strength was contributed by solid-solution strengthening of carbon element originated from VGCFs in α -Ti matrix.

Introduction. Ti-6Al-4V alloy (Ti64) is the most well-known among Ti alloys, and used in many industries. High specific strength, good corrosion resistance and biocompatibility promoted a widely use of Ti and its alloys such as in aerospace and automobile industries, or medical devices and prosthesis [1, 2]. Many researchers studied the effect of hot working on microstructure and mechanical properties of wrought or cast Ti64. A. Momeni et al. studied the effect of deformation temperature and strain rate on microstructure and flow stress of wrought Ti64 under hot compression test [3]. Ti64 specimens, which experienced a hot compression test at 1273 and 1323 K, exhibited a large recrystallized α -grain with low flow stress on the microstructure. This correlated with the results proposed by T. Seshacharyulu et al. and R. Ding et al. for the cast Ti64 [4, 5]. G.Z. Quan et al. studied the modelling for dynamic recrystallization in Ti-6Al-4Al by hot compression test. The result shows that a flow stress decreases with the increasing of deformation temperature. The high deformation temperature promotes the mobility at the boundaries for annihilation of dislocation, and the nucleation and growth of dynamic recrystallization [6]. H.Z. Niu et al. studied the phase transformation and dynamic recrystallization (DRX) behaviour of Ti-45Al-4Nb-2Mo-B (at-%) alloy. The results show that the DRX modes were strongly depends on deformation temperature, and a decomposition of lamellar structure along with the DRX of γ and B2/ β grain occurred at low forging temperature [7]. D.L. Ouyang et al. studied the recrystallization behaviour of Ti-10V-2Fe-3Al alloy after hot compression test. They reported that a partial grain refinement related to incomplete DRX was observed even after a large strain of 1.6, and an increment of strain resulted in an increasing of volume fraction of recrystallized grain. The full grain refinement accompanied by the completely DRX was developed at lower temperature of 1223 K by severe deformation [8]. The dynamic recrystallization behaviour of Ti-5Al-5Mo-5V-1Cr-1Fe alloy was reported by H. Liang et al. The DRX always occur when the store energy in a material reaching the critical value. During hot deformation, the increase of flow stress caused by dislocation generation and interaction resulted in an improvement of strength of Ti alloys. The sample deformed at 1073 K exhibited higher tensile strength compared to sample deformed at 1153 K because more dislocations were generated [9]. There are many reports related to dynamic recrystallization of Ti alloys but no report in dynamic recrystallization behaviour of Ti64 composite

with VGCF, and its effect on tensile properties of composite material was found yet [10, 12]. The objective of this research is to study the texture of Ti64 and Ti64 composites fabricated by spark plasma sintering, and subsequently hot extruded. The effect of dynamic recrystallization on tensile properties of monolithic Ti64 and Ti64/VGCF composite materials were investigated through this research. The samples cut from the end and middle part of extruded rod (extruded temperature lower than 1243 K) show a DRX structure which many of small nucleated grains were observed. Tensile sample obtained from the part that experienced extrusion at low temperature exhibited a high tensile strength because a large amount of defects was generated in a sample.

Experimental procedure. Ti-6Al-4V atomization powder (Osaka Titanium Technology Co., Ltd. TIOP64-45) with a spherical shape and diameter of 45 μm (fig. 1a), and vapor grown carbon fibers (Showa Denko K.K., VGCFsTM) with 8 μm in length and diameter of 150 nm (fig. 1b) were applied in this research. The chemical composition of Ti64 powder was listed in Table 1. Ti64 powder was mixed with cleasafe oil (0.15 g) by table milling equipment for 3.6 ks with rotation speed of 90 rpm and subsequently mixed with VGCFs by rocking milling for 7.2 ks. Rocking milling was performed for long time in order to provide a uniform distribution of VGCFs on powder surface. The Ti64 composite materials were fabricated in three compositions such as 0, 0.1 and 0.4 wt-% of VGCFs. The Ti64/VGCFs mixed powder was poured in the carbon container, which has an inner diameter of 42 mm. The inner wall of container was sprayed with boron nitride to prevent a reaction between Ti64 powder and carbon container during SPS. The monolithic Ti64 and mixed Ti64/VGCFs powder were pre-compactated by hydraulic hand press under pressure of 20 MPa before sintering. The green compacts were consolidated by spark plasma sintering (Syntech CO. SPS103S) at 1273 K with heating rate of 0.54 K/s for 1.8 ks, and the pressure of 30 MPa was introduced to a green compact under vacuum atmosphere of 5 Pa. Afterwards, the sintered billets were preheated in a horizontal image furnace at 1323 K for 0.6 ks under argon atmosphere before hot extruded into 12 mm in diameter rod by 200 ton press machine (THK Slidepack FBW3950R 1200L) with an extrusion speed of 6 mm/s. The sintered billets and extruded specimens were cut for microstructure observation. For extruded rod, the samples were cut from three positions which are shown in fig. 2. The samples were ground with SiC abrasive paper, polished with Al_2O_3 colloidal and etched by Kroll etchant ($\text{H}_2\text{O}:\text{HNO}_3:\text{HF} = 100:5:1$) for microstructure observation. For EBSD analysis, the specimens were polished with SiO_2 colloidal by vibratory polisher. The microstructures observation and phase analysis of sintered and extruded specimens were performed by optical microscope and scanning electron microscope (JEOL JSM6500F). The grain size and texture were analysed by electron back-scatter diffraction (EBSD) method. The tensile samples were machined from three positions in extruded rod (fig. 2) with 20 mm in gauge length and 3 mm in diameter. The universal tensile test machine (Autograph AGX 50 kN, Shidmazu) was applied for tensile test with strain rate and cross head speed of $5 \times 10^{-4} \text{ s}^{-1}$ and 6 mm/min, respectively.

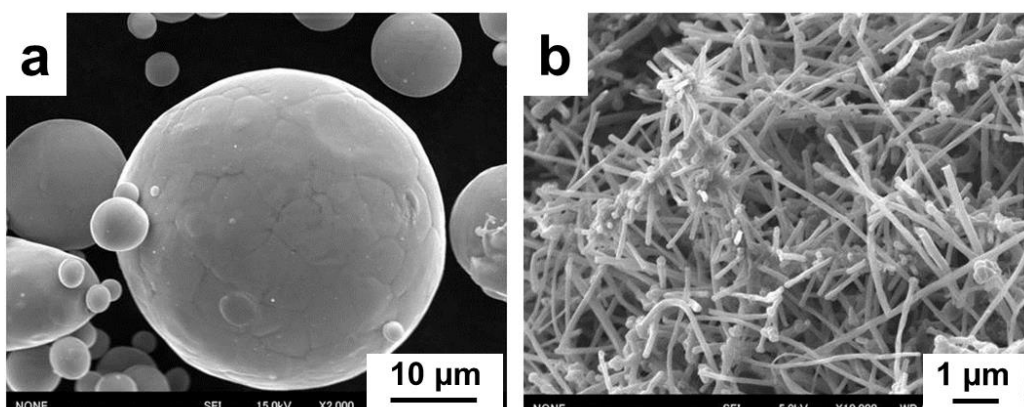


Fig. 1. SEM micrograph of (a) Ti-6Al-4V atomization raw powder, (b) Vapor grown carbon fibers (VGCFs).

Table 1. Chemical composition of Ti-6Al-4V atomization raw powder (wt-%).

Material	Al	V	Fe	C	O	N	H	Ti
Ti-6Al-4V	6.12	4.48	0.03	0.01	0.13	0.014	0.006	Bal

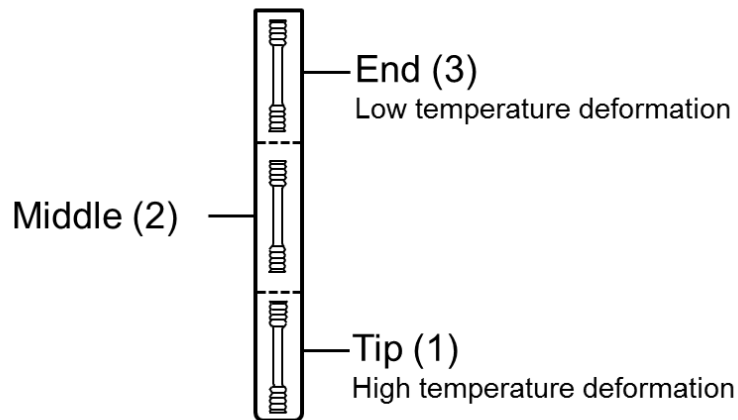


Fig. 2. Microstructure observation positions in extruded rod.

Results and discussion. The microstructures of Ti64 and Ti64+0.1wt-%VGCFs after SPSed including texture information such as pole figure (PF), inverse pole figure (IPF) and intensity of each plane direction are shown in fig.3. The monolithic Ti64 that was SPSed at 1273 K, which is above β transus temperature (1243 K) shows a large prior β grains of 170 μm (separated by yellow dash line) and α -lamellar colonies inside β grain (fig. 3a). The microstructure evolution was explained by the change of allotropy at 1243 K from α (hcp) to β (bcc) during heating followed by precipitation of α -lamellar phase inside grain and along the grain boundaries of prior β during cooling. On the other hand, Ti64+0.1wt-%VGCFs shows a different microstructure structures compared to monolithic Ti64 (fig. 3b). The microstructure of Ti64+0.1-wt%VGCFs consisted of α -lamellar and α -equiaxed which formed during cooling from β region to $\alpha+\beta$ region, and $\alpha+\beta$ region to α region, respectively [13, 14]. This microstructure evolution was also observed in Ti64+0.4-wt%VGCFs. The difference in microstructure between monolithic Ti64 and Ti64/VGCFs composite material was explained by an effect of α stabilizer of carbon that increased β transus temperature of composite material. Crystal orientation of Ti64 and Ti64+0.1wt-%VGCFs after SPSed was shown in fig. 3c and 3d, respectively. The random crystal orientation was observed in both materials including Ti64+0.4wt-%VGCFs, which was similar to cast alloy [15].

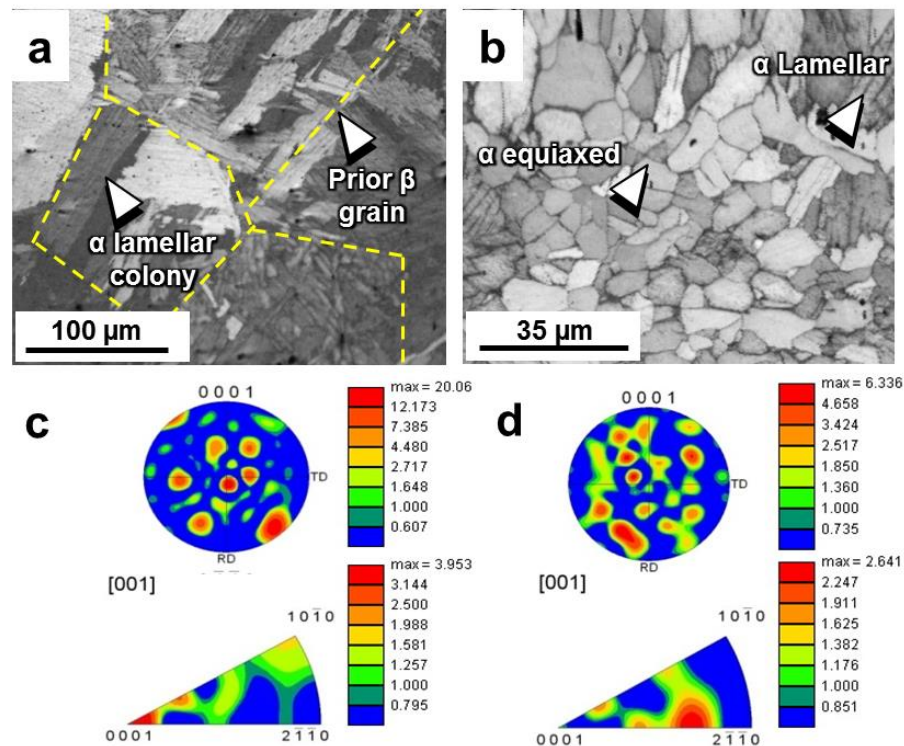


Fig. 3. SEM micrograph of (a) Ti64 and (b) Ti64+0.1wt-%VGCFs with attached pole figure (PF) and inverse pole figure (IPF) of (c) Ti64 and (d) Ti64+0.1wt-%VGCFs.

The microstructure of Ti64 and Ti64+0.4-wt% VGCFs observed from different positions in extruded rod in transversal direction by optical microscope were shown in fig. 4. Henceforth, monolithic Ti64, Ti+0.1-wt% VGCFs and Ti+0.4-wt% VGCFs will be name as T0, T0.1 and T0.4, respectively. Figure 4 shows a microstructure of T0-1 and T0.4-1 cut from a tip of extruded rod (A-X represents a sample name, in which A is a material and X is a position in extruded rod showed in fig. 2). A fine α -lamellar and α -equiaxed structure compared to SPSed sample was observed in extruded sample due to an effect of plastic deformation. The size of α -lamellar colony and α -equiaxed observed in T0 and T0.4 at position 2 and 3 (fig. 4b-4c and 4e-4f) was finer compared to sample obtained from position 1 (fig. 4a and 4d). This phenomenon was also observed in Ti0.1 as well. A large additional amount of VGCF in Ti0.4 resulted in a carbide phase formation, its periodic formulae was evaluated by EDS as $Ti_6C_{3.75}$.

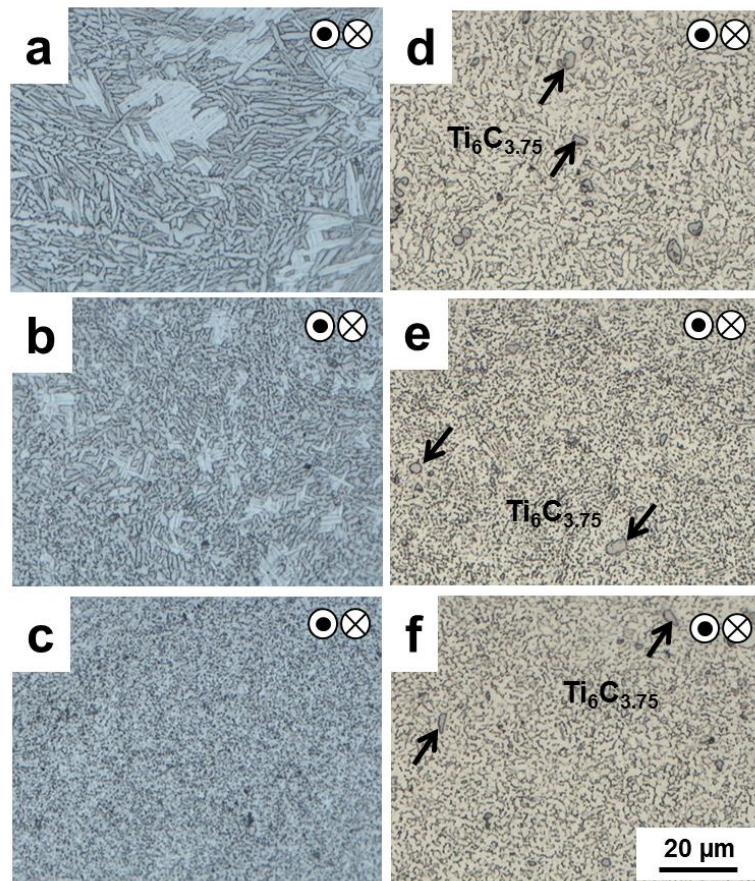


Fig. 4. Optical microstructure of Ti64 (a) T0-1; (b) T0-2; (c) T0-3 and Ti64+0.4-wt%VGCFs (d) Ti0.4-1; (e) Ti0.4-2; (f) Ti0.4-3 in transversal direction.

Figure 5 shows crystal orientation, pole figure (PF) and inverse pole figure (IPF) from three positions in Ti0 rod analyzed by EBSD. Figure 5a shows a crystal orientation of Ti0-1, which was extruded at temperature higher than β transus (1243 K). This sample exhibited a strong intensity in [0001] direction which parallel to extrusion direction, and a grain size of 16 μm was observed. Ti0-2, which was extruded at temperature lower than β transus (1173 K), shows some small nucleated grains on microstructure with a decreasing in intensity in [0001] direction. This sample shows a grain size of 10 μm , which was smaller, compared to Ti0-1 (fig. 5b). For Ti0-3, this position was extruded at temperature lower than 1173 K. A very small grain size of 1.3 μm and a large amount of nucleated grain was observed, grain morphology was changes from α -lamellar to α -equiaxed. The intensity in [0001] direction was decreased compared to Ti0-2. These results indicated that a dynamic recrystallization (DRX) was occurred in Ti0-3 sample (fig. 5c). The important factor that induced a DRX during hot extrusion was a deformation temperature, which different at each position in extruded rod. The deformation temperature will control a stored energy in extruded material [16]. Ti0-1 was extruded at highest temperature compared to other position (over β transus temperature), deformation at high temperature in a β phase region lead to an insufficient stored energy for DRX. The stored energy in Ti0-2 (fig. 4b) was higher than Ti0-1 because more defects such as dislocation and stress was generated in a material deformed at low temperature compared to high temperature [17]. Similarly, a large amount of dislocations was generated in a material after cold deformation. This phenomenon was clearly observed in Ti0-3, a high degree of DRX resulted in a random crystal orientation.

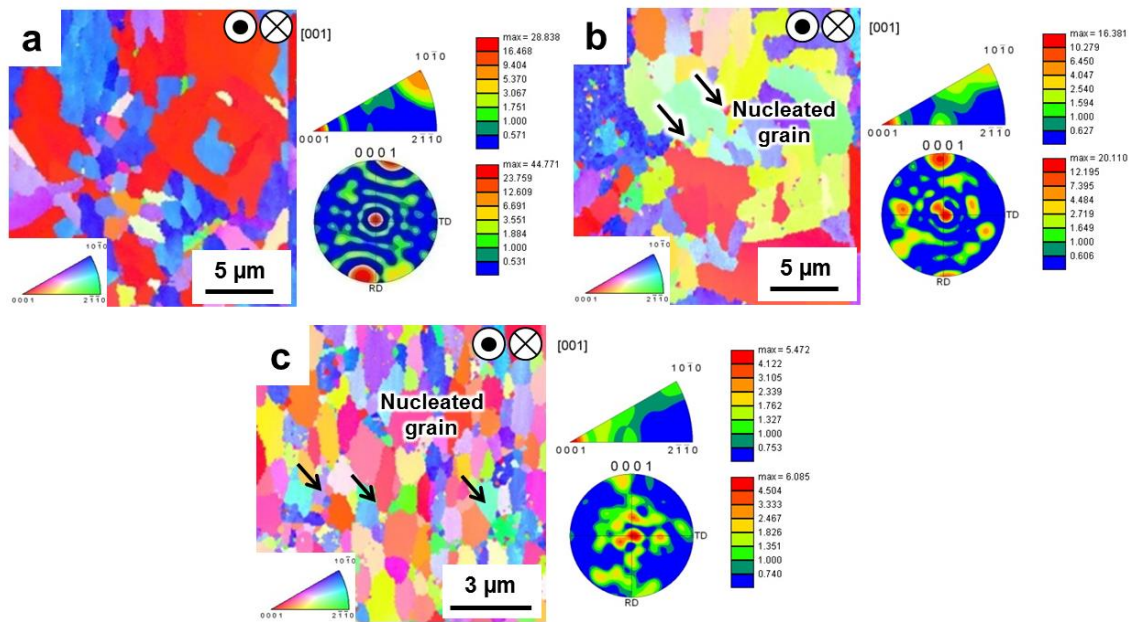


Fig. 5. Crystal orientation, inverse pole figure (IPF) and pole figure (PF) in transversal direction of (a) Ti0-1; (b) Ti0-2; (c) Ti0-3.

Figure 6 shows a crystal orientation, PF and IPF of extruded Ti composited with 0.1 wt-% VGCFs. Ti64 with 0.1wt-% VGCFs shows a nucleation of new grain in a high extruded temperature position (fig. 6a). The grain morphology of Ti0.1-1 was different from Ti0-1 because microstructure of Ti+0.1wt-%VGCFs was α -equiaxed after SPSed. An average grain size of Ti0.1-1 was 2 μm after extrusion but not uniform. The microstructure of Ti0.1-1 composed of prior α -equiaxed grain and a small nucleated grain, which indicated that DRX was not completed due to low stored energy. The small nucleated grain was ceased to growth during cooling, and a final microstructure was non-uniform. A DRX was easier to observe in samples mixed with VGCFs compared to monolithic Ti64 because an interstitial solid solution of carbon in Ti64 matrix acted as a defect, which increased a stored energy when material was deformed [16]. Ti0.1-2 shows a similar grain morphology, grain size and intensity in [0001] direction to Ti0.1-1 (fig. 6b). However, Ti0.1-3 shows a uniform grain size of 1.5 μm , and intensity in [0001] direction was decreased compared to Ti0.1-2 (fig. 6c). The uniform grain size and a random crystal orientation indicated that Ti0.1-3 exhibited higher DRX degree compared to Ti0.1-2 [18].

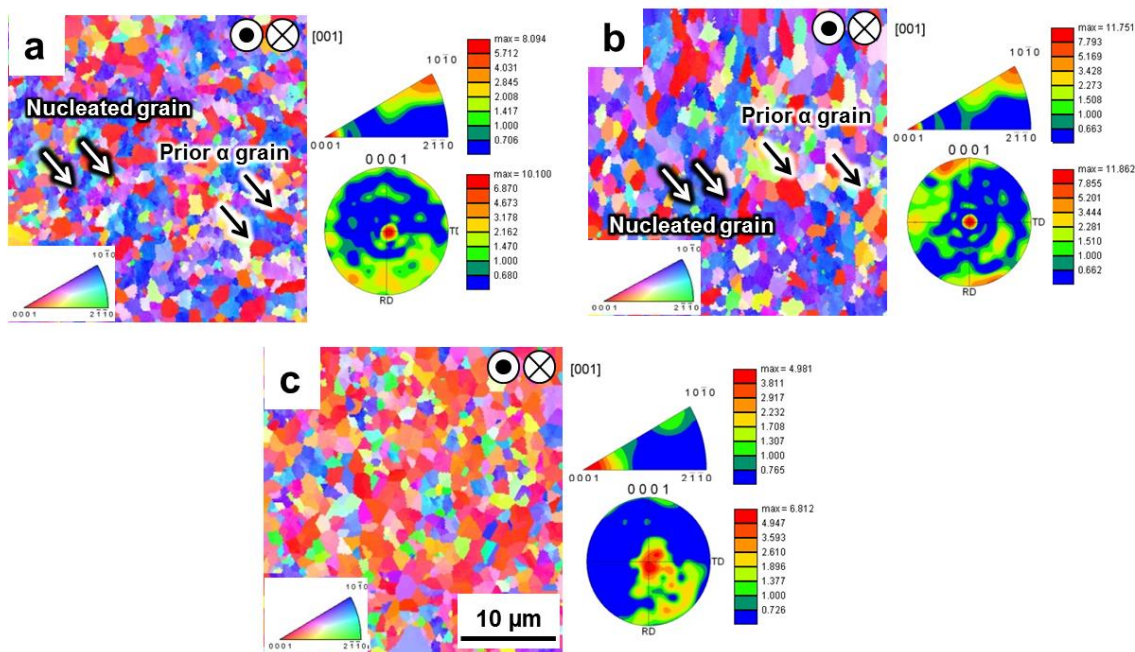


Fig. 6. Crystal orientation, inverse pole figure (IPF) and pole figure (PF) in transversal direction of (a) Ti0.1-1; (b) Ti0.1-2; (c) Ti0.1-3.

Figure 7 shows a crystal orientation, PF and IPF of extruded Ti compositized with 0.4wt-% VGCFs. Ti64+0.4wt-% VGCF shows a similar microstructure to Ti64+0.1wt-% VGCF that a small nucleated grain and prior α -grain with a size of 2 μm was observed in Ti0.4-1 and Ti0.4-2 (fig. 7a and 7b). For Ti0.4-3, a uniform grain size of 1.5 μm was observed after nucleated grain growth, and a lowest intensity in [0001] direction among three samples was detected (fig. 7c). From crystal orientation, PF and IPF results, a DRX was strongly depended on a stored energy in a material. The stored energy was increased by decreasing of deformation temperature or an effect of solid solution of carbon. A. LUCCI et al. reported that an addition of various substitution alloying elements to Cu in a low content enable to induced a dynamic recrystallization after deformation by increasing a stored energy in a material [19].

Tensile properties of Ti64, Ti64+0.1wt-% VGCF and Ti64+0.4wt-% VGCF obtained from different position in extruded rod were listed in table 2. For all materials, the lowest and highest of 0.2%YS and UTS was obtained from tip and end of extruded rod, respectively. During hot extrusion, position 1 was extruded at highest temperature (the first part to be extruded) compared to other position resulted in a low shear stress, and small amount of dislocation was formed in material. The flow stress was decreased by increasing of deformation temperature [3]. Samples that were obtained from position 2 and 3 show an increasing in tensile strength and yield strength compared to position 1 instead of decreasing because of dislocation removal by an effect of DRX. This was implied that shear stress generated by hot extrusion induced a DRX, and simultaneously generated a new dislocations at grain boundary during DRX. The size of new grains were very fine (fig. 4c and 4f) then a considerable amount of dislocations was formed in material resulted in an improvement of tensile strength with a traded off of elongation. Ti64 composite with VGCFs exhibited higher tensile strength compared to monolithic Ti64 obtained from same position because an effect of solid solution strengthening of carbon [20]. 0.2%YS and UTS of Ti64+0.4wt-% VGCFs was small decreased compared to Ti64+0.1wt-% VGCFs for sample obtained from same position due to a large amount of brittle carbide phase formation (fig. 4).

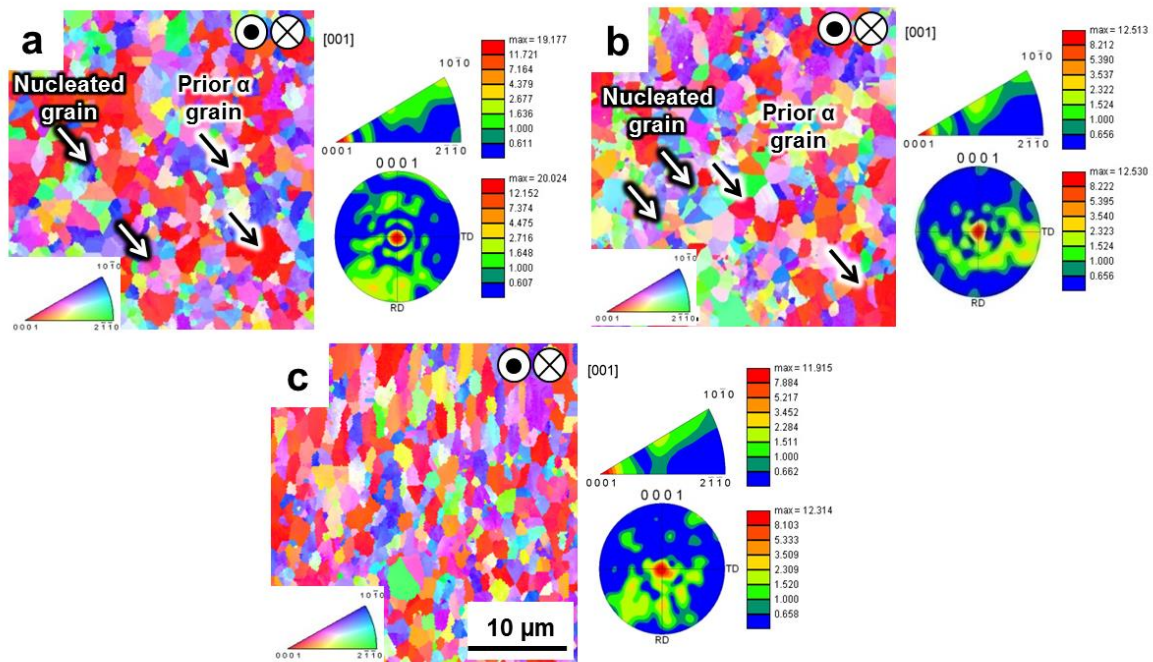


Fig. 7. Crystal orientation, inverse pole figure (IPF) and pole figure (PF) in transversal direction of (a) Ti0.4-1; (b) Ti0.4-2; (c) Ti0.4-3.

Table 2. Tensile properties of Ti0, Ti0.1 and Ti0.4 obtained from different position in extrusion rod.

Position	Ti64			Ti64+0.1wt-%VGCF			Ti64+0.4wt-%VGCF		
	UTS (MPa)	0.2%YS (MPa)	Elongation (%)	UTS (MPa)	0.2%YS (MPa)	Elongation (%)	UTS (MPa)	0.2%YS (MPa)	Elongation (%)
1	990	943	15.2	1127	1087.0	17.7	1191	1069	10.9
2	1121	1002	12.9	1166	1165	18.1	1150	1150	9.1
3	1131	1092	9.4	1190	1170	12.0	1192	1192	7.4

Stress-strain curve of Ti0, Ti0.1 and Ti0.4 extruded material obtained from different positions in extruded rod was shown in fig. 8. For monolithic Ti64, Ti0-1 and Ti0-2 shows ductile behaviour that stress-strain curve exhibited no yield point. On the other hand, Ti0-3 obtained from DRX region exhibited a yield point in stress-strain curve with highest UTS of 1130.8 MPa (fig. 8a). This is because a considerable amount of dislocation formed in a part that extruded at low temperature. In the case of Ti0.1, yield point was observed in Ti0.1-2 and Ti0.1-3 (fig. 8b and c). From a principle, yield point was developed in a material that gained a sufficient shear stress, resulted in a permanent displacement of atom [9]. This was occurred in sample which experienced a deformation at low temperature such as the end part in extruded rod. For Ti64/VGCFs composite material, yield point was observed in samples obtained from position 2 because interstitial solid solution of carbon provided an additional shear stress in material [20]. Ductility of Ti0.4 was much lower than monolithic Ti0 and Ti0.1 due to a formation of large amount of Ti₆C_{3.75} brittle intermetallic phase.

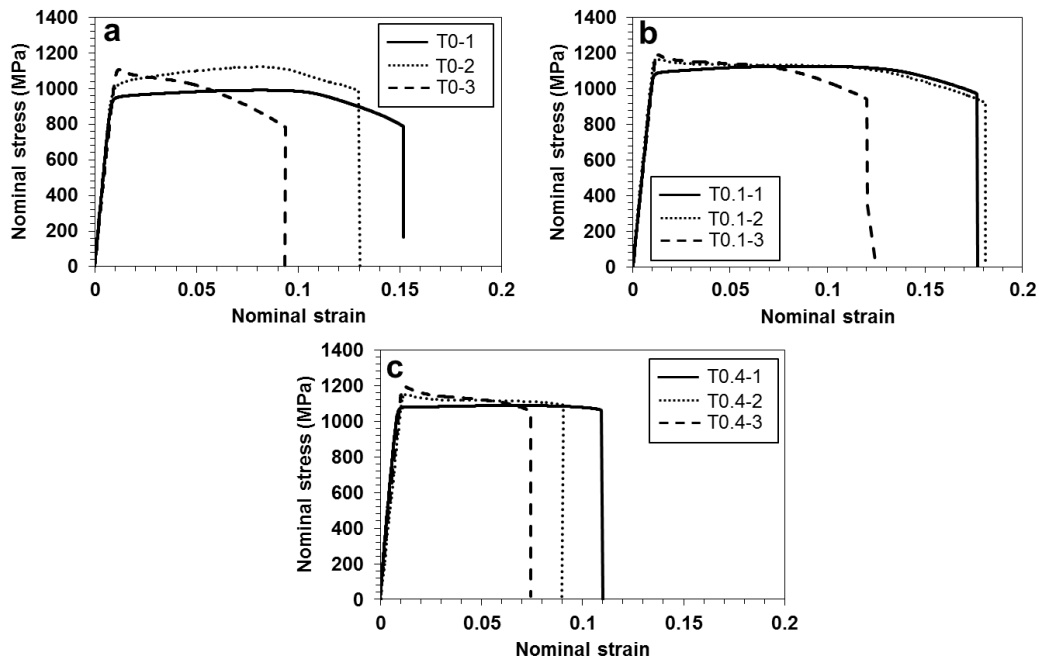


Fig. 8. Stress-strain curve of extruded materials obtained from different positions (a) Ti0; (b) Ti0.1; (c) Ti0.4.

Summary. The high stored energy in monolithic Ti or Ti composites was obtained when material experienced a deformation at low temperature or by an effect of solid solution of carbon, resulted in a DRX. The improvement of tensile strength of Ti0, Ti0.1 and Ti0.4 was obtained by DRX followed by dislocation formation during hot extrusion. The details are mentioned below.

1. The dynamic recrystallization (DRX) was occurred in sample that extruded at low temperature resulted in high stored energy in material. The small recrystallized grain was observed as evidence.
2. The solute carbon atom from vapor grown carbon fibers (VGCFs) in Ti64/VGCFs composite materials acted as a defect that provided additional stored energy in material during hot extrusion, and facilitate a DRXed.
3. The formation of dislocations at grain boundary during DRX at low deformation temperature which many small nucleated grains were formed resulted in improvement in yield and tensile strength. The increased value was small but systematically occurred for all samples.

References

- [1] L.G. Zhen and L.R. Ze, Non-aerospace application of Ti materials with a great many social and economic benefits in China, *Mater. Sci. Eng. A*, 2000, 280, 25-29, DOI: 10.1016/S0921-5093(99)00651-6.
- [2] D. Mareci, R. Cheraliu, D.M. Gordin and T. Gloriant, Comparative corrosion study of Ti-Ta alloys for dental applications, *Acta Biomater.*, 2009, 5, 3625-3639, DOI: 10.1016/j.actbio.2009.05.037.
- [3] A. Momeni and S.M. Abbasi, Effect of hot working on flow behaviour of Ti-6Al-4V alloy in single phase and two phase regions, *Mater. Des.*, 2010, 31, 3599-3604, DOI: 10.1016/j.matdes.2010.01.060.

[4] T. Seshacharyulu, S.C. Medeiros, W.G. Frazier and Y.V.R.K. Prasad, Hot working of commercial Ti-6Al-4V with an equiaxed α - β microstructure: materials modeling considerations, *Mater. Sci. Eng. A*, 2000, 284, 184-194, DOI: 10.1016/S0921-5093(00)00741-3.

[5] R. Ding, Z.X. Guo and A. Wilson, Microstructural evolution of a Ti-6Al-4V alloy during thermomechanical processing, *Mater. Sci. Eng. A*, 2002, 327, 233-245, DOI: 10.1016/S0921-5093(01)01531-3.

[6] G.Z. Quan, G.C. Lua, J.T. Liang, D.S. Wu, A. Mao and Q. Liu, Modelling for the dynamic recrystallization evolution of Ti-6Al-4V alloy in two-phase temperature range and a wide strain rate range, *Comput. Mater. Sci.*, 2015, 97, 136-147, DOI: 10.1016/j.commatsci.2014.10.009.

[7] H.Z. Niu, Y.F. Chen, Y.S. Zhang, J.W. Lu, W. Zhang and P.X. Zhang, Phase transformation and dynamic recrystallization behaviour of a β -solidifying γ -TiAl alloy and its wrought microstructure control, *Mater. Des.*, 2016, 90, 196-203, DOI: 10.1016/j.matdes.2015.10.133.

[8] D.L. Ouyang, M.W. Fu and S.Q. Lu, Study on the dynamic recrystallization behaviour of Ti-alloy Ti-10V-2Fe-3V in β processing via experiment and simulation, *Mater. Sci. Eng. A*, 2014, 619, 26-34, DOI: 10.1016/j.msea.2014.09.067.

[9] H. Liang, H. Guo, Y. Ning, X. Peng, C. Qin, Z. Shi and Y. Nan, Dynamic recrystallization behaviour of Ti-5Al-5Mo-5V-1Cr-1Fe alloy, *Mater. Des.*, 2014, 63, 798-804, DOI: 10.1016/j.matdes.2014.06.064.

[10] C.H. Park, J.H. Kim, J.T. Yeom, C.S. Oh, S.L. Semiatin and C.S. Lee, Formation of a submicrocrystalline structure in a two-phase titanium alloy without severe plastic deformation, *Scr. Mater.*, 2013, 68, 996-999, DOI: 10.1016/j.scriptamat.2013.02.055.

[11] Y.Q. Ning, X. Luo, H.Q. Liang, H.Z. Guo, J.L. Zhang and K. Tan, Competition between dynamic recovery and recrystallization during hot deformation for TC18 titanium alloy, *Mater. Sci. Eng. A*, 2015, 635, 77-85, DOI: 10.1016/j.msea.2015.03.071.

[12] Y. Chen, J. Li, B. Tang, H. Kou, X. Xue and Y. Cui, Texture evolution and dynamic recrystallization in a beta titanium alloy during hot-rolling process, *J Alloys Compd.*, 2015, 618, 146-152, DOI: 10.1016/j.jallcom.2014.08.129.

[13] G.C. Obasi, OM. Ferri, T. Ebel and R. Bormann, Influence of processing parameters on mechanical properties of Ti-6Al-4V alloy fabricated by MIM, *Mater. Sci. Eng. A*, 2010, 527, 3929-3935, DOI: 10.1016/j.msea.2010.02.070.

[14] G.G. Yapici, I. Karaman, Z.P. Luo and H. Rack, Microstructure and mechanical properties of severely deformed powder processed Ti-6Al-4V using equal channel angular extrusion, *Scr. Mater.*, 2003, 49, 1021-1027, DOI: 10.1016/S1359-6462(03)00484-6.

[15] S. Roy, S. Suwas, S. Tamirisakandala, R. Srinivasan and D.B. Miracle, Microstructure and texture evolution during extrusion of boron modified Ti-6Al-4V alloy, *Mater. Sci. Eng. A*, 2012, 540, 152-163, DOI: 10.1016/j.msea.2012.01.120.

[16] J.D. Verhoeven, *Fundamentals of Physical Metallurgy*, 1st edn, 55-74; 1975, Canada, John Wiley and sons, Inc, ISBN: 978-0-471-90616-2.

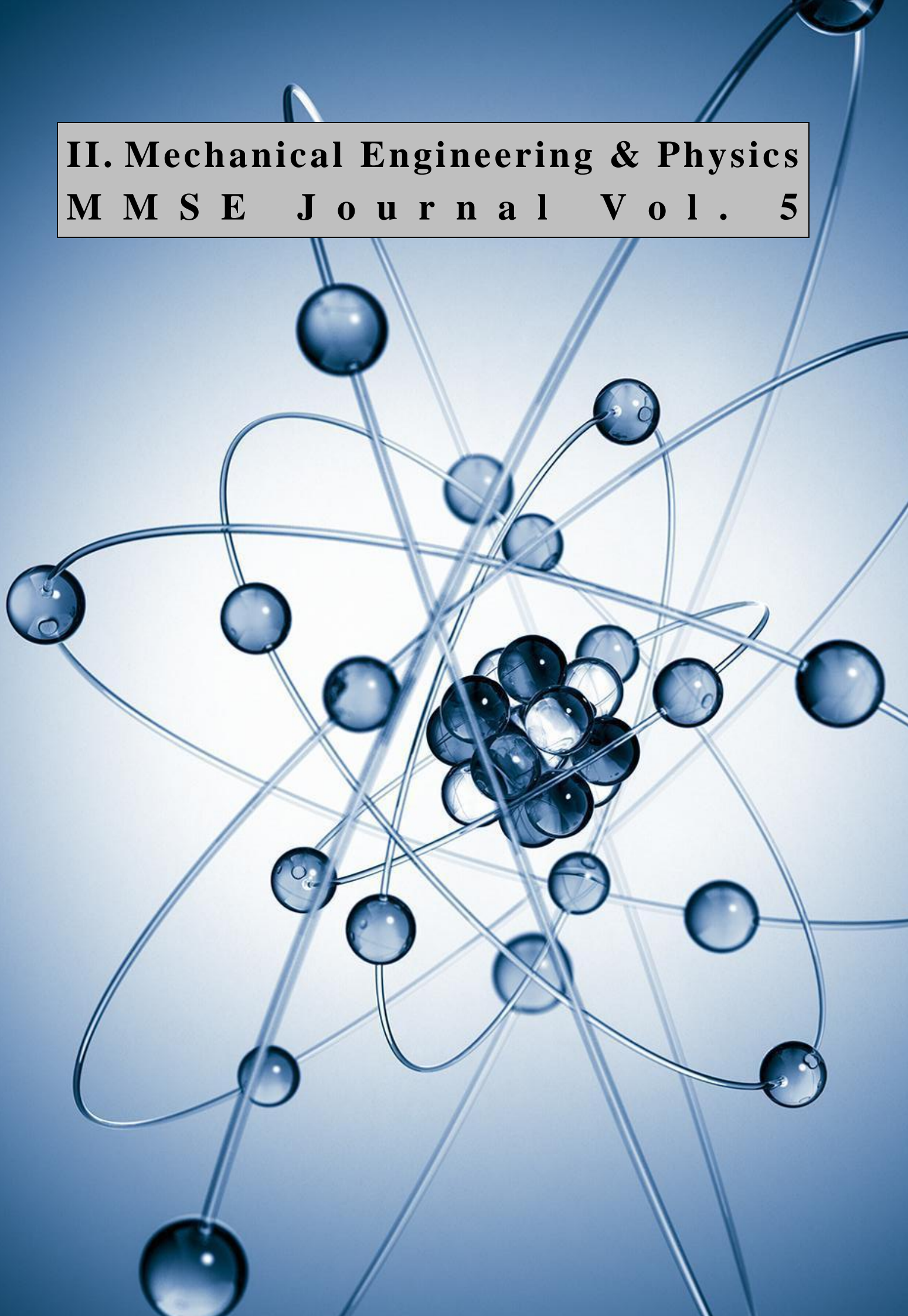
[17] I. Sen, R.S. Kottada and U. Ramamurty, High temperature deformation processing maps for boron modified Ti-6Al-4V alloys, *Mater. Sci. Eng. A*, 2010, 527, 6157-6165, DOI: 10.1016/j.msea.2010.06.044.

[18] H. Matsumoto, M. Kitamura, Y Li, Y. Koizumi and A. Chiba, Hot forging characteristic of Ti-5Al-5V-5Mo-3Cr alloy with single metastable β microstructure, *Mater. Sci. Eng. A*, 2014, 611, 337-344, DOI: 10.1016/j.msea.2014.06.006.

[19] A. Lucci, G. Riontino, M.C. Tabasso, M. Tamanini and G. Venturello, Recrystallization and stored energy of dilute copper solid solutions with substitutional transition elements of the 4th period, *Acta Metall.*, 1978, 26, 615-622, DOI: 10.1016/0001-6160(78)90113-X.

[20] F. Pedix, M.-F. Trichet, J.-L. Bonnentian, M. Cornet and J. Bigot, Relationships between interstitial content, microstructure and mechanical properties in fully lamellar Ti-48Al alloys, with special reference to carbon, *Intermetallics*, 2010, 9, 807-815, DOI: 10.1016/S0966-9795(01)00066-8.

II. Mechanical Engineering & Physics
M M S E J o u r n a l V o l . 5



Strength Analysis of Flat Spring of the Resonant Vibro-Impact Module

Volodymyr Gursky ¹, Igor Kuzio ¹

1 – Lviv Polytechnic National University, Ukraine



DOI **10.13140/RG.2.1.2504.0240**

Keywords: flat spring, vibro-impact, resonance, finite element method (FEM), eigenfrequencies, contact stress.

ABSTRACT. The rod model of the resonant vibro-impact module with an electromagnetic drive is considered. Construction's design implemented an asymmetrical elastic characteristic by one flat spring with two absolutely rigid intermediate supports. Eigenfrequency is defined for corresponding location intermediate supports based on the finite element method. Stress-strain state of the elastic element is graphically represented at the expense of static displacement of local mass. Contact task is considered and contact force between the flat spring and cylindrical support is calculated. Also, contact stiffness is determinate. The parameters of volumetric stress state of the contact, calculated analytically and by modeling in SolidWorks Simulation are shown. The dynamics of the vibro-impact rod system with kinematic's disturbance is modeled. Contact and equivalent stresses during operation of the vibro-impact rod system are determined.

1. Introduction. Vibro-impact systems are the basis of technological machines and processes of environments with challenging physical and mechanical characteristics. This is due the presence challenging modes as imposing the main and sub-harmonic oscillations, acceleration polyfrequency range by asymmetry of displacement of the operating mass. The resulting polyfrequency system generates wave processes, resonance phenomena and power conversion in environments more effective than harmonic movement law of worker mass. So, the use of frequency vibro-impact processes and systems is almost justified and promising. However, this requires challenging practical solutions for the implementation of nonlinear systems and special theoretical analysis to evaluation the relevant modes.

2. Analysis of recent research and literature. The application of structural nonlinearities is most appropriate among to the known practical solutions for the implementation of vibro-impact systems [1, 2]. A few practical solutions are in patents [3–6]. The feature of such systems functioning is the emergence of sub- and superresonance modes with different multiplicities orders [7, 8]. Implementation of such is possible by matching of the system parameters and power options [3].

3. Aim of the article. The main objective for developing the new vibration module is providing regulated resonant harmonic and vibro-impact modes. Proposed to implement it by resetting the stiffness properties of a flat spring relative to its base design. The task of reducing the complexity of operations for the implementation of the various modes as a practical matter is pursued. This is not enough in presented solutions [3–6].

Adjustable asymmetrical resilient characteristic (fig. 1) will be implemented by the flat spring with presented functional condition:

$$F_{stiffness}[y(t)] = \begin{cases} c_I y(t), & y(t) + \Delta \geq 0 \\ c_{II} y(t) + (c_{II} - c_I)\Delta, & y(t) + \Delta < 0 \end{cases} \quad (1)$$

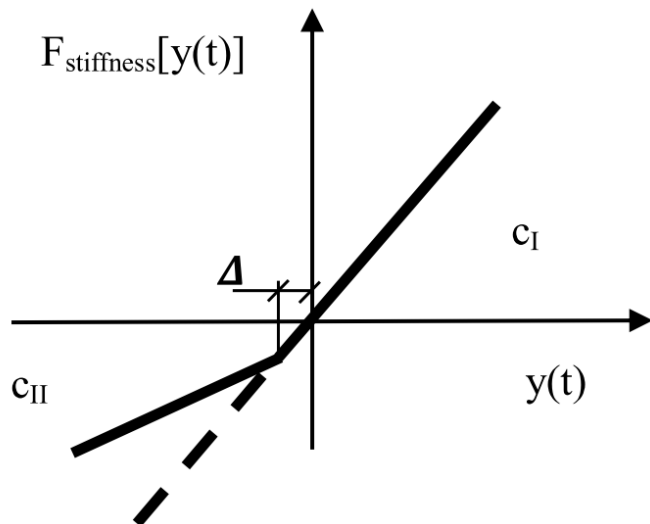


Fig. 1. Renewable characteristic of stiffness element.

Implementation of the regulated modes is carried out by a constructive influence on the stiffness characteristic. It is supposed that the following conditions: $c_I = \text{const}$, a $c_{II} = \text{var}$, $\Delta = \text{var}$, $\frac{c_{II}}{c_I} = n_c = 1; 2; 3$.

4. Problem statement. Implementation of vibro-impact systems by movement limiters is accompanied by contact phenomena. That is confirmed in subsequent works [9-12]. It should be noted that the elastic elements are an important hub of the resonant vibration machines. Strength characteristics along with the task of rigidity must be complying. Therefore, the lack of integrated techniques for analyzing stress-strain states in the implementation of the vibro-impact modes is a problematic.

5. Research materials. Resonant vibration module designed by the two-mass oscillation system with active 1 and reactive 2 masses, which are connected by one flat spring 3. Active mass 1 is designed as a frame with an horizontal grooves for hard fixing brackets 4. Brackets 4 have vertical slots for adjustable cylindrical rods 5. Two core 6 are placed on the active mass 1. The reactive mass 2 contains anchors 7. The resonance module can be the basis for creating of the vibratory technological machine. Module also can be used as a stand for dynamic testing.

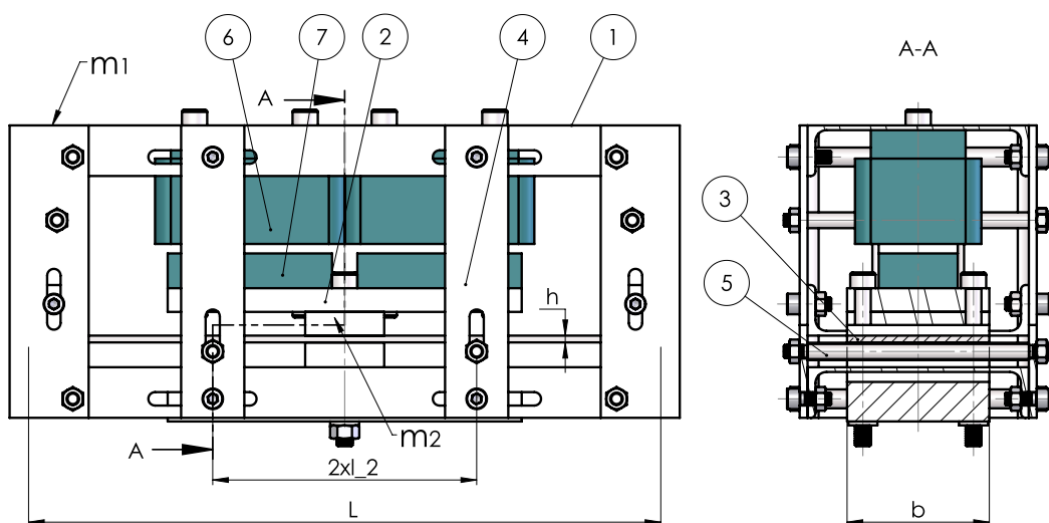


Fig. 2. General view of the vibro-impact module.

This structural implementation allows to use one a flat spring 3 to implement the basic harmonic mode in the lower frequency region by stiffness coefficient c_I . Cylindrical shafts 5 are mounted in vertical grooves of brackets 4 and are used as adjustable intermediate stops for flat springs 3. Using the horizontal grooves changes the location of the intermediate support along the flat springs. Accordingly is changes stiffness coefficient c_{II} . The appropriate gap Δ between flat spring and intermediate stops set by using the vertical grooves. So, adjustable asymmetric piecewise linear characteristics of a flat spring and adjustable oscillations modes with different amplitude and frequency spectrum will be realized.

With appropriate settlement schemes, which describe asymmetric transverse stiffness change according to (1), also taking $\Delta = 0$, the stiffness coefficient c_{II} is a necessary to define with the stress-strain state analysis.

For the analysis of rod systems appropriate to use finite element method [13]. Finite-element scheme of the vibration system in vibro-impact mode based on flat spring implemented on fig. 2.

The standard matrix of nodal reactions (transverse forces and bending moments) of one finite element rod has the form [13]:

$$[\bar{\mathbf{Z}}_{i,i+1}] = \begin{pmatrix} R_i \\ M_i \\ R_{i+1} \\ M_{i+1} \end{pmatrix} = EJ \begin{bmatrix} 12/l_i^3 & -6/l_i^2 & -12/l_i^3 & -6/l_i^2 \\ -6/l_i^2 & 4/l_i & 6/l_i^2 & 2/l_i \\ -12/l_i^3 & 6/l_i^2 & 12/l_i^3 & 6/l_i^2 \\ -6/l_i^2 & 2/l_i & 6/l_i^2 & 4/l_i \end{bmatrix} \quad (2)$$

where EJ – is a bending stiffness of the rod.

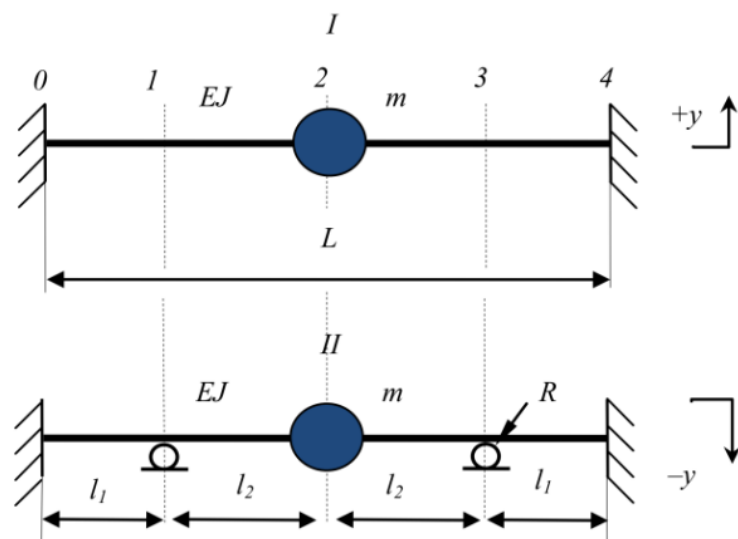


Fig. 3. Operation scheme of the vibro-impact system.

Bending rigidity EJ of a flat spring is calculated to realization of the necessary natural frequency $\omega_{0I} = \sqrt{c_I/m}$ of the harmonic oscillation mode for scheme I:

$$EJ = mL^3\omega_{0l}^2/192, \quad (3)$$

where $m = \frac{m_1m_2}{(m_1+m_2)}$ – is reduced mass of vibrating system.

Finite-element scheme during movement in a negative direction is based on these boundary conditions:

$$\begin{pmatrix} y_0 = 0 \\ \varphi_0 = 0 \end{pmatrix}, \begin{pmatrix} y_1 = 0 \\ \varphi_1 = var \end{pmatrix}, \begin{pmatrix} y_2 = var \\ \varphi_2 = var \end{pmatrix}, \begin{pmatrix} y_3 = 0 \\ \varphi_3 = var \end{pmatrix}, \begin{pmatrix} y_4 = 0 \\ \varphi_4 = 0 \end{pmatrix}. \quad (4)$$

The system with 10 degrees of freedom obtained in general form by using the division by 4 rods finite elements: y_i, y_{i+1} i φ_i, φ_{i+1} – according vertical movement and angles of rotation of the rod nodal's points ($i = 0 \dots 4$). According to general stiffness matrix of a rod (2) are formed stiffness matrix with dimension 10×10 of finite elements rods in the global coordinate system in accordance with the boundary conditions (4).

$$\begin{aligned} \mathbf{C}_{01} &= EJ \begin{bmatrix} (1 & 2 & 3 & 4) \\ 1 & 0 & 0 & 0 \\ 0 & 1 & 0 & 0 \\ 0 & 0 & 1 & 0 \\ 0 & 0 & 0 & 4/l_1 \end{bmatrix} \begin{pmatrix} 1 \\ 2 \\ 3 \\ 4 \end{pmatrix}, \\ \mathbf{C}_{12} &= EJ \begin{bmatrix} (3 & 4 & 5 & 6) \\ 1 & 0 & 0 & 0 \\ 0 & 4/l_2 & -6/l_2^2 & 2/l_2 \\ 0 & -6/l_2^2 & 12/l_2^3 & -6/l_2^2 \\ 0 & 2/l_2 & -6/l_2^2 & 4/l_2 \end{bmatrix} \begin{pmatrix} 3 \\ 4 \\ 5 \\ 6 \end{pmatrix}, \\ \mathbf{C}_{23} &= EJ \begin{bmatrix} (5 & 6 & 7 & 8) \\ 12/l_2^3 & 6/l_2^2 & 0 & 6/l_2^2 \\ 6/l_2^2 & 4/l_2 & 0 & 2/l_2 \\ 0 & 0 & 1 & 0 \\ 6/l_2^2 & 2/l_2 & 0 & 4/l_2 \end{bmatrix} \begin{pmatrix} 5 \\ 6 \\ 7 \\ 8 \end{pmatrix}, \\ \mathbf{C}_{34} &= EJ \begin{bmatrix} (7 & 8 & 9 & 10) \\ 1 & 0 & 0 & 0 \\ 0 & 4/l_1 & 0 & 0 \\ 0 & 0 & 1 & 0 \\ 0 & 0 & 0 & 1 \end{bmatrix} \begin{pmatrix} 7 \\ 8 \\ 9 \\ 10 \end{pmatrix}, \end{aligned} \quad (5)$$

The resulting stiffness matrix of finite-element rod system:

$$= EJ \begin{bmatrix} 1 & 0 & 0 & 0 & 0 & 0 & 0 & 0 & 0 \\ 0 & 1 & 0 & 0 & 0 & 0 & 0 & 0 & 0 \\ 0 & 0 & 2 & 0 & 0 & 0 & 0 & 0 & 0 \\ 0 & 0 & 0 & 4/l_1 + 4/l_2 & -6/l_2^2 & 2/l_2 & 0 & 0 & 0 \\ 0 & 0 & 0 & -6/l_2^2 & 24/l_2^3 & 0 & 0 & 6/l_2^2 & 0 \\ 0 & 0 & 0 & 2/l_2 & 0 & 8/l_2 & 0 & 2/l_2 & 0 \\ 0 & 0 & 0 & 0 & 0 & 0 & 2 & 0 & 0 \\ 0 & 0 & 0 & 0 & 6/l_2^2 & 2/l_2 & 0 & 4/l_1 + 4/l_2 & 0 \\ 0 & 0 & 0 & 0 & 0 & 0 & 0 & 0 & 1 \\ 0 & 0 & 0 & 0 & 0 & 0 & 0 & 0 & 1 \end{bmatrix}. \quad (6)$$

Free oscillations equation of a rod system is written in matrix form:

$$\mathbf{M} \times \ddot{\mathbf{X}} + \mathbf{C}_{04} \times \mathbf{X} = 0, \quad (7)$$

where, $\mathbf{X} = \mathbf{column}(y_0, \varphi_0, \dots, y_4, \varphi_4)$ – nodal's displacements vector of the finite element;

$\mathbf{M} = \mathbf{diag}(0,0,0,0, m, 0,0,0,0,0)$ – diagonal matrix of local masses inertial parameters;

\mathbf{C}_{04} – system's stiffness matrix.

Based on the determinant for the frequency equation

$$\det(-\mathbf{M} \times \Omega^2 + \mathbf{C}_{04}) = 0, \quad (8)$$

is defined natural frequency of bending vibrations:

$$\omega_{0II} = \sqrt{\frac{6EJ(l_1+4l_2)}{m(l_1+l_2)l_2^3}}, \quad (9)$$

Reduced stiffness coefficients of rod systems according to the formulas (1) and (9) have the next forms:

$$c_I = \frac{192EJ}{L^3}, \quad c_{II} = \frac{6EJ(l_1+4l_2)}{(l_1+l_2)l_2^3}, \quad (10)$$

Thus, obtained parametric dependence of the system's stiffness coefficient as function of l_1 .

Stiffness coefficients ratio, taking into account $l_2 = \frac{L}{2} - l_1$ has a view:

$$n_c = \frac{c_{II}}{c_I} = \frac{L^2(L-1,5l_1)}{(L-2l_1)^3}, \quad (11)$$

The eigenfrequencies ratio is $n_\omega = \frac{\omega_{0II}}{\omega_{0I}} = \sqrt{n_c}$.

By the condition of multiplicities of natural frequencies of the rod systems

$$n_\omega = 2, \quad (12)$$

formulas for positioning intermediate supports are the next

$$l_1 = 0.275L, l_2 = 0.225L. \quad (13)$$

For verification must be $l_1 + l_2 = 0.5L$.

Stress-strain state analysis. The vector of nodal displacements for statically loaded rod system type *II* can be determined from the relationship:

$$\mathbf{Y} = \mathbf{C}_{04}^{-1} \times \mathbf{P}, \quad (14)$$

where \mathbf{P} – vector of external loads reduced to nodes.

Nodal's displacement vectors each finite element-rod:

$$\mathbf{Y}_{01} = \begin{bmatrix} y_0 \\ \varphi_0 \\ y_1 \\ \varphi_1 \end{bmatrix}, \mathbf{Y}_{12} = \begin{bmatrix} y_1 \\ \varphi_1 \\ y_2 \\ \varphi_2 \end{bmatrix}, \mathbf{Y}_{23} = \begin{bmatrix} y_2 \\ \varphi_2 \\ y_3 \\ \varphi_3 \end{bmatrix}, \mathbf{Y}_{34} = \begin{bmatrix} y_3 \\ \varphi_3 \\ y_4 \\ \varphi_4 \end{bmatrix}. \quad (15)$$

The vectors of nodal reactions each finite element defines by matrix expression (2). The hogging line of each finite element-rod is based on the known forms functions at nodes single displacement [13]:

$$y_{01}(x) = \begin{bmatrix} \frac{2x^3 - 3l_1x^2 + l_1^3}{l_1^3} \\ \frac{x^3 - 2l_1x^2 + l_1^2x}{l_1^2} \\ \frac{-2x^3 + 3l_1x^2}{l_1^3} \\ \frac{x^3 - l_1x^2}{l_1^2} \end{bmatrix} \times \mathbf{Y}_{01}, \quad y_{12}(x) = \begin{bmatrix} \frac{2(x-l_1)^3 - 3l_2(x-l_1)^2 + l_2^3}{l_2^3} \\ \frac{(x-l_1)^3 - 2l_2(x-l_1)^2 + l_2^2(x-l_1)}{l_2^2} \\ \frac{-2(x-l_1)^3 + 3l_2(x-l_1)^2}{l_2^3} \\ \frac{(x-l_1)^3 - l_2(x-l_1)^2}{l_2^2} \end{bmatrix} \times \mathbf{Y}_{12}, \quad (16)$$

$$y_{23}(x) = \begin{bmatrix} \frac{2(x-l_1-l_2)^3 - 3l_2(x-l_1-l_2)^2 + l_2^3}{l_2^3} \\ \frac{(x-l_1-l_2)^3 - 2l_2(x-l_1-l_2)^2 + l_2^2(x-l_1-l_2)}{l_2^2} \\ \frac{-2(x-l_1-l_2)^3 + 3l_2(x-l_1-l_2)^2}{l_2^3} \\ \frac{(x-l_1-l_2)^3 - l_2(x-l_1-l_2)^2}{l_2^2} \end{bmatrix} \times \mathbf{Y}_{23},$$

$$y_{34}(x) = \begin{bmatrix} \frac{2(x-l_1-2l_2)^3 - 3l_1(x-l_1-2l_2)^2 + l_1^3}{l_1^3} \\ \frac{(x-l_1-2l_2)^3 - 2l_1(x-l_1-2l_2)^2 + l_1^2(x-l_1-2l_2)}{l_1^2} \\ \frac{(-2x-l_1-2l_2)^3 + 3l_1(x-l_1-2l_2)^2}{l_1^3} \\ \frac{(x-l_1-2l_2)^3 - l_1(x-l_1-2l_2)^2}{l_1^2} \end{bmatrix} \times \mathbf{Y}_{34}.$$

The resulting displacement and flex curve of a rod system *II* are determined by the following dependency:

$$y(x) = \begin{cases} y_{01}(x), & 0 < x \leq l_1, \\ y_{12}(x), & l_1 < x \leq l_1 + l_2, \\ y_{23}(x), & l_1 + l_2 < x \leq l_1 + 2l_2, \\ y_{34}(x), & l_1 + 2l_2 < x \leq 2l_1 + 2l_2, \end{cases} \quad (17)$$

Resilient condition of the rod evaluated by the bending moment, transverse force, normal and tangential stresses:

$$M(x) = EJ \frac{d^2}{dx^2} y(x), Q(x) = EJ \frac{d^3}{dx^3} y(x), \sigma(x) = \frac{M(x)}{W}, \tau(x) = \frac{Q(x)S_{max}}{bJ}, \quad (18)$$

where $S_{max} = bh^2/8$, $J = bh^3/12$, $W = bh^2/6$ – geometric characteristics of the flat spring's cross-section;

$b \times h$ – width and thickness of the flat spring.

The vector of nodal loads is presented with concentrated force with peak value F , acting at the local oscillating mass. Diagrams of deflection line, angle of rotation, transverse forces and bending moments will be obtained by solving of the equations (14)-(18). The value of the maximum bending stresses are determined by the known formulas and given for appropriate settlement schemes:

$$\sigma_{maxI} = \frac{M_{maxI}}{W}, \sigma_{maxII} = \frac{M_{maxII}}{W}, \quad (19)$$

where $M_{maxI} = \frac{FL}{8}$, $M_{maxII} = [\bar{\mathbf{Z}}_{12}]_4 = \frac{Fl_2(l_1+2l_2)}{2(l_1+4l_2)}$ are maximum bending moments in dangerous sections for consideration rod systems.

The maximum shear stress is acting on the central section of the rod:

$$\tau_{maxI} = \tau_{maxII} = \frac{1.5F}{bh}, \quad (20)$$

The equivalent (von Mises) stress:

$$\sigma_{eq} = \sqrt{\sigma_{max}^2 + 4\tau_{max}^2}. \quad (21)$$

Research results. Analysis of stress-strain state of the rod systems offered to implement by static displacement of local mass y_m . The value of renewable forces is set by effected displacement for the corresponding settlement schemes with formulas: $F_I = c_I y_m$, $F_{II} = c_{II} y_m$. System parameters for analysis: $\omega_{0I} = 314 \text{ rad/s}$, $\omega_{0II} = 628 \text{ rad/s}$, $m = 20 \text{ kg}$, $L = 0.5 \text{ m}$, $E = 2.05 \times 10^5 \text{ MPa}$, $b = 0.080 \text{ m}$, $R = 0.006 \text{ m}$, $EJ = 1.284 \times 10^5 \text{ Nm}^2$, $l_1 = 0.113 \text{ m}$, $l_2 = 0.137 \text{ m}$, $h = 9.79 \times 10^{-3} \text{ m}$, $c_I = 1.972 \times 10^6 \text{ N/m}$, $c_{II} = 7.888 \times 10^6 \text{ N/m}$. Taking $y_m = 0.24 \text{ mm}$ received: $\sigma_{eqI} = 23.2 \text{ MPa}$, $\sigma_{eqII} = 59.5 \text{ MPa}$. Diagrams of stress-strain state for half flat springs in scheme II ($x = 0.. \frac{L}{2}$) shown on the fig. 4.

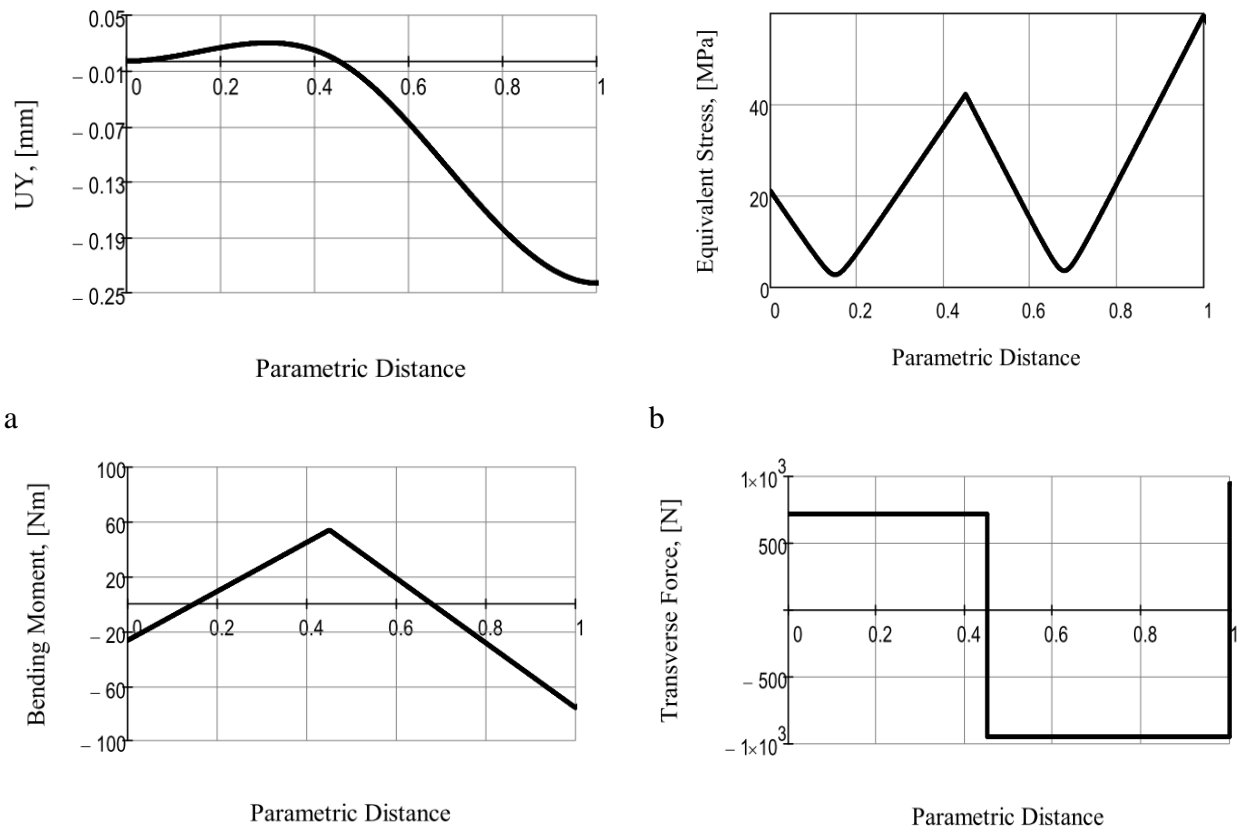


Fig. 4. Theoretical dependence of stress-strain state of elastic half-length rod.

Determination of contact stress. Determination of contact stress is exercise on Hertz formulas by value of reactions at intermediate supports (transverse force) [11, 14]. The cylindrical support reaction is the sum of transverse forces in the rod's nodes:

$$Q_1 = |[\bar{Z}_{01}]_3 + [\bar{Z}_{12}]_1| = \frac{F_{II}(l_1^2 + 4l_1l_2 + 3l_2^2)}{2l_1(l_1 + 4l_2)}. \quad (22)$$

The pressure in contact zone is calculated by the formula [14]:

$$p_{max} = \frac{2Q_1}{\pi b t}, \quad (23)$$

where, $t = K_t \sqrt{Q_1}$, $K_t = \sqrt{\frac{2}{\pi b} \frac{\frac{1-\mu_1^2}{E_1} + \frac{1-\mu_2^2}{E_2}}{\frac{1}{2R}}}$, b – length of contact (width of flat spring);

R – radius of intermediate support;

μ_1 ta μ_2 – Poisson's ratio of materials in contact.

Vectors of volumetric stress state determined as [14]:

$$\begin{aligned} \sigma_x &= -p_{max} \left(\frac{1+2\zeta_b(y)^2}{\sqrt{1+\zeta_b(y)^2}} - 2|\zeta_b(y)| \right), \\ \sigma_y &= -p_{max} \frac{1}{\sqrt{1+\zeta_b(y)^2}}, \\ \sigma_z &= -2\mu_1 p_{max} \left(\sqrt{1 + \zeta_b(y)^2} - |\zeta_b(y)| \right). \end{aligned} \quad (24)$$

where, $\zeta_b(y) = y/t$.

The main stresses are identical accordingly to axial components:

$$\sigma_1 \equiv \sigma_x, \sigma_2 \equiv \sigma_z, \sigma_3 \equiv \sigma_y. \quad (25)$$

The maximum shear and equivalent von Misses stress presented graphically (fig. 5) by the formulas for volumetric stress state [15]. Tangential and von Misses stresses:

$$\tau_{max} = \frac{\sigma_1 - \sigma_3}{2}, \quad (26)$$

$$\sigma_{von\ Mises} = \sqrt{\frac{1}{2} [(\sigma_1 - \sigma_2)^2 + (\sigma_2 - \sigma_3)^2 + (\sigma_3 - \sigma_1)^2]}. \quad (27)$$

The maximum value of these stresses with static displacement $y_m = 0.24\ mm$ at $\zeta_b(y) = 0.786$: $\tau_{max} = 104.3\ MPa$, $\sigma_{von\ Mises} = 194.7\ MPa$. Also received $Q_1 = 1.66\ kN$.

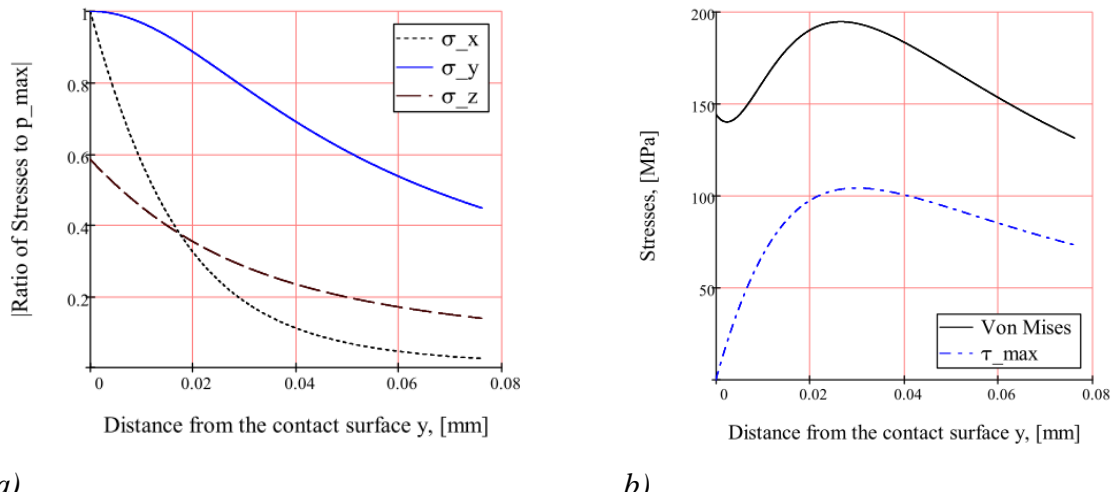
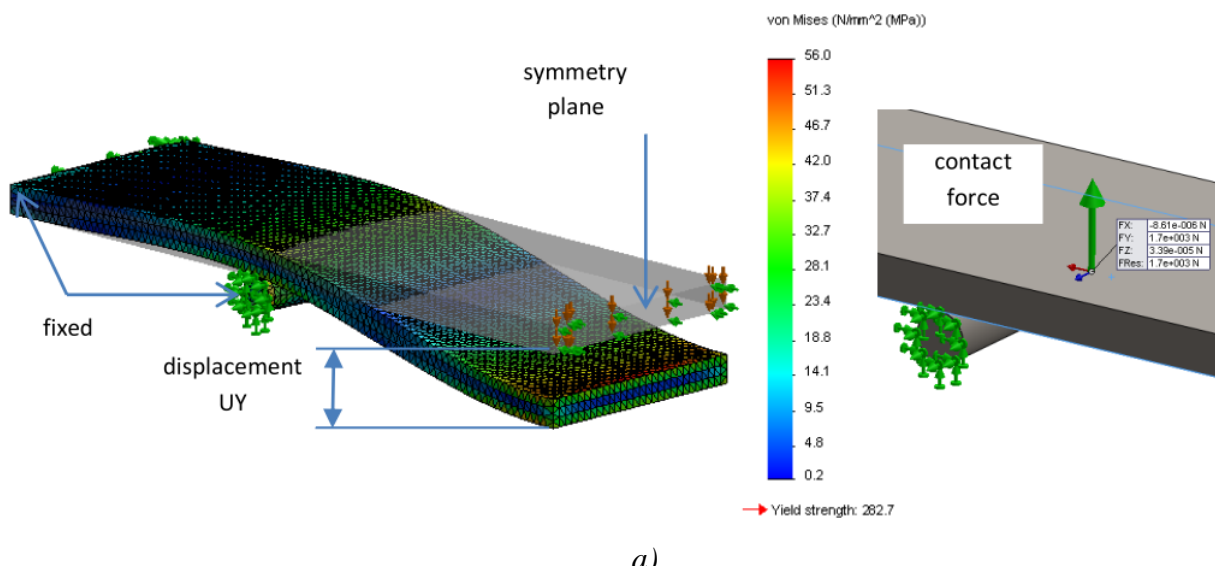


Fig. 5. The ratio of stress to the contact pressure (a); value of von Mises and shear stresses relative to the distance from the contact (b).

For comparison the results of the stress-strain state analysis of half flat spring in SolidWorks [8] with symmetrical scheme are conducted (fig. 6). A condition as no penetration between flat spring and cylindrical support is applied in the setting of contact task. The results for the curve of deflection and von Mises stress are an enough to near with the theoretical values (fig. 6, b and c). Also the contact force is set as 1.7 kN (fig. 6, a).



a)

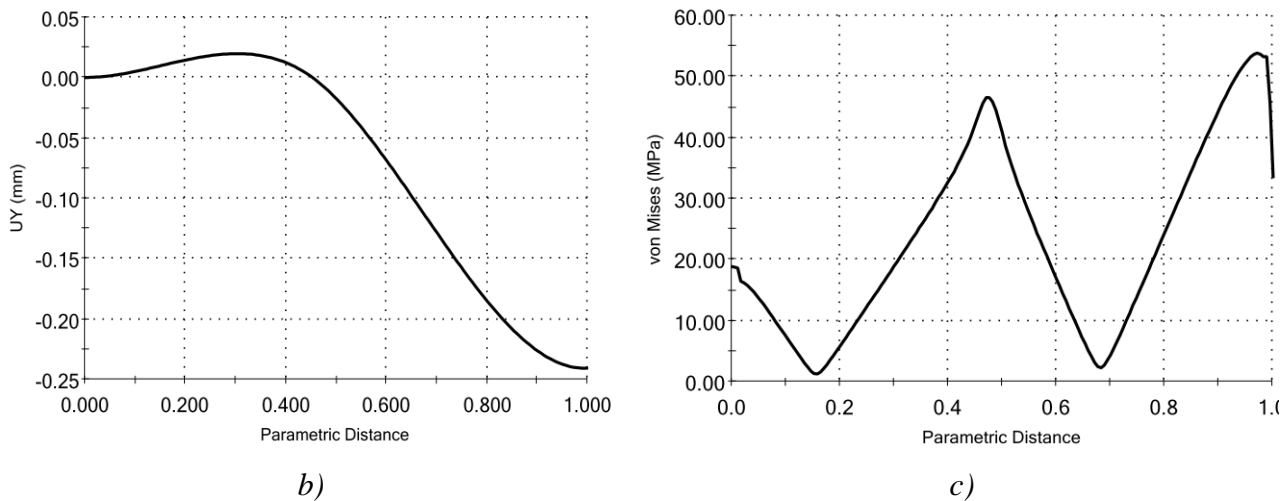


Fig. 6. Design model of stress-strain state (a), deflection curve (b) and von Mises stress (c) parametric changes regarding of the half long of the flat spring.

The procedure of nonlinear analysis is done with the setting as bounded contact for the flat stress. The maximum stress in the contact zone is 195.5 MPa. This value is almost identical to the theoretical result.

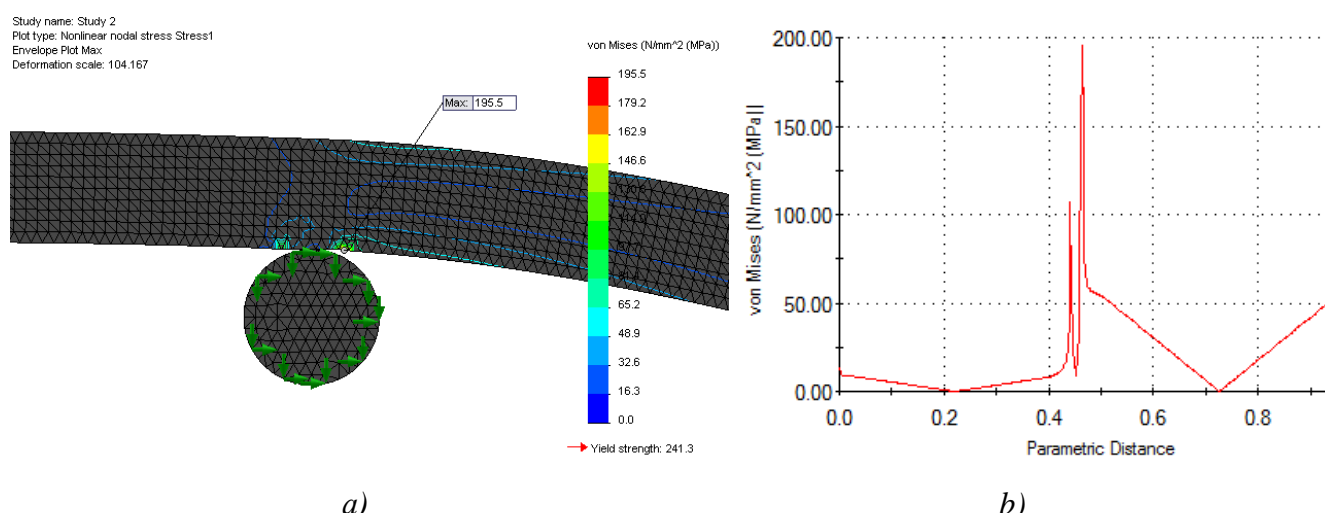


Fig. 7. Diagrams of contact stresses (a – flat section, b – the value of along the parametric length of the spring).

The pliability of intermediate supports is caused by relative displacement Δ_c of flat spring and support at the contact zone. Determined by the following expression [15]:

$$\Delta_c = 0.83 \sqrt[3]{\frac{Q_1^2}{R} \left(\frac{1-\mu_1^2}{E_1} + \frac{1-\mu_2^2}{E_2} \right)^2}, \quad (28)$$

The stiffness coefficient in the contact point $c_y = Q_1/\Delta_c$. The resulted formula has a simplified view for contact with materials steel and steel:

$$\Delta_c = 1.23 \sqrt[3]{\left(\frac{Q_1}{E}\right)^2 \frac{1}{R}}, \quad (29)$$

$$c_y = 0.81 \sqrt[3]{Q_1 R E^2}. \quad (30)$$

The last formula allows to consider the contact stiffness in intermediate support on implementation of vibro-impact modes. In this case, parametric contact stiffness is depending from the contact force through the instantaneous movement of local mass y_m . For $y_m = 0.24 \text{ mm}$ contact stiffness is $c_y = 6.1 \times 10^7 \text{ N/m}$.

Dynamics of stress-strain state. The resulting static characteristics can be used for dynamic stress state analysis of the vibro-impact system with kinematic's disturbance of local mass (fig. 8).

The characteristics of local mass movement takes in the form $y(t) = y_m \sin(314t)$. Contact force depends of the instantaneous movement of local mass according to conditions of the system:

$$Q_c(t) = \begin{cases} 0, & y(t) \geq 0, \\ \frac{c_{II}y(t)(l_1^2 + 4l_1l_2 + 3l_2^2)}{2l_1(l_1 + 4l_2)}, & y(t) < 0, \end{cases} \quad (31)$$

Given a parametric dependence c_y contact stiffness from the contact force Q_1 , confirmed their nonlinearity in the fig. 9.

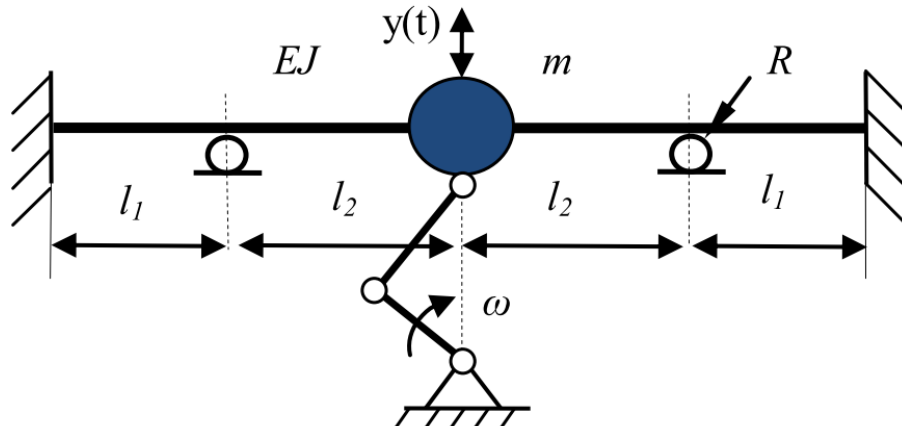


Fig. 8. Kinematic's disturbance scheme of the vibro-impact rod system.

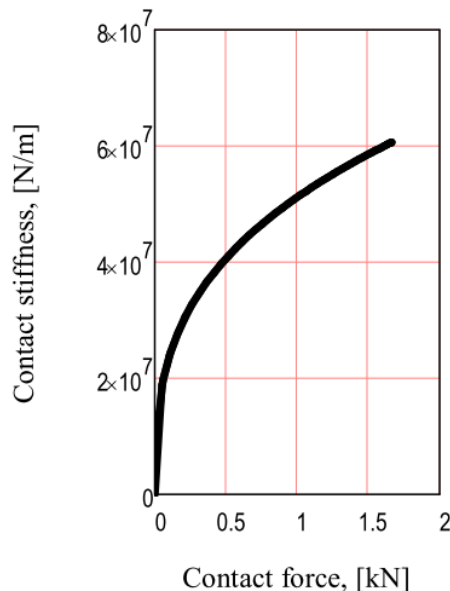


Fig. 9. Dependence of the stiffness coefficient of intermediate support of the magnitude of the contact force (by the displacement $y(t)$ of local mass).

The equivalent bending stress is determined by the conditions of the rod system operation:

$$\sigma_{eq}(t) = \begin{cases} \sigma_{eqI}(t), & y(t) \geq 0, \\ \sigma_{eqII}(t), & y(t) < 0, \end{cases} \quad (32)$$

Depending in time the equivalent stresses for bending and contact presented at the fig. 10. They have asymmetrical pulse character, caused by implementation of the vibro-impact mode scheme.

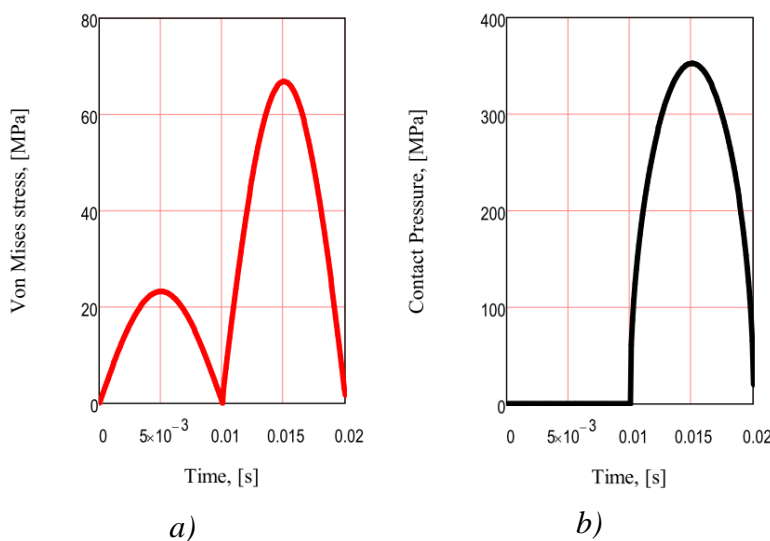


Fig. 10. The time dependence of bending (a) and contact stresses (b) in vibro-impact rod system.

Parametric dependents of calculated stress values from the instantaneous displacement of local mass $y(t)$ are shown in fig. 11. Contact stress is nonlinear from displacement in time.

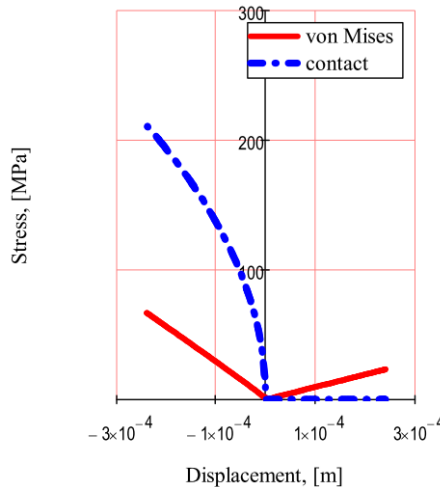


Fig. 11. Parametric dependence von Mises and contact stresses in the vibro-impact rod system.

Summary. The construction of resonance module capable to operate in a harmonious and vibro-impact modes is made. Formula of the bending rigidity of flat spring to implement the given the asymmetric elastic characteristic is obtained by finite element method. A value and character of stress-strain state of the flat spring analytically is determined. The result is approved by modeling in SolidWorks Simulation. Contact stiffness in intermediate cylindrical support in contact with a flat spring is determined. Dynamics for example of the kinematic disturbance is considered and built a parametric characteristic of equivalent stresses.

References

- [1] Yoon, J. Y., & Kim, B. (2015). Vibro-Impact Energy Analysis of a Geared System with Piecewise-Type Nonlinearities Using Various Parameter Values. *Energies*, 8(8), 8924-8944.
- [2] Chu, S., Cao, D., Sun, S., Pan, J., & Wang, L. (2013). Impact vibration characteristics of a shrouded blade with asymmetric gaps under wake flow excitations. *Nonlinear Dynamics*, 72(3), 539-554.
- [3] Patent USSR № 1351696 A, B 06 B 1/14 (1987), Method to tune to resonance oscillations of the vibratory machine with piecewise-linear characteristics of the elastic ties, in Russian
- [4] Patent USSR № 1727928 A1, B 06 B 1/14 (1992), Method the settings for a given mode of oscillation of the vibratory machine with nonlinear elastic connections and operating mass, in Russian.
- [5] Patent USSR № 1634335 A2, B 06 B 1/14 (1991), Vibratory device, in Russian.
- [6] Patent USSR № 1381282 A1, F 16 F 13/00 (1988), Eastic suspension, in Russian.
- [7] Peter, Simon, Pascal Reuss, and Lothar Gaul. (2014), Identification of Sub-and Higher Harmonic Vibrations in Vibro-Impact Systems. *Nonlinear Dynamics*, Volume 2. Springer International Publishing, 131-140.
- [8] Belovodskiy V. N., Bukin S. L., Sukhorukov M. Y., Babakina A. A. (2015), 2:1 Superharmonic Resonance in Two-Masses Vibrating Machine // *Journal of Vibration Engineering & Technologies*, 3(2), 123-135.
- [9] Ostasevicius, V., Gaidys, R., & Dauksevicius, R. (2009), Numerical analysis of dynamic effects of a nonlinear vibro-impact process for enhancing the reliability of contact-type MEMS devices. *Sensors*, 9(12), 10201-10216.

[10] Bazrafshan, M., Ahmadian, H., & Jalali, H. (2014). Modeling the interaction between contact mechanisms in normal and tangential directions. International Journal of Non-Linear Mechanics, 58, 111-119.

[11] Serweta, W., Okolewski, A., Blazejczyk-Okolewska, B., Czolczynski, K., & Kapitaniak, T. (2014). Lyapunov exponents of impact oscillators with Hertz' s and Newton' s contact models. International Journal of Mechanical Sciences, 89, 194-206.

[12] Fayyad, S. M. (2013). Analysis and Simulation of Contact Stresses of Convex Punch Analysis, IOSR Journal of Engineering, Vol. 3, Issue 12, 59-67.

[13] David, V. Hutton. (2004), Fundamentals of finite element analysis. Editorial McGraw– Hill, USA.

[14] Shigley, Joseph Edward. (2011), Shigley's mechanical engineering design. Tata McGraw-Hill Education.

[15] G.S. Pisarenko, A.P. Yakovlev, V.V. Matveev. (1988), Hand book on Strength of Materials, Naukova Dumka, Kiev, in Russian.

Modelling of Station of Pumping by Variable Speed

Benretem A. ¹

1 – Electromechanical Engineering Laboratory, Badji-Mokhtar Annaba University P.O. Box12, 23000, Annaba, Algeria



DOI 10.13140/RG.2.1.4707.0324

Keywords: energetic efficiency, centrifugal pump, motor, variable speed drive, inverters, modelisation, simulation.

ABSTRACT. An increased energetic efficiency will make it possible to decrease the factory operating costs and hence to increase productivity. The centrifugal pumps are largely used because of their relatively simple operation and of their purchase price. One analyses thorough requirements imposed by the pumping plants is decisive. It is important to keep in mind the fact that the pumps consume approximately 20% of energy in the world. They constitute the possibility for the most significant efficiency improvement. They can reach their maximum effectiveness only with one pressure and a given flow. The approach suggested makes it possible to adapt with accuracy and effectiveness of system output of the industrial process requirements. The variable speed drive is one of best and effective techniques studied to reach this objective.

The appearance of this technique comes only after the evolution obtained in the field of power electronics systems precisely static inverters as well as the efforts made by the researchers in the field of electric drive systems. This work suggested is the result of an in-depth study on the effectiveness of this new technique applied for the centrifugal pumps.

1. Introduction. Due to their operating closer to the optimum, variable speed pumping plants are reliable: energy saving, maintenance intervals saving and hence stop costs reduction. According to the structure of the user, it is also possible, by the intermediary of a speed regulation, to reduce the number of the pumps size. The complexity of a centrifugal pump drive makes its study and design difficult as well as during its normal operation. To overcome this difficulty, one generally carries out simplifications: linearization of some characteristics, addition of inertias of all the moving parts to that of the engine, etc. in function of the objectives of modelling, these simplifications can give satisfactory results[3]. With the aim of reducing the costs and risks of bad operations in the evaluation phase and training of complex systems, the use of data-processing tools for digital simulation seems a justifiable intermediate stage between the theoretical study and the tests on real installations. Pump centrifuges P-102.b P-102.a several tools (specialized or not) for simulation are used in the field of the machines electric and of the power electronics [4] [5]:ATOSEC5, EMTP, SPICE, SIMNON, MATLAB, etc. [3].**2. Modelisation of the System of Pumping.** Figure 1 presents prone pumping plant the "of study"; unit of ammonia NH₃ of the Asmidal factory - Annaba - Algeria and more precise the centrifugal pumps P-102 intended for fed the units of nitric acid, acid nitrate and of acid phosphates in product ammonia "to see figure 1".

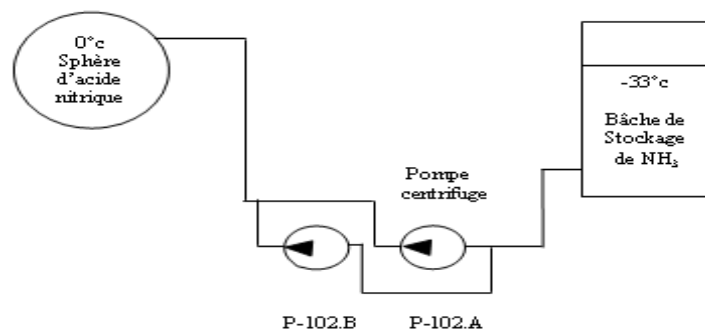


Fig. 1. diagram of the pumping plant of ammonia.

2.1 Mathematical modelling of the centrifugal pump.

Generally, the manufacturers do not give the characteristics of the pumps physical parameters performances $H = F(Q)$ is offered. Thus; knowing speed, the load height, and reference flow; it is possible to determine the system characteristics; the following relations can be used:

$$N_{sq} = \frac{1000 \left(\frac{N}{60} \right) \sqrt{Q}}{\left(\frac{gH}{N_{ep}} \right)^{3/4}}$$

$$Q = K_{sp} N (D_f)^3$$

$C_r = 0.3 + 3.9 \times 10^{-4} (\varpi)^{1.8}$ The modelling characteristic diagram of the centrifugal pump equations system is presented in figure 2.[8]

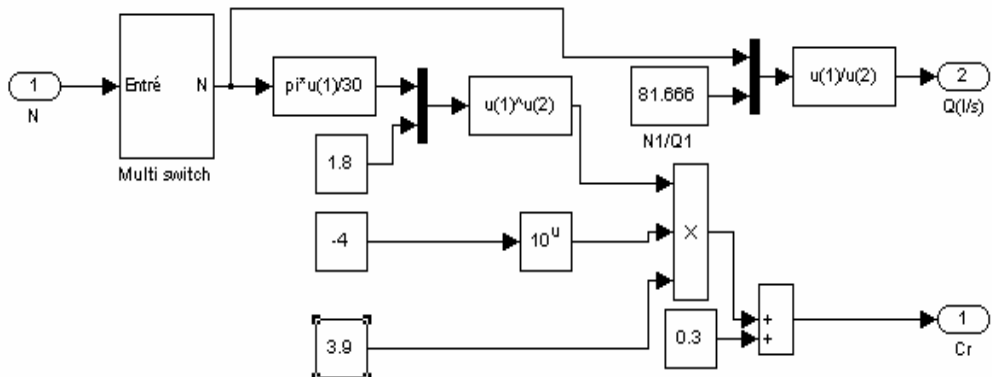


Fig. 2. Structure of the centrifugal pump unit.

2.2 Modeling of the squirrel cage induction motor. The drive is designed as an integrated block of which the goal is the optimal conversion of the electric power into mechanical energy and hydraulics by taking into account the performance criterion defined in the specifications. The modelling of the principal parts of the suggested pumping system (converter - engine - pump) are gathered and presented in figure 3.

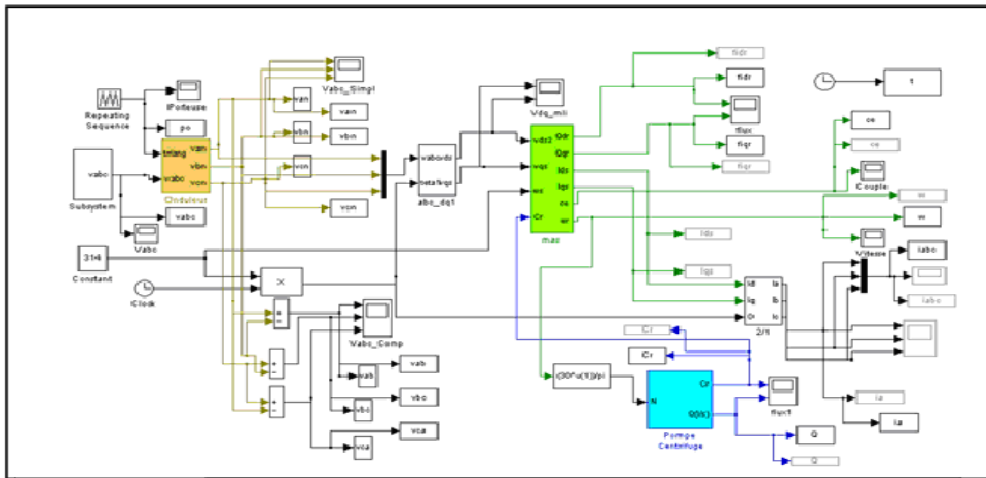


Fig. 3. Model of the pumping system.

3. Results of the system simulation.

3.1 Simulation of the system with constant speed. The figure.4 takes the stator current curve in transient state and permanent modes as well as the magnetic flux of the centrifugal pump drive motor with load and with no-load in the d- q plan. During the no-load, it can be noticed that flow is inversely proportional to the stator current; the introduction of the load "pumps centrifuges" does not present any remarkable evolution, always flow is inversely proportional to the stator current.

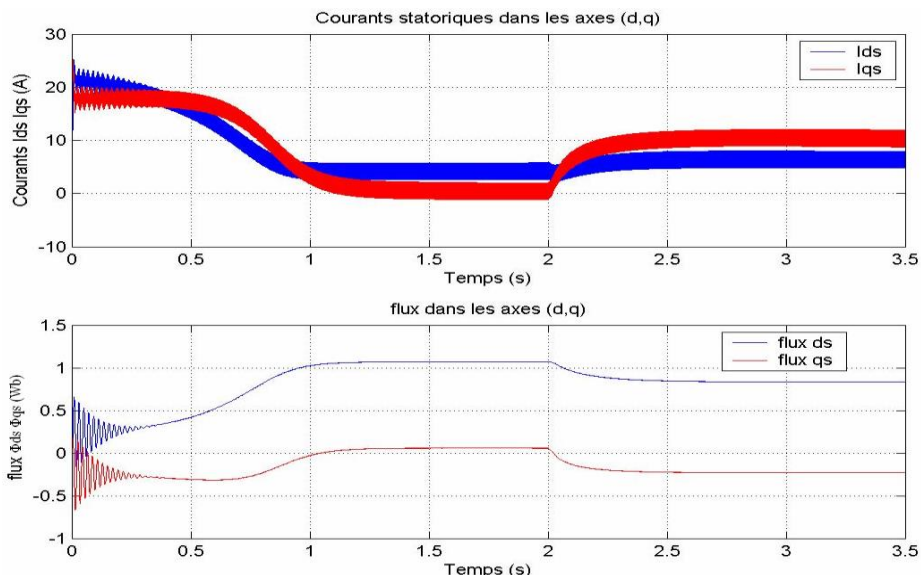


Fig. 4. Current stator and magnetic flux according to axes' (D, Q) in no-load and load (load applied at the moment $T = 2s$).

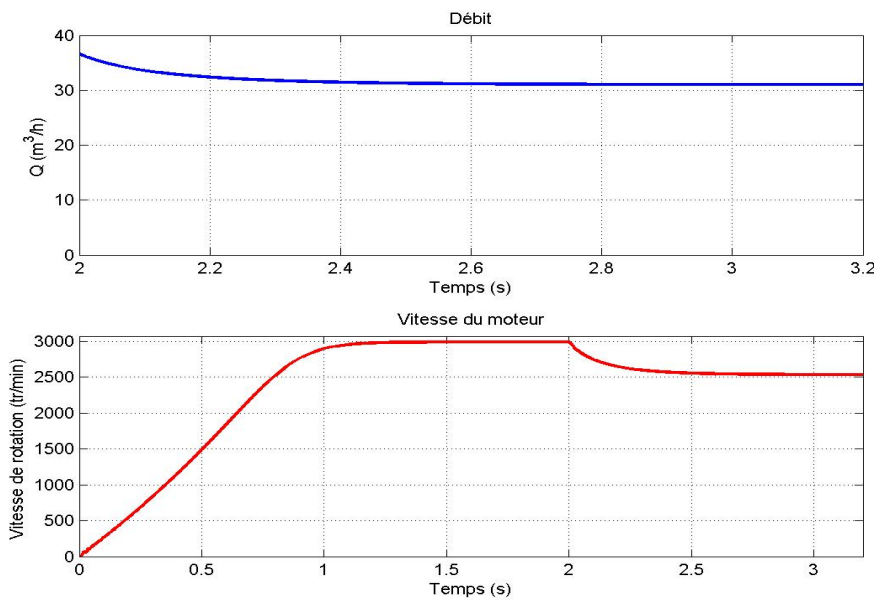


Fig. 5. Variation the motor speed: pump Flow corresponds at a speed of 2500 rev/min.

Figure.5 illustrates the variation of the pump revolutions number according to the flow. For a flow equal to $31 \text{ m}^3/\text{h}$, the number of revolutions takes a value equal to 2500 rev/min., at the time "t = 2 s" time of introduction of the load "the centrifugal pump" generates a reduction in the number of revolutions of the drive motor. On the other hand one records an increase in the values of the motor torque (electromagnetic torque) for the same time "t=2 S" as it is shown in figure.6.

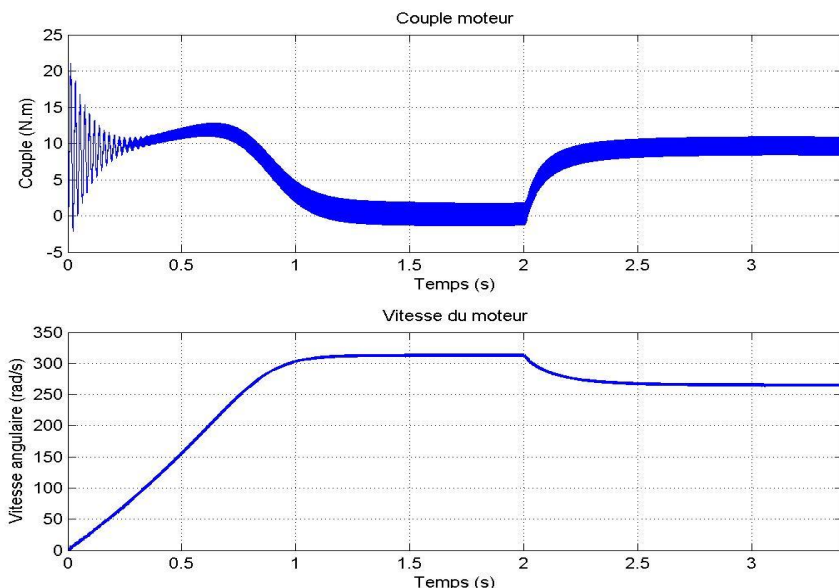


Fig. 6. Motor torque and angular velocity of the engine in a no-load and load (load applied at the time $T = 2s$).

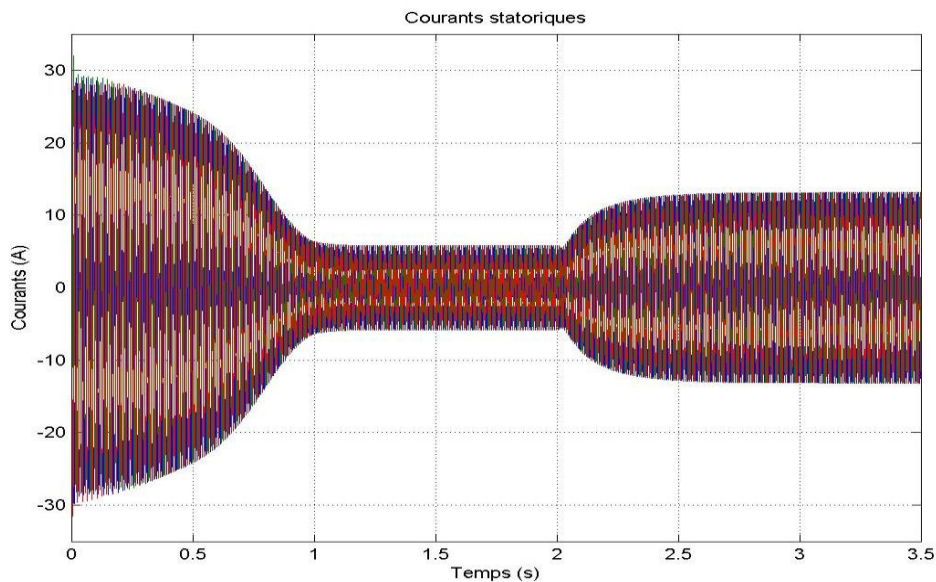


Fig. 7. Motor stator current with no-load and load (load applied at the time $T = 2s$).

Figure 7 shows that the motor torque is inversely proportional to the motor revolutions number; whereas the above mentioned torque is proportional to the motor stator current as shown in the figure 8.d' where the two curves take the same form except that one records an increase in the current amplitude of line beyond that time "t = 2 s".

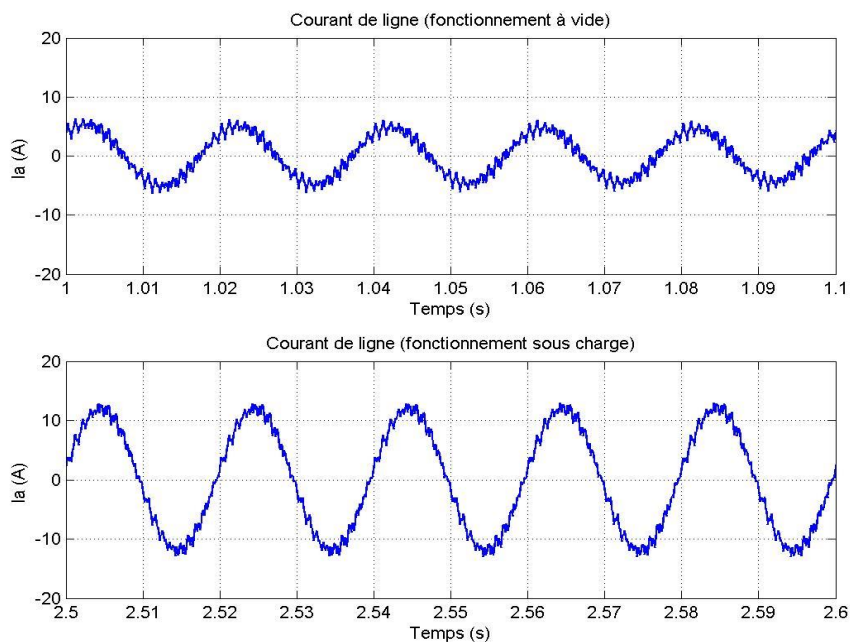


Fig. 8. Current of line (no-load and load).

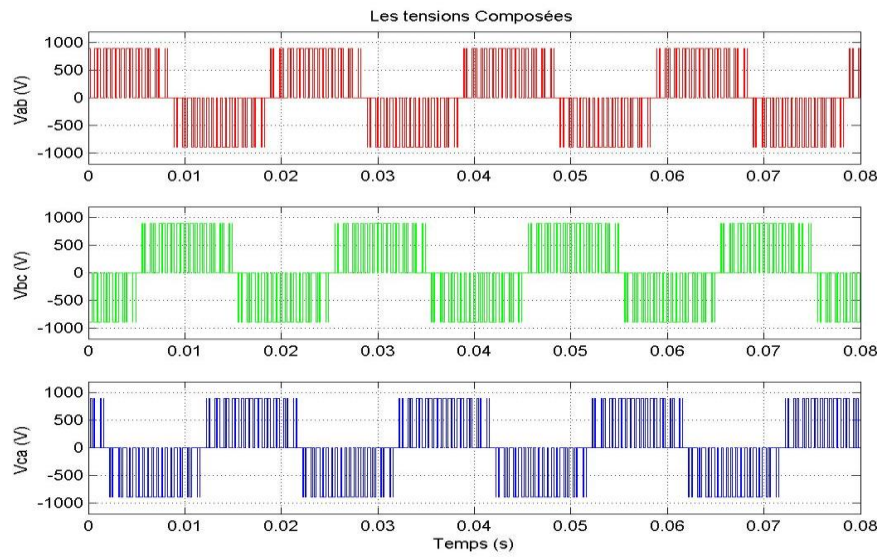


Fig. 9. Voltage made up of the 3 phases (operation under load).

Both **figures.9** and **10** respectively represent the voltage waveform made up and simple of the three phases of the motor operating in load.

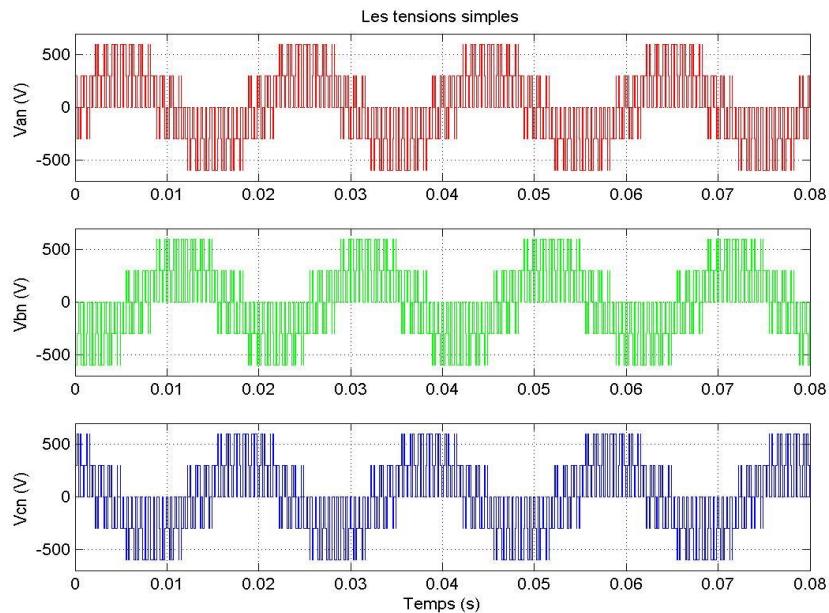


Fig.10. Simple voltage of the 3 phases (operation under load).

3.2 Simulation of a variable speed system The second part of simulation includes a new system because of the introduction of a variable speed control system; this technique can offer substantial cost saving in the electric power system when necessary flows or pressures variations were done in the system. Figure 11 shows that the flow and the number of revolutions take the same form according to time; in which the increase in flow causes the increase in the motor speed and its reduction generates the reduction of the latter (figure 11).

It can be noticed that there is a great improvement in the parameters compared to figure 5

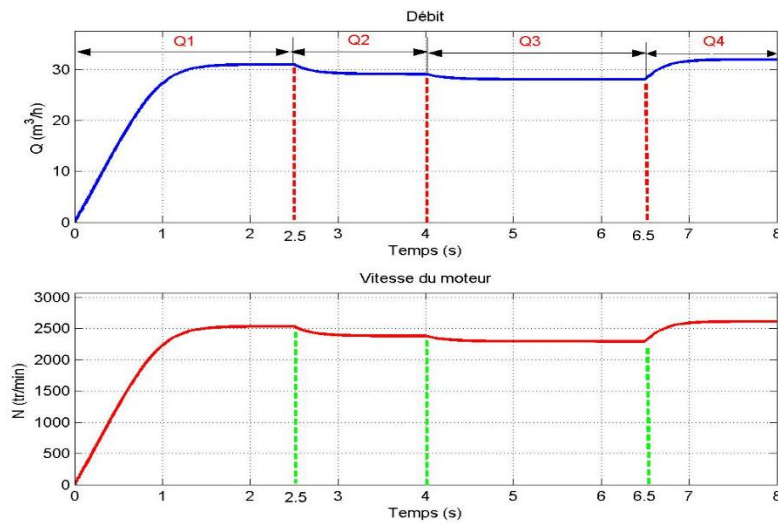


Fig. 11. Motor speed variation and the pump flow against time.

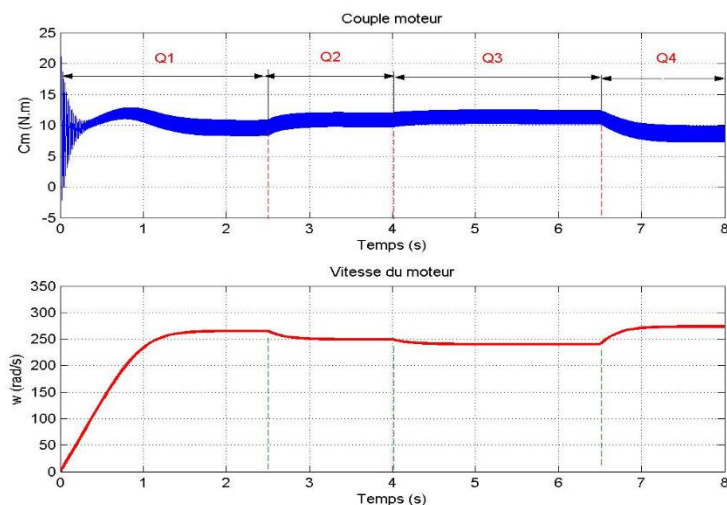


Fig. 12. Motor torque operating with load in function of speed variation.

Figure 12 shows that the torque is always inversely proportional to the motor speed

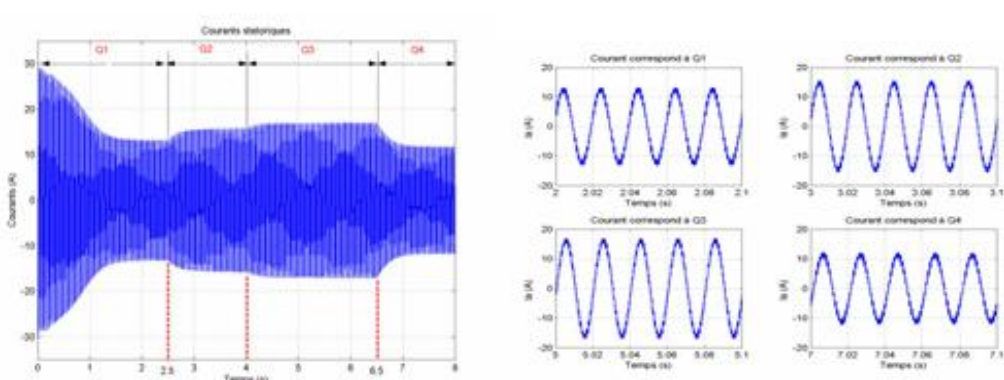


Fig. 13. The motor Stator current operating under load with speed variation.

The stator current results from this variation speed is shown in Figure 13; this current is proportional to the motor torque evolving with the variation of the pump flow. This proves that this technique is likely to improve the energy effectiveness of the centrifugal pump and to reduce the energy losses, as illustrated by this load profile of Figure.14

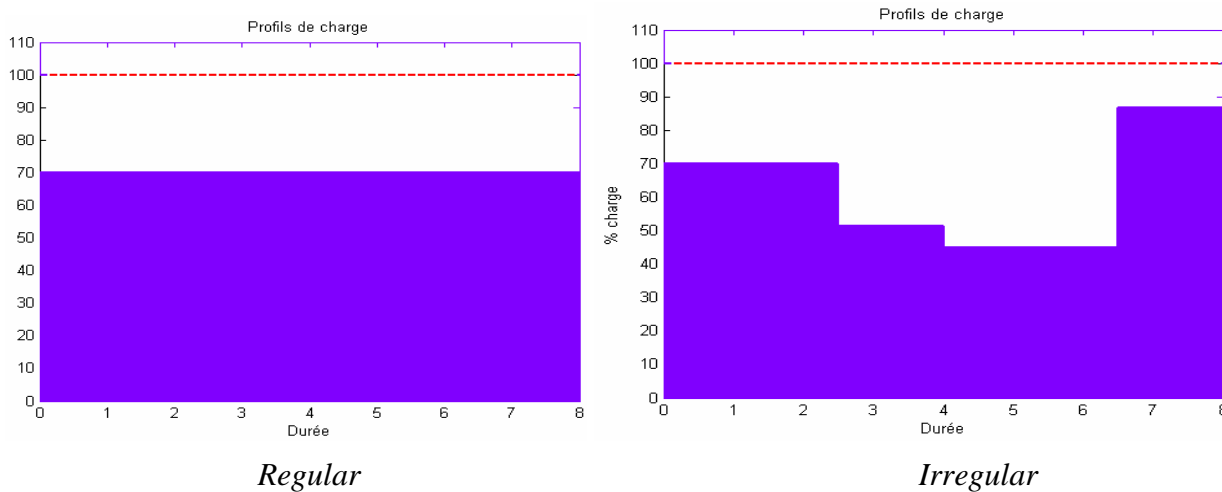


Fig. 14. Load profile of the pump operating at variable speed.

Summary. From an economic point of view, it is often more judicious to adapt the flows desired by the implementation of a variable speed drive. With a continuous speed variation, the consumption of energy is adapted to the needs and there is no energy dissipation.

The wear of the pumps, the bodies of throttling and the installation decreases, since the installation functions only in the necessary operation. The motor is definitely under loaded; and the pump has the possibility of starting smoothly and of the unfavourable hydraulic reactions is avoided. This intelligent method makes it possible to prolong the lifespan of the pump and the installation as a whole and increases the availability of the installations.

In general, the results obtained confirms the reliability of modelling carried out, the possibility of optimization of the system and minimization of the energy losses.

These satisfactory and clear results show that the use of the variable speed drive in centrifugal pumps is an optimal solution in spite of its complexity and its relatively high price.

References

- [1] Peeic (Programmer of Energy Saving in Canadian Industry), "Guide of evaluation of the output of the energy driving systems ".Natural resources Canada 2004.
- [2] Arene, "The true cost of the pumps".Hydro more, N 128.November 2002.
- [3] Doumbia.M.L, "Tool of assistance to the systems design of electric drive of machine, example of application ".Thesis of PhD of the polytechnic school of Montreal. 2000.
- [4] Boubacar.N, "Design techno - economic of a system of autonomous pumping photovoltaic - aero generator ".Memory of M.Sc.A of the polytechnic school of Montreal. February 1999.
- [5] Mohan.N, Undeland.T and Robbins.W, "Simulation of Power Electronic and Motion Systems Control - Year Overview» Proceeding of the IEEE, vol. 82, No 8, August, 1989.
- [6] Etxeberria- Otadui.I, "On the system of the electronics of power dedicate has the electric distribution - application has the quality of energy ".Thesis of doctorate of the Institut National Polytechnique of Grenoble.September 2003.
- [7] Stpanoff. A. J, "Centrifugal pump and pumps Propellers ".Dunod. Paris.1961

- [8] Betka Achour Perspectives for the sake of photovoltaic pumping development in the south thesis for doctorate of state Biskra Science.
- [9] Automatic alpha issaga diallo Sélection of the asynchronous motors in the industrial drives thesis for obtaining Master be sciences (M.Sc) University Laval 1998.

A Thermal Force Drifting Particles along a Temperature Gradient

Amelia Carolina Sparavigna¹

1 – Department of Applied Science and Technology, Politecnico di Torino, Torino, Italy



DOI [10.13140/RG.2.1.2347.7365](https://doi.org/10.13140/RG.2.1.2347.7365)

Keywords: Thermal gradient, Thermal transport, Thermal forces, Entropic forces.

ABSTRACT. In 1972, V. Gallina and M. Omini of the Polytechnic of Turin proposed a phenomenological model for the thermal diffusion in liquid metals, explaining the isotope separation as provoked by a thermal force which is arising when a temperature gradient is established in the material. Here, we discuss this thermal force and its statistical origin from the bulk. We will see that it can be considered as a force of the form $F = -S \text{ grad } T$, that is as a thermal/entropic force obtained from the derivative of the Helmholtz free energy with respect to the volume.

Introduction. With the works of Ludwig Boltzmann, physics and thermodynamics started recognizing the stochastic and probabilistic aspect of natural processes. Besides introducing a fundamental equation widely used for thermal and charge transport [1-5], Boltzmann linked the second law of thermodynamics to the disorder of thermodynamic systems, proposing a fundamental relation between entropy S and probability through the formula $S = k_B \ln W$ (k_B is the Boltzmann's constant and W is for Wahrscheinlichkeit, that is “probability” in German).

The Boltzmann formulation of entropy was fundamental for the “doctrine of energy and entropy” that rules the thermodynamic world [6], a doctrine where the energy is deterministic and the entropy is favouring randomness. In this framework of natural systems governed by energy and entropy, forces can arise from the Helmholtz free energy $A = U - TS$, where U is the internal energy, T the temperature and S the entropy. Such as the pressure, the mechanical force divided by a surface, is coming from the derivative of internal energy U with respect to the volume, the same derivative of the product TS is giving rise to the thermal and entropic forces. These are forces which are coming from the statistical nature of the system, rather than from a particular microscopic interaction existing in it [6].

Entropic forces had been proposed and used in [7,8] for the Brownian motion and for the elasticity of polymers. For the Brownian motion, the force is in the form of a diffusional driving force or radial force, which has a mean value $\langle F_r \rangle = T \langle dS/dr \rangle$, where r is a radial distance [9]. We can understand this mean value considering its dimensionality: the force is an energy - here given by the product TS - divided by a length. However, besides the entropic force which is coming from a local variation or gradient of entropy, we can have also a force in which it is appearing as the gradient of temperature T multiplied by an entropy, that is $F = -S \text{ grad } T$. A thermal force of this kind is used for the magnetic flux structures in superconductors [10,11]. In these references, this force is also considered as an entropic force.

In the following discussion, we will show another example of such thermal force, which is concerning the isotope separation in liquid metals driven by a thermal gradient. It was proposed in 1972, by V. Gallina and M. Omini of the Turin Polytechnic in a phenomenological model for the thermal diffusion in liquid metals [12]. In their study, the authors aimed giving a formula for the isotope separation in a liquid metal, separation which is observed when a temperature gradient is established in the fluid [13]. In fact, the approach and the related model proposed in [12] is more general: it embraces completely the problem of thermal diffusion in fluids.

The focus of authors was in investigating the force that is moving atoms through a liquid when there is a thermal gradient in it. In a good approximation, this force has a simple expression: $\mathbf{F} = -k_B \operatorname{grad} T$, where T is the temperature. In this paper we will see that it can be considered as the thermal/entropic force $\mathbf{F} = -S \operatorname{grad} T$, [10,11]. It means that this is one of the two partners of a pair of forces coming from the derivative of $T S$ with respect to volume, the other member being the entropic force $\mathbf{F} = -T \operatorname{grad} S$.

Let us start discussing the thermal force appearing in [12].

The thermal force. The central part of Reference 12 is discussing the force responsible for the drift velocity of particles in a temperature gradient. This drift of particles, appearing when a thermal gradient exists, is an experimental fact. It appears in observed effects and named as thermodiffusion, thermophoresis, thermomigration or Ludwig-Soret effect [14]. This phenomenon, which we find in mixtures of particles where the different types of particles exhibit different responses to the temperature gradient, has a number of practical applications. In fact, due to the different behavior, the particle types can be separated. Several recent papers on isotope separation in silicate melts for instance, are evidencing the present interest on this subject [15-18].

In a first approximation, a particle with radius r in a solvent has a drift velocity $w = F/(4\pi\eta r)$ [12]. η is the coefficient of shear viscosity of the solvent. F is the force drifting the particle. To give an expression of this force, in [12], the authors evaluated first the net force acting on an atom of a solid lattice when it is subjected to a thermal gradient. Each atom of the lattice is a scatterer of thermal waves (phonons). In the second quantization, the displacements of waves are considered as quasiparticles, the phonons, having energy and momentum. If we consider an atom of the lattice, we can imagine it in a local oscillatory motion. It becomes a phonon scatterer, exhibiting a cross-section $\sigma(\mathbf{q}, \mathbf{q}')$ for an elastic scattering in which a phonon having wave vector \mathbf{q} is deviated into a phonon of wave vector \mathbf{q}' . In fact, this approach would be true only for an impurity scattering: in a perfect lattice, we need at least three phonons involved in scattering processes. However, Gallina and Omini are showing in [12], that using the general theory of phonon-phonon interactions, the same result is obtained.

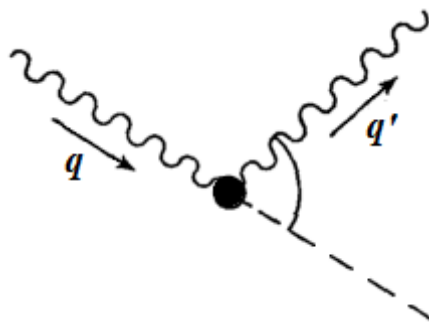


Fig. 1. An atom of the lattice as a scatterer, with transferred momentum equal to $\hbar(\mathbf{q} - \mathbf{q}')$.

In the diagram of Fig.1, we can see that the momentum transferred to the atom is $\hbar(\mathbf{q} - \mathbf{q}')$, where \hbar is the reduced Planck constant.

Adding the contributions of all the scattering processes, which are occurring in unit time, we have the force imparted to the atom by the thermal vibrations. The result is:

$$\bar{F} = \frac{\hbar}{N} \sum_q g_q v_q \bar{q} \frac{1}{\lambda_q} \quad (1)$$

In (1), N is the total number of atoms, v_g the group velocity, λ_q the mean free path and g_q the deviation from the Bose-Einstein equilibrium function. Since g_q is proportional to the mean free path in the relaxation-time approximation [5], we have a result independent of the phonon mean-free path. Therefore, in this approximation, the net force turns out to be simply $\mathbf{F} = -k_B \nabla T$. This force has no real effect if the atom belongs to the solid lattice, because this force is simply transmitted to the centre of mass of the crystal. In a liquid, where the atom is not bound to any particular site of the system, the force becomes a driving force, moving the atom towards the cold end of the sample [12].

Are we justified in using this force for an atom in the liquid, since it has been deduced for a solid? [12]. In the reference, the authors are giving specific arguments for a positive answer. First, we have a phenomenological argument: the thermal force only depends upon the atomic specific heat $c = 3k_B$, and this is a quantity which is presumed to be almost unaffected by the solid-liquid transition. Second: consider an atom O in the cage of its neighbors. Imagine we have Σ atoms surrounding O. Since the atom can move isotropically toward any of its Σ surrounding, the probability of one of this atoms of moving toward O is $1/\Sigma$. Thus the atom O, at a certain instant, has the probability $p = 1/\Sigma$ of being struck by one of its neighbors. The time required for an interaction with its i -neighbor, is $t_i = a/v_i$, where a is the nearest-neighbor distance and v_i the speed of i -atom.

After some passages, we can find that the mean force acting on O is [12]:

$$\langle \vec{F}_O \rangle = -\frac{1}{\Sigma} \sum_i \frac{mv_i^2}{a} \vec{u}_i = -\frac{1}{\Sigma} \sum_i \frac{3k_B T_i}{a} \vec{u}_i \quad (2)$$

In (2), \vec{u}_i is the unit vector from O to i -neighbor. T_i is the temperature of the i -neighbor. Moreover, $T_i = T_O + a \vec{u}_i \cdot \nabla T$. Therefore, if we have a statistical environment which is isotropic, we can average on the solid angle:

$$\langle \vec{F}_O \rangle = -\frac{1}{a \Sigma} \frac{\Sigma}{4\pi} \int d\Omega 3k_B a (\vec{u}_i \cdot \nabla T) \vec{u}_i = -k_B \nabla T \quad (3)$$

Let us consider again a particle moving in a solvent; if no other forces are present, the drift velocity is given by:

$$-4\pi\eta r \vec{w} - k_B \nabla T = 0 \quad \rightarrow \quad \vec{w} = -\frac{k_B \nabla T}{4\pi\eta r} \quad (4)$$

As the authors are remarking, this force has not to be considered as due to a potential gradient, that is, to an external action; it is a statistical force, originated from the bulk of the material, which accounts for the possibility of an atom of making a random walk in the liquid.

To have (3), an atom which is vibrating at temperature T has an energy $3k_B T$. This is true in the approximation of an atom considered as an Einstein harmonic oscillator. However, this energy has to be modified when an anharmonicity exists [12].

Role of surfaces. Summing the thermal force over all the atoms of the sample, we should have $F = -N k_B \text{grad } T$. For $|\text{grad } T| = 1^\circ\text{C}/\text{cm}$ and $N=10^{23}$, we have $F \approx 100 \text{ N}$. Why do we not observe this force? [12]. Let us see how the authors answered. In the case of a solid, we can have that on the wall which is at higher temperature, there is an excess of phonon pressure with respect to the wall at lower temperature. This extra pressure gives rise to a force directed along $\text{grad } T$, which is exactly counterbalanced by the resultant of the thermal forces. In the case of a fluid, we can see that atoms at the surface of the material give different pressures; there is a force on surfaces which is equal and opposite to the thermal force [12].

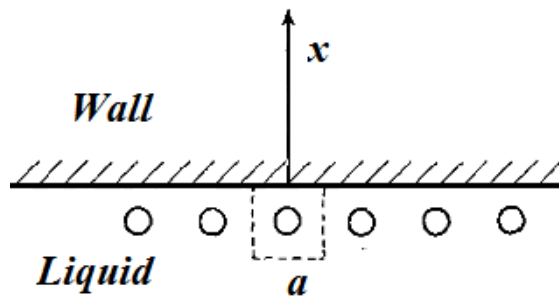


Fig. 2. Atoms at the surface of liquid.

For a liquid, let us take an atom of the liquid near the wall (Fig. 2). It makes a random oscillation in a cage of the order of the atomic volume a^3 . The atom oscillates. If t is the period of the oscillation, we can write $v_x t \approx 2a$, where v_x is the average velocity normal to the wall. Whenever the atom arrives at the wall, we assume an elastic reflection. The transferred momentum is $2mv_x$. If n is the number density of atoms in the liquid, the total number of atoms facing the wall with surface Σ is $na\Sigma$. Then the force on the wall is:

$$na\Sigma \cdot \frac{2mv_x}{t} = n\Sigma m v_x^2 = n\Sigma k_B T$$

where $m v_x^2 = \frac{1}{3}m(v_x^2 + v_y^2 + v_z^2) = k_B T$ (5)

$$F_{\text{surface}} = n\Sigma k_B T_1 - n\Sigma k_B T_0 = n\Sigma L k_B \frac{T_1 - T_0}{L} = N k_B \nabla T \quad (6)$$

In (6), we have that an unbalanced force on surfaces exists. However, the bulk thermal force balances this surface force. It happens when the two walls at different temperatures have the same surface Σ . If we have different surfaces, we need to consider the role of the lateral surface, in order to have a net force equal to zero. The conservation of momentum tells us that the net force must be zero.

Thermal and entropic forces. Let us consider the Helmholtz free energy $A = U - TS$, and its derivative with respect to the volume V . Then, let us multiply this derivative by the surface Σ . We can consider a generalized force as $F = \Sigma dA/dV = \Sigma dU/dV - \Sigma S dT/dV - T \Sigma dS/dV$. The first term is the pressure multiplied by the surface, that is, the mechanical force.

In the case that we assume the volume variation dV as equal to Σdx , we have a force F given by three terms, $F = \Sigma p - S dT/dx - T dS/dx$. Then, besides the term containing the pressure, we have the two thermal/entropic terms.

Is the thermal force $\mathbf{F} = -N k_B \text{grad } T$ previously discussed the term $-S dT/dx$? The Boltzmann constant has the dimensions of an entropy S ; therefore, dimensionally [19], we have the thermal force $\mathbf{F} = -N k_B \text{grad } T$ as $\mathbf{F} = -S \text{grad } T$, and a thermal/entropic force of this kind was used for the magnetic flux structures in superconductors [11,12]. However, we can find a more convincing reason for a positive answer in [20]. In this paper, the Debye model is used instead of the Einstein model. In the case of a phononic assembly, the bulk force is [20]:

$$\vec{F}_{ph,diff} = -3N k_B \nabla T \times \left(\frac{T}{\theta_D} \right)^3 \int_0^{\theta_D/T} y^4 e^y (e^y - 1)^{-2} dy \quad (7)$$

If we are at low temperatures, the entropy S can be considered as $S = C/3$, where C is the heat capacity [21]. In a Debye model [19]:

$$S \approx \frac{C}{3} = 3N k_B \left(\frac{T}{\theta_D} \right)^3 \int_0^{\theta_D/T} y^4 e^y (e^y - 1)^{-2} dy \quad (8)$$

Then, the thermal force (7) given by Omini in [20], seems coincident with a thermal/entropic force, in the abovementioned approximation. In fact, using (8) in (7), we have:

$$\vec{F}_{ph,diff} = -S \nabla T \quad (9)$$

Also in the case of Eq.3, we can repeat the same observation given above on heat capacity and entropy and have a force $\mathbf{F} = -S \text{grad } T$.

However, besides having the force $\mathbf{F} = -S \text{grad } T$, when we derive the Helmholtz energy we can have $\mathbf{F} = -T \text{grad } S$ too. It means that in the cases discussed in [12] and [20], this entropic force could exist. It is possible because entropy is depending on temperature, and temperature is a function of the spatial coordinates. Therefore a gradient of entropy exists and consequently an entropic force. Since this force could be written as $\mathbf{F} = -T (dS/dT) \text{grad } T$, its effective role in the system requires a further evaluation.

References

- [1] Cercignani, C. (1975). Theory and application of the Boltzmann equation. Scottish Academic Press. ISBN: 978-1-4612-6995-3.
- [2] Succi, S. (2001). The lattice Boltzmann equation: for fluid dynamics and beyond. Oxford University Press. DOI: 10.1016/S0997-7546(02)00005-5
- [3] Omini, M., & Sparavigna, A. (1995). An iterative approach to the phonon Boltzmann equation in the theory of thermal conductivity. *Physica B: Condensed Matter*, 212(2), 101-112. DOI: 10.1016/0921-4526(95)00016-3
- [4] Omini, M., & Sparavigna, A. (1996). Beyond the isotropic-model approximation in the theory of thermal conductivity. *Physical Review B*, 53(14), 9064. DOI: 10.1103/physrevb.53.9064
- [5] Sparavigna, A. C. (2016). The Boltzmann equation of phonon thermal transport solved in the relaxation time approximation – I – Theory. *Mechanics, Materials Science & Engineering Journal*, 3, 1-13. DOI: 10.13140/RG.2.1.1001.1923

[6] Müller, I. (2007). *A History of thermodynamics: The doctrine of Energy and Entropy*, Springer Science & Business Media. ISBN 978-3-540-46226-2

[7] Neumann, R. M. (1980). Entropic approach to Brownian movement. *American Journal of Physics*, 48(5):354. DOI: 10.1119/1.12095.

[8] Neumann, R. M. (1977). The entropy of a single Gaussian macromolecule in a noninteracting solvent. *The Journal of Chemical Physics* 66(2):870. DOI: 10.1063/1.433923

[9] Roos, N. (2014). Entropic forces in Brownian motion. *American Journal of Physics*, 82(12), 1161-1166.

[10] Huebner, R. P. (1979). *Magnetic flux structures in superconductors*, Springer Verlag. DOI: 10.1007/978-3-662-02305-1

[11] Pengcheng Li (2007). Novel transport properties of electron - doped superconductors $\text{Pr}_{2-x}\text{Ce}_x\text{CuO}_{4-\delta}$, UMD Theses and Dissertations.

[12] Gallina, V., & Omini, M. (1972). On thermal diffusion in liquid metals. *Il Nuovo Cimento*, 8B(1):65-89. DOI: 10.1007/bf02743508

[13] Ott, A. (1969). Isotope separation by thermal diffusion in liquid metal. *Science*, 164(3877):297. DOI: 10.1126/science.164.3877.297

[14] Platten, J. K. (2006). The Soret effect: a review of recent experimental results. *Journal of applied mechanics*, 73(1):5-15. DOI: 10.1115/1.1992517

[15] Huang, F., Chakraborty, P., Lundstrom, C. C., Holmden, C., Glessner, J. J. G., Kieffer, S. W., & Lesher, C. E. (2010). Isotope fractionation in silicate melts by thermal diffusion. *Nature*, 464(7287):396-400. DOI: 10.1038/nature08840

[16] Richter, F.M. (2011). Isotope fractionation in silicate melts by thermal diffusion. *Nature*, 472(7341):E1. DOI: 10.1038/nature09954

[17] Goel, G., Zhang, L., Lacks, D. J., & Van Orman, J. A. (2012). Isotope fractionation by diffusion in silicate melts: Insights from molecular dynamics simulations. *Geochimica et Cosmochimica Acta*, 93:205-213. DOI: 10.1016/j.gca.2012.07.008

[18] Bindeman, I. N., Lundstrom, C. C., Bopp, C., & Huang, F. (2013). Stable isotope fractionation by thermal diffusion through partially molten wet and dry silicate rocks. *Earth and Planetary Science Letters*, 365:51-62. DOI: 10.1016/j.epsl.2012.12.037

[19] Sparavigna, A. C. (2015). Dimensional equations of entropy. *International Journal of Sciences*, 4(8):1-7. DOI: 10.18483/ijsci.811

[20] Omini, M. (1999). Thermoelasticity and thermodynamics of irreversible processes. *Physica B*, 270:131-139. DOI: 10.1016/s0921-4526(99)00172-6

[21] Peter Atkins, P., & De Paula, J. (2014). Atkins' Physical Chemistry, OUP Oxford. ISBN 9780199543373

Error Analysis of Method for Calculation of Non-Contact Impact on Space Debris from Ion Thruster

Alpatov A.P.¹, Fokov A.A.¹, Khoroshylov S.V.¹, Savchuk A.P.¹

1 – Institute of Technical Mechanics of National Academy of Sciences of Ukraine and State Space Agency of Ukraine, Dnipropetrov'sk, Ukraine



DOI [10.13140/RG.2.1.3986.1361](https://doi.org/10.13140/RG.2.1.3986.1361)

Keywords: space debris removal, ion beam shepherd technology, spacecraft - space debris object system, contour of the central projection, simplified calculation of the impact, error analysis, simulation of the relative motion.

ABSTRACT. A simplified approach to determine the impact on a space-debris object (a target) from the ion thruster of a spacecraft (a shepherd), which was proposed before in the context the ion beam shepherd technology for space debris removal, was considered. This simplified approach is based on the assumption of the validity of the self-similar model of the plasma distribution in the thruster plume. A method for the calculation of the force impact using the information about the contour of the central projection of the object on a plane, which is perpendicular to the ion beam axis, was proposed within the framework of this model. The errors of this method, including the errors caused by an inaccuracy of its realization, are analyzed. The results of the analysis justify the admissibility of the application of the specified approach within the self-similar model of the plasma distribution. The preliminary conclusion has been made that this simplified approach can be used to control the relative motion of the shepherd - target system as well. This conclusion is based on the results of the simulation of the system motion, when the “real” value of the thruster impact is calculated by the direct integration of the elementary impacts over the target surface and the value of the same impact used in the control algorithms is determined using the information about the contour of the target. A number of factors such as the orbital motion of the system, external perturbations, and the attitude motion of the shepherd were neglected in the simplified model which was used for the simulation. These factors and errors in the interaction model are necessary to consider during a more detailed analysis of this approach. The analysis of the calculation errors presented in this paper can be used during implementation of the ion beam shepherd technology for active space debris removal.

Introduction. The technology for the removal of large debris from the low-Earth-orbit called ion beam shepherd is presented in the papers [1], [2]. This technology provides space debris de-orbiting due to the impact of the ion plume of the electric thruster (ET) of a spacecraft (a shepherd) located in close proximity to space debris object (a target). A certain distance between ion beam shepherd (IBS) and the target must be maintained to provide effectiveness of the impact of the ion beam. The ion beam impact can be determined by integration over the surface of a target when the mechanism of the ion interaction [3] with an elementary area of the surface and its relative position are known. This approach can be used for modeling of the system motion but not recommended to apply in a control loop due to its computational costs and the incomplete information about the position and shape of the target. A simplified approach to calculate the impact from the ion beam on the target, based on the information about the contour of its central projection on the image plane of the IBS camera was proposed in [4, 5]. The central projection of the target on the reference plane, which is perpendicular to the beam axis, is considered within the framework of this approach instead of its surface. This paper justifies the application of this approach to control the relative motion of the shepherd - target system by analyzing errors of the determination of the plasma beam impact on the target

Calculation of the force impact by the direct integration over the target surface. The model of the interaction of the ion beam with a space debris object, as well as the model of the ion plume should be considered for the calculation of the impact from the ET force on the target.

Neglecting the sputtering of the target material, the escaping ions from the target surface, and the electron pressure, the elementary force $d\mathbf{F}_s$ transmitted to the target can be calculated as follows [6]:

$$d\mathbf{F}_s = mn\mathbf{u}(-\mathbf{v} \cdot \mathbf{u})ds, \quad (1)$$

where m – is the ion mass;

\mathbf{u} – is the vector of the ion velocity;

ds – is the elementary area of the surface, which location will be characterized by the radius vector ρ_s of its midpoint;

\mathbf{v} – is the unit normal vector to the element of the surface;

n – is the density of the plasma.

The force and torque transmitted from the ion beam to the target can be calculated by the integration of the elementary forces from equation (1) over the exposed surface S

$$\mathbf{F}_{\text{srf}} = \int_S d\mathbf{F}_s, \quad \mathbf{M}_{\text{srf}} = \int_S \rho_s \times d\mathbf{F}_s. \quad (2)$$

There are ion beam models for the near and far regions of the plasma plume [7]. The far region of the plume presents the main interest in the context of the non-contact space debris removal, because this is where the plasma interacts with the target. Models with different degrees of complexity and accuracy were proposed for the description of the far region of an ET beam [8]. The so-called self-similar model of the beam is chosen for this study. Taking into account the fact that the Mach number at the beginning of the far region of the beam is much greater than 1, the character of the plasma distribution approaches to a cone. The plasma density can be determined for this case using the self-similar model at an arbitrary point as follows [8]:

$$n = \frac{n_0 R_0^2}{z^2 \operatorname{tg}^2 \alpha_0} \exp\left(-3 \frac{r^2}{z^2 \operatorname{tg}^2 \alpha_0}\right), \quad (3)$$

where r , z – are radial (distance from the midpoint of the surface element to the axis of the beam cone) and axial (the distance from the vertex of the cone along the axis of the beam) coordinates of the point;

R_0 – is the radius of the beam at the beginning of the far region (at the exit of the ET nozzle, $z = R_0 / \operatorname{tg}^2 \alpha_0$);

n_0 – is the plasma density at the beginning of the far region;

α_0 – is the divergence angle of the beam.

Axial u_z and radial u_r velocity components of the plasma ions can be represented as follows:

$$u_z = u_{z0} = \text{const}, \quad u_r = u_{z0} r / z, \quad (4)$$

where u_{z0} is the axial component of the ion velocity at the beginning of the far region.

The target surface is divided into elements for determination of the integral force $\mathbf{F}_{\text{sr}}^{\text{f}}$ transmitted to the target by the ion beam. After that, the coordinates of the surface elements and the unit normal towards them are set with respect to the target reference frame (RF). Then the coordinates of the surface elements and their normals recalculated with respect to the IBS RF, or more precisely, to whose origin that is at the cone vertex of the ion beam. We can assume for simplicity reason that this RF coincides with the IBS RF. The elementary force is determined for each element of the surface using the equation (1) and taking into account its "visibility" from ET side and its position inside or outside of the beam cone. The integral force is determined using the expression (2).

Calculation of the force impact using the contour of the target. The simplified approach [5] for determination of the impact from the ion plume uses the information about the contour of the central projection of the target. According to this approach the force applied to an element of the surface is approximately equal to the force acting on the central projection of this area on a plane that is perpendicular to the axis of the beam cone, for a example the plane of camera sensor placed next to the ET. This assumption is explained by the fact that the cone cross-section increases with the square of the distance from the vertex of the cone and the plasma density decreases in inverse proportion to the square of the distance from the vertex of the cone.

The equation that determines the force $d\mathbf{F}_{\sigma}$ transmitted through the element of the surface can be written as follows:

$$d\mathbf{F}_{\sigma} = mn_c \mathbf{u}_c^2 \mathbf{e}_u d\sigma, \quad \mathbf{u}_c = u_{z0} \cdot [x_c / f \quad y_c / f \quad 1]^T, \quad (5)$$

$$n_c = \frac{n_0 R_0^2}{f^2 \tan^2 \alpha_0} \exp \left(-3 \frac{x_c^2 + y_c^2}{f^2 \tan^2 \alpha_0} \right), \quad (6)$$

where T – is the transposition symbol;

$d\sigma$ – is the elementary area of the target projection on the camera image plane;

\mathbf{e}_u – is the unit vector of the direction of the ion velocity \mathbf{u} ;

x_c, y_c – are coordinates of the point in the camera RF;

f – is the focal length of the camera.

The full force \mathbf{F}_{cnt} transmitted from the ion plume to the target is calculated by this expression:

$$\mathbf{F}_{\text{cnt}} = \int_{\Sigma} d\mathbf{F}_{\sigma}, \quad (7)$$

where Σ is the part of the image plane of the camera which is bounded by the contour.

Analysis of the errors caused by the simplified calculation method. Let us make a more detail analysis of the assumption about the equality of two elementary forces from the ion plume used in the simplified method. The first force acts on an element of the target surface and the second one is applied to the central projection of this area on a plane, that is perpendicular to the axis of the cone

beam. First, we restrict ourselves to the case when the area ds of the target surface is perpendicular to the direction of the ion beam. The equations (1), (3), (4) can be rewritten for this area as follows:

$$d\mathbf{F}_s = mn\mathbf{u}^2 \mathbf{e}_u ds, \mathbf{u}^2 = u_{z0}^2 (1 + \tan^2 \theta), \quad (8)$$

$$n = m \frac{n_0 R_0^2}{z^2 \tan^2 \alpha_0} \exp\left(-3 \frac{\tan^2 \theta}{\tan^2 \alpha_0}\right), \quad ds = z^2 (\tan \theta / \cos \theta) d\theta d\varphi, \quad (9)$$

where θ – is the angle between the direction of the beam distribution and the axis of the ion beam cone;

φ – is the azimuth of the direction of the ion distribution, $\mathbf{e}_u = \mathbf{e}_u(\theta, \varphi)$.

The equations (8), (9) show that value $d\mathbf{F}_s = d\mathbf{F}_s(\theta, \varphi)$ is a function of variables θ and φ , and doesn't depend from the coordinates of the element z of the surface. The "visible" area of the surface element varies in the case of its arbitrary orientation depending from the inclination angle of the element to the plane that is perpendicular to the direction of the ion beam. This variation of the area is taken into account in the equation (1) by the factor $(-\mathbf{v} \cdot \mathbf{u})$, that is equal to use the orthogonal projection of the area on the defined perpendicular plane. However, we do not deal with the orthogonal projection during the calculation of the force impact using the target contour but with the central one. In other words, a contour error is added during the calculations. Let's consider the following example on Fig. 1 to evaluate this error.

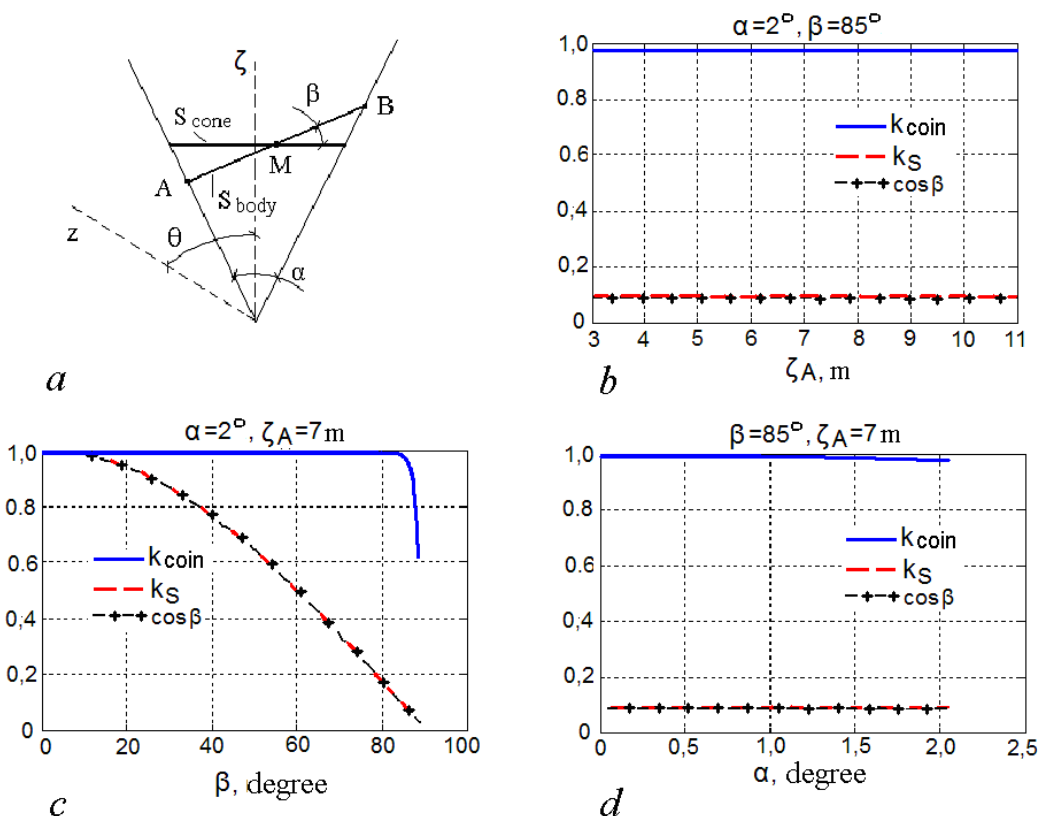


Fig. 1. Analysis of error caused by the replacement of the orthogonal projection by the central projection.

We consider a part of the beam cone in the form of a small cone with the vertex angle α and name it elementary cone. Fig. 1a shows a cross-section of the cone by a vertical plane. The elementary cone "cuts" the element of the surface in the form of an ellipse (the segment AB in Fig. 1a). We assume that the plane of the ellipse is inclined to the plane which is perpendicular to the axis ζ of the elementary cone at an angle β . The area S_{cone} of the perpendicular cross-section of the elementary cone passing through the midpoint M is the area of the central projection of the surface element on plane of this section. We also define the ratio k_s of the area S_{cone} to the area S_{body} of the surface element. The difference between the value of this ratio and the value of $\cos \beta$ characterizes the error of the application of the equations (8) and (9). We introduce the so-called a coincidence coefficient defined by the function: $k_{\text{coin}} = 1 - (k_s - \cos \beta) / \cos \beta$.

The analysis of this function is not presented here due to its cumbersome, but it still shows the following: the independence of the coincidence coefficient of from the distance from a surface element to the cone vertex; this kind of error appears only when the values of β are close to 90° ; the acceptable results can be achieved by reducing the cone vertex angle α even when values of β are close to 90° . Fig. 1 illustrates these conclusions by graphs of the variations of the coincidence coefficient from the following variables: the coordinate ζ_A (Fig. 1b); the cone vertex angle α (Fig. 1c); the inclination angle β (Fig. 1d). One of these variables is varying while the other two variables are fixed in these graphs.

Analysis of the errors caused by the implementation of the simplified approach. Another kind of errors of the simplified approach can be caused by an inaccuracy of the camera placement. According to the approach the camera must be located so as its focal point coincides with the vertex of the imaginary cone of the ET beam. This requirement is difficult to meet from the engineering point of view and it is worth to consider an offset of the camera from the position which stipulated by the simplified method.

To analyze this offset we introduce the camera RF $O_c x_c y_c z_c$, whose origin O_c is on the camera optical axis. The plane $x_c y_c$ coincides with the plane of the camera sensor. The axis z_c is directed towards the target.

We consider the vector \mathbf{d} , which connects the vertex of the imaginary cone of the beam and a point P of the target. In the ideal case of the camera placement, the coordinates of the projection point P on the plane of the camera sensor that included in the equation (5) are defined by following relations:

$$x_c = f \frac{d_1^{(\text{cam})}}{d_3^{(\text{cam})}}, \quad y_c = f \frac{d_2^{(\text{cam})}}{d_3^{(\text{cam})}}, \quad (10)$$

where x_c , y_c – are the coordinates of the projection point in the camera RF, the subscript indicates the component number of the column $d^{(\text{cam})}$ corresponding to the vector \mathbf{d} .

Let us consider the case where the camera is mounted with a small offset relative to the ET beam. The target contour obtained using images from the camera with such offset is different from the one with the ideal placement of the camera. We will illustrate this considering the example of the contour determination.

The target is a circular cylinder. The height of the cylinder is 2,6 m. The diameter of the foundation of the cylinder is 2,2 m. The geometric center of the target is located on the axis of the beam cone

on a distance of 7 m from its vertex. The line 1 in Fig. 2 shows the contour corresponding to the case when the focal point of the camera coincides with the vertex of the imaginary cone of the beam and the line 2 depicts the contour for the case when the camera offset is 0,2 m .

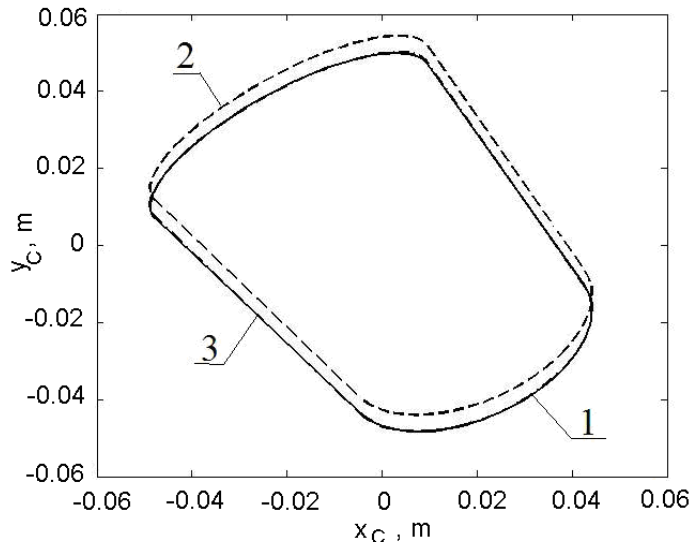


Fig. 2. Contours of a target projection.

A method to correct coordinates of the contour points obtained using the equations (10) were proposed in [9] for the case when the cameras focal point is placed with offset from the imaginary vertex of the beam cone at the \tilde{x} and \tilde{y} along $O_c x_c$ and $O_c y_c$ axes, respectively. According to this method, the coordinates can be corrected as follows:

$$x_c^{\text{corr}} = x_c - f \frac{\tilde{x}}{z_{\text{nom}}}, \quad y_c^{\text{corr}} = y_c - f \frac{\tilde{y}}{z_{\text{nom}}}, \quad (11)$$

where x_c^{corr} , y_c^{corr} are the corrected coordinates of the point of the target projection;

z_{nom} – is the nominal distance between the geometric center of the target and the vertex of the beam cone.

Line 3 in Fig. 2 shows the contour corrected according to the equation (11) for the case when $z_{\text{nom}} = 7 \text{ m}$. This figure shows that the corrected contour is almost identical to the one for the no offset case (line 1).

The possibility to use the simplified approach to control the shepherd-target relative motion. The preliminary assessment of the possibility to use the simplified approach to determine the beam impact for the control of the shepherd-target relative motion is made on the basis of the simulation results. The "real" value of the beam impact is calculated by direct integration over the target surface and the values of the beam impact that used in the control algorithm are determined using the information about the target contour. The confirmation of such possibility is an indirect justification of the simplified approach for the calculation of the impact on a space debris object.

A simplified model of the motion was used for the preliminary evaluation where a number of factors were not taken into account, such as:

- the orbital motion of the IBS and target;

- external perturbations;
- the IBS attitude motion.

We start describing the reference frames that are required for a full model and then will apply the simplifying assumptions introduced above. The following reference frames are used:

$Ox_0y_0z_0$ is the inertial RF, the origin O is located in the center of the Earth, axis Oy_0 is directed towards the north pole of the Earth, axis Oz_0 is the midpoint of the spring equinox;

$Sx_1y_1z_1$, $Tx_3y_3z_3$ are the orbital reference frames of the IBS and target, respectively, the origin of the RF S and T are located at their centers of mass, axis z is directed along the radius vector connecting the center of the earth and the center of mass of the IBS or the target, axis x is in the orbital plane and directed towards the orbital motion;

$Sx_2y_2z_2$, $Tx_4y_4z_4$ are the body RF of the IBS and the target respectively, the axes of which coincide with main central axes of inertia. For the ideal orientation of the IBS and target, these RF are parallel and coincide with the appropriate orbital reference frame.

We will also refer to this reference frames by zero, the first ,..., the fourth according to the subscripts which are used in their notation. The transitions matrixes from ν -th RF to μ -th RF are denoted like Γ_ν^μ , $\nu, \mu = 0, 1, \dots, 4$.

The IBS attitude position is determined by the following rotations of its body RF relative to its orbital RF on the angles: pitch ϑ_2 (around the y axis), roll φ_2 (around the x axis) and yaw ψ_2 (around the z axis). In order to avoid singularity of the kinematics relations for the case of the uncontrolled motion of the target, the attitude position of the target is more convenient to describe by four parameters of Rodrigues-Hamilton [10]. The parameters λ_0 , λ_1 , λ_2 , λ_3 is used to specify the position of the body RF with respect to the orbital RF.

The dynamic equations of the attitude motion of the IBS and target is used in the Euler form [11]:

$$\begin{cases} J_{\nu x} \dot{\omega}_{\nu x} + (J_{\nu z} - J_{\nu y}) \omega_{\nu y} \omega_{\nu z} = M_{\nu x}, \\ J_{\nu y} \dot{\omega}_{\nu y} + (J_{\nu x} - J_{\nu z}) \omega_{\nu x} \omega_{\nu z} = M_{\nu y}, \\ J_{\nu z} \dot{\omega}_{\nu z} + (J_{\nu y} - J_{\nu x}) \omega_{\nu x} \omega_{\nu y} = M_{\nu z}, \end{cases} \quad (12)$$

where $J_{\nu x}$, $J_{\nu y}$, $J_{\nu z}$ are the moments of inertia of the IBS and target with respect to their principal central axes;

$M_{\nu x}$, $M_{\nu y}$, $M_{\nu z}$ – are projections of external torques acting on the IBS ($\nu = 2$) and target ($\nu = 4$).

These dynamic equations are supplemented with the kinematics relations:

$$\begin{cases} \omega_{2x} = \dot{\vartheta}_2 \cos \psi_2 + \dot{\vartheta}_2 \cos \varphi_2 \sin \psi_2 + \omega_{20} \cos \varphi_2 \sin \psi_2, \\ \omega_{2y} = \dot{\vartheta}_2 \cos \varphi_2 \cos \psi_2 - \dot{\vartheta}_2 \sin \psi_2 + \omega_{20} \cos \varphi_2 \cos \psi_2, \\ \omega_{2z} = \dot{\psi}_2 - \dot{\vartheta}_2 \sin \varphi_2 - \omega_{20} \sin \varphi_2, \end{cases} \quad (13)$$

$$\begin{cases} \omega_{4x} = 2(\lambda_0\lambda_1 - \lambda_1\lambda_0 + \lambda_2\lambda_3 - \lambda_3\lambda_2), \\ \omega_{4y} = 2(\lambda_0\lambda_2 - \lambda_2\lambda_0 + \lambda_3\lambda_1 - \lambda_1\lambda_3), \\ \omega_{4z} = 2(\lambda_0\lambda_3 - \lambda_3\lambda_0 + \lambda_1\lambda_2 - \lambda_2\lambda_1), \end{cases} \quad (14)$$

$$\begin{cases} \dot{\phi}_2 = \omega_{2x} \cos \psi_2 - \omega_{2y} \sin \psi_2, \\ \dot{\vartheta}_2 = (\omega_{2x} \sin \psi_2 + \omega_{2y} \cos \psi_2) / \cos \varphi_2 - \omega_0, \\ \dot{\psi}_2 = \omega_{2z} + (\omega_{2x} \sin \psi_2 + \omega_{2y} \cos \psi_2) \operatorname{tg} \varphi_2, \end{cases} \quad (15)$$

$$\begin{cases} 2\dot{\lambda}_0 = -(\omega_{4x}\lambda_1 + \omega_{4y}\lambda_2 + \omega_{4z}\lambda_3), \\ 2\dot{\lambda}_1 = \omega_{4x}\lambda_0 - \omega_{4y}\lambda_3 + \omega_{4z}\lambda_2, \\ 2\dot{\lambda}_2 = \omega_{4y}\lambda_0 - \omega_{4z}\lambda_1 + \omega_{4x}\lambda_3, \\ 2\dot{\lambda}_3 = \omega_{4z}\lambda_0 - \omega_{4x}\lambda_2 + \omega_{4y}\lambda_1, \end{cases} \quad (16)$$

where $\omega_{\nu x}, \omega_{\nu y}, \omega_{\nu z}$ are the projections of the angular velocities of the IBS and target to their body RF, $\nu = 2, 4$;

ω_0 – is the orbital angular velocity.

The components $\Gamma_\nu^{\nu-1}$, $\nu = 2, 4$ of the transition matrixes from the body RF to the corresponding orbital ones are given by:

$$\Gamma_2^1 = \begin{bmatrix} c\vartheta_2 c\psi_2 + s\vartheta_2 s\varphi_2 s\psi_2 & -c\vartheta_2 s\psi_2 + s\vartheta_2 s\varphi_2 c\psi_2 & s\vartheta_2 c\varphi_2 \\ c\varphi_2 s\psi_2 & c\varphi_2 c\psi_2 & -s\varphi_2 \\ -s\vartheta_2 c\psi_2 + c\vartheta_2 s\varphi_2 s\psi_2 & s\vartheta_2 s\psi_2 + c\vartheta_2 s\varphi_2 c\psi_2 & c\vartheta_2 c\varphi_2 \end{bmatrix}, \quad (17)$$

$$\Gamma_4^3 = \begin{bmatrix} \lambda_0^2 + \lambda_1^2 - \lambda_2^2 - \lambda_3^2 & 2(\lambda_1\lambda_2 - \lambda_0\lambda_3) & 2(\lambda_1\lambda_3 + \lambda_0\lambda_2) \\ 2(\lambda_1\lambda_2 + \lambda_0\lambda_3) & \lambda_0^2 + \lambda_2^2 - \lambda_3^2 - \lambda_1^2 & 2(\lambda_2\lambda_3 - \lambda_0\lambda_1) \\ 2(\lambda_1\lambda_3 - \lambda_0\lambda_2) & 2(\lambda_2\lambda_3 + \lambda_0\lambda_1) & \lambda_0^2 + \lambda_3^2 - \lambda_1^2 - \lambda_2^2 \end{bmatrix}, \quad (18)$$

where $c\gamma$ and $s\gamma$ are $\cos \gamma$ and $\sin \gamma$, respectively.

As mentioned above, the orbital motion ($\omega_0 = 0$) is neglected in this study and it is assumed that $Ox_0y_0z_0$ is the inertial RF and the axes of reference frames $Sx_1y_1z_1$ and $Tx_3y_3z_3$ are parallel to the corresponding axes of $Ox_0y_0z_0$, and for the ideal orientation of the IBS and target their body RF coincide with the corresponding orbital one. The RF for this case are shown in Fig. 3, where ρ , \mathbf{d} , \mathbf{R} are the radius vectors of a point P in the corresponding reference frames; \mathbf{r}_{ST} is the radius vector of center of mass (CoM) of the target in the IBS body RF; \mathbf{r}_S , \mathbf{r}_T are the radius vectors of CoM the IBS and target in $Ox_0y_0z_0$ RF.

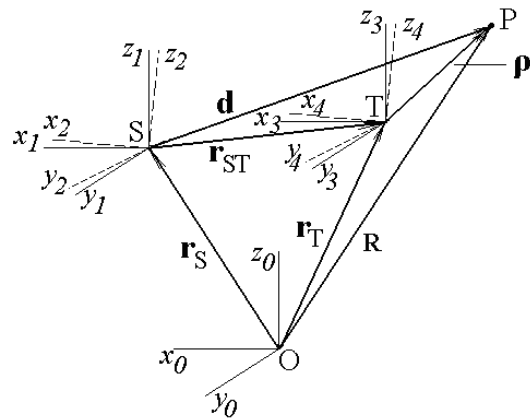


Figure 3. Reference frames.

With these assumptions the following equations are correct:

$$d^{(2)} = (\Gamma_2^1)^T \cdot r_{ST}^{(0)} + (\Gamma_2^1)^T \Gamma_4^3 \cdot \rho^{(4)}, \quad r_{ST}^{(0)} = r_T^{(0)} - r_S^{(0)}, \quad (19)$$

where the variables with superscript in parenthesis refer to the column of the vector projections to the axes of RF with the appropriate index.

These relations are necessary to determine the impact of the ion plume on the area of the target surface with the conditional center at a point P . The attitude angles and Rodrigues-Hamilton parameters included in the matrixes Γ_2^1 , Γ_4^3 were determined integrating the equations (12) - (16) during the modeling of the system motion. Due to the accepted assumptions, the values of the components \mathbf{r}_S , \mathbf{r}_T , are calculated integrating the following equations:

$$m_S \cdot \ddot{r}_S^{(0)} = \mathbf{F}_S^{(0)}, \quad m_T \cdot \ddot{r}_T^{(0)} = \mathbf{F}_T^{(0)}, \quad (20)$$

where $\mathbf{F}_S^{(0)}$, $\mathbf{F}_T^{(0)}$ are the vectors of the resultant force \mathbf{F}_S , \mathbf{F}_T , applied to the IBS and target respectively;

m_S and m_T – masses of the IBS and target. In this way, according to accepted simplified model, the system motion is described by the equations (12) - (20) under the condition $\omega_0 = 0$.

In the absence of external perturbations on the system, the force impact on the target is created only by the ion plume from the shepherd ET. This impact slows the orbital velocity of the target and allows to de-orbit it faster. The IBS concept assumes that two ETs are installed on the IBS. The second thruster is necessary to compensate the impact on the IBS motion from the main one, directed towards the target. However, in order to the IBS and target remain in the same orbit, the result of the force action on CoM of the IBS has to be the same as the result of the force impact on CoM of the target. This condition can be achieved by adjustment of the thrust of the second compensating thruster. The algorithm to adjust the thrust \mathbf{F}_{E2} of compensating ET was chosen in the following simple form:

$$\mathbf{F}_{E2} = (m_S / m_T) \cdot \mathbf{F}_{cnt} - \mathbf{F}_{E1}, \quad (21)$$

where \mathbf{F}_{E1} is the thrust of the main ET.

Assuming that the IBS attitude position is unchanged, this algorithm can be simplified as follows:

$$F_{E2_x} = (m_S / m_T) \cdot F_{cnt_x} - F_{E1_x}, \quad (22)$$

where the letter x in the subscripts is used to denote the x -th component of the column, that corresponded to the thrust vector in the RF $Ox_0y_0z_0$ or the body RF of the IBS.

The algorithm to determine the target contour for solving modeling tasks is described in details in [5] and can be represented by the following steps:

- Approximate the target surface by basic elements;
- Project the central points of the surface elements on the image plane of the camera;
- Calculate the contour of the target projection by solving the problem of the polygon construction, which covers a set of points projected on a plane.

We assume that the origin O_c of the camera RF coincides with the origin S of the body RF of the IBS and the z_c axis is directed opposite to the axis x_2 of the body RF of the IBS. Then, the coordinates of the point P of the target is projected on the plane defined by the equations (10) or calculated using the relations (11) in the case of their correction.

The components of column $d^{(cam)}$ which are included in these equalities are given by

$$d^{(cam)} = \Gamma_2^{cam} \cdot d^{(2)}, \quad (23)$$

where Γ_2^{cam} is the transition matrix from the body RF of the IBS to the camera RF.

Simulation results. The assumption was made for the calculations that the only forces from the main and compensating ETs act on the IBS. The line of action of these forces passes through CoM of the IBS.

The following values of parameters were used during the simulation.

Parameters of the ETs are the following: the radius of the beam at the beginning of the far region $R_0 = 0,0805 \text{ m}$; the plasma density at the beginning of the far region $n_0 = 4,13 \cdot 10^{15} \text{ m}^{-3}$; the divergence angle of the beam $\alpha_0 = 7^\circ$; the axial component of the velocity of the plasma ions $u_{z0} = 71580 \text{ m/s}$; the ion mass $m = 2.18 \cdot 10^{-25} \text{ kg}$.

The IBS parameters were chosen as follows: the matrix of inertia is $\text{diag}(1283,4; 1379,5; 169,3) \text{ kg} \cdot \text{m}^2$; the mass is 500 kg.

The following parameters of the cylindrical target were used: the mass is 1000 kg; the height is 2,6 m; the diameter is 2,2 m. The inertia matrix of the target was calculated according to the formulas for the moments of inertia of a hollow cylinder.

The distance of 7 m from CoM of the IBS to the target along the axis z of the camera RF was chosen as nominal. The focal length of the camera is 0,2 m.

The simulation results show that the difference between the nominal and the calculated distance from the target to the IBS is less than 1 sm after 800 s of the simulation when the initial location of CoM of the target is on the beam axis. The figures presented below show the results of the simulations for the case when the initial location of CoM of the target is 1 m away from the beam axis, the initial attitude position of the target is defined by the angle of 45° about the axis y of the body RF of the target, the camera offset from its nominal position is 0,2 m along the abscissa axis of the camera RF.

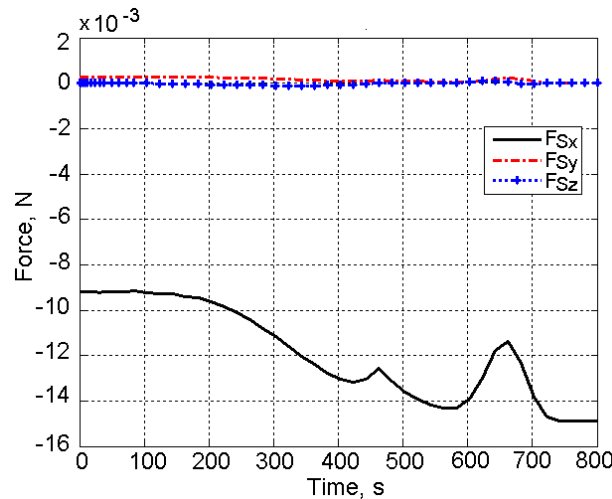


Fig. 4. The force acting on the IBS.

Fig. 4 and Fig. 5 show the graphs of the forces acting on the IBS and target, respectively. Ideally these graphs should coincide with each other up to the scale. The variation of the target position (Fig. 6) from the nominal one for 800 s of the simulation is no more than 5 sm (this variation is denoted as $\delta^0 r_x$ in the figure) for the ideal camera position, and does not exceed 8 sm for the case when the camera has the position offset. The variations that obtained through the simulation (i.e. the errors of maintaining the nominal distance to the target) are not significant, taking into account to the real control algorithms will use the information about the distance between the target and IBS or its estimation unlike the applied simple algorithm (21), which does not use this information.

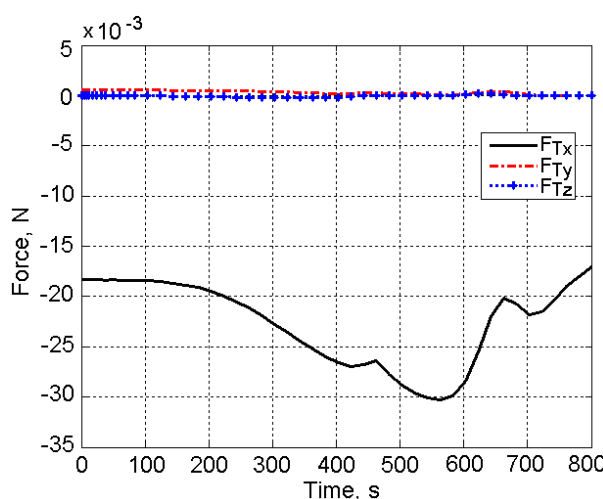


Fig. 5. The force acting on the target.

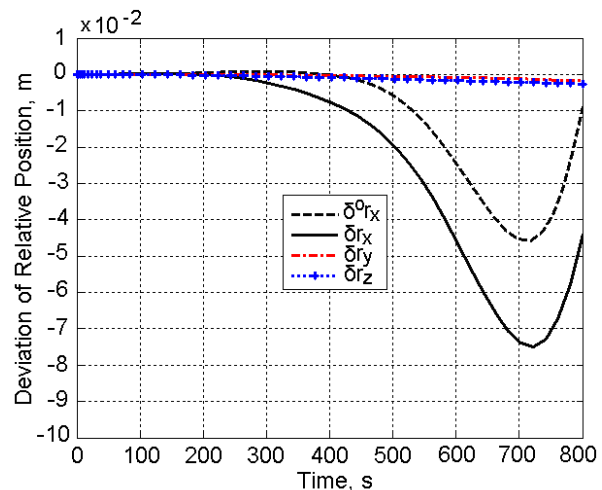


Fig. 6. The deviation of the target relative position.

Fig. 7 and Fig. 8 show the graphs of the torque acting on the target and the graph the angular velocity of the target, respectively.

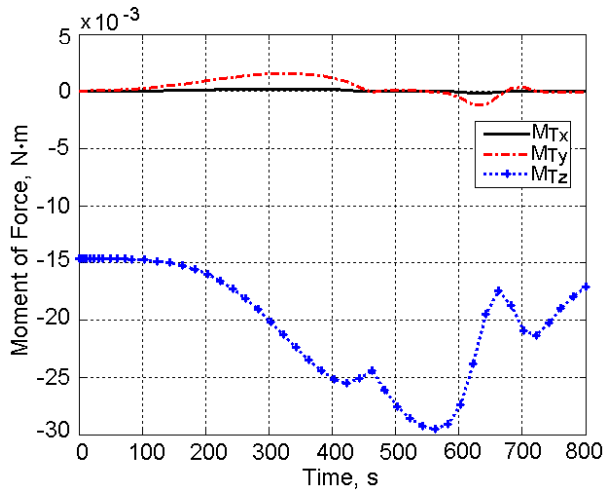


Fig. 7. The torque acting on the target.

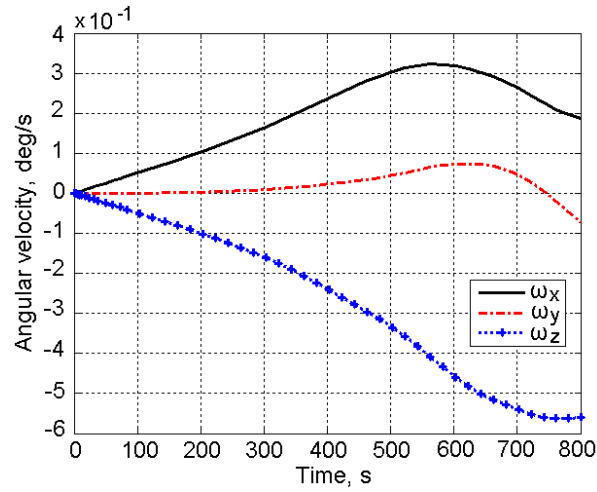


Fig. 8. The angular velocity of the target.

Conclusions. The errors of the simplified approach [5] to determine the impact from the ion thruster of a spacecraft (a shepherd) on a space debris object (a target) within the context the IBS technology [1, 2] has been analyzed. The approach is based on the information about the contour of the central projection of the target on a plane, which is perpendicular to the axis of the ion beam. The plane of the camera sensor, which is installed on the shepherd, has been considered as such a plane. The results of the error analysis justify the admissibility of the application of this simplified approach for the determination of the force impact of the ion thruster to the space debris within self-similar model of the plasma distribution [6]. The research results also allow to make a preliminary conclusion about the possibility to use this simplified approach for the control of the relative motion of the IBS- space debris object system. However, a more detailed analysis of this possibility is needed which require to consider the orbital motion, all range of acting disturbances, errors of the model of the interaction of the ion plume with the surface of the space debris object, and errors of implementation of the simplified approach.

Acknowledgement. The research leading to these results has received funding from the European Union Seventh Framework Program (**FP7/2007-2013**) under grant agreement n°607457.

References

- [1] Bombardelli, C., Pelaez, J. *Ion Beam Shepherd for Contactless Space Debris Removal* // Journal of Guidance, Control and Dynamics. – 2011. – Vol. 34, #3. – Pp. 916 – 920.
- [2] Bombardelli, C., Alpatov A.P., Pirozhenko, A.V., Baranov, E.Y., Osinov, G.G., Zakrzhevskii, A.E. *Project "Space shepherd" with ion beam. Ideas and problems* // Space science and technology. – 2014. – V. 20, #2. – Pp. 55 – 60.
- [3] Merino, M., Ahedo, E., Bombardelli, C., Urrutxua, H., Peláez, J. *Ion beam shepherd satellite for space debris removal* // Progress in Propulsion Physics. – 2013. – Vol. 4. – Pp. 789 – 802.
- [4] Alpatov, A., Cichocki, F., Fokov, A., Khoroshyllov, S., Merino, M., Zakrzhevskii, A. *Algorithm for determination of force transmitted by plume of ion thruster to orbital object using photo camera* // 66th International Astronautical Congress, Jerusalem, Israel. –2015. – Paper IAC-15-A6.5.5-x27732. – Pp. 1 – 9.
- [5] Alpatov A., Cichocki F., Fokov A., Khoroshyllov S., Merino M., Zakrzhevskii A. *Determination of the force transmitted by an ion thruster plasma plume to an orbital object* // Acta Astronautica. – 2016. – V. 119. – Pp. 241–251

[6] Bombardelli C., Urrutxua H., Merino M., Ahedo E., Peláez J. *Relative dynamics and control of an ion beam shepherd satellite* // Spaceflight mechanics. – 2012. – Vol. 143. – Pp. 2145 – 2158.

[7] Merino M., Cichocki F., Ahedo E. *A collisionless plasma thruster plume expansion model* // Plasma Sources Science and Technology. – 2015. – Vol. 24(3), – Pp. 1 – 12.

[8] Bombardelli C., Merino M. Ahedo E., Peláez J. Urrutxua H., Iturri-Torreay A., Herrera-Montojoy J. *Ariadna call for ideas: Active removal of space debris ion beam shepherd for contactless debris removal* // Technical report. – 2011. – 90 p.

[9] Alpatov A.P. Zakrzhevskii A.E. Merino M. Fokov A.A., Khoroshyllov S.V. Cichocki, F. *Determination of a force transmitted by a plume of an ion thruster to an orbital object* // Space science and technology. – 2016. – V. 22, #1. – Pp. 52 – 63.

[10] Kravets V.V., Kravets T.V., Kharchenko A.V. *Using quaternion matrices to describe the kinematics and nonlinear dynamics of an asymmetric rigid body* // Int. Appl. Mech. – 2009. – 44.#2. – Pp. 223-232.

[11] Lurie A.I. *Analytical Mechanics*. – M. Fizmatgiz. – 1961. – 824 p.

Increased Wear Resistance of Surfaces of Rotation Bearings Methods Strengthening-Smoothing Processing

A.A. Tkachuk ^{1,a}, V.U. Zablotskyi ^{1,b}, T.V.Terletskyi ^{1,c}, O.L. Kaidyk ^{1,d}, S.A. Moroz ^{1,e}

1 – Lutsk National Technical University, Lutsk, Ukraine

a – a.tkachuk@lntu.edu.ua

b – v.zablotsky@lntu.edu.ua

c – t.terletskyi@lntu.edu.ua

d – o.kaidyk@lntu.edu.ua

e – s.moroz@lntu.edu.ua



DOI **10.13140/RG.2.1.1757.9125**

Keywords: bearing, grinding in, microprofile surfaces, the wear resistance, strengthening-smoothing processing.

ABSTRACT. Trends of modern engineering put forward higher requirements for quality bearings. This is especially true on production of bearings for special purposes with high speeds of rotation and resource. Much more opportunities in the technology management quality surface layers appear in the application of smoothing-strengthening methods, based on superficial plastic deformation. Working models of cutting lathes, grinders and tool smoothing sequence revealed the formation of operational parameters in the technological cycle of roller rings. The model of the dynamics of elastic deformation of the work piece tool helps identify actions radial force in the contact "surface - indenter." Using mathematical modeling resolved a number of issues relevant process.

Introduction. Trends of modern engineering put forward higher requirements for quality bearings. This is due to the fact that the reliability and durability of the machine mechanical largely depends on the operability established in her bearings. Most of the mechanisms operating in roller bearings are subjected to loads that differ from the calculation. Due to the large number of operational factors and mechanisms of their random nature complicated forecasting bearing behavior in real conditions. This leads to a premature loss of the performance of the bearing. This is especially true on production of bearings for special purposes with high speeds of rotation and resource.

During work bearing an intense local working surfaces wear rings. Tangent surfaces tend to acquire a geometric shape and roughness that best match specific operating conditions. During this emerging higher contact stresses, which can lead to leakage of thermal processes in the surface layer of the metal and reduce its physical and mechanical properties. In areas of maximum deformation of the surface layer of the metal contact stresses the rise to critical values.

However, if during the forming roll surface to ensure optimum operational microgeometry profile and physical and mechanical properties of the surface layer, the reduced period of time grinding in and accelerate the acquisition of stable operating condition. Traditional technologies forming working surfaces bearing rings, does not fully ensure the rational combination microgeometrical characteristics and physical and mechanical properties of the surface layer of abrasive treatment after surgery. Analysis of manufacturing defects functional surfaces showed that ends traditional technologies do not provide a sufficient level of quality required for their manufacture through that, reduced roller wear resistance in general. Much more opportunities in the technology management quality surface layers appear in the application of reinforcing – processing methods, based on superficial plastic deformation, through the emergence of an enabling technological factors. Providing high performance characteristics of the working surfaces of rings by using roller-fixing

operations is an actual scientific and practical problem [1].

Research results. Qualitative and quantitative assessment methods for forming mutual rotation surface details and operational requirements for surface rotation rings, served as the basis for modeling relationships structural and technological factors, processes of strengthening processing performance indicators. To evaluate the durability work surfaces rings used composite index J - intensity of wear that takes into account the impact of technological factors, material properties and performance rings. Dependin deduced grinding in mode:

$$J_n = \frac{1,2 Ra^{2/3}}{n \lambda Sm t_p^{3/2} (H\mu_0)} \left(\frac{p}{H\mu_0} \right)^{7/6} \sqrt{15\pi (2\pi W_z H_{\max})^{1/3} \left[1 + \frac{2\pi H\mu_0 (1 - \mu^2)}{E} \right]} , \quad (1)$$

and the set mode:

$$J_p = \frac{1,2\pi p^{7/6}}{n \lambda t_p^{3/2} H\mu_0^{2/3}} \sqrt{\frac{30 (1 - \mu^2) \cdot (2\pi Ra W_z H_{\max})^{1/3}}{E Sm}} , \quad (2)$$

where Ra – arithmetic mean deviation of surface roughness profile;

n – the number of cycles, leading to displays of material destruction;

λ – coefficient taking into account the impact of surface residual stress on the process of wear;

Sm – average step of roughness profile roughness;

t_p – the relative length of the reference line roughness profile;

p – working pressure tangential surface;

$H\mu_0$ – surface micro hardness;

W_z – the average height of the waves;

H_{\max} – maximum height macro deviations;

μ and E – Poisson's ratio and modulus of elasticity of the material details.

Analysis of theoretical and empirical relationships operational properties of details roller shown that they depend on the system parameters of quality of functional surfaces:

- ✓ macro deviations – H_{\max} , H_p ;
- ✓ waviness – W_z , W_p , Smw ;
- ✓ roughness – Ra , R_z , R_{\max} , R_p , Sm , t_p ;
- ✓ subjectivity – Ra' , Sm' ;
- ✓ physical and mechanical properties – σ_0 (surface residual stresses);
- ✓ $h\sigma_0$ (depth of surface residual stress);
- ✓ $H\mu_0$, h_n (hardened layer depth);
- ✓ I_g (grain size);
- ✓ ρ_D (dislocation density).

Working models processing blade, abrasive and ironed tool sequence revealed the formation operational parameters in the technological cycle of roller rings [2].

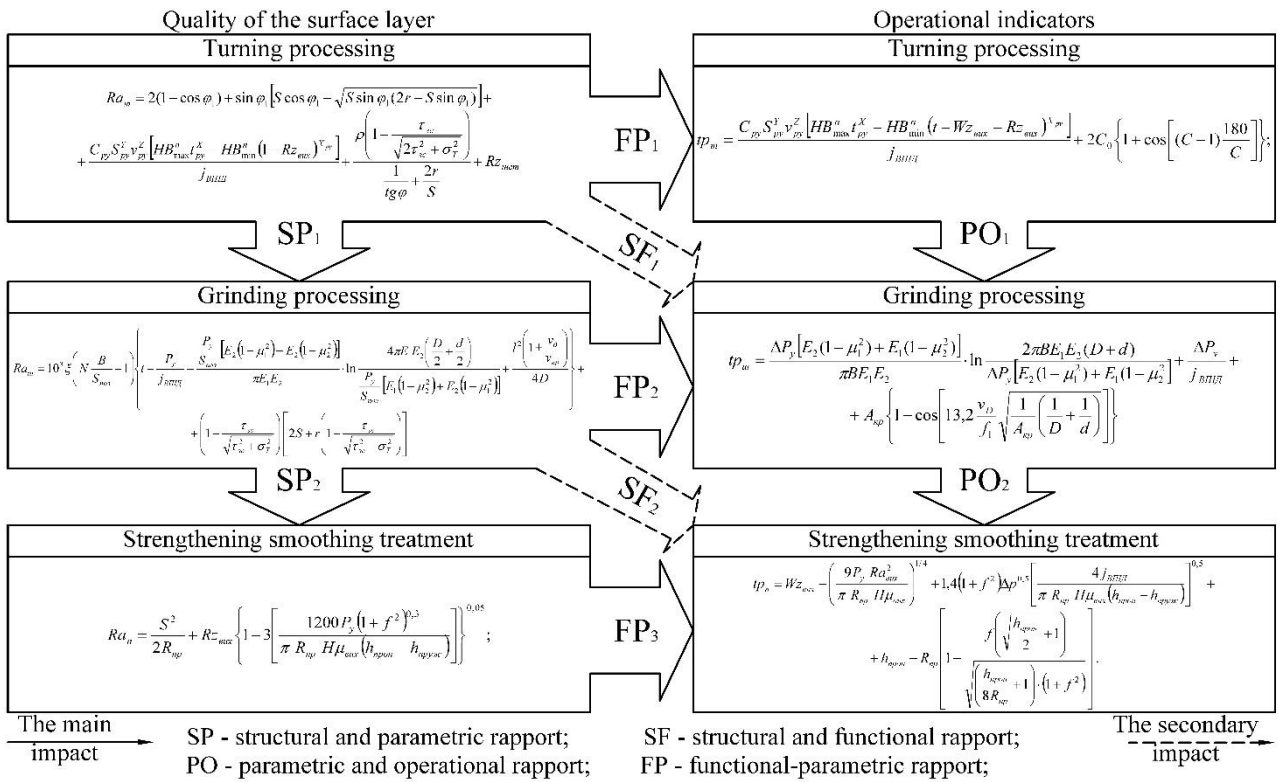


Fig. 1. Generalized model of communications quality parameters and performance indicators in the technological cycle processing functional surfaces.

It was established that during the formation of edge cutting processing roughness depends on the initial roughness and fluctuations Rz original micro hardness of the surface layer $H\mu_{max}$, $H\mu_{min}$. The average roughness pitch Sm depends on its initial value, from Rz and changes in the surface micro hardness $H\mu$. Initial ironed have partial heredity and the next processing depending on the initial physical and mechanical parameters of the surface layer, namely micro hardness and depth of the residual stress ($H\mu_0$, $h\mu$, σ_0 , $h\sigma_0$). Formation of physical and mechanical properties of the surface layer during machining largely depends on their initial state. Based on the analysis of the impact of quality parameters of the surface layer of processing conditions established hereditary nature and effect relationship of quality parameters of the surface layer of performance (fig. 1).

To analyze the performance of selected material length of profile at the level c surface roughness. Analysis of different profiles showed that the bearing capacity of the surface layer at a constant height R_{max} (Rz) and Ra value is greater, the less smooth height Rp (distance from the line appearances to the midline). Over the same values Rp and R_{max} (Rz) bearing capacity of the surface of the greater, the larger parameter (Ra). With decreasing height R_{max} microscopic parameters Ra and Rp decreases and increases carrying capacity. Established that the bearing capacity of the surface asperities depends on the parameter R_{max} (Rz), height Rp and smoothing of the arithmetic mean deviation of profile Ra . According constructed diagrams of distribution of equivalent stress (fig. 2) indenter different geometry configurations and on the basis of the calculations set optimal shape deforming element (fig. 2a).

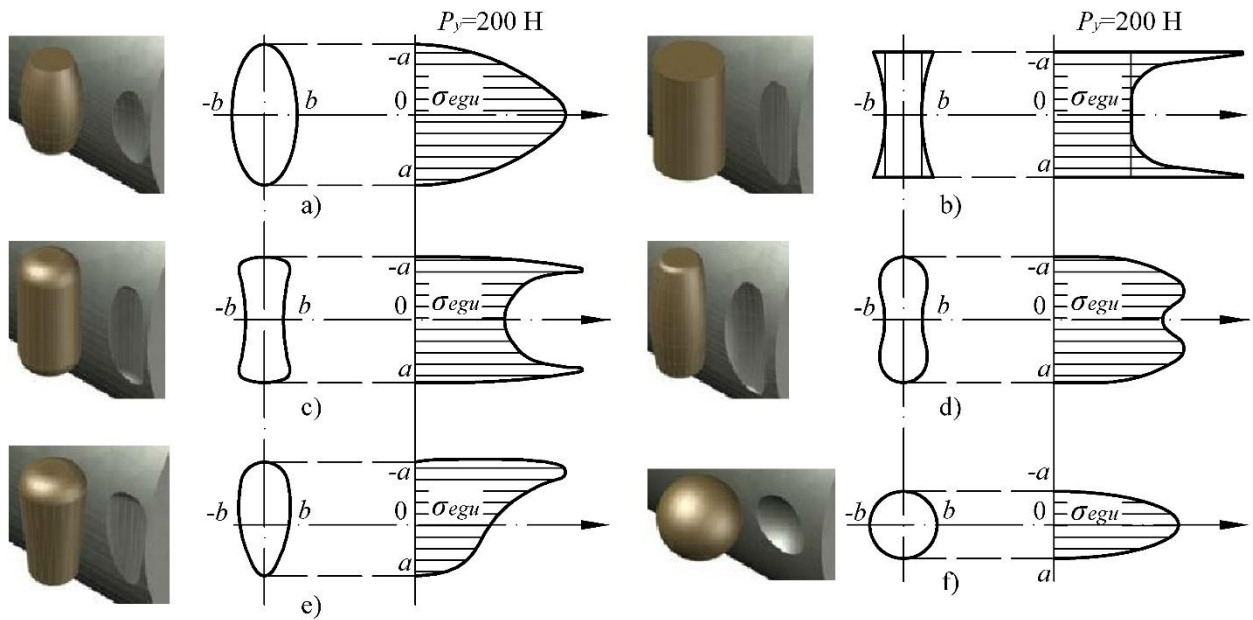


Fig. 2. Change the equivalent stress distribution diagram based on the shape of the indenter.

Stress state in the contact details of the indenter is not determined by starting and plastically deformed as a result of pressing shape its surface. With this in mind when calculating the stresses arising details should be considered not only primary, but also formed curvature plastically deformed surface. In addition, the plastic deformation of the material parts diagrams equivalent stress within the curved deformable layer, reflecting the history of the load. As the flow deformation maximum yield strength increases and deeper until, until it reaches a position which meet peak loads. In the process of strengthening the cross section of the metal surface layer is usually fixed by this result, and micro hardness point alignment determines the limit plastically deformed layer depth is strengthening h_σ . For the general case of contact bodies of arbitrary curvature main stress σ_x , σ_y , σ_z planes perpendicular to the axes of which z normal to the contact surface, and x coincides with the main axis of the elliptical contact areas are defined as:

$$\begin{aligned}
 \sigma_x &= -P_y \frac{\frac{b}{a}}{1 - \frac{b^2}{a^2}} \left\{ -\sqrt{\frac{b^2 + z^2}{a^2 + a^2}} + 2 \frac{z}{a} (L - K) - 2\mu \left[1 - \frac{a^2}{b^2} \sqrt{\frac{b^2 + z^2}{a^2 + a^2}} + \frac{z}{a} \left(\frac{a^2}{b^2} L - K \right) \right] \right\}; \\
 \sigma_y &= -P_y \frac{\frac{b}{a}}{1 - \frac{b^2}{a^2}} \left\{ \frac{1 + \frac{z^2}{a^2} \left(2 \frac{a^2}{b^2} - 1 \right)}{\sqrt{1 + \frac{z^2}{a^2}} \sqrt{\frac{b^2}{a^2} + \frac{z^2}{a^2}}} - 2 \frac{z}{a} \left(\frac{a^2}{b^2} L - K \right) - 1 + 2\mu \left[1 - \sqrt{\frac{b^2 - z^2}{a^2 - a^2}} + \frac{z}{a} (L - K) \right] \right\}; \\
 \sigma_z &= -P_y \frac{1}{\sqrt{1 + \frac{z^2}{a^2}} \sqrt{1 + \frac{z^2}{b^2}}}.
 \end{aligned} \quad (3)$$

where P_y – radial load;

a, b – axis elliptical contact in the axial and transverse sections respectively.

The main stress is expressed as a function of the ratio of semiaxes b and a a fingerprint, the ratio z coordinates occurrence study point to the semi axes of the ellipse and the maximum pressure P_y in the contact center. In the formula (3) for σ_x , σ_y appear Poisson coefficient μ and elliptic integrals of

the first $K(e, \theta) = \int_0^\theta \frac{d\theta}{\sqrt{1 - e^2 \sin^2 \theta}}$ and second race $L(e, \theta) = \int_0^\theta \sqrt{1 - e^2 \sin \theta} d\theta$, which depend on the

parameter $\theta = \text{arcctg } z/a$ and eccentricity of the ellipse $e = \sqrt{1 - (b/a)^2}$. For steel **100Cr6** the coefficient $\mu=0,3$, here you can define the number of values b/a and z/b , main (3) and equivalent stress (4):

$$\sigma_{egu} = \sqrt{\frac{1}{2} [(\sigma_x - \sigma_y)^2 + (\sigma_y - \sigma_z)^2 + (\sigma_z - \sigma_x)^2]}. \quad (4)$$

After equating, according to Huber-Misses condition, medium shear stresses σ_{egu} to the yield strength of the material parts in the initial state, found coordinate $z=h_\sigma$ limits plastically deformed layer:

$$\sigma_T = \frac{3}{2} \cdot \frac{P_y}{\pi ab} \sqrt{\frac{1}{2P_y^3} [(\sigma_x - \sigma_y)^2 + (\sigma_y - \sigma_z)^2 + (\sigma_z - \sigma_x)^2]}. \quad (5)$$

The model of the dynamics of deformation of the workpiece elastic action tool helps identify radial force P_y in the contact "surface – indenter". Design model (fig. 3) corresponds to the scheme axial cam mechanism, where 1 – body, 2 – moving the slider with the indenter 3, are pressed against the workpiece 5 with 4 spring stiffness c with power $P_{y0}=Q_0=cY_0$ through the nut section 6. Rated piece is shaped like a circle 7 of radius ρ_0 . Actual section piece is presented as a wavy curve, which has a maximum height W_{\max} , corner step φ_s wave, a nominal profile section 7 is the average m_w line waviness 8, which determines the actual radius blank $\rho(\varphi)$.

In the calculation scheme envisaged action following forces:

$P_{y0} = Q_0 = cY_0$ – nominal power smoothing;

$P_y = Q$ – the impact of the resultant force of the indenter to the surface in the contact area;

$\overline{m\ddot{y}}$ – inertia of moving parts of the tool;

\overline{P}_y – reaction force on the workpiece indenter;

\overline{P}_z – burnishing resistance force;

\overline{P} – smoothing the resultant force;

\overline{mg} – the weight of the moving parts of the tool;

$\overline{N}_1, \overline{N}_2$ – reaction forces on the bearings slider;

$\overline{F}_1, \overline{F}_2$ – slip-friction force occurring during driving slider;

$\eta \dot{Y}$ – moment of resistance proportional to the velocity of the slider caused by the presence of cutting fluid.

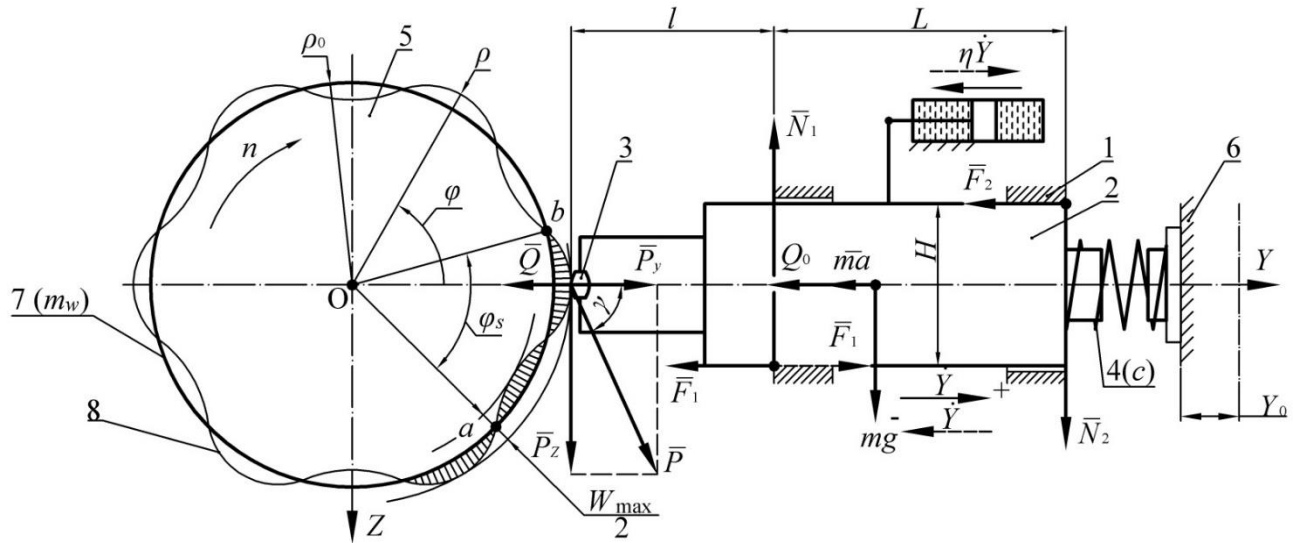


Fig. 3. The estimated combined scheme of smoothing surfaces of revolution which have deviations from roundness.

Using mathematical modeling resolved a number of issues:

– Set the necessary conditions for sustainable harvesting and indenter contact no possibility of separation indenter and indenter occurrence of impact on the surface of the workpiece:

$$f(\omega t) = f(\varphi) = \rho, \quad (6)$$

– Speed range defined smoothing (v_{\min} , v_{\max}), within which the power will be stored in the smoothing Q acceptable range (Q_{\min} , Q_{\max}), which must endure in order to create quality parameters of the surface layer of the regulated reliability.

$$Q_0 - \Delta Q \leq Q_0 + cf(\omega t) + M\omega^2 f''(\omega t) \leq Q_0 + \Delta Q. \quad (7)$$

– Identified a number of additional conditions tool to select the optimal technological modes of processing, such as:

a) Acceleration slider:

$$\ddot{y}(t) = \omega^2 f''(\varphi) = \omega^2 f''(\omega t); \quad (8)$$

b) Jamming condition slider:

$$\operatorname{tg} \gamma_{\text{kr}} = \frac{1}{f \left(1 + \frac{2h}{L} \right)}; \quad (9)$$

c) Equation of forced oscillations:

$$\ddot{Y} + 2n\dot{Y} + \omega_0^2 Y = \frac{cf(t)}{m}; \quad (10)$$

d) Factor of dynamism:

$$\mu = \frac{a}{Y_{\text{cr}}} = \frac{1}{\sqrt{\left(1 - \frac{\omega^2}{\omega_0^2} \right)^2 + \frac{4\omega^2 n^2}{\omega_0^4}}}; \quad (11)$$

e) Vibration amplitude:

$$a = \frac{Y_{\text{cr}}}{\sqrt{\left(1 - \frac{\omega^2}{\omega_0^2} \right)^2 + \left(\frac{ka^{n-1}}{c} \right)^2}}. \quad (12)$$

Experimental study of the effect of quality parameters of the surface layer on the wear resistance of working surfaces on strengthening rings roller-smoothed operations [3]. The influence of burnishing force P_y in depth, width, height, and area roughness flows in cross section determined by means of test passes. Fragments studied surfaces and their indicators are shown (fig. 5).

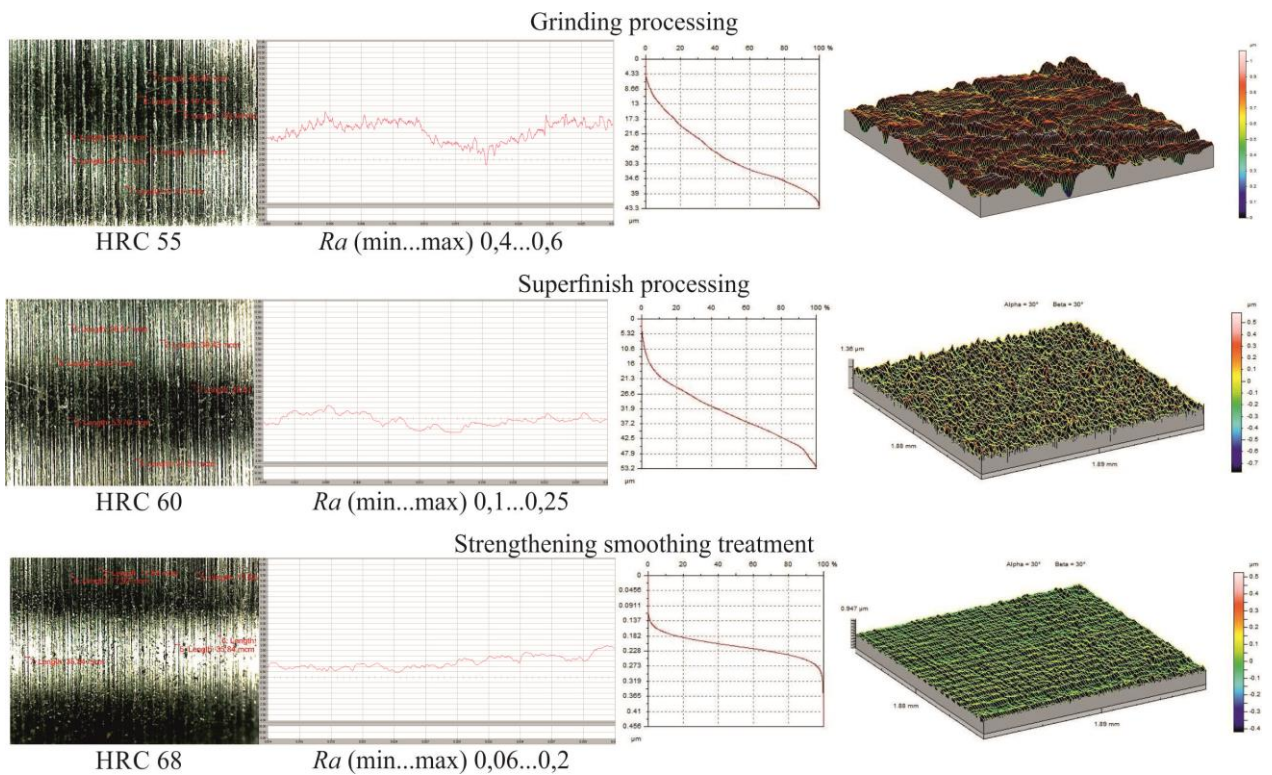


Fig. 5. Analysis micro geometrical parameters of functional surfaces.

Study parameters as rolling surfaces for surface plastic deformation operations performed by multivariate regression model that reflects the quantitative relationship between radial force burnishing (P_y), supply (S), spindle speed (n), output parameters as the surface layer R_{sou} (mean deviation profile, original) Sm_{sou} (average step of roughness profile, basic) and surface layer quality parameters (Ra , Sm , $H\mu$), developed at the pilot plant.

Influence of technological factors on the geometric parameters of micro-relief and durability investigated on samples of steel 100Cr6 accordance with our methodology. These samples were rough grinding operation, hardness 55...60 HRC, the initial surface roughness is $R_{sou}=0,5...0,7$ micrometers.

The effect of technological factors (effort burnishing P_y , radius deforming element R_{pr} , filing tool S , speed spindle n) on the geometric parameters of the micro profile (depth h_σ , width b_n height sag h_{pn} relative bearing area t_p , the average step of roughness profile Sm , average arithmetic mean deviation of profile Ra), physical and mechanical properties of the surface layer (surface microhardness $H\mu$). The results of experimental studies and mathematical modeling of the empirical dependence (13) (14) (15) parameters of the surface layer after burnishing combined modes of P_y , S , n microgeometrical for strengthening operations using instrument one inventory elastic action.

$$\begin{aligned}
 Ra = & 2,761 \cdot 0,0225 \cdot P_y + 7,01 \cdot S - 0,0184 \cdot n - 1,255 \cdot R_{sou} - 0,0415 \cdot Sm - \\
 & - 0,000009 \cdot P_y \cdot n + 0,00676 \cdot P_y \cdot R_{sou} + 0,00018 \cdot P_y \cdot Sm + 0,0277 \cdot S \cdot n - 0,178 \cdot S \cdot Sm + (13) \\
 & + 0,00744 \cdot R_{sou} \cdot n + 0,000143 \cdot n \cdot Sm + 0,01492 \cdot R_{sou} \cdot Sm + 0,59 \cdot P_y \cdot S.
 \end{aligned}$$

$$\begin{aligned}
 Sm = & -116,7 + 0,032 \cdot P_y - 106 \cdot S \cdot n + (-0,275 \cdot n) + 35,5 \cdot R_{sou} + \\
 & + 5,787 \cdot Sm_{sou} - 0,00069 \cdot P_y \cdot n + 429 \cdot S \cdot R_{sou} - 23,3 \cdot S \cdot Sm_{sou} + (14) \\
 & + 0,0896 \cdot R_{sou} \cdot n - 2,118 \cdot R_{sou} \cdot Sm_{sou} + 3,17 \cdot n \cdot S - 0,00245 \cdot n \cdot Sm_{sou}.
 \end{aligned}$$

$$\begin{aligned}
 H\mu = 3601 + 77,4 \cdot P_y - 3910 \cdot S - 2,04 \cdot n - 11,93 \cdot Ra_{sou} - 41 \cdot Sm - 0,019 \cdot P_y \cdot n - \\
 - 1,75 \cdot P_y \cdot Ra_{sou} + 10185 \cdot S \cdot Ra_{sou} + 100 \cdot S \cdot Sm + 0,032 \cdot n \cdot Sm + \\
 + 16,4 \cdot Ra_{sou} \cdot Sm - 626 \cdot P_y \cdot S.
 \end{aligned} \tag{15}$$

Based on experimental and theoretical research built graphic options, depending on surfaces treated microgeometry mode burnishing P_y , S , n enabling to optimize technological factors reinforcing-ironed operations for surfaces with predicted values of the parameters microgeometry surface layer and improved performance properties.

Summary. In order to improve the performance of roller rings and reduce the cost of production offered in the technological cycle of the rings redistribute allowances for grinding operations processing and operation superfinish processing combined burnishing.

Working empirical (13) (14) (15) and graphic dependences revealed that the reduction Ra 6 times reduces the intensity of wear surfaces also 6 times, reducing Sm 2,5 times the intensity reduces wear surface 4,4 times, an increase of 5 $H\mu$ increases the wear resistance of the surface 7,5 times (all other equal conditions). Thus, the most significant impact wear resistance surface microhardness $H\mu$, arithmetic mean deviation of profile Ra and the average roughness pitch Sm .

Research roller burnishing strengthening treated for wear resistance were conducted in the following modes: $F_a=21$ kg/cm², $F_r=12$ kg/cm² (axial and radial load, respectively); $n=6000$ rev/min; $T_{10}=229$ hours. Found that through the use of reinforcing-ironed technologies durability surfaces bearing rings roller increases by 15-20%. Physical picture experimental fact increase the durability of functional surfaces after smoothing operations strengthens confirmed the reliability of theoretical positions.

1. Contact the strength of bearing surfaces is provided not only by methods of thermal and chemical-thermal effects, but methods of rational combination of grinding and strengthening ironed-treatment as directed smoothing effect on surface asperities peaks, providing effect of the surface layer, and as a result reduce the period of grinding in contacting surfaces by 30% and increase the service life of 10%;
2. According to the research highly developed technology combined grinding and strengthening ironed-processing surfaces bearing rings, providing an enhanced level of wear resistance roller by 15-20% and reduces the cost of finishing operations by 12%;
3. The mathematical model of burnishing tool one indentation elastic action on the basis of which is determined radial force in the contact "surface – indenter" $P_y=200$ H. The conditions to ensure continuous contact of the indenter piece to piece band rotation – 400...600 rev/min that is the foundation of stability during the process of burnishing process design;
4. Based on modeling the dynamics of the process of smoothing based strain gradient workpiece material reasonably geometric configuration deforming element (indenter) ellipsoid-type core radius $R_{pr}=20$ mm and the ratio of the length of the vertical axis (l_a) to the horizontal (l_b) – 1÷0,63 respectively and developed a design tool unit with the mechanism of P_y .

References

- [1] A. Tkachuk Technological foundations of strengthening smoothing processing surfaces of revolution. Monograph - Lutsk: SAP Hadyak Joan Volodymyrivna. Printing «Volynpolihraf»TM, 2014. - 196 p.
- [2] V. Marchuk, A. Tkachuk, S. Prustupa Thermophysical analysis process diamond smoothing, Computer Aided Production Engineering – Lublin: Politechnika Lubelska, 2013. - P. 67-74.
- [3] A. Tkachuk Ukraine Patent 87877, МІІК B24B 39/00 (2014.01). Device for smoothing surfaces of revolution. The applicant and the patentee: Lutsk National Technical University, Lutsk; appl.

09/08/2013; publ. 02/25/2014; Newsletter №4. - 4 p.

[4] P.W Gold, J Loos, *Wear resistance of PVD-coatings in roller bearings*. *Wear*. Volume 253, Issues 3–4, August 2002, Pages 465–472, doi:10.1016/S0043-1648(02)00145-X.

[5] P.L. Hurricks, *Some metallurgical factors controlling the adhesive and abrasive wear resistance of steels. A review*. *Wear*. Volume 26, Issue 3, December 1973, Pages 285-304, doi:10.1016/0043-1648(73)90184-1.

Kinetostatics of Wheel Vehicle in the Category of Spiral-Screw Routes

Kravets V.V.^{1, a}, Bas K.M.¹, Kravets T.V.², Zubarev M.S.^{1, b}, Tokar L.A.¹

1 – State Higher Educational Institution “National Mining University”, Dnipropetrovsk, Ukraine

2 – National University of Railway Transport, Dnipropetrovsk, Ukraine

a – prof.w.kravets@gmail.com

b – mykola.zubariev@gmail.com



DOI [10.13140/RG.2.1.1010.3921](https://doi.org/10.13140/RG.2.1.1010.3921)

Keywords: dynamic design, mathematical model, Euler-Lagrange equations, kinetostatics, contact forces, spiral-screw trajectory, hodograph.

ABSTRACT. Deterministic mathematical model of kinetostatics of wheel vehicle in terms of different modes of spatial motion in the context of curved route is proposed. Earth-based coordinate system is introduced which pole and axial orientation are determined by the convenience of route description as well as vehicle-related coordinates which pole axial orientation are determined within inertial space with the help of natural trihedral. Turn of the natural trihedral within inertial coordinates is described by means of quaternion matrices in the context of Rodrigues-Hamilton parameters. Rodrigues-Hamilton parameters are in matrix form in direct accordance with specified hodograph. Kinetostatics of wheel vehicle is considered in terms of spatial motion with an allowance for three-dimensional aerodynamic forces, gravity, and tangential and centrifugal inertial forces. In the context of spiral-screw lines deterministic mathematical model of wheel vehicle kinetostatics is proposed in the form of hodograph in terms of uniform motion, accelerated motion, and decelerated motion within following route sections: straight and horizontal; in terms of vertical grade; in terms of horizontal plane. Analytical approach to determine animated contact drive-control forces of wheel vehicle for structural diagrams having one and two support points involving of a driving-driven wheel characteristic is proposed based on kinetostatics equations. Mathematical model of wheel vehicle kinetostatics in terms of spatial motion is constructed on the basis of nonlinear differential Euler-Lagrange equations; it is proposed to consider physically implemented motion trajectories of wheel vehicles in the context of spiral-screw lines; hodograph determines spatial displacement; Rodrigues-Hamilton parameters determines spatial turn; Varignon theorem is applied to identify components of drive (control) force. The obtained results make it possible to solve a wide range of problems connected with dynamic design of wheel vehicles involving controllability, and estimation of dynamic load of both system and support surface.

Introduction. In the context of uniform, accelerated, and decelerated motion, modes of front-drive, rear-driven, and four-wheel drive vehicle in terms of spatial curved route within junctions and turns, grades and straights, problems connected with estimation of dynamic load of structure and road surface [1,2,3] as well as stability and controllability [4,5,6] are topical. Solving of problems of dynamic design [7,8] of wheel vehicle help determine equivalent contact loads on supporting points taking into consideration characteristic of driver wheel, synthesize required control components, and identify relevant torque of driver wheel to provide desired motion mode of a vehicle in terms of specified route [9].

Problem definition. Inertial and geometrical parameters of wheel vehicle; configuration of supporting points taking into consideration characteristic of driver wheel for front-drive, rear-driven, and four-wheel drive vehicle; external force effect on a vehicle (gravity force and aerodynamic force); route geometry (straight, turn, grade, junction, manoeuvring); mode of a vehicle motion (uniform, accelerated, decelerated) are supposed as preselected.

Equivalent contact driving force (internal resulting constraint reaction of support surface) providing desired mode of a vehicle motion in terms of preselected route should be identified. It is required to

distribute equivalent contact driving force on supporting points involving of drive wheel characteristic for front-drive, rear-driven, and four-wheel drive structural schemes of wheel vehicle.

Mathematical model of wheel vehicle kinetics. Spatial deterministic mathematical model of wheel vehicle kinetics in the context of different modes of motion within curved route is based upon nonlinear differential Euler-Lagrange equations in the form of quaternion matrices [10]. In this context, weight-specified material point (m) with application of aerodynamic forces, gravity, inertial forces, and unknown contact driving forces (controlling forces) providing desired mode of motion in terms of predetermined spatial curved route is taken as dynamic model of a vehicle.

Following coordinates (Earth-based coordinate system which pole and axial orientation are determined by the convenience of route description as well as vehicle-related coordinates which pole axial orientation are determined within inertial space with the help of natural trihedral) are introduced.

In the context of the taken problem, definition mathematical model bears following simplifications: centre of vehicle masses coincides with a pole of related coordinates; matrix of inertia of a vehicle degenerates into zero matrix; that is gyrodynamics of a vehicle is not considered.

Dynamics of vehicle advance is described with one quasivelocity (V_τ) being projection of a vector of linear velocity of vehicle mass centre on the tangent to motion trajectory (route) and two quasiaccelerations (W_τ , W_n): tangential (W_τ) and normal (centripetal) W_n .

In the context of the assumptions, Euler-Lagrange equations describing kinetics of wheel vehicle take the simple form:

$$\begin{vmatrix} 0 \\ W_\tau \\ W_n \\ 0 \end{vmatrix} = g A^t \cdot {}^t A^t \begin{vmatrix} 0 \\ 0 \\ 0 \\ -1 \end{vmatrix} + \frac{qS}{m} R_d \cdot {}^t R_d \cdot \begin{vmatrix} 0 \\ C_{1d} \\ C_{2d} \\ C_{3d} \end{vmatrix} + \frac{1}{m} \begin{vmatrix} 0 \\ N_\tau \\ N_n \\ N_b \end{vmatrix}, \quad (1)$$

where m – is vehicle mass;

g – is gravity acceleration;

q – is velocity pressure;

S – is specific area;

C_{1d} , C_{2d} , and C_{3d} – are aerodynamic coefficients;

W_τ , and W_n – are quasiaccelerations;

A – is quaternion matrix in terms of Rodrigues-Hamilton parameters determining orientation of natural trihedron within Earth-based coordinate system;

R_d – is quaternion matrix determining orientation of aerodynamic axes relative to natural ones;

N_τ , N_n , and N_b – are driving forces.

Mathematical model of vehicle motion within route section in the context of various modes. Spatial curve supporting trajectory-route as well as motion mode of a vehicle within the route is categorically determined in Earth-based coordinate system by means of hodograph [11]:

$$\bar{r}(t) = \bar{i}r_1 + \bar{j}r_2 + \bar{k}r_3, \quad (2)$$

where \bar{i} , \bar{j} , are $-\bar{k}$ basis vectors of Earth-based coordinate system.

It is proposed to determine hodograph combined with physically implemented trajectories of vehicle motion in the context of spiral and screw lines [9]:

$$\bar{r}(t) = \|\rho_0 \rho_1 \rho_2 \rho_3\| \begin{vmatrix} 1 \\ t \\ t^2 \\ t^3 \end{vmatrix} (\bar{i} \cos \omega t + \bar{j} \sin \omega t) + \bar{k} \|h_0 h_1 h_2 h_3\| \begin{vmatrix} 1 \\ t \\ t^2 \\ t^3 \end{vmatrix}, \quad (3)$$

where $\rho_i h_i (i = 0, 1, 2, 3)$ are running parameters determined on prescribed boundary conditions;

ω – is average turn rate equal to $\omega = \frac{\varphi_0}{t_0}$. In this context φ_0 is complete turn angle; and t_0 is

specified time for turn.

Components of hodograph are determined as follows:

$$r_1 = \|\rho_0 \rho_1 \rho_2 \rho_3\| \begin{vmatrix} 1 \\ t \\ t^2 \\ t^3 \end{vmatrix} \cos \omega t, \quad r_2 = \|\rho_0 \rho_1 \rho_2 \rho_3\| \begin{vmatrix} 1 \\ t \\ t^2 \\ t^3 \end{vmatrix} \sin \omega t, \quad r_3 = \|h_0 h_1 h_2 h_3\| \begin{vmatrix} 1 \\ t \\ t^2 \\ t^3 \end{vmatrix}. \quad (4)$$

It should be noted that highly developed world countries continue research to determine new forms of transit curves providing smooth changes in curve [2]. Transit curves in the form of cubic parabola, sinusoid, lemniscate, three- or four-leafed roses, and pseudospiral, which is circular curve, logarithmic spiral, Euler spiral etc. in special cases, are known. Transit curves proposed from heuristic or criteria viewpoints should correspond to true guide path of transport vehicle both in the context of constant velocity and variable one [2].

Depending upon values of running parameters hodograph proposed in the context of spiral and screw lines makes it possible simulate various particular cases of implemented trajectories and modes of vehicle motion within the routes.

a) Route section is straight ($\omega = 0$) and horizontal ($h_0 = 0$, $h_1 = 0$, $h_2 = 0$, $h_3 = 0$); mode of motion is uniform ($V_{1A} = V_{1B}$, $V_{2A} = 0$, $V_{2B} = 0$, $V_{3A} = 0$, $V_{3B} = 0$). Then $r_2(t) = 0$, $r_3(t) = 0$,

$$r_1(t) = r_{1A} + V_{1A}t; \quad (5)$$

that is hodograph is:

$$\bar{r}(t) = \bar{i}(r_{1A} + V_{1A}t). \quad (6)$$

In this context $0 \leq t \leq t_0$ where t_0 is time to travel predetermined route section ($r_{1B} - r_{1A}$); that is:

$$t_0 = \frac{r_{1B} - r_{1A}}{V_{1A}}. \quad (7)$$

b) Route section is straight and horizontal; mode of motion is not uniform:

- decelerated ($V_{1A} > V_{1B}$);
- accelerated ($V_{1A} < V_{1B}$).

Then hodograph is:

$$\bar{r}(t) = \bar{i} \left(r_{1A} + V_{1A}t + \frac{1}{4} \frac{V_{1B}^2 - V_{1A}^2}{r_{1B} - r_{1A}} t^2 \right). \quad (8)$$

c) Route section is in vertical plane (\bar{i} , \bar{k}); it has:

- rise ($r_{3A} = 0$, $r_{3B} > 0$),
- grade ($r_{3A} = 0$, $r_{3B} < 0$).

Mode of motion is determined with the help of boundary conditions: $V_{1A} = V_{1B}$, $V_{2A} = 0$, $V_{2B} = 0$, $V_{3A} = 0$, $V_{3B} = 0$.

Then hodograph is:

$$\bar{r}(t) = \bar{i}(r_{1A} + V_{1A}t) + \bar{k} \left(3 - 2 \frac{V_{1A}}{r_{1B} - r_{1A}} t \right) \left(\frac{V_{1A}}{r_{1B} - r_{1A}} \right)^2 r_{3B} t^2. \quad (9)$$

Appropriate profile of the route section (motion trajectory) within vertical plane ($0xz$) is obtained in the form of combination of square parabola and cubic parabola:

$$z = 3x^2 - 2x^3, \quad (10)$$

where

$$x = \frac{r_1(t) - r_{1A}}{r_{1B} - r_{1A}}, \quad z = \frac{r_3(t)}{r_{3B}}. \quad (11)$$

In the context of route section under consideration:

- Variation range of variables is: $0 \leq x \leq 1$, $0 \leq z \leq 1$;

- Extremum points are: $x_1^3 = 0, x_2^3 = 1$;
- Extreme values are: $z_{\min}(0) = 0, z_{\max}(1) = 1$;
- Bending point is: $\left(\frac{1}{2}, \frac{1}{2}\right)$;
- Concavity interval is: $0 < x < \frac{1}{2}$;
- Convexity interval is: $\frac{1}{2} < x < 1$.

d) Route section is within horizontal plane (i, j) providing $\varphi_0 = \frac{\pi}{2}$ angle turn; mode of motion is determined with the help of boundary conditions:

$$\begin{aligned} r_{1A} > 0, \quad r_{2A} = 0, \quad r_{3A} = 0, \quad r_{1B} = 0, \quad r_{2B} > 0, \quad r_{3B} = 0; \\ V_{1A} = 0, \quad V_{2A} > 0, \quad V_{3A} = 0, \quad V_{1B} > 0, \quad V_{2B} = 0, \quad V_{3B} = 0. \end{aligned}$$

Then hodograph is:

$$\bar{r}(t) = \left[r_{1A} + \frac{12}{\pi^2} \left(\frac{V_{2A}}{r_{1A}} \right)^2 (r_{2B} - r_{1A}) t^2 - \frac{16}{\pi^3} \left(\frac{V_{2A}}{r_{1A}} \right)^3 (r_{2B} - r_{1A}) t^3 \right] \cdot \left[\bar{i} \cos \left(\frac{V_{2A}}{r_{1A}} t \right) + \bar{j} \sin \left(\frac{V_{2A}}{r_{1A}} t \right) \right]. \quad (12)$$

In this context kinematical connection is available:

$$V_{2A} \cdot r_{2B} = V_{1B} \cdot r_{1A}. \quad (13)$$

Relevant plan of the route section (motion trajectory) within horizontal plane is obtained in polar coordinate system in the form of quadratic Archimedean spiral and cubic one:

$$\frac{r(\varphi) - r_{1A}}{r_{2B} - r_{1A}} = \frac{12}{\pi^2} \varphi^2 - \frac{16}{\pi^3} \varphi^3, \quad (14)$$

where

$$\varphi = \frac{V_{2A}}{r_{1A}} t, \quad r^2(\varphi) = r_1^2(\varphi) + r_2^2(\varphi). \quad (15)$$

In the context of the route section under consideration, variables domain is: $0 \leq \varphi \leq \frac{\pi}{2}$, $r_{1A} \leq r \leq r_{2B}$; that is $r(0) = r_{1A}$, $r\left(\frac{\pi}{4}\right) = \frac{r_{1A} + r_{2B}}{2}$, $r\left(\frac{\pi}{2}\right) = r_{2B}$.

In terms of special case if $V_{2A} = V_{1B}$ then $r_{1A} = r_{2B}$ and $r(\varphi) = r_{1A}$ in the context of any φ ; that is motion trajectory takes a form of radial arc if right-angle turn takes place.

Kinematics of a vehicle within predetermined route section. Kinematics of a vehicle under different motion modes is identified with the help of predetermined hodograph $\vec{r}(t)$. Formulas for components of tangential acceleration and normal one are represented by means of laconic vector notation [12]:

$$W_\tau = \frac{\dot{\vec{r}} \cdot \ddot{\vec{r}}}{|\dot{\vec{r}}|}, \quad W_n = \frac{|\dot{\vec{r}} \times \ddot{\vec{r}}|}{|\dot{\vec{r}}|}, \quad W_b = 0, \quad (16)$$

where $\dot{\vec{r}}$ and $\ddot{\vec{r}}$ – are time derivatives 1 and two of vector function – hodograph;

$|\dot{\vec{r}}|$ – is module of time derivative 1 of hodograph that is velocity value of vehicle motion;

$|\dot{\vec{r}} \times \ddot{\vec{r}}|$ – is module of 1 and 2 time derivatives of hodograph;

$\dot{\vec{r}} \cdot \ddot{\vec{r}}$ – is scalar product of 1 and 2 time derivatives of hodograph.

Formulas for velocity components:

$$V_\tau = |\dot{\vec{r}}|, \quad V_n = 0, \quad V_b = 0. \quad (17)$$

In terms of Earth-based coordinate system and axes of natural trihedron, components of vehicle velocity are of following kinematic relations:

$$\begin{aligned} \begin{vmatrix} 0 \\ \dot{\vec{r}}_1 \\ \dot{\vec{r}}_2 \\ \dot{\vec{r}}_3 \end{vmatrix} &= A \cdot {}^t A \begin{vmatrix} 0 \\ V_\tau \\ V_n \\ V_b \end{vmatrix}, & \begin{vmatrix} 0 \\ V_\tau \\ V_n \\ V_b \end{vmatrix} &= A^t \cdot {}^t A^t \begin{vmatrix} 0 \\ \dot{\vec{r}}_1 \\ \dot{\vec{r}}_2 \\ \dot{\vec{r}}_3 \end{vmatrix}, \end{aligned} \quad (18)$$

where A , ${}^t A$, A^t , ${}^t A^t$ are quaternion matrices in the context of Rodrigues-Hamilton parameters: a_0 , a_1 , a_2 , a_3 [5, 10, 11]; in this context Rodrigues-Hamilton parameters describing a turn (orientation) of natural trihedron (vehicle-related dynamical frame of reference) in terms of terrestrial, fixed, inertial coordinates are determined directly according to specified hodograph with the help of following matrix equation:

$$\begin{vmatrix} 1 & 1 & 1 & 1 \\ 1 & 1 & -1 & -1 \\ 1 & -1 & 1 & -1 \\ 1 & -1 & -1 & 1 \end{vmatrix} \begin{vmatrix} a_0^2 \\ a_1^2 \\ a_2^2 \\ a_3^2 \end{vmatrix} = \frac{1}{|\dot{\vec{r}}| |\dot{\vec{r}} \times \ddot{\vec{r}}|} \begin{vmatrix} |\dot{\vec{r}}| |\dot{\vec{r}} \times \ddot{\vec{r}}| \\ |\dot{\vec{r}} \times \ddot{\vec{r}}| \dot{\vec{r}}_1 \\ \ddot{\vec{r}}_2 (\dot{\vec{r}}_1^2 + \dot{\vec{r}}_3^2) - \dot{\vec{r}}_2 (\dot{\vec{r}}_1 \dot{\vec{r}}_1 + \dot{\vec{r}}_3 \dot{\vec{r}}_3) \\ |\dot{\vec{r}}| (\dot{\vec{r}}_1 \ddot{\vec{r}}_2 - \dot{\vec{r}}_2 \ddot{\vec{r}}_1) \end{vmatrix}, \quad (19)$$

where $|\dot{\vec{r}}|^2 = \dot{\vec{r}}_1^2 + \dot{\vec{r}}_2^2 + \dot{\vec{r}}_3^2$,

$$|\dot{\vec{r}} \times \ddot{\vec{r}}|^2 = (\dot{\vec{r}}_2 \ddot{\vec{r}}_3 - \dot{\vec{r}}_3 \ddot{\vec{r}}_2)^2 + (\dot{\vec{r}}_3 \ddot{\vec{r}}_1 - \dot{\vec{r}}_1 \ddot{\vec{r}}_3)^2 + (\dot{\vec{r}}_1 \ddot{\vec{r}}_2 - \dot{\vec{r}}_2 \ddot{\vec{r}}_1)^2.$$

It should be noted that the matrix

$$\begin{vmatrix} 1 & 1 & 1 & 1 \\ 1 & 1 & -1 & -1 \\ 1 & -1 & 1 & -1 \\ 1 & -1 & -1 & 1 \end{vmatrix}$$

is symmetrical and nondegenerate; moreover, it has following property of orthogonality:

$$\begin{vmatrix} 1 & 1 & 1 & 1 \\ 1 & 1 & -1 & -1 \\ 1 & -1 & 1 & -1 \\ 1 & -1 & -1 & 1 \end{vmatrix} \cdot \begin{vmatrix} 1 & 1 & 1 & 1 \\ 1 & 1 & -1 & -1 \\ 1 & -1 & 1 & -1 \\ 1 & -1 & -1 & 1 \end{vmatrix} = 4 \begin{vmatrix} 1 & 0 & 0 & 0 \\ 0 & 1 & 0 & 0 \\ 0 & 0 & 1 & 0 \\ 0 & 0 & 0 & 1 \end{vmatrix}, \quad (20)$$

That is inverse matrix is:

$$\frac{1}{4} \begin{vmatrix} 1 & 1 & 1 & 1 \\ 1 & 1 & -1 & -1 \\ 1 & -1 & 1 & -1 \\ 1 & -1 & -1 & 1 \end{vmatrix}. \quad (21)$$

Then required solution may be identified by means of following matrix form:

$$\begin{vmatrix} a_0^2 \\ a_1^2 \\ a_2^2 \\ a_3^2 \end{vmatrix} = \frac{1}{4|\dot{\vec{r}}| |\dot{\vec{r}} \times \ddot{\vec{r}}|} \begin{vmatrix} 1 & 1 & 1 & 1 \\ 1 & 1 & -1 & -1 \\ 1 & -1 & 1 & -1 \\ 1 & -1 & -1 & 1 \end{vmatrix} \begin{vmatrix} |\dot{\vec{r}}| |\dot{\vec{r}} \times \ddot{\vec{r}}| \\ |\dot{\vec{r}} \times \ddot{\vec{r}}| \dot{\vec{r}}_1 \\ \ddot{\vec{r}}_2 (\dot{\vec{r}}_1^2 + \dot{\vec{r}}_3^2) - \dot{\vec{r}}_2 (\dot{\vec{r}}_1 \dot{\vec{r}}_1 + \dot{\vec{r}}_3 \dot{\vec{r}}_3) \\ |\dot{\vec{r}}| (\dot{\vec{r}}_1 \ddot{\vec{r}}_2 - \dot{\vec{r}}_2 \ddot{\vec{r}}_1) \end{vmatrix}. \quad (22)$$

$\bar{\tau}$, \bar{n} , \bar{b} basis vectors of natural trihedron of space curved route are determined with the help of specified hodograph in terms of the vector form:

$$\bar{\tau} = \frac{\dot{\bar{r}}}{|\dot{\bar{r}}|}, \quad \bar{n} = \frac{\dot{\bar{r}} \times (\ddot{\bar{r}} \times \dot{\bar{r}})}{|\dot{\bar{r}}| |\dot{\bar{r}} \times \ddot{\bar{r}}|}, \quad \bar{b} = \frac{\dot{\bar{r}} \times \ddot{\bar{r}}}{|\dot{\bar{r}} \times \ddot{\bar{r}}|}. \quad (23)$$

Kinetostatics of ground transport vehicles. Equivalent contact driving (controlling) force of ground transport vehicles is determined by means of kinetic equations.

a) Schematic of vehicle having one supporting point.

In this case internal resulting constraint force of supporting surface is determined with the help of matrix formula:

$$\frac{1}{m} \begin{vmatrix} 0 \\ N_\tau \\ N_n \\ N_b \end{vmatrix} = \begin{vmatrix} 0 \\ W_\tau \\ W_n \\ 0 \end{vmatrix} + g A^t \cdot {}^t A^t \begin{vmatrix} 0 \\ 0 \\ 0 \\ 1 \end{vmatrix} - \frac{qS}{m} R_d \cdot {}^t R_d \begin{vmatrix} C_{1d} \\ C_{2d} \\ C_{3d} \end{vmatrix}. \quad (24)$$

b) Schematic of vehicle having two supporting points.

For two-wheel vehicle resulting driving force (N_τ , N_n , N_b) should be distributed on two supporting points involving drive wheel characteristic in the form of required system of two equivalent driving forces (\bar{F}_1 , \bar{F}_2). In this context the two structural schemes to locate supporting points (0_1 , 0_2) are possible:

- Tandem scheme; and
- Parallel one.

The schemes are shown in Fig.1 where geometrical parameters are set within coordinates related to a vehicle; $\bar{\tau}$ is driving direction.

The formulated problem of dynamic design of two-wheel ground transport vehicle is static problem; its solution should involve Varignon theorem [12]:

$$\bar{r}_1 \times \bar{F}_1 + \bar{r}_2 \times \bar{F}_2 = \bar{r} \times \bar{N}, \quad (25)$$

where $\bar{r}_1 = \bar{r} + \bar{\tau} l_1$, $\bar{r}_2 = \bar{r} - \bar{\tau} l_2$.

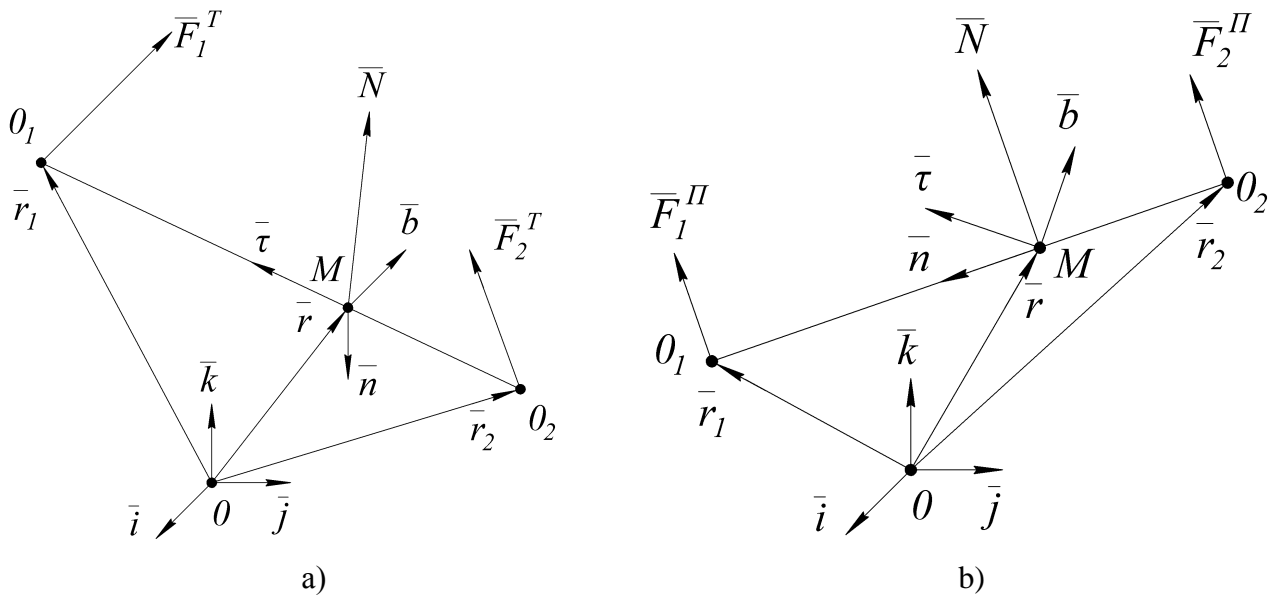


Fig.1. Tandem structural scheme (a) and parallel one (b) to locate supporting points

Specifically, bringing pole 0 in coincidence with supporting point two O_2 results in:

$$\bar{r} = \bar{\tau} l_2, \quad \bar{r}_2 = 0, \quad \bar{r}_1 = (l_1 + l_2) \bar{\tau} \quad \text{for tandem scheme};$$

$$\bar{r} = \bar{n} h_2, \quad \bar{r}_2 = 0, \quad \bar{r}_1 = (h_1 + h_2) \bar{n} \quad \text{for parallel scheme}$$

where l_1, h_1 is $M0_1$ section (distance from centre of mass to supporting point one);

l_2, h_2 is $M0_2$ section (distance from centre of mass to supporting point two).

Then within axes of natural trihedron, Varignon theorem is represented in the form of determinants:

$$\begin{vmatrix} \bar{\tau} & \bar{n} & \bar{b} \\ l_1 + l_2 & 0 & 0 \\ F_{1\tau}^T & F_{1n}^T & F_{1b}^T \end{vmatrix} = \begin{vmatrix} \bar{\tau} & \bar{n} & \bar{b} \\ l_2 & 0 & 0 \\ N_\tau & N_n & N_b \end{vmatrix} \quad \text{for tandem scheme};$$

$$\begin{vmatrix} \bar{\tau} & \bar{n} & \bar{b} \\ 0 & h_1 + h_2 & 0 \\ F_{1\tau}^{\text{II}} & F_{1n}^{\text{II}} & F_{1b}^{\text{II}} \end{vmatrix} = \begin{vmatrix} \bar{\tau} & \bar{n} & \bar{b} \\ 0 & h_2 & 0 \\ N_\tau & N_n & N_b \end{vmatrix} \quad \text{for parallel scheme}.$$

Whence it follows:

- In terms of tandem scheme: $F_{1\tau}^T$ is uncertain, $F_{1n}^T = \frac{l_2}{l_1 + l_2} N_n$, $F_{1b}^T = \frac{l_2}{l_1 + l_2} N_b$;

- In terms of parallel scheme: $F_{1\tau}^{\text{II}} = \frac{h_2}{h_1 + h_2} N_\tau$, F_{1n}^{II} is uncertain, $F_{1b}^{\text{II}} = \frac{h_2}{h_1 + h_2} N_b$.

Bringing 0 pole in coincidence with supporting point one O_1 results in:

$$\bar{r} = -l_1 \bar{\tau}, \quad \bar{r}_1 = 0, \quad \bar{r}_2 = -(l_1 + l_2) \bar{\tau} \quad \text{for tandem scheme};$$

$$\bar{r} = -h_1 \bar{n}, \quad \bar{r}_1 = 0, \quad \bar{r}_2 = -(h_1 + h_2) \bar{n} \quad \text{for parallel scheme.}$$

Then within axes of natural trihedron, Varignon theorem is:

$$\begin{vmatrix} \bar{\tau} & \bar{n} & \bar{b} \\ l_1 + l_2 & 0 & 0 \\ F_{2\tau}^T & F_{2n}^T & F_{2b}^T \end{vmatrix} = \begin{vmatrix} \bar{\tau} & \bar{n} & \bar{b} \\ l_2 & 0 & 0 \\ N_\tau & N_n & N_b \end{vmatrix} \quad \text{for tandem scheme;}$$

$$\begin{vmatrix} \bar{\tau} & \bar{n} & \bar{b} \\ 0 & h_1 + h_2 & 0 \\ F_{2\tau}^{\text{II}} & F_{2n}^{\text{II}} & F_{2b}^{\text{II}} \end{vmatrix} = \begin{vmatrix} \bar{\tau} & \bar{n} & \bar{b} \\ 0 & h_2 & 0 \\ N_\tau & N_n & N_b \end{vmatrix} \quad \text{for parallel scheme.}$$

Whence it follows:

- In terms of tandem scheme: $F_{2\tau}^T$ is uncertain, $F_{2n}^T = \frac{l_1}{l_1 + l_2} N_n$, $F_{2b}^T = \frac{l_1}{l_1 + l_2} N_b$;

- In terms of parallel scheme: $F_{2\tau}^{\text{II}} = \frac{h_1}{h_1 + h_2} N_\tau$, F_{2n}^{II} is uncertain, $F_{2b}^{\text{II}} = \frac{h_1}{h_1 + h_2} N_b$.

To verify the results obtained and cope with uncertainty in the process of the problem solving apply static invariant one [6]:

$$\bar{F}_1 + \bar{F}_2 = \bar{N}. \quad (26)$$

Within axes of natural trihedron for tandem scheme, the equation

$$F_{1n}^T + F_{2n}^T = N_n, \quad F_{1b}^T + F_{2b}^T = N_b \quad (27)$$

is performed identically while following equation

$$F_{1\tau}^T + F_{2\tau}^T = N_\tau \quad (28)$$

becomes resolvable if technical specifications are involved in terms of driving-driven wheel characteristic.

Example 1. Four-wheel drive structural scheme; that is

$$F_{1\tau}^T > 0, \quad F_{2\tau}^T > 0 \quad (29)$$

and design parameter is assumed to be constrained

$$\left| \frac{F_{1\tau}^T}{F_{2\tau}^T} \right| = k. \quad (30)$$

Then $F_{1\tau}^T = kF_{2\tau}^T$.

From which $kF_{2\tau}^T + F_{2\tau}^T = N_\tau$,

that is $F_{2\tau}^T = \frac{1}{1+k} N_\tau, \quad F_{1\tau}^T = \frac{k}{1+k} N_\tau$.

Particularly, if driving contact forces are equal within front axle 0_1 and back axle 0_2 then $k = 1$, and hence

$$F_{2\tau}^T = \frac{1}{2} N_\tau, \quad F_{1\tau}^T = \frac{1}{2} N_\tau. \quad (31)$$

Example 2. If front drive structural scheme then

$$F_{1\tau}^T > 0, \quad F_{2\tau}^T < 0. \quad (32)$$

Subsequently $F_{1\tau}^T - F_{2\tau}^T = N_\tau$

or $kF_{2\tau}^T - F_{2\tau}^T = N_\tau$ that is

$$F_{2\tau}^T = \frac{1}{k-1} N_\tau, \quad F_{1\tau}^T = \frac{k}{k-1} N_\tau, \quad (33)$$

where $k > 1$.

Example 3. If rear-driven structural scheme then

$$F_{1\tau}^T < 0, \quad F_{2\tau}^T > 0. \quad (34)$$

Subsequently $-F_{1\tau}^T + F_{2\tau}^T = N_\tau$

or $-kF_{2\tau}^T + F_{2\tau}^T = N_\tau$, то есть

$$F_{2\tau}^T = \frac{1}{1-k} N_\tau, \quad F_{1\tau}^T = \frac{k}{1-k} N_\tau, \quad (35)$$

where $k < 1$.

Comparable result is available while considering parallel scheme. The equations

$$F_{1\tau}^{\Pi} + F_{2\tau}^{\Pi} = N_\tau, \quad F_{1b}^{\Pi} + F_{2b}^{\Pi} = N_b \quad (36)$$

are performed identically. Then the equation

$$F_{1n}^T + F_{2n}^T = N_n \quad (37)$$

is solvable in terms of extra conditions.

In this context lateral contact forces are assumed as those related to technically reasonable conditions:

$$F_{1n}^{\Pi} > 0, \quad F_{2n}^{\Pi} > 0, \quad \frac{F_{1n}^{\Pi}}{F_{2n}^{\Pi}} = \mu, \quad (38)$$

where μ is predetermined coefficient (design parameter).

Then $F_{1n}^{\Pi} = \mu F_{2n}^{\Pi}$.

Where $\mu F_{2n}^{\Pi} + F_{2n}^{\Pi} = N_n$,

That is $F_{2n}^{\Pi} = \frac{1}{1+\mu} N_n, \quad F_{1n}^{\Pi} = \frac{\mu}{1+\mu} N_n$.

In particular, it is assumed that $\mu = 1$ for symmetrical structural scheme. Consequently

$$F_{2n}^{\Pi} = \frac{1}{2} N_n, \quad F_{1n}^{\Pi} = \frac{1}{2} N_n. \quad (39)$$

Summary. Deterministic mathematical model of wheel vehicle kinetics in terms of different modes of spatial motion in the context of curved route has been proposed. The model is based upon nonlinear Euler-Lagrange equations. In the category of spiral-screw lines deterministic mathematical model of wheel vehicle kinematics has been proposed in the form of hodograph in the context of uniform motion, accelerated motion, and decelerated motion within following route sections: straight and horizontal; in terms of vertical grade; in terms of turn in horizontal plane. Analytical approach to determine contact drive-control forces of wheel vehicle for structural schemes having one and two support points involving of a driving-driven wheel characteristic (four-

wheel drive scheme, front-wheel drive scheme, and rear-wheel drive scheme) has been proposed on the basis of kinetostatics equations.

References

- [1] Hachaturov, A.A., Afanasiev, V.L., Vasiliev, V.S. Dynamics of “road-tire-vehicle-driver” system (in Russian). – M.: “Mashinostroenie”, 1976. – 535 P.
- [2] Martynyuk, A.A., Lobas, L.G., Nikitina, N.V. Dynamics and sustainability of transport vehicle wheelsetmovement (in Russian). – Kiev: Tekhnika, 1981. – 223 P.
- [3] Kravets, V.V., Kravets, T.V. Evaluation of the Centrifugal, Coriolis and Gyroscopic Forces on a Railroad Vehicle Moving at High Speed. *Int. Appl. Mech.* 2008. 44, No.1. P. 101-109.
- [4] Igdalov, I.M., Kuchma, L.D., Poliakov, N.V., Sheptun, Yu.D. Rocket as a controlled object (in Russian). – Dnipropetrovsk.: ART-press. 2004. – 544 P.
- [5] Kravets, T.V. Control forces and moments determining in the process of asymmetric aircraft along program trajectory of complex spatial configuration. *Technical Mechanics.* 2003. No. 1. P. 60-65.
- [6] Beshta O., Kravets V., Bas K., Kravets T., Tokar L. Control of tandem-type two-wheel vehicle at various notion modes along spatial curved lay of line. *Power Engineering, Control and Information Technologies in Geotechnical Systems*, 2015 Taylor and Francis Group, London, ISBN 978-1-138-02804-3, P. 27-32. DOI: 10.1201/b18475-6
- [7] Gerasiuta, N.F., Novikov, A.V., Beletskaia, M.G. Flight dynamics. Key tasks of dynamic design of rockets (in Russian). – Dnipropetrovsk.: M.K. Yangel State Design Office “Yuzhnoe”. 1998. – 366 P.
- [8] Kravets V.V., Bass K.M., Kravets T.V., Tokar L.A. Dynamic Design of Ground Transport With the Help of Computation Experiment. *Mechanics, Materials Science and Engineering*, October 2015 – ISSN 2412-5954, MMSE Journal. Open Access www.mmse.xyz. DOI: 10.13140/RG.2.1.2466.6643
- [9] Kravets, V., Kravets, T., Bas, K., Tokar, L. Mathematical model of a path and hodograph of surface transport // *Transport problems*. – 2014. – Pp. 830-841.
- [10] Kravets, V.V., Kravets, T.V., Kharchenko, A.V. Using quaternion matrices to describe the kinematics and nonlinear dynamics of an asymmetric rigid body // *Int. Appl. Mech.* – 2009. – 44. #2. – Pp. 223-232. DOI 10.1007/s10778-009-0171-1
- [11] Lobas, L.G., Lyudm G. Theoretical mechanics (in Russian). Kiev: DETUT, 2009. 407 P.
- [12] Kravets T.V. On the use of quaternion matrices in the analytical and computational solid mechanics. *Technical Mechanics.* 2013. Issue 3: 91-102 P.

An Instrumented Macro-Indentation Method for Determining the Mechanical Properties of Coconut Shell (Coco Nucifera of Cameroon)

E. Njeugna^{1,2}, M.B.K. Ganou^{1,3,a}, D. Ndapeu^{4,5}, J.N.T. Foba^{6,7}, N.R.T. Sikame^{4,5}, P.W.M. Huisken^{1,8}

1 – Laboratory of Mechanics and Production (LMP)-UFD, University of Douala-Cameroon

2 – Professor, Senior researcher, Head of LAMMA, Laboratory of Mechanics and Appropriate Materials (LAMMA)-ENSET, University of Douala-Cameroon

3 – Master's Degree Student, researcher in LAMMA, Laboratory of Mechanics and Appropriate Materials (LAMMA)-ENSET, University of Douala-Cameroon

4 – PhD, Senior researcher in LAMMA, Head of LAMMA, Laboratory of Mechanics and Appropriate Materials (LAMMA)-ENSET, University of Douala-Cameroon

5 – Laboratory of Mechanics and Modelling of Physical System (L2MSP)-University of Dschang, Cameroon

6 – Professor, Senior researcher in LAMMA, Laboratory of Mechanics and Appropriate Materials (LAMMA)-ENSET, University of Douala-Cameroon

7 – Laboratory of Chemistry-University of Buea-Cameroon

8 – PhD Student, Senior researcher in LAMMA, Laboratory of Mechanics and Appropriate Materials (LAMMA)-ENSET, University of Douala-Cameroon

a – morinoganou@yahoo.fr



DOI **10.13140/RG.2.1.1447.3846**

Keywords: macro-indentation, coconut shell, hardness, young modulus, creep ratio, abrasives.

ABSTRACT. An instrumented macro-indentation test was used to determine the viscoelastic parameters and hardness of the shell of Coco Nucifera from Cameroon in order to promote their use in the manufacture of abrasives. Samples measuring 10 mm x 10 mm x 3 mm were cut out from the bottom of the fruit, close to the natural indentations (the eye) of an approximately round-shaped fruit. The indentation load ranged from 50 to 500 N with an increment of 50 N. A comparator with digital display and a camera attached to the machine measured the total penetration and rate of penetration. The Oliver and Pharr indentation model and Hertz contact theory were used to determine the Young's modulus, hardness and creep ratio of coconut shells. Young's modulus determined in the polar zone was 3.52×10^3 MPa and 1.45×10^3 MPa in the equatorial zone. The hardness was 1.16×10^2 MPa in the polar zone and 0.7×10^2 MPa in the equatorial zone. The creep ratio was 16 in the polar region and 8 in the equatorial zone. Validation of the procedure and results will be done with indentation tests on a kind of wood: Azobé (Lophira alata).

Introduction. Coconut Shell of Coco Nucifera (CSCN) is a product of the coconut tree (Coco nucifera) which is exploited for the valuable flesh (copra) enclosed in the hard shell. Important quantities of CSCN are generated during the production of copra [1]. The CSCN alone occupies about 25% by weight of the nuts and with about 54 million tons of coconuts produced annually worldwide [2], an estimated 13.5 million tonnes of CSCNs is generated. A small part of these shells is used in the production of activated carbon. [3]. However, most of CSCN is not used, presenting a challenge for solid waste management [4]. Usually the CSCN is simply discarded in nature with negative environmental impact (occupying land that could otherwise be used for agriculture, breeding sites for mosquitos). In recent years, the instrumented indentation test has been used as an alternative method for determining mechanical properties of materials [5]. The hard nature and the abrasiveness of the shell makes it a potential food processing material. A good knowledge of the properties of this hull allows it to be used as a green alternative in agro-processing tools to plump goods such as beans, maize and groundnuts, otherwise like abrasives for woods. Preliminary

characterisation of this shell by Njeugna et al. [5] was bend tests and beam theory to determine Young's modulus. The rectangular test pieces used in their study showed an unavoidable curvature due to shape of the coconut shell. Young's modulus calculated by this method is expected to be strongly influenced by the curved shape of the test pieces. We propose in this work to use an instrumented macro-indentation testing as Oliver and Pharr method to determine some mechanical properties of the shell. The validation of the procedure and results will be done with indentation tests on a kind of wood: Azobé (*Lophira alata*) part of the harder and dense wood species.

Materials and methods.

Materials. Coconut shell used in this work came from the Littoral region of Cameroon. To prepare prismatic test pieces, we chose mature round hulls because of ease of cutting out specimens 10 mm x 10 mm x 3 mm by grinding of the faces. Sampling was done in two zones: Equatorial and Polar zones as shown in Fig. 1. In a test rig, we performed 5 indentation tests after conditioning the shells at ambient temperature in the laboratory for 2 months.

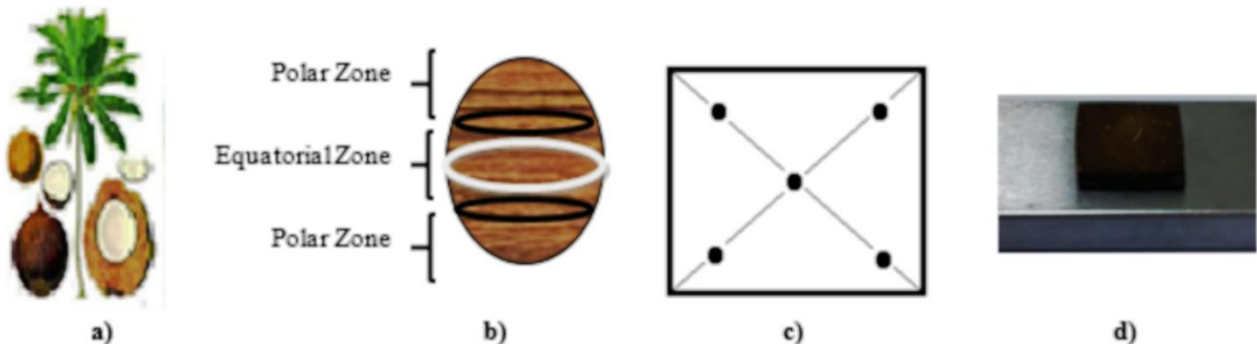
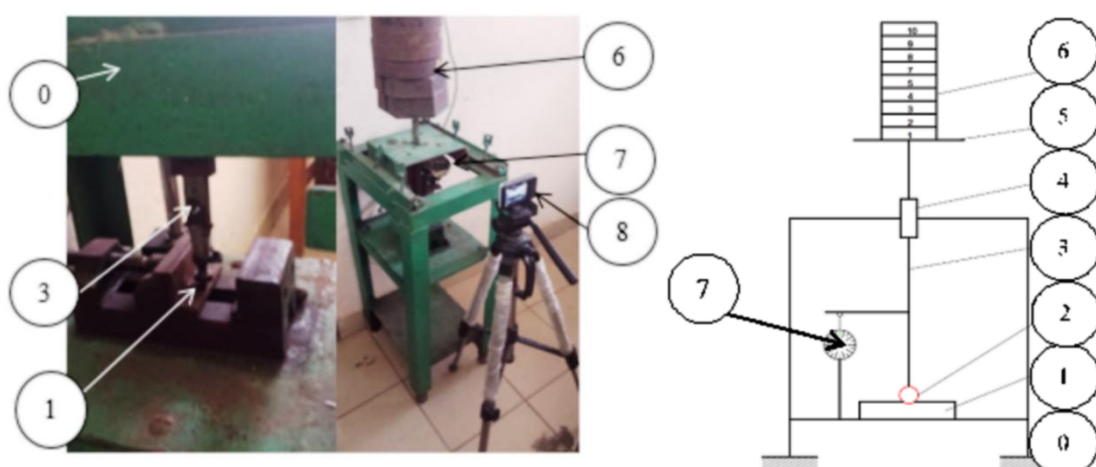


Fig. 1. Localisation of indentation points: a) Coconut tree b) and Sampling from a shell c) indication of indentation d) plates samples indented.

A Dial gauge to the thousandth and a Facom brand digital display was used to measure displacement. A Canon camera provided video monitoring of comparator variations throughout the duration of the test. The indentation was done with an adapted macro-indentation device designed and constructed in our laboratory [11] (Figs. 2, 3).



0 – Built, 1 – Specimen of CSCN, 2 – Indenter Ball, 3 – indenter rod, 4 – Slide the rod, 5 – Loading platform, 6 – load, 7 – Dial gauge to the thousandth, 8 – Canon camera

Fig. 2. Image Test device.

Fig. 3. Device block diagram.

Methods. The instrumented macro-indentation test takes place in three phases: a charging phase; a hold phase and an unloading phase [10]. Loading is achieved by the masses placed on the tray 5. The loads applied ranged from 50N to 500N with an increment of 50N. For Each load there are equivalent penetration of the steel ball in the sample was measured. The comparator measured and displayed the value of penetration. When the maximum load of 500N was reached, a hold time of 30 minutes was maintained and the flow of the CSCN was observed as the continuous penetration of the indentation ball in the shell sample. The camera recorded the display of comparator over the entire hold time. During the unloading phase, we reduced the load from 500N to 50N in stepwise reduction of 50N. The elastic recovery of the material was displayed by the comparator. The pairs of load vs penetration depth during loading and unloading were plotted to obtain the characteristic curve of the CSCN material covering the three phases as shown in figure 4. 50 samples were tested.

To exploit these curves, we adopted the method of Oliver and Pharr [6, 18, 21], this method describes the upper limit of the discharge curve by the law in Eq. (1):

$$P = P_{max} \left(\frac{h-h_f}{h_{max}-h_f} \right)^m, \quad (1)$$

where P – is the force;

P_{max} – is the maximum applied force;

h – is the depth of indentation;

h_f – is the indentation depth unloading;

h_{max} – is the maximum indentation depth at F_{max} ;

m – is a function of the geometry of the indenter [12-15]. For a spherical indenter $m = 1$.

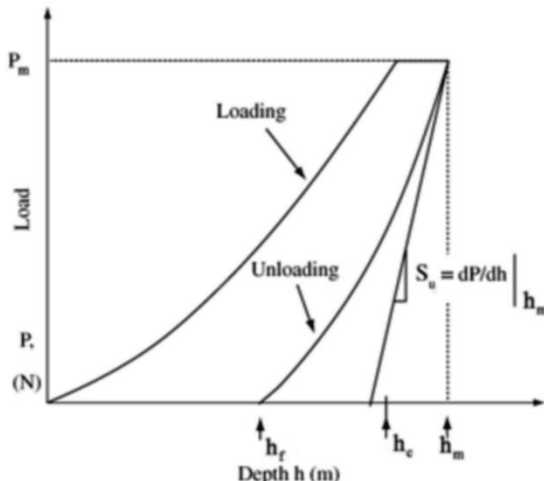


Fig. 4. Load vs depth plot.

Modulus of elasticity (Young's modulus). The determination of Young's modulus is based on the assumption that during the unloading curve the removal of the indenter is accompanied by a spring back due to the elasticity of the material [7]. Thus the slope of the unloading curve provides a measure Young's modulus. The method is based on the recovery theory of Hertz and Bulychev,

later developed by Snedon [8, 20]. It provides for the modelling of the unloading slope with a function that relates the contact area to the reduced Young's modulus according to the Eq. (2):

$$S = \left(\frac{dP}{dh} \right)_{h=h_{max}} = \frac{2}{\sqrt{\pi}} E_r \sqrt{A_c}, \quad (2)$$

Where S – is the stiffness of the contact between the intention and the material when unloading, measured at the maximum penetration (h_{max}) recorded;

A_c – is the projected contact area given by the Eq. (3):

$$A_c = \pi \cdot a^2 = 2 \cdot \pi \cdot R \cdot h_c - \pi \cdot h_c^2 \quad (3)$$

where a – projected contact radius;

R – radius of the indenter;

h_c – penetration depth given by the Eq. (4):

$$h_c = h_{max} - \varepsilon \frac{P_{max}}{S}, \quad (4)$$

where ε – a constant related to the geometry of the indenter, which is 0.75 for a spherical indenter [12, 19];

E_r – Reduced Young's modulus from the theory of elastic contact of Hertz [8], given by Eq. (5).

$$\frac{1}{E_r} = \frac{(1 - \nu_m^2)}{E_m} + \frac{(1 - \nu_i^2)}{E_i}. \quad (5)$$

In this equation the indices i and m refer to the characteristics of the indenter and the material respectively.

Since the indenter is made of stainless steel, we consider that: $\nu_i = 0.3$ and $E_i = 210.000$ MPa.

Thus, Young's modulus of the CSCN is given by Eq. (6):

$$E_m = (1 - \nu_m^2) \cdot \left[\frac{2}{\sqrt{\pi}} \frac{1}{S} \sqrt{A_c} - \frac{(1 - \nu_i^2)}{E_i} \right]^{-1} \quad (6)$$

Hardness. Once the method for the calculation of the contact area is available, it is possible to calculate hardness. [9, 15, 17]. This is done using the formula from Eq. (7) and the contact area A_c is obtained by Eq. (3):

$$H = \frac{P}{A_c}. \quad (7)$$

Creep ratio. C_{IT} denoted indentation creep ratio is defined by the relative change in depth of corresponding penetration, according to Eq. (8):

$$C_{IT} = \frac{h_2 - h_1}{h_1} \times 100 \% . \quad (8)$$

Results and discussion. Figure 5 is an example of the instrumented macro-indentation curve of CSCNs.

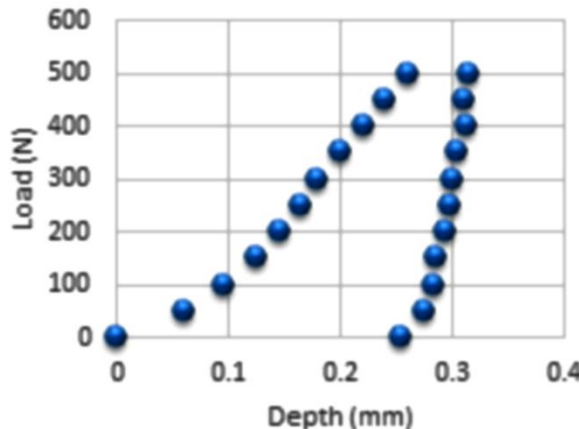


Fig. 5. Sample of macro-indentation curve CSCNs.

The Oliver and Pharr method and Hertz's theory were applied to curves obtained by testing samples from polar and equatorial zones. The values of Young's modulus, hardness and creep ratio obtained are presented in Table 1.

Table 1. Features of the CSCN by macro-instrumented indentation

	Young Modulus E	Hardness H	Creep ratio
Equatorial zone	$1.45 (\pm 0.179) \cdot 10^3$ MPa	$0.70 (\pm 0.12) \cdot 10^2$ MPa	8.31 ± 1.35
Polar zone	$3.52 (\pm 0.562) \cdot 10^3$ MPa	$1.16 (\pm 0.10) \cdot 10^2$ MPa	16.2 ± 3.51

Looking at the results shown in Table I, we find that the Young's modulus, hardness and creep coefficient are relatively higher in the polar zone than in the equatorial zone. A possible explanation could be differences in thickness from the equatorial to polar zones. It was observed that the nut is thicker in the polar zone compared to the equator.

These results are significantly different from results obtained by Njeugna et al. [5]. The difference could be attributed to difference in test method. The values of Young's modulus obtained in this study are closer to values for polymers and gypsum (Table 2), an indication that the instrumented macro-indentation test may be more suitable for characterising the mechanical properties of this material.

Applying the same indentation tests (Fig. 6) on wood named Azobé with a moisture content of 12% in the same conditions and protocols, we got Young modulus $E_{az} = 12.304$ GPa. This value falls

within the values gotten from literature review [21]. We found an indentation hardness $H(az) = 41.5398$ MPa and with this hardness $H(az)$, It is clear the CSCNs can be used for sanding wood.

Table 2. Comparison of specific rigidities

Materials	Young modulus in GPa	References
Polyethylene	0.20	[5]
Polycarbonate	2.40	[5]
Epoxide	2.40	[5]
Polyester	5.00	[5]
EDP (Gypsum A)	9.90	[16]
EDP (Gypsum B)	2.58	[16]
Azobé	12.30	[21]

		Instrumented indentation test	3 points flexural test	[5]
		3.52	19,80	
Coconuts shells	Polar zone	1.45	12,70	
	Equatorial zone			

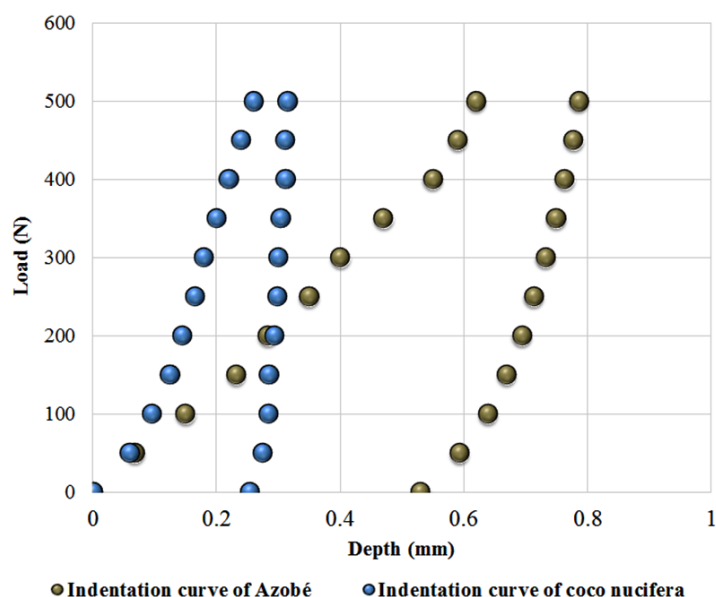


Fig. 6. Comparison between the indentation of CSCNs and Azobé.

Summary. Our work focused on determining the mechanical properties of coconut shell from Coco nucifera by an instrumented macro-indentation test. A series of tests were conducted on prismatic samples extracted from 10 mm x 10 mm x 3 mm elongated CSCNs. Sampling was done in two areas: the equatorial zone and polar zone and 50 samples were tested. The method of Oliver and Pharr was applied to analyse the behaviour of the material at the upper limit of loading and the Hertz contact theory was used to calculate fundamental mechanical properties of CSCN. Thus, the

Young's modulus, hardness and the creep ratio were determined. The Young's modulus determined is of the order of $3.52 \times 10^3 \pm 562.81$ MPa in the polar zone and $1.45 \times 10^3 \pm 179.29$ MPa in the equatorial zone. The hardness is $1.16 \times 10^2 \pm 10.69$ MPa in the polar zone and $0.70 \times 10^2 \pm 12.01$ MPa in the equatorial zone. The creep ratio is 16.2 ± 3.51 in the polar region and 8.31 ± 1.35 in the equatorial zone. Currently, we are using these shells after grinding in the manufacturing of abrasives and composites. Therefore, it is imperative to know its mechanical properties for more valorisation.

References

- [1] J.A. Banzon, J.R. Velasco: Coconut: production and utilization, Philippine Coconut Res. and Dev., pp. 417, 1982.
- [2] B. Warner, Q. Derek, C. Longmore: A review of the future prospects for the world coconut industry and past research in coconut, production and product, Australian Centre for International Agricultural Research, 2007.
- [3] U. Tomas, J.R. Ganiron: Sustainable Management of Waste Coconut Shells as Aggregates in Concrete Mixture, Journal of Engineering Science and Technology Review 6 (5), 7-14, 2013.
- [4] N. Lesage, M. Sperandio, C. Cabassud: Study of a hybrid process: Adsorption on activated carbon/membrane bioreactor for the treatment of an industrial wastewater, Chemical Engineering and Processing: Process Intensification 10th French Congress on Chemical Engineering, Volume 47, pp. 303–307, 2005, doi:10.1016/j.cep.2007.01.021
- [5] E. Njeugna, D. Ndapeu, S. Bistac, J.Y. Drean N.J. Foba, M. Fogue: Contribution to the Characterisation of the Coconut Shells (Coco Nucifera) of Cameroon, International Journal of Mechanics Structural, Volume 4, Number 1, pp.1-22, 2013.
- [6] W.C. Olivier, G.M. Pharr: An improved technique for determining hardness and elastic-modulus using load and displacement sensing indentation experiments, J. Mater. Res. 7, 1564–1583, 1992.
- [7] D. Tabor: Review of Physics in Technology, 1970.
- [8] H. Hertz: Über die Berührung fester elastischer Körper, Journal für die reine und angewandte Mathematik 92, 156-171, 1881.
- [9] Standard Test for Microhardness of material, ASTM Standard Method E 384, Annual Book of Standards 3.01, American Society for Testing and Materials, p469, 1989.
- [10] C. Gauthier, A.L. Durier, C. Fond, R. Schirrer: Scratching of a coated polymer and mechanical analysis of a scratch resistance solution, Tribology International, Volume 39, pp 88–98, 2006, doi:10.1016/j.triboint.2005.04.014
- [11] D. Ndapeu : Caractérisation physico-chimique et mécanique des coques de noix de coco nucifera du Cameroun, en vue de leur utilisation dans l'élaboration des matériaux abrasifs, Thèse de doctorat Ph/D de l'Université de Dschang, 2015.
- [12] D.J.A. Mendoza : Détermination des propriétés mécaniques et des lois de comportement par indentation instrumentée, Thèse de Doctorat de l'Université de Lille 1, 2009.
- [13] J. Breuils, L. Jacomine, H. Pelletier, P. Peyre : Identification par méthode inverse des propriétés mécaniques de surfaces grenaillées par chocs laser, 19^{ème} Congrès Français de Mécanique, 2009.
- [14] T. Chatel : Fluage et recouvrance d'empreintes et de sillons sur surface de polymère, Thèse de Doctorat de l'Université de Strasbourg, 2010.
- [15] P.E. Mazeran, M. Beyaoui, M. Bigerelle, M. Guigon: Determination of mechanical properties by nanoindentation in case of viscous materials, International Journal of Materials Research, 103, 2012, doi: 10.3139/146.110687

[16] C. Philippe : Détermination des propriétés mécaniques de céramiques poreuses par essais de microindentation instrumentée sphérique, Mémoire de Thèse de l’Institut national des sciences appliquées de Lyon, 2013.

[17] T. Chatel, V. LeHouérou, H. Pelletier, C. Gauthier: Numerical analysis of the creep of the contact and recovery of the imprint on amorphous polymer surfaces. *Mechanics of Time-Dependent Materials*, 17(4), 581–595, 2013, doi: 10.1007/s11043-012-9205-x

[18] G.M. Pharr, W.C. Oliver, F.R. Brotzen: On the generality of the relationship among contact stiffness, contact area, and elastic modulus during indentation, *Journal of Materials Research* 7, pp. 613-619, 1992.

[19] W.C. Oliver, G.M. Pharr: Measurement of hardness and elastic modulus by instrumented indentation: Advances in understanding and refinements to methodology, *Journal of Materials Research*, Volume 19 No. 1, 2004.

[20] E. Barthel, D. Chicot, J.P. Guin, E. LeBourhis, G. Mauvoisin : L’indentation : un outil de caractérisation multi-échelle des matériaux, aSF2M Info, 2014.

[21] J. Menčík: Determination of mechanical properties by instrumented indentation. *Meccanica*, 42(1), 19-29, 2007.

[22] J.W.G. Van de Kuilen, H.J. Blass: Mechanical properties of azobé (*Lophira alata*). *Holz als Roh-und Werkstoff*, 63(1), 1-10, 2005.

Macroscopic Geometrical Modelling of Oil Palm Mesocarp Fibers of Three Varieties of Palm Nut

E. Njeugna^{1, 2}, P. W. M. Huisken^{1, 2, a}, D. Ndapeu², N. R. T. Sikame², J. Y. Dréan³

1 – Laboratory of Mechanics and Production (LMP), Douala, Cameroon;

2 – Laboratory of Mechanics and Appropriate Materials (LAMMA), Douala, Cameroon;

3 – Laboratory of Physics and Mechanics Textile (LPMT), Mulhouse, France;

a – huiskenwilliam@gmail.com



DOI [10.13140/RG.2.1.2275.9921](https://doi.org/10.13140/RG.2.1.2275.9921)

Keywords: Oil Palm Mesocarp fibers, modeling, geometry, cross section, profile.

ABSTRACT. This work is part of a process of characterization of plant fibers. The macroscopic geometric parameter of Oil Palm Mesocarp Fibers (length, diameter) was measured. A mathematical model of the evolution of the cross-section is provided in order to facilitate a digital reconstruction of the geometry of these fibers. In this context, we manually isolated with great care many fibers of several oil palm varieties *Dura*, *Tenera* and *Pissifera* distinguishing for the last two varieties two extraction position. Five different partitions of fibers have been studied. The lengths of these fibers were measured and the transverse dimensions of each of the fibers were taken at five equally spaced discrete and different sections. For each section, we made two measurements at 90 ° in the front plane and the profile view. The mathematical model of the evolution of the profile were determined in each plan and the evolution of the cross section model was described for each of the five partitions on the basic assumption that this cross section is elliptical according to SEM images and flattening rate of the cross section we calculated.

Introduction. The use of vegetable fibers as reinforcement in composite materials to replace synthetic fibers is growing rapidly. Many researches are interested in it in order to optimize their physical and mechanical properties [1-5]. Many fibers (sisal, coir, raffia, jute ...) are studied in the literature [6]. The fibers from palm oil tree (EFBF¹, OPMF², OPTF³) also have a particular interest [2, 3, 5, 7, 8].

It is clear from the various work that knowing the geometry of the fiber (section and length) is indispensable for the analysis of the results of a physicochemical characterization test (water absorption kinetic of fiber) [9], mechanical characterization (determination of Young's modulus of the fiber) [7, 10, 11] and during predictive calculations of composite properties [12, 13] (application of composites homogenization theories). All Authors are unanimous on the versatility of the geometry of the cross section and its non-uniformity along the vegetable fibers. It is shown [14-18] that the mechanical properties of sisal, jute, hemp, bamboo and coconut fiber may be influenced by the dimensions and aspect of their cross-section. Most of the works in the literature consider an approximation of vegetable fibers to a straight beam of constant circular cross section [6, 19] (in this case, the diameter measurement is made on a singular section); on the other hand, consider that the fiber is a straight beam of elliptic section and constant (measuring the major axis and the minor axis of a singular cross section) on which several measurements can be made and the average of these measurements considered as mean cross section of the fiber. Some author [11] propose a

¹ Empty Fruit Bunch Fibers

² Oil Palm Mesocarp Fibers

³ Oil Palm Trunk Fibers

method for assessing the cross section of kenaf fibers by image analysis but this study is limited to a single section by considering it to be constant. Other authors [20] propose a characterization approach considering the variability of the cross section along the hemp fibers and its non-circularity.

These various techniques have some inaccuracies including:

- (i) Some are an average of local measures that do not take into consideration all the variations and features of the fiber profile;
- (ii) Others exclude non circularity of the cross section of plant fibers.

In this context, the physicochemical and mechanical properties such as Young's modulus, tensile stress limits, the kinetics of water absorption and drying kinetics will be determined with some imprecision introducing a measurement uncertainty.

In the particular case of Oil Palm Mesocarp Fiber (OPMF), very few works are devoted to their study. Okafor and Owolarafe et al [12, 21, 22] indicate that there are three main types of palm fruit (*Tenera*, *Pissifera* and *Dura*) depending on the size of the shell and the oil content. They consider as [23-24] that the cross section of OPMF is circular and constant along the fiber.

In this study, we want to make a contribution on the evaluation of the shape of the cross section of fiber from the mesocarp of the three varieties of palm nuts and its evolution along the mean line. We will develop a method for measuring the cross section and detecting the profile of the OPMF. We will determine with precision the real geometry of the profile of OPMF and propose a mathematical model of evolution of the cross section of fiber from the three varieties of palm nuts extracted at different positions.

Materials and Methods.

Materials. Oil Palm Mesocarp Fiber (OPMF). The fibers (OPMF) objects of study are from a palm tree farm in Nkongsamba, a city of Mungo division in Littoral region in Cameroon.

We worked on the three varieties of palm nuts as described in the literature [12, 21, 22] and illustrated in Figure 1: (*Pissifera*, *Tenera* and *Dura*).

- *Dura* (wild variety having a thick shell);
- *Tenera* (hybrid variety having a small shell);
- *Pissifera* (variety without shell).

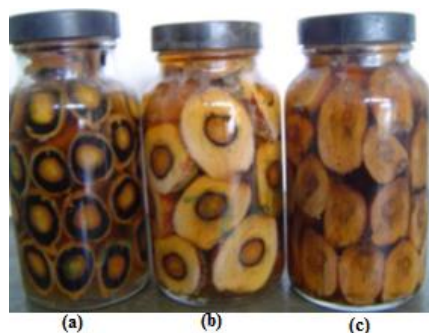


Fig. 1. Different types of palm fruit: (a) *Dura*, (b) *Tenera*, (c) *Pissifera* [22].

These fibers were extracted manually after having been placed dry nut in pure water for 20 days. They were later rinsed thoroughly in water heated at 60 ° C. They were then dried in open air and stored in plastic bags. To check the influence of the position of the fiber on the morphology, we had each nut partitioned into two extraction zones for *Tenera* and *Pissifera* varieties: the peripheral

fibers (external position) and those near the shell (internal position) as shown in Figure 2. For the variety *Dura*, the size of the shell did not allow us to distinguish the two areas. So we distinguished 5 different partitions of fibers. We worked with 54 fibers per partition thus a total of 270 fibers.

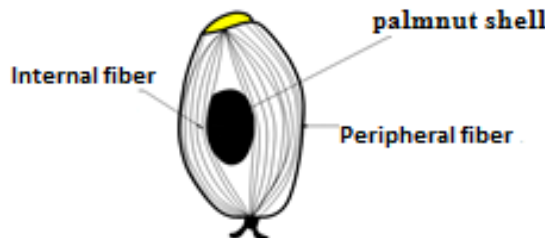


Fig. 2. Schematic illustration of internal and peripheral fibers of palm fruit.

Collecting images and measurement equipment. We used a Celestron LCD Digital Microscope with the lens corresponding to a magnification of 40x to collect images. The measurement of each section was then carried out by using a COOLING Tech USB 8LEDS microscopic camera previously calibrated on its operating software. The lengths of fibers were measured using a digital slide caliper having 0.01mm of accuracy. We processed the data collected using Matlab R2009b.

Methods.

Data collection techniques. We measured the transverse dimensions of the fibers on the five sections of the face (a_1, a_2, a_3, a_4 and a_5) and profile (b_1, b_2, b_3, b_4 and b_5) along the fiber as illustrated in Figure 3 below. We were inspired by the technique stated by Ilczyszyn et al. [20]. Section 1 is positioned at a distance of 3 to 5 mm from the fiber tip and section 5 is defined by the beginning of dislocation of the fiber.

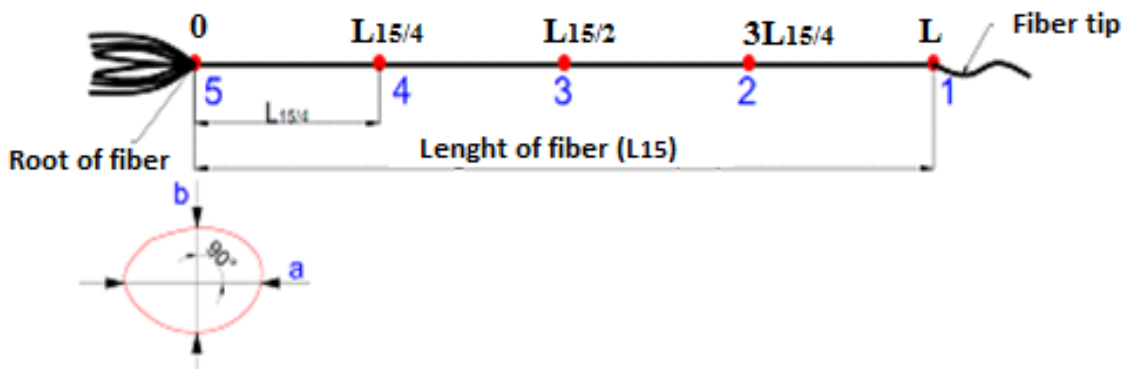


Fig. 3. Illustration of the measuring points of transverse dimensions.

The measurement process is performed in several steps. The first step is to immobilize the fibers and marking measuring points. Six fibers are positioned on the front plan, strained and then bonded by adhesive tape on wooden plates of rectangular shape, dimension 800x300 mm covered by graph paper. On each fiber we placed five equidistant points on the working length of the fiber.

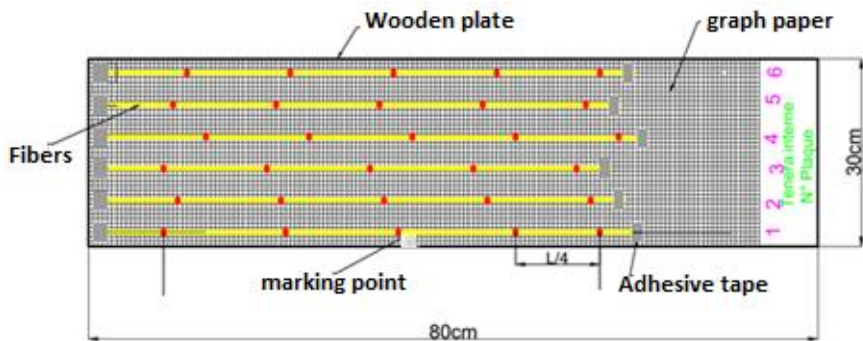


Fig. 4. Schematic illustration of the fixation of fibers.

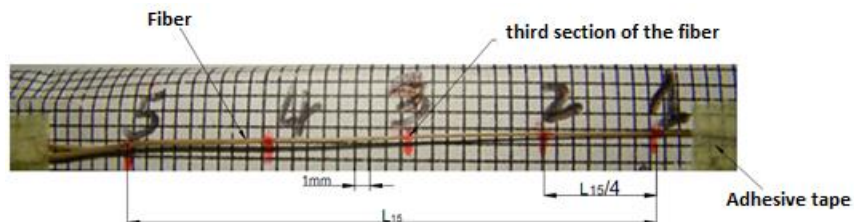


Fig. 5. Photo of a bonded fiber divided into five sections.

The second step consists of images taken from the vicinity of each section labeled with the LCD Digital Microscope Celestron. A light source is used to illuminate the fibers to have a clear image on the microscope screen. A magnification of 40x is used to film the sections of fibers.

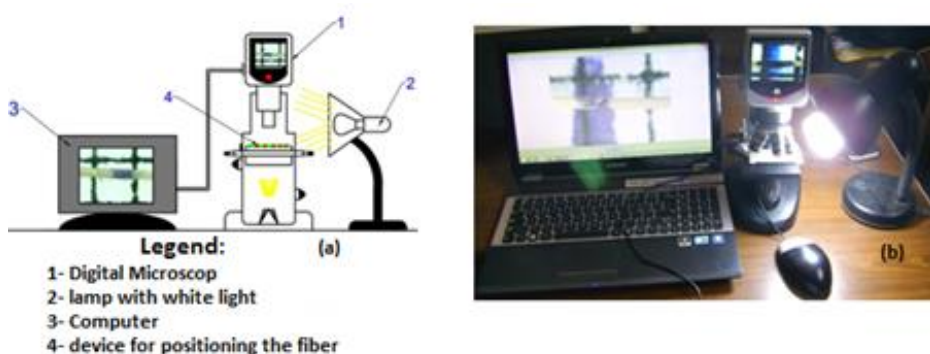


Fig. 6. Diagram showing the principle (a) and image editing and filming equipment for the fibers (b).

After all marked sections are filmed, the images are stored in Microscope memory and then transferred and stored in a computer. The measurements of each section are made from the Cooling Tech driven software. At this stage we obtain the values of a_1, a_2, a_3, a_4 and a_5 with 0.001mm accuracy.

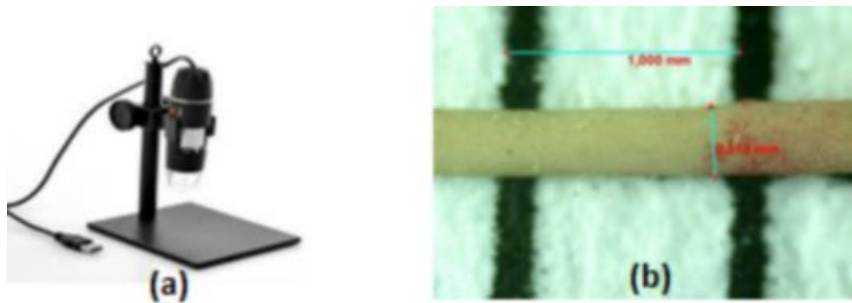


Fig. 7. Microscopic camera Cooling USB 8LEDS (a) and illustration of the measured image.

The fibers are then carefully peeled off and turned over 90° to the position on the profile plane. The previous steps are repeated to permit measurement of the second transverse dimension on the same sections. The values of b_1 , b_2 , b_3 , b_4 and b_5 with 0.001mm accuracy were thus obtained. At the end, the length of each fiber is measured by a digital caliper. This is the distance between the two extreme points (point 1 and 5).

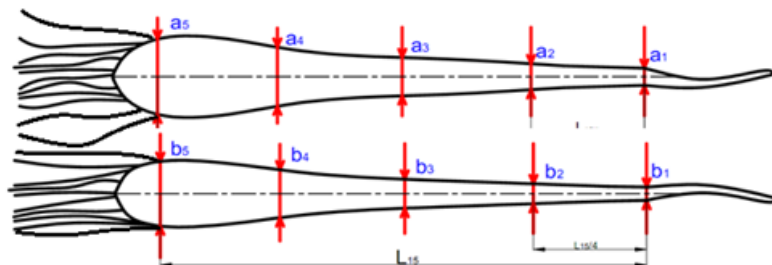


Fig. 8. Illustration of measurement according to the front plan (a_i) and the profile plane (b_i).

Theoretical considerations. We have been working under the assumption that the cross section is elliptical (it admits two planes of symmetry: the front plan and the profile plane) with regard to the observations made in the scanning electron microscope, an example is shown in Figure 9. The shape and proportions of the lumen have been neglected in this work. This hypothesis has also been stated by Ilczyszyn et al. [20] in the context of the characterization of hemp fiber.



Fig. 9. SEM image of the cross section of OPMF (LPMT Mulhouse).

Under these conditions, the calculation of the cross section is done by equation (1) [21].

$$S = \frac{\pi}{4} a \cdot b \quad (1)$$

With S the fiber section in mm^2 , a and b transverse dimensions in mm (major and minor axis of the ellipse).

Considering that the cross section is variable along the fiber, we set that:

$$s(x) = \frac{\pi}{4} a(x) \cdot b(x) \quad (2)$$

$$\text{With } a(x) = f(x) \text{ and } b(x) = g(x) \quad (3)$$

We are thus supposed to search for the respective functions $f(x)$ and $g(x)$ that best fit the discrete experimental data a_i and b_i respectively.

Moreover we will focus on the statistical distribution of a_i and b_i to get an idea about the law of distribution of these experimental data.

For this purpose we will focus on the determination of the mean μ , standard deviation σ , and shape parameters of the distribution [25] that are the skewness (asymmetry coefficient) γ_1 and the kurtosis (flattening coefficient) γ_2 of a_i and b_i .

The standard deviation σ is calculated using equation (4).

$$\sigma^2 = \frac{1}{N} \sum (X_i - \bar{X})^2 \quad (4)$$

The skewness coefficient γ_1 is calculated by relation (5).

$$\gamma_1 = \mathbb{E} \left[\left(\frac{X - \mu}{\sigma} \right)^3 \right] \quad (5)$$

The flattening γ_2 also called normalized Kurtosis coefficient is calculated by equation (6).

$$\gamma_2 = \mathbb{E} \left[\left(\frac{X - \mu}{\sigma} \right)^4 \right] - 3 \quad (6)$$

For this, recall that the probability density function of the normal distribution or Gauss-Laplace law is given by equation (7).

$$q(x) = \frac{1}{\sigma \sqrt{2\pi}} e^{-\frac{1}{2} \left[\frac{(X - \mu)^2}{\sigma^2} \right]} \quad (7)$$

where μ – is the mean and σ^2 the variance.

Results and Discussion.

Statistical Distribution of Geometric Parameters of OPMF.

Determination of statistical parameters. Considering the number of surveys, we conducted a statistical study to investigate the distribution of measurements around the mean values. For each sample we determined statistical distribution parameters that are the mean value and standard deviation. To find out whether the trend is centered or decentered (left or right of the mean), we calculated the skewness. We also calculated the kurtosis to deduce the spreading of data to conclude whether the distribution [25] is normal (mesokurtic) or not (leptokurtic or platikurtic). Table 1 summarizes these parameters for each variety of fibers.

Table 1. Summary table of statistical distribution parameters

	Statistical Parameters	Front Plan					profile Plan				
		a ₁	a ₂	a ₃	a ₄	a ₅	b ₁	b ₂	b ₃	b ₄	b ₅
OPMF-Pe ⁷	μ	0,154	0,158	0,173	0,198	0,232	0,142	0,151	0,164	0,186	0,218
	σ	0,035	0,028	0,039	0,047	0,052	0,046	0,038	0,032	0,037	0,041
	γ ₁	1,167	0,589	0,696	0,237	-0,063	0,797	1,407	0,449	0,115	-0,521
	γ ₂	1,559	0,466	-0,074	-0,875	-1,036	0,080	1,596	0,056	-0,664	-0,508
OPMF-Pi ⁸	μ	0,171	0,183	0,206	0,237	0,288	0,170	0,177	0,197	0,220	0,270
	σ	0,031	0,031	0,033	0,038	0,044	0,035	0,029	0,031	0,031	0,035
	γ ₁	0,100	0,588	0,362	0,022	-0,187	0,087	0,509	0,421	0,105	-0,271
	γ ₂	-0,776	0,148	-0,544	-0,391	-0,708	-0,979	0,132	0,713	-0,148	0,266
OPMF-Te ⁹	μ	0,193	0,201	0,221	0,247	0,297	0,186	0,195	0,209	0,232	0,274
	σ	0,030	0,035	0,037	0,039	0,051	0,035	0,034	0,035	0,038	0,043
	γ ₁	0,248	0,300	0,279	0,150	0,235	-0,045	-0,245	0,094	0,291	0,599
	γ ₂	0,126	-0,664	-0,810	-0,501	-0,338	-0,565	-0,614	-0,418	0,016	2,297
OPMF-Ti ¹⁰	μ	0,231	0,245	0,263	0,296	0,343	0,216	0,230	0,251	0,276	0,314
	σ	0,043	0,045	0,048	0,059	0,054	0,045	0,042	0,050	0,060	0,057
	γ ₁	0,044	0,460	0,926	0,590	0,331	-0,275	0,430	0,804	0,348	0,122
	γ ₂	-0,766	0,164	1,388	-0,126	-0,300	-0,960	0,323	0,497	-0,478	-0,510
OPMF-Du ¹¹	μ	0,208	0,218	0,247	0,275	0,312	0,202	0,215	0,234	0,260	0,306
	σ	0,047	0,049	0,050	0,049	0,051	0,042	0,051	0,054	0,047	0,048
	γ ₁	0,448	0,359	0,542	0,240	0,042	0,289	0,491	0,553	0,291	-0,326
	γ ₂	-0,527	-0,595	-0,122	-0,478	-0,431	-0,350	-0,330	0,092	-0,028	0,118

⁷ OPMF-Pe: Oil Palm Mesocarp Fiber of the Peripheral *Pissifera*

⁸ OPMF-Pi: Oil Palm Mesocarp Fiber of the Internal *Pissifera*

⁹ OPMF-Te: Oil Palm Mesocarp Fiber of the Peripheral *Tenera*

¹⁰ OPMF-Ti: Oil Palm Mesocarp Fiber of the Internal *Tenera*

¹¹ OPMF-Du: Oil Palm Mesocarp Fiber of *Dura*

The mean values and standard deviations in Table 1 show the existing disparity between the measures when going from one fiber to another partition. This demonstrates the interest of modeling distinguishing several different partitions (each partition is unique in its kind).

The asymmetry coefficient values oscillate around zero; we can say that the distribution is centered in all partitions.

Kurtosis also oscillates in almost all cases around zero; under these conditions, it can be said that the distribution of the geometric parameters of OPMF follows a normal distribution. So this distribution is mésokurtic.

Distribution according to the Normal Law or Gauss-Laplace Law. Considering the foregoing conclusions about the nature of the distribution, we have built a density probability curve of Normal distribution for transverse dimensions of each partition of fiber defined by equation (7).

We determined the number of class using equation (8):

$$n = 1 + 3.3 \log N \quad (8)$$

where n – is the number of classes;

N – the number of samples.

Having worked with 54 fibers per partition, equation (8) allows us to get 7 classes for each partition.

For each partition, we plotted the Gaussian curve using the equation (7). Figure 10 is an example of a Gaussian curve to the transverse dimension of the internal a_3 *Pissifera* variety. The shape of this curve is generalized for other partitions.

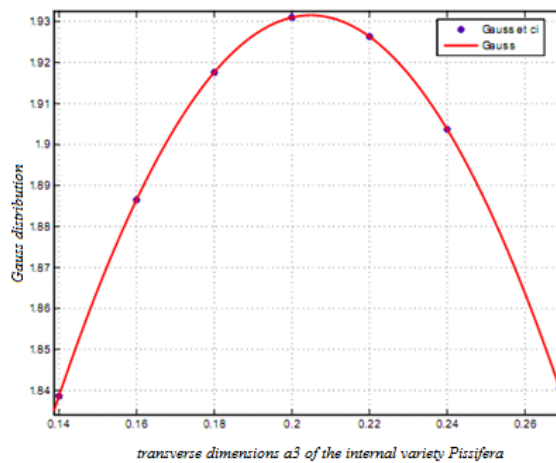


Fig. 10. Gauss distribution curve of transverse dimensions a_3 (section 3) of the internal variety *Pissifera*.

Distribution parameters of front plan. Here we study the evolution of the transverse dimensions on the front plan. The distribution of Figure 11 shows how these data are changing along the fiber in each extraction zone.

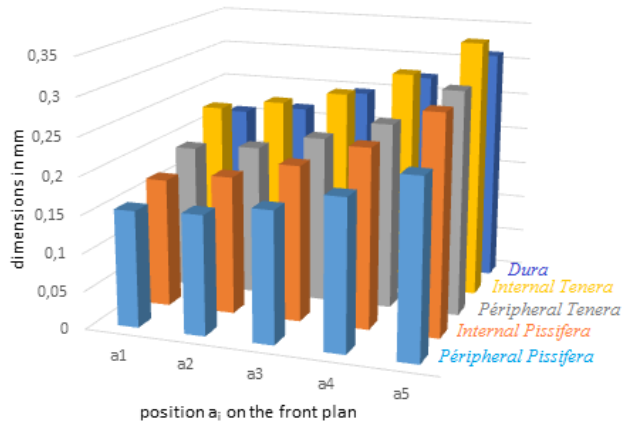


Fig. 11. Distribution of dimensions of cross-sections of OPMF in front plan.

From the distribution of figure 11, it appears that the external fibers have smaller transverse dimensions than the internal fibers whatever the variety. This distribution on the front plan shows that the variety *Dura* is intermediate between *Pissifera* variety that has the lowest transverse dimensions and *Tenera* variety that has the largest dimensions. It is also noted that for all varieties, the profile evolves increasingly from position 1 to position 5 (from the tip of the fiber to the root) as one might have imagined by visual inspection.

Distribution parameters of profile plan. We also conducted the study of the evolution of the transverse dimensions of the profile plan. The distribution of Figure 12 shows the distribution of these parameters.

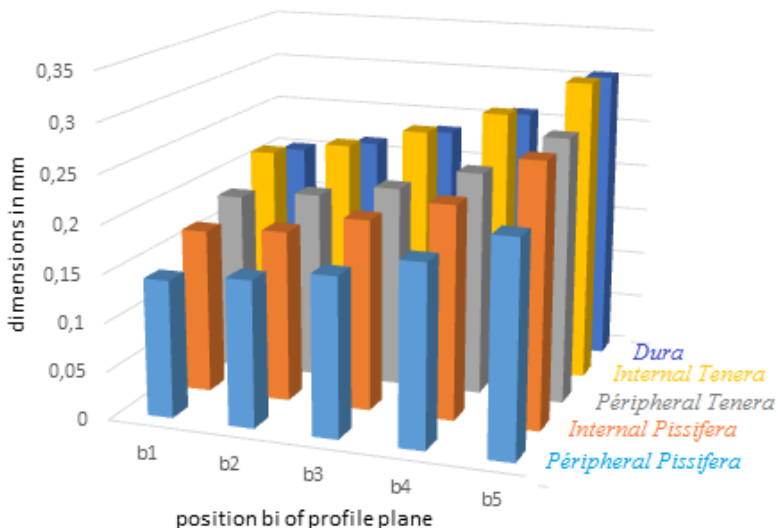


Fig. 12. Distribution of dimensions of cross-sections of OPMF in profile plan.

This distribution reinforces the thesis that the peripheral fibers have lower transverse dimensions than the internal fibers whatever the variety. In the profile plan too, the *Dura* range is intermediate between *Pissifera* variety that has the lowest transverse dimensions and *Tenera* variety that has the largest dimensions. Just as on the front plan, profile dimensions here are evolving increasingly from the head of the fiber (section 1) to the base (section 5).

Aspect Ratio (Specific length) of the fibers. The specific length is an important parameter in the knowledge of plant fibers. From This parameter it can be concluded if the fiber is short, long or belongs to the family of particles. It describes the ratio of the length to the diameter by equation (9).

$$\text{Specific length} = l = \frac{L}{d} \quad (9)$$

where L – the length of the fiber in mm;

d – is the diameter of the fiber in mm.

Given the fact that the OPMF section varies along the fiber and is non-circular and taking into consideration that:

$$a_i < a_{i+1}; b_i < b_{i+1} \text{ and } a_i > b_i \text{ with } i \in [1; 5],$$

We can write the equations (10) and (11) below:

$$l_{min} = \frac{L}{b_5} \quad (10)$$

$$l_{max} = \frac{L}{a_1} \quad (11)$$

We summarized in Table 2 the average values of aspect ratio for each partition of fibers.

Table 2. Table of average specific lengths (aspect ratio)

Type of Fiber	a_{1m} (mm)	b_{5m} (mm)	L_m (mm)	l_{min}	l_{max}
OPMF-Pe	0,147	0,218	29,12	133,578	198,095
OPMF-Pi	0,171	0,302	29,23	96,788	170,936
OPMF-Te	0,194	0,242	24,65	101,859	127,062
OPMF-Ti	0,277	0,341	26,99	79,149	97,437
OPMF-Du	0,212	0,306	18,11	59,183	85,424

According to the classification proposed in the literature, it is concluded in relation to the values in the table 2 that OPMF belong to the class of short fibers ($50 < L/D < 1000$). We also note that whatever the variety, internal fibers are far shorter than peripheral fibers. *Tenera* fibers are intermediate between *Dura* (the shortest) and *Pissifera* (the longer).

Flattening rate of the fibers. The flattening rate also called circularity rate is an important parameter in describing the shape of the cross section of a fiber or particle. It is the relationship between two diameters measured along the same section as described by equation (12).

$$\tau = \frac{d}{D} \quad (12)$$

With τ with the flattening rate, d and D are respectively the small and large diameter value of the same cross section in mm.

As part of our work, we calculate the average flattening rate of each cross section by equation (13).

$$\tau_{im} = \frac{b_{im}}{a_{im}} \quad (13)$$

With τ_{im} , b_{im} and a_{im} respectively the average values of the flattening rate, the small diameter and large diameter section number i .

We present in Table 3 the mean values of the flattening rate of five sections on which we performed the measurements for each partition of fibers.

Table 3. Table of flattening rates per section

Nº of section	1	2	3	4	5
τ /section	τ_1	τ_2	τ_3	τ_4	τ_5
OPMF-Pe	0,922	0,955	0,947	0,939	0,939
OPMF-Pi	0,994	0,967	0,956	0,928	0,937
OPMF-Te	0,963	0,970	0,945	0,939	0,922
OPMF-Ti	0,935	0,938	0,954	0,932	0,915
OPMF-Du	0,966	0,982	0,943	0,938	0,936
min value	0,922	0,938	0,943	0,928	0,915
max value	0,994	0,982	0,956	0,939	0,939
Standard Deviation	0,022	0,012	0,004	0,004	0,009

In view of the values obtained, we can say that the OPMF section is not circular ($\tau_i \neq 1 \forall i$). This section, however, may be likened to an ellipse.

Geometric Modeling.

From the experimental data we have collected, we plotted curves materializing the profile of each of the fibers (Figure 13). We have subsequently shown in a graph the overall trend of the average profile of each partition of the fibers on the front plan (a) and the profile plane (b).

We note that OPMF have a wider front plan than the profile plan. Moreover, the two plans seem to evolve in the same manner along the fiber. Generally, the internal fibers have a larger section than those of the periphery.

Given the absence of data on the geometric model of this type of fiber, we performed a test of convergence with several mathematical functions. We got the best correlations (in the field of definition of fiber lengths) for the second-order polynomial model and the exponential model with two elements.

Modeling with a second order polynomial function. Figure 14 below shows the case of modeling with a second order polynomial function to the fibers of the periphery of *Tenera* partition (*Te*) on the front plan (a) and side view (b).

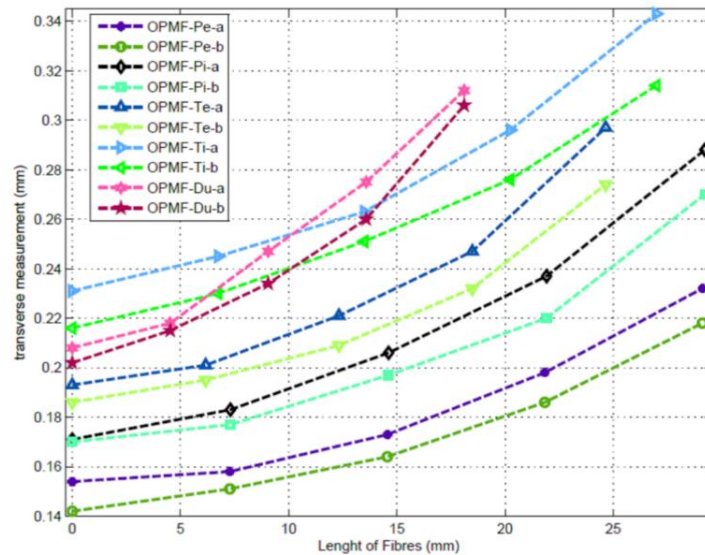


Fig. 13. Geometry of front (a) and side view (b) of OPMF.

Under these conditions, we considered:

$$a(x) = f(x) = \alpha_0 x^2 + \alpha_1 x + \alpha_2 , \quad (14)$$

$$b(x) = g(x) = \beta_0 x^2 + \beta_1 x + \beta_2 \quad (15)$$

where $\alpha_0, \alpha_1, \alpha_2, \beta_0, \beta_1$ and β_2 – are constants.

Table 4 summarizes the parameters of the polynomial model for the different partitions of the fibers on the front plan (a) and the profile view (b).

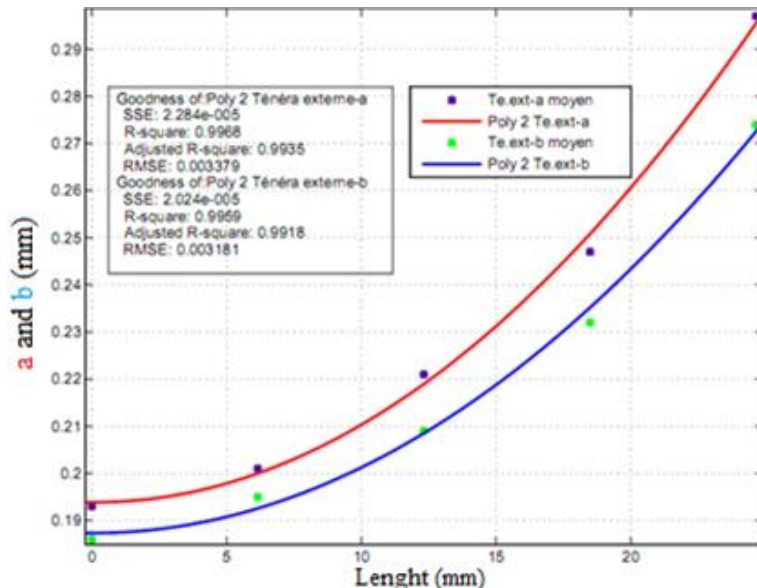


Fig. 14. Geometric modeling by the polynomial function of the mean fibers of the periphery of Tenera partition.

Table 4. Parameters of the polynomial mathematical model of the geometry of OPMF

Type of fibers	Model coefficients			R^2	RSME
	α_0	α_1	α_2		
Front Plan	OPMF-Pe-a	9,43 e-5	-5,49 e-5	0,1540	0,9999
	OPMF-Pi-a	1,15 e-4	5,79 e-4	0,1717	0,9987
	OPMF-Te-a	1,69 e-4	-5,10 e-5	0,1939	0,9967
	OPMF-Ti-a	1,27 e-4	6,46 e-4	0,2322	0,9985
	OPMF-Du-a	1,85 e-4	2,51 e-3	0,2066	0,9968
Profile view		β_0	β_1	β_2	
	OPMF-Pe-b	7,41 e-5	4,10 e-4	0,1427	0,9989
	OPMF-Pi-b	1,19 e-4	-1,54 e-4	0,1709	0,9944
	OPMF-Te-b	1,41 e-4	-2,09 e-5	0,1873	0,9959
	OPMF-Ti-b	8,16 e-5	1,39 e-3	0,2164	0,9991
	OPMF-Du-b	2,54 e-4	9,81 e-4	0,2032	0,9968

Modeling by an exponential function with two elements. Figure 15 below shows the case of the modeling by an exponential function with two elements for the fibers of the periphery of the partition *Tenera* (Te) on the front plan (a) and side view (b).

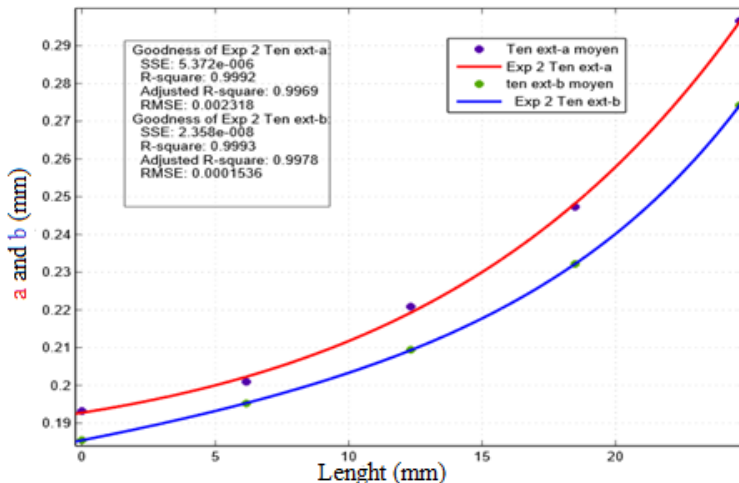


Fig. 15. Geometric modeling by the exponential function with two elements of the average Tenera peripheric fibers.

Under these conditions we have,

$$a(x) = f(x) = \alpha'_0 e^{\gamma_0 x} + \alpha'_1 e^{\gamma_1 x} \quad (16)$$

$$b(x) = g(x) = \beta'_0 e^{\delta_0 x} + \beta'_1 e^{\delta_1 x} \quad (17)$$

where α'_0 , α'_1 , β'_0 , β'_1 , γ_0 , γ_1 , δ_0 and δ_1 – are constants.

Table 5 summarizes the parameters of the exponential model with two elements for different fiber partitions on the front plan (a) and the profile view (b).

Table 5. Parameters of exponential mathematical model with two elements of the geometry of OPMF

Type of fibers	Model coefficients				R ²	RSME
	α'_0	α'_1	γ_0	γ_1		
Front plan	OPMF-Pe-a	0,0481	0,1058	-0,0634	0,0258	0,9999
	OPMF-Pi-a	0,1393	0,0314	-0,0025	0,0553	0,9997
	OPMF-Te-a	0,1327	0,0605	-0,0184	0,0508	0,9985
	OPMF-Ti-a	0,2017	0,0295	-0,0014	0,0599	0,9997
	OPMF-Du-a	0,0137	0,1943	-0,6626	0,0259	0,9992
Profile view		β'_0	β'_1	δ_0	δ_1	
	OPMF-Pe-b	0,1172	0,0249	-0,0033	0,0515	0,9999
	OPMF-Pi-b	0,1638	0,0053	0,0039	0,0954	0,9981
	OPMF-Te-b	0,1816	0,0043	0,0041	0,1145	0,9999
	OPMF-Ti-b	0,0611	0,1553	-0,0352	0,0231	0,9992
	OPMF-Du-b	0,1825	0,0198	0,0013	0,0987	0,9994

According to the correlation coefficients of the models tested (polynomial and exponential), we can say that these two models can describe with some accuracy the geometry of OPMF whatever the variety and the position of the latter. However, the exponential model with two elements appears to be more appropriate for its stability (the exponential function is monotonically increasing). So we have chosen the exponential model with two elements in the rest of the study.

Evolutionary model of the fiber section. The fiber cross section is assumed to be elliptical and the profile is described by an exponential model with two elements, the equations (1) and (2) are used to write the model of the section.

$$S(x) = \frac{\pi}{4} (\alpha'_0 e^{\gamma_0 x} + \alpha'_1 e^{\gamma_1 x}) (\beta'_0 e^{\delta_0 x} + \beta'_1 e^{\delta_1 x}) \quad (18)$$

To simplify the calculations, we pose

- $A = \alpha'_0 \beta'_0$; $B = \alpha'_0 \beta'_1$; $C = \alpha'_1 \beta'_0$; $D = \alpha'_1 \beta'_1$ with A, B, C et $D \in \mathbb{R}$
- $K_0 = \gamma_0 + \delta_0$, $K_1 = \gamma_0 + \delta_1$, $K_2 = \gamma_1 + \delta_0$, $K_3 = \gamma_1 + \delta_1$ with K_0, K_1, K_2 et $K_3 \in \mathbb{R}$

The cross section $S(x)$ of the fiber can be written:

$$S(x) = \frac{\pi}{4} [A e^{K_0 x} + B e^{K_1 x} + C e^{K_2 x} + D e^{K_3 x}] \quad (19)$$

The parameters of the section model for all five partitions are given in Table 6 below.

Table 6. Mathematical model parameters of the cross section of OPMF.

Type of fibers	Model coefficients							
	A	B	C	D	K ₀	K ₁	K ₂	K ₃
OPMF-Pe	0,005637	0,001197	0,012399	0,002634	-0,0667	-0,0119	0,0225	0,0773
OPMF-Pi	0,022817	0,000738	0,005143	0,000166	0,0014	0,0929	0,0592	0,1507
OPMF-Te	0,024098	0,000570	0,010987	0,000260	-0,0143	0,0961	0,0549	0,1653
OPMF-Ti	0,012324	0,031324	0,001802	0,004581	-0,0366	0,0217	0,0247	0,0830
OPMF-Du	0,002500	0,000271	0,035459	0,003847	-0,6613	-0,5639	0,0272	0,1246

Worth noting that the presentation of the results in Table 6 is based on average values. In practice, we researched the coefficients $[(A, B, C, D); (K_0, K_1, K_2, K_3)]$ for each of the 270 fibers; i.e. 54 fibers per partition. Thus the evolution of the section of each fiber should help in the counting of a single fiber tensile test by implementing the variation of the strain energy.

The knowledge of the mean models of the section is also of some interest for the implementation of certain calculation theories [12-13] and the digital multi-scale modeling of composite that would be reinforced by OPMF.

Summary. Our interest in this study was focused on the geometrical modeling of five fibers partitions from three varieties of palm nuts (*Tenera*, *Pissifera* and *Dura*) cultivated in the Mungo division in Cameroon. It appears that whatever the varieties, the OPMF are short fibers having a flattened cross-section and assimilated to a variable ellipse along the fiber. The peripheral fibers (on the pulp) are thinner and slightly shorter than those near the shell. We have proposed a geometrical model of diameter evolution as a function of the length of both the front plan than profile plan in exponential form with two elements. We have also written the model equation of the cross section in exponential form with four elements. A statistical study on the fiber diameters concluded that each of these fibers is unique although data follow a normal distribution whose parameters have been defined.

References

- [1] M. Z. M. Yusoff, M. S. Salit, N. Ismail and R. Wirawan, Mechanical properties of short random oil palm fiber reinforced epoxy composites, *Sains Malaysiana* 39, 87-92, 2010.
- [2] M. Baskaran, R. Hashim, N. Said, S. M. Raffi, K. Balakrishnan, K. Sudesh, O. Sulaiman, T. Arai, A. Kosugi, Y. Mori, T. Sugimoto and M. Sato, Properties of binderless particleboard from oil palm trunk with addition of polyhydroxyalkanoates, *Compos. Part B Eng.*, 43, 1109-1116, 2012, doi:10.1016/j.compositesb.2011.10.008
- [3] M. Jawaid, H.P.S. A. Khalilb, A. Hassana, R. Dunganic and A. Hadiyanec, Effect of jute fiber loading on tensile and dynamic mechanical properties of oil palm epoxy composites, *Compos. Part B Eng.*, 45, 619-624, 2013, doi:10.1016/j.compositesb.2012.04.068
- [4] R. S. Odera, O. D. Onukwuli and E. C. Osoka, Tensile and Compression Strength Characteristic Raffia Palm Fibre-Cement Composites, *J. Emerg. Trends Eng. Appl. Sci.* 2, 231-234, 2011.
- [5] S. Taj, M. A. Munawar and S. Khan, Natural fiber-reinforced polymer composites, *proc. Pakistan Acad. sci.* 44, 129-144, 2007.

[6] S. N. Monteiro, K. G. Satyanarayana, A. S. FerreiraI, D.C.O. Nascimento, F. P. D. Lopes, I. L. A. Silva, A. B. Bevitori, W. P. Inácio, J. B. Neto and T. G. Portela, Selection of high strength natural fibers, *Rev. Matéria*, 15, 488-505, 2011, doi: 10.1590/S1517-70762010000400002

[7] M. S. Sreekala, M. G. Kumaran and S. Thomas, Stress relaxation behaviour in oil palm fibres, *mater. Lett.*, 50, 263-273, 2001, doi:10.1016/S0167-577X(01)00237-3

[8] M. S. Sreekala, M. G. Kumaran and S. Thomas, Water sorption in oil palm fiber reinforced phenol formaldehyde composites, *Compos. Part A Appl. Sci. Manuf.*, 33, 763-777, 2002, doi:10.1016/S1359-835X(02)00032-5

[9] N. R. Sikame, E. Njeugna, M. Fogue, J.-Y. Drean, A. Nzeukou and D. Fokwa, Study of Water Absorption in Raffia vinifera Fibres from Bandjoun, Cameroon, *Sci. World J.*, <http://dx.doi.org/10.1155/2014/912380>, 2014.

[10] J. Moothoo, D. Soulat, P. Ouagne and S. Allaoui, Caractérisations mécaniques de renforts à base de fibres naturelles pour l'analyse de la déformabilité, *Proc. 17eme Journées Nationales des Composites JNC 17*, hal-00597931 pp.55, 2011.

[11] Y. Nitta, K. Goda, J. Noda and W-II lee, cross-sectional area evaluation and tensile properties of alkali-treated kenaf fibers, *Compos. Part A Appl. Sci. Manuf.*, 49, 132-138, 2013.

[12] F. O. Okafor and S. Sule, Models for prediction of structural properties of palmnut fibre-reinforced cement mortar composites, *Niger. J. Technol.*, 27, 13-21, 2008.

[13] H. Moussaddy, M. Lévesque and D. Therriault, évaluation des performances des modèles d'homogénéisation pour des fibres aléatoirement dispersées ayant des rapports de forme élevés, *Proc. 17eme Journées Nationales des Composites hal-00598129*, pp.83, Poitiers, 2011.

[14] W. P. Inacio, F. P. D. Lopes and S. N. Monteiro, Diameter dependence of tensile strength by weibull analysis: part III sisal fiber, *Rev. Matéria*, 15, 124-130, 2010.

[15] B. Bevitori, I. L. A. Silva and F. P. D. Lopes, Diameter dependence of tensile strength by Weibull analysis: part II jute fiber, *Rev. Matéria*, 15, 117-123, 2010.

[16] V. Placet, F. Trivaudey, O. Cisse, V. Guicheret-Retel and L. Boubakar, Influence du diamètre sur le module d'Young apparent des fibres de chanvre. Effet géométrique ou microstructural, *Proc. 20ème Congrès Français de Mécanique*, ISBN 978-2-84867-416-2 (CFM 20), 3864-3869, Besançon, 2012.

[17] L. L. da Costa, R. L. Loiola and S. N. Monteiro, Diameter dependence of tensile strength by Weibull analysis: part I bamboo fiber, *Rev. Matéria*, 15, 110-116, 2010.

[18] F. Tomczak, T. H. D. Sydenstricker and K. G. Satyanarayana, studies on lignocellulosic fibers of Brazil. Part II: Morphology and properties of Brazilian coconut fibers, *Compos. Part A Appl. Sci. Manuf.*, 38, 1710-1721, 2007.

[19] M. A. Norul izani, M. T. Paridah, U. M. K. Anwar, M. Y. Mohd Norb and P. S. H'ng, effect of fiber treatment on morphology; tensile and thermo-gravimetric analysis of oil palm empty fruit bunches fibers, *Compos. Part B Eng.*, 45, 1241-1257, 2013.

[20] F. Ilczysyn, A. Cherouat and G. Montay, Nouvelle approche pour la caractérisation mécanique des fibres naturelles, *Proc. 20ème Congrès Français de Mécanique*, ISBN 978-2-84867-416-2 (CFM 20), 3828-3833, Besançon, 2012.

[21] F. O. Okafor, Span Optimization for palmnut fibre-reinforced mortar roofing tiles, *Ph. D. Dissertation University of Nigeria Nsukka, Nigeria*, 1994.

[22] O. K. Owolarafe, M. T. Olabige and M. O. Faborode, Physical and mechanical properties of two varieties of fresh oil palm fruit, *J. Food Eng.*, 78, 1228-1232, 2007.

[23] Y. Y. Then, N. A. Ibrahim, N. Zainuddin, B. W. Chieng, H. Ariffin, and W. M. Z. Wan Yunus, Influence of Alkaline-Peroxide Treatment of Fiber on the Mechanical Properties of Oil Palm Mesocarp Fiber/Poly(butylene succinate) Biocomposite, *BioResources*, 10, 1730-1746, 2015.

[24] C. C. Eng, N. A. Ibrahim, N. Zainuddin, H. Ariffin, W. M. Z. Wan Yunus, Chemical Modification of Oil Palm Mesocarp Fiber by Methacrylate Silane: Effect on Morphology, Mechanical, and Dynamic Mechanical Properties of Biodegradable Hybrid Composites, *BioResources*, 11, 861-872, 2016.

[25] B. Régis and T. Michel, *Analyse des séries temporelles*, 2eme édition, p. 296, Dunod, 2008.

Comparison of Assemblies of Four-Link Structural Groups of 3rd Class on the Transmission Angle

Matsyuk I.N.¹, Morozova T.I.^{1,a}, Shlyakhov E.M.^{1,b}

1 – State Higher Educational Institution “National Mining University”, city of Dnipropetrovsk, Ukraine,

a – tanya_dp@mail.ru

b – shlyahove@nmu.org.ua



DOI [10.13140/RG.2.1.2348.6969](https://doi.org/10.13140/RG.2.1.2348.6969)

Keywords: Mathcad, planar mechanism, vector, complex number, group assemblies, transmission angle, structural group of third class.

ABSTRACT. Comparison of various assemblies of four-link structural group of 3rd class with revolute joints on the transmission angle is performed. Equations of the trajectories of plug points of one of the groups of joint are obtained to determine transmission angles. Derived functions of these equations enable to determine the values of transmission angles for each assembly group. It is shown that only two assemblies of maximum possible assembling number of such group (six) have practical value. The solution of this problem was performed with the help of Mathcad program.

Introduction. One of the criteria determined synthesis quality of planar linkage is a parameter, which characterizes the quality of power transmission by one link to another one.

Historically, pressure angle according to the theory of mechanism in Russian scientific literature is taken as this parameter. It is the angle between the vector of power transmission and the velocity vector of application point of this power.

The term “transmission angle” is often used in English literature. Transmission angle is the angle between the vectors of absolute and relative velocities of the common link points. For example, as for crank-rocker mechanism it is the angle between coupler and rocker. It is more difficult to determine this angle within mechanisms with the great number of links (for instance, between two couplers).

It is well known, that these angles complement each other up to $0,5 \pi$ radian.

Analysis of the recent research. In classical problem setting the task of synthesis of the planar crank-rocker mechanism was formulated as follows – to determine link lengths in terms of the given rocker rotation angle and to provide for minimal deviation of the transmission angle from 90°.

In other words, the first synthesis criterion is to provide for the given angle of rocker rotation when crank makes a complete turn. This task will be solved geometrically in [1] while designing the drive of ratchet-wheel where desired turn angle was formed by the end points of the rocker. Analytical definition of the dead rocker positions is given in [2].

The problem of determining of the transmission angle for crank-rocker mechanism was set and solved in 1972 in [2], however, the papers devoted to various aspects of this problem for relatively simple mechanism appears up to the present days [3, 4, 5].

Formulation of work objectives. Therefore, the problem of estimation of this parameter for mechanisms with the complex structure especially for mechanisms of 3rd class is of great interest.

E.E. Peisakh in the paper [6] gives an example of determining six variants of four-link structural group of 3rd class assemblies containing revolute joints.

Visualization of this example was performed by one of the authors of this paper in [7] with the help of Mathcad program. It enables to evaluate approximately the values of the transmission angle from the coupler to the basic link within various assemblies.

Statement of the basic material. Let's take as an example mechanism (Fig. 1) containing four-link structural group of 3rd class. This group was taken from [6]. It is shown that it has six variants of assemblies under the fixed position of its external joints.

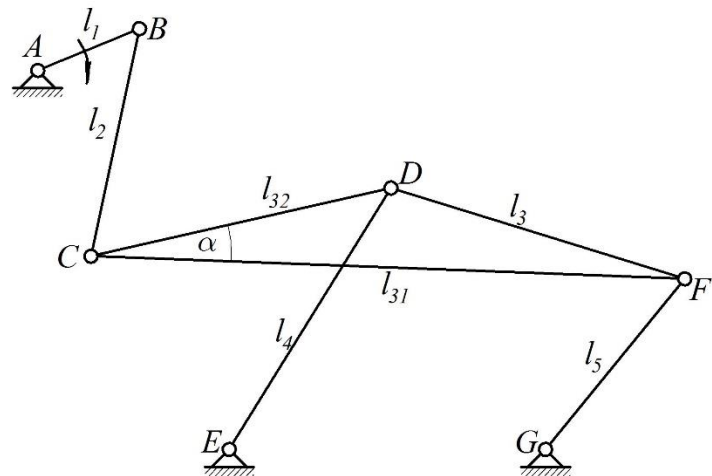


Fig. 1. Diagram of 3rd class mechanism.

Research task is to determine the values of the transmission angles between coupler BC and basic link CDF for each of the possible assemblies which are the part of the given mechanism.

Coordinates of the external linkage joint of the group: $x_B = -10$; $y_B = 0$; $x_E = 19,5$; $y_E = -122$; $x_G = 91,5$; $y_G = -122$. Other parameters of the group have following values: $l_2 = 78$; $l_3 = 70$; $l_4 = 78$; $l_5 = 70$; $l_{31} = 135$; $l_{32} = 70$.

Vector interpretation of the group links is given in Fig. 2.

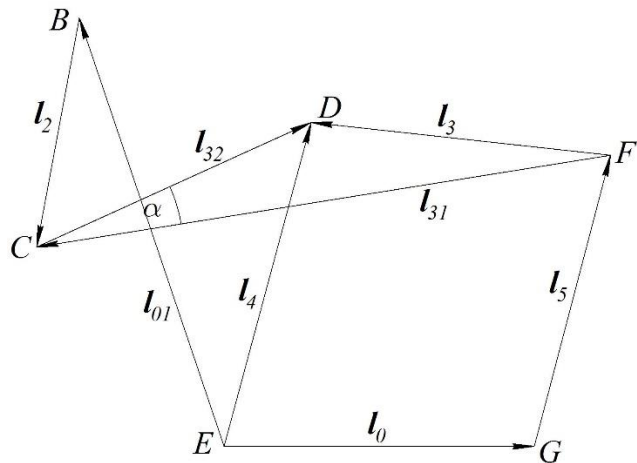


Fig. 2. Vector image of the 3rd class group.

To determine the angles of the transmission angle let's disconnect joint C. For each point of the plugs (C₂ within the link 2 and C₃ within the link 3) we can derive an equation of their trajectories.

Radius circle l₂ with the centre in the point B will be the trajectory of the point C₂. The trajectory of the point C₃ is determined by the four-link chain geometry EDFG.

To obtain the trajectory of the point C₃ we use Freudenstein equation for jointed four-link chain [2]. For four-link chain EDFG it will be:

$$\cos(\varphi_5 - \varphi_4) = k_1 \cos \varphi_5 - k_2 \cos \varphi_4 + k_3. \quad (1)$$

Coefficients of this equation have the values:

$$k_1 = \frac{l_0}{l_4}, \quad k_2 = \frac{l_0}{l_5}, \quad k_3 = \frac{l_0^2 + l_4^2 + l_5^2 - l_3^2}{2l_4l_5}. \quad (2)$$

Using universal trigonometric substitution:

$$\sin \varphi_4 = \frac{2 \operatorname{tg} \frac{\varphi_4}{2}}{1 + \operatorname{tg}^2 \frac{\varphi_4}{2}} \quad \text{and} \quad \cos \varphi_4 = \frac{1 - \operatorname{tg}^2 \frac{\varphi_4}{2}}{1 + \operatorname{tg}^2 \frac{\varphi_4}{2}}, \quad (3)$$

And replaced:

$$x = \operatorname{tg} \frac{\varphi_4}{2}, \quad (4)$$

We obtain quadratic equation:

$$A(\varphi_5)x^2 + B(\varphi_5)x + C(\varphi_5) = 0. \quad (5)$$

Coefficients of this equation are:

$$A(\varphi_5) = -(1 + k_1) \cos \varphi_5 - k_2 - k_3, \quad (6)$$

$$B(\varphi_5) = 2 \sin \varphi_5, \quad (7)$$

$$C(\varphi_5) = (1 - k_1) \cos \varphi_5 + k_2 - k_3. \quad (8)$$

Solution of quadratic equation enables to find out two values of the angle φ_4 . From now on mathematical expressions are given in the form of Mathcad - 11 program fragments.

$$\begin{aligned} \varphi_{4a}(\varphi_5) &:= 2 \operatorname{atan} \left(\frac{-B(\varphi_5) + \sqrt{B(\varphi_5)^2 - 4A(\varphi_5) \cdot C(\varphi_5)}}{2A(\varphi_5)} \right) \\ \varphi_{4b}(\varphi_5) &:= 2 \operatorname{atan} \left(\frac{-B(\varphi_5) - \sqrt{B(\varphi_5)^2 - 4A(\varphi_5) \cdot C(\varphi_5)}}{2A(\varphi_5)} \right). \end{aligned} \quad (9)$$

After that, we can obtain two vector values of the point C_3 .

$$\begin{aligned} l_{3a}(\varphi_5) &:= l_4 \cdot \exp(\varphi_{4a}(\varphi_5) \cdot i) - l_0 \cdot \exp(i \cdot \beta) - l_5 \cdot \exp(i \cdot \varphi_5) \\ l_{3b}(\varphi_5) &:= l_4 \cdot \exp(\varphi_{4b}(\varphi_5) \cdot i) - l_0 \cdot \exp(i \cdot \beta) - l_5 \cdot \exp(i \cdot \varphi_5) \\ \phi_{3a}(\varphi_5) &:= \operatorname{arg}(l_{3a}(\varphi_5)) \quad \phi_{3a}(\varphi_5) = -80 \text{ deg} \\ \phi_{3b}(\varphi_5) &:= \operatorname{arg}(l_{3b}(\varphi_5)) \quad \phi_{3b}(\varphi_5) = 161.509 \text{ deg} \\ l_{Ca}(\varphi_5) &:= z_E + l_0 \cdot \exp(i \cdot \beta) + l_5 \cdot \exp(\varphi_5 \cdot i) + l_{31} \cdot \exp[(\phi_{3a}(\varphi_5) + \alpha) \cdot i] \\ l_{Cb}(\varphi_5) &:= z_E + l_0 \cdot \exp(i \cdot \beta) + l_5 \cdot \exp(\varphi_5 \cdot i) + l_{31} \cdot \exp[(\phi_{3b}(\varphi_5) + \alpha) \cdot i] \end{aligned} \quad (10)$$

Two closed trajectories of the point C_3 are as follows (Fig. 3).

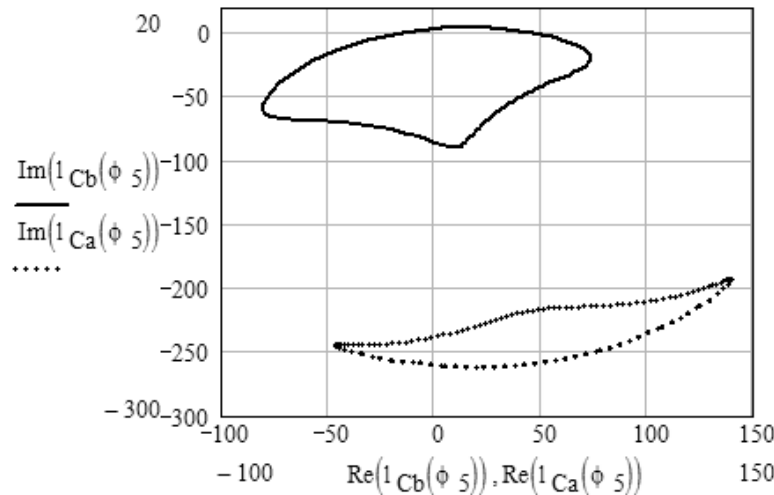


Fig. 3. Two possible trajectories of the point C_3 .

Equation of the point C_2 trajectory

$$z(\phi_2) := 1_2 \cdot (\cos(\phi_2) + 1i \cdot \sin(\phi_2)) \quad (11)$$

It's easy to see that the circle with the centre in the point B $(-10; 0)$ and radius $l_2 = 78$ cannot have common points with the low trajectory. Thus, possible assemblies can exist only on the upper trajectory. Let's draw the trajectory of the point C_2 .

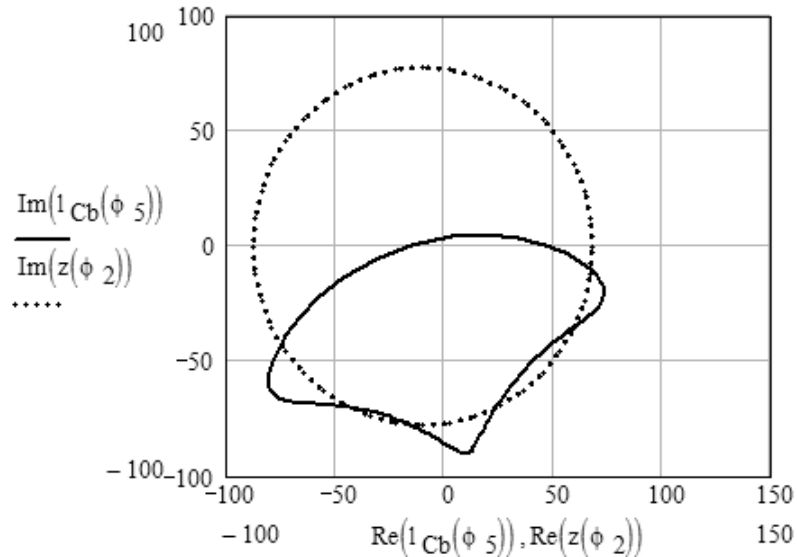


Fig. 4. On determining possible assemblies of 3rd class group

Therefore, there are four common points of trajectories in Fig. 4. They confirm the existence of six assemblies of the given group of 3rd class. The same result was obtained earlier by one of the authors of this paper and described in [7].

Table 1 below shows angle values, which determine the position of group links in various assemblies.

Table 1. Angle values determining group assemblies (radian)

Assembly	1	2	3	4	5	6
φ_2	3.72	4.254	4.646	5.148	5.82	6.15
φ_5	2.791	1.592	0.97	5.438	4.367	3.591

Let us put

$$x(\phi_5) := \operatorname{Re}(l_{Cb}(\phi_5)) \quad y(\phi_5) := \operatorname{Im}(l_{Cb}(\phi_5)) \quad (12)$$

These expressions are parametric equations of the trajectory point C_3 which parameter is the turn angle of the link 5. For the trajectory of the point C_2 analogue equations will be:

$$x(\phi_2) := \operatorname{Re}(z(\phi_2)) \quad y(\phi_2) := \operatorname{Im}(z(\phi_2)), \quad (13)$$

where the angle of the link turn 2 is a parameter.

Let us determine the derived functions described the trajectories of the points C_2 and C_3 .

$$g_1(\phi_2) := \operatorname{atan} \left(\frac{\frac{d}{d\phi_2} \operatorname{Im}(z(\phi_2))}{\frac{d}{d\phi_2} \operatorname{Re}(z(\phi_2))} \right) \quad g_2(\phi_5) := \operatorname{atan} \left(\frac{\frac{d}{d\phi_5} \operatorname{Im}(l_{Cb}(\phi_5))}{\frac{d}{d\phi_5} \operatorname{Re}(l_{Cb}(\phi_5))} \right) \quad (14)$$

As is known, their values in the intersection points of trajectories are tangents of slope angles concerning trajectories. Tangent as for the trajectory of the point C_3 characterizes the line of action of the absolute velocity of point C. Tangent as for trajectory of the point C_2 is the line of action of the relative velocity of point C. The angle between these tangents is the transmission angle between couplers 2 and 3 of the mechanism. Its diagram is given in Fig. 1.

Values of the acute transmission angles determined for six mechanism assemblies are given in the table 2.

Rational values of the transmission angles [2]:

$$40^\circ < \gamma < 140^\circ.$$

Table 2. Transmission angles γ (degree)

Assembly	1	2	3	4	5	6
γ	63.652	18.886	19.581	32.703	28.821	57.241

Summary. On the basis of the study we can draw the following conclusions:

- Only the first and the sixth assemblies of possible ones can be adaptable for given mechanism;
- The four rest assemblies have only theoretical interest;
- While synthesizing complex mechanisms, which can have various assemblies it is required to approach minimal number of assemblies where the probability of obtaining rational values of the transmission angle is higher;
- If four-link group of 3rd class has maximum number of assemblies (six) it is required to be at least one of the work drivers of the crank.

References

- [1] H. Alt. Ueber die Totlagen des Gelenkvierecks, Z.A.M.M. 1925, Vol. 5 (No. 1), 347-354.
- [2] F. Freudenstein, E.J. Primrose, The classical transmission-angle problem, The Institution of Mechanical Engineers, C96/72, Mechanisms 1972, London.
- [3] Eres Söylemez, Classical transmission-angle problem for slider-crank mechanism, Mechanism and Machine Theory, Vol. 37 (2002), 419-425, doi: 10.1016/S0094-114X(01)00083-0.
- [4] S. Youliang, Optimization design of crank rocker mechanism based on maximum of minimum transmission angle, Journal of machine design, Vol. 31, Jul. 2014, pp. 29-33.
- [5] Y. Jinhu, Research of the Transmission Angle Function of Offset Crank Rocker Mechanism, Journal of Mechanical, Vol. 38, Aug. 2014, pp. 43-46.
- [6] E.E. Peisakh, Determining link position of three and two work drivers of four-link Assura with turning pairs // Mechanical engineering. – 1985. -No 5. – P. 55-61.
- [7] I.N. Matsyuk, Geometrical analysis of two work driver structural group of 3rd class in the Mathcard program. Bulletin of Kryvyi Rih Technical University – Kryvyi Rih, 2013. – Vol. 35. – P. 209–213.

The Mechanics of a Cantilever Beam with an Embedded Horizontal Crack Subjected to an End Transverse Force, Part A: Modelling

Panos G. Charalambides¹ and Xiaomin Fang¹

1 – Department of Mechanical Engineering, The University of Maryland, Baltimore County, 1000 Hilltop Circle, Baltimore, MD 21250, USA



DOI 10.13140/RG.2.1.3874.4560

Keywords: cantilever, beam, model, embedded, horizontal, crack, mechanics, modelling.

ABSTRACT. This study addresses the mechanics of a cracked cantilever beam subjected to a transverse force applied at its free end. In this Part A of a two Part series of papers, emphasis is placed on the development of a four-beam model for a beam with a fully embedded horizontal sharp crack. The beam aspect ratio, crack length and crack centre location appear as general model parameters. Rotary springs are introduced at the crack tip cross sections as needed to account for the changes in the structural compliance due to the presence of the sharp crack and augmented load transfer through the near-tip transition regions.

Guided by recent finite element findings reported elsewhere, the four-beam model is advanced by recognizing two key observations, *(a) the free surface and neutral axis curvatures of the cracked beam at the crack center location match the curvature of a healthy beam (an identical beam without a crack under the same loading conditions), (b) the neutral axis rotations (slope) of the cracked beam in the region between the applied load and the nearest crack tip matches the corresponding slope of the healthy beam*. The above observations led to the development of close form solutions for the resultant forces (axial and shear) and moment acting in the beams above and below the crack. Axial force and bending moment predictions are found to be in excellent agreement with 2D finite element results for all normalized crack depths considered. Shear force estimates dominating the beams above and below the crack as well as transition region length estimates are also obtained. The model developed in this study is then used along with 2D finite elements in conducting parametric studies aimed at both validating the model and establishing the mechanics of the cracked system under consideration. The latter studies are reported in the companion paper Part B-Results and Discussion.

Introduction. Over the last two decades, the frequency response [1-5] of a component or a structure has been used to assess “structural health” as one of several methods used in damage detection [6-13] and structural health monitoring. In most of such studies, the effects of damage on the structural frequency response has been explored using a cantilever beam geometry. With the above in mind, diffused damage detection studies have been developed [7-13] using optimization algorithms that minimize an “error estimate”. Typically, the employed “error estimates” are calculated by comparing the experimentally measured frequencies of the structure [8] to the respective frequencies predicted by a physics based model that solves a problem of the same structural geometry but with reduced localized properties at a prescribed location [9]. Often, the optimization algorithms identify the model structure that best matches the experimental results, thus identifying the likely location and degree of structural damage manifested through the EI, structural

⁴ This research was partially supported through a University of Maryland, Baltimore County DRIF award and Graduate Assistantship in the Department of Mechanical Engineering.

⁵ Professor Charalambides would like to acknowledge many useful discussions with Mechanical Engineering Professor Weidong Zhu and Professor Emeritus Christian von Kerczek.

stiffness reduction. For example, Xu *et al.* [8] developed a damage detection algorithm that monitors the changes in the first 10 transverse frequencies of a vibrating beam as a means of detecting the location and degree of damage along the axis of the beam as measured through a reduced localized structural stiffness. The promising outcomes of their initial studies have been validated through model experiments and have sparked new interest in expanding the studies to include detection of diffused damage in more complicated structures such as frames and bolted joints [11-15].

While the above efforts address damage assumed to be diffused over a prescribed region, in recent years a few studies have attempted to address the effects of sharp cracks on the modal response of a structure [16-27], a few of which employ basic fracture mechanics concepts [22-27]. Such studies require prior knowledge of the fracture mechanics stress fields and related stress intensity factors. The near-tip fracture quantities are thought to be required in assessing the energy changes due to the introduction of a crack and the related changes in the structural compliance or associated stiffness changes induced by the presence of a sharp crack. As a result, fracture mechanics based studies have been limited to systems with edge cracks for which the stress intensity factors [28-32] dominating the crack tip region is known. Furthermore, most such studies also assume the presence of a mode I “breathing” crack thus preserving the linearity of the system that would otherwise be violated due to non-linear crack surface contact effects. More recently, Jing *et al.* [27] employed a variation of the model presented in this work in obtaining the natural frequencies of a cantilever beam containing a horizontal crack capable of relative crack surface sliding but not opening.

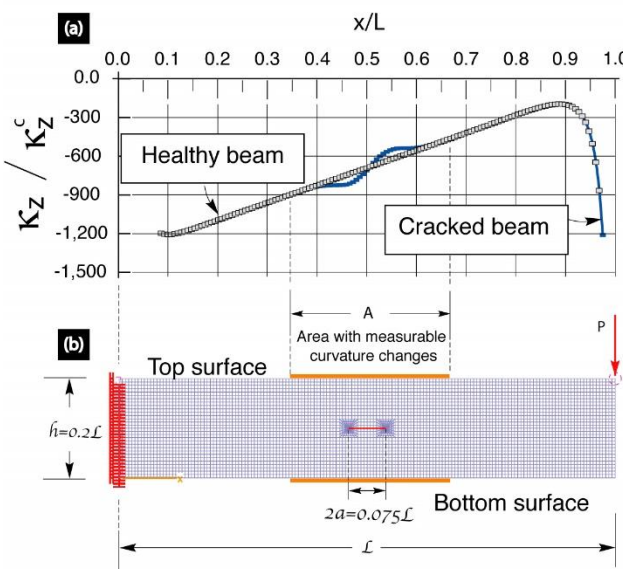


Fig. 1. Normalized top surface beam curvatures for a healthy and cracked beams generated using 2D finite elements.

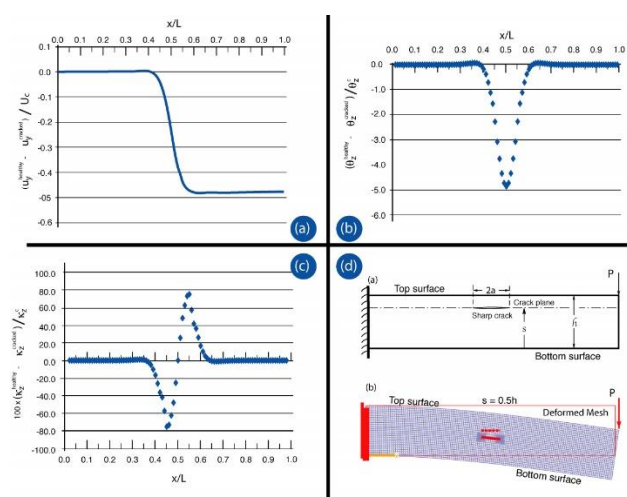


Fig. 2. Normalized (a) deflections, (b) slope and (c) curvature differences between a cracked and a “healthy” beam subjected to an end loading P .

Recently, Two-Dimensional (2D) Finite Element (FE) studies [33-35] on the cantilever specimen shown in Figs. 1-4, suggest that predominately mode II conditions dominate both crack tip regions for a fully embedded horizontal sharp crack subjected to the loading conditions shown in Fig. 1b. As such, and under ideally flat crack surface condition, surface contact should minimally affect the overall load transfer and deformation mechanics of the specimen shown in Fig. 3. Furthermore,

finite element findings reported in [33, 34] (see Figs. 1-3) led to the following two key observations; (a) *the free surface and neutral axis curvatures of the cracked beam at the crack center location match the curvature of a healthy beam, i.e., an identical beam without a crack under an end force condition, and (b) the neutral axis rotations (slope) of the cracked beam in the region between the applied load and the nearest crack tip matches the corresponding slope of the healthy beam.*

Guided by the above finite element findings, in this study a four-beam model [33] is developed in an effort to establish simple but effective physics based models capable of predicting the load transfer and deformation mechanics as well as the near tip fracture conditions, the frequency and modal response of structures with fully embedded cracks of the type shown in Fig. 4. The development of the four-beam model shall be presented next.

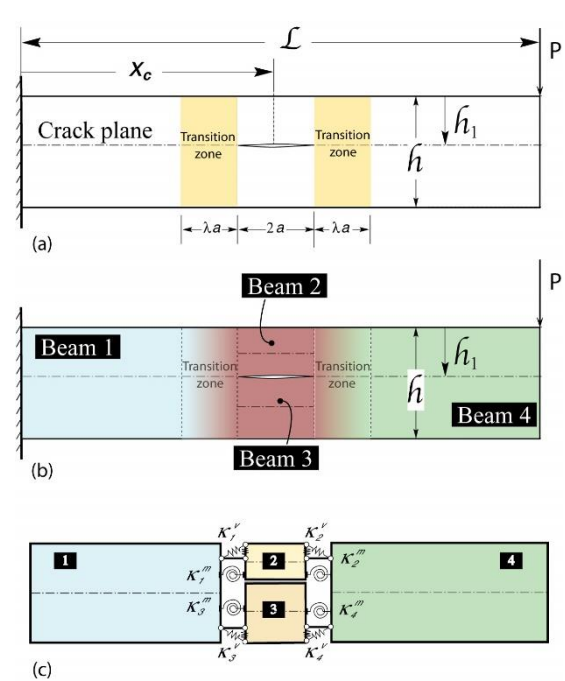
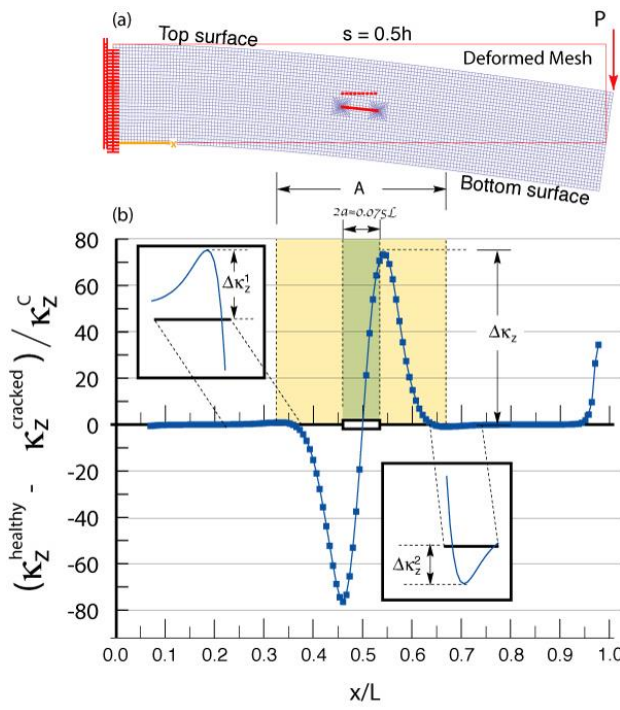


Fig. 3. Normalized curvature differences between a cracked and a healthy beam extracted for the top beam surface using 2D finite element models. In this simulation for the cracked beam, a horizontal sharp crack of normalized length $2a = 0.15L$ was placed at the center of the beam as shown in (a) above. The beam aspect ratio used was $h/L = 0.2$. The results support the existence of transition regions of equal length at the left and right crack tips.

Fig. 4. Schematics highlighting the four beam model development. Rotary springs are introduced at the interfaces between beams 1 and 2, 2 and 4, 1 and 3, and 3 and 4. (a) A schematic showing the geometry and boundary conditions applied on the cracked beam. (b) The identification of the four beams. (c) The four beams connected through rotary springs at their interfaces.

Development of the four-beam model. The results presented in Figs. 1-3 were obtained as part of a broad finite element study aimed at establishing the deformation and fracture mechanics of a cantilever beam containing a fully embedded sharp crack positioned at any admissible location and orientation within the beam domain. The results of those studies are reported in greater detail elsewhere [33]. In Fig. 1, the curves shown represent the curvatures of a healthy and a cracked

beam extracted from respective finite element models at the top beam surfaces. As indicated in Fig. 1, the results correspond to a beam of aspect ratio $L/h = 5$, with the cracked beam containing a horizontal through thickness sharp crack of length $l = 0.075L$ located at the center of the beam at $x_C = 0.5L$. The curvature results for the healthy beam i.e., a beam without a crack but otherwise geometrically identical to the one with the crack, are represented by the rectangular open symbols. As expected, away from the ends, the healthy beam curvatures form a linear profile with position x consistent with the bending theory prediction of $d^2 y/dx^2 = M(x)/EI$, where $y(x)$ represents the deflection of the beam neutral axis, $M(x)$ is the bending moment at location x , E is the elastic modulus and I is the second moment of inertia with respect to the bending axis. On the other hand, the top surface curvatures predicted for the cracked beam are shown using the solid blue symbols. As shown in Fig. 1, the curvature results for the cracked beam deviate from those of the healthy beam only in the crack region exhibiting a sinusoidal-like profile over a distance A that appears to be approximately two to three times the crack length size. Most importantly for this study, one observes that the curvature of the cracked beam intersects the healthy beam curvature profile at the center of the crack consistent with Figs. 1-3. This observation has been validated through broad parametric studies reported in [33]. In fact, the observation has been found to hold true for curvature estimates for the top and bottom beam surfaces as well as for the mid-planes above and below the crack in the crack region. Informed by the above observations, the following hypothesis used in constructing the proposed four-beam model is put forward.

Proposed deformation hypothesis. *For any cantilever beam system containing a horizontal sharp crack and subjected to an end transverse loading, the curvatures of the mid-planes above and below the crack match the curvature of the healthy beam at the crack center location.*

Guided by the above observation, let's consider the cracked cantilever beam shown in Fig. 4a. The beam has a length L , height h while containing a horizontal sharp crack of length $l = 2a$ located at position x_C from the fixed end at depth h_l from the top surface. In this study, the above domain is divided into four sub-domains, each forming a beam as shown in Fig. 4b labeled Beam-1, Beam-2, Beam-3 and Beam-4. As will be discussed later on in this work and as suggested by finite element studies reported in [33] and in Figs 1-3, a transition region exists between Beam-1 and Beams 2 and 3 at the left crack tip and the same Beams 2 and 3 and Beam-4 at the right crack tip. While the effects of the transition regions will be incorporated into the four-beam model, at present we shall focus on the mechanics of Beams 2 and 3 since their response appears to be directly linked to the deformation hypothesis stated above. More specifically, let's consider the beam free body diagrams shown in Fig. 5.

As shown, at the crack center cross sections, Beam-2, i.e., the beam above the crack plane, is subjected to an axial force resultant N_t , shear force resultant V_t and bending moment resultant M_t . Similarly, Beam-3 also referred to in this study as the bottom beam denoted by a subscript b , is subjected to force and moment resultants N_b , V_b and M_b respectively. Meanwhile, Section/Interface 1, which is the left end of the top beam, is subjected to the force and moment resultants N_1 , V_1 and M_1 whereas the right end of the same beam is subjected to N_2 , V_2 and M_2 at Interface 2. Similarly, the bottom beam or Beam-3 is subjected to end forces and moments N_3 , V_3 and M_3 at Section/Interface 3 and N_4 , V_4 and M_4 at Section 4 as shown in Fig. 5c.

Based on the proposed deformation hypothesis, the curvature of Beams 2 and 3 at the center of the crack should be equal to the curvature of the healthy beam, i.e.,

$$\frac{d^2 y_2}{dx^2} = \frac{d^2 y_3}{dx^2} = \frac{d^2 y}{dx^2} \text{ at } x = x_c \quad (1)$$

where $y_2(x)$ – is the mid-plane deflection of Beam 2;

$y_3(x)$ – is the mid-plane deflection of Beam 3;

$y(x)$ – is the mid-plane deflection of the healthy beam.

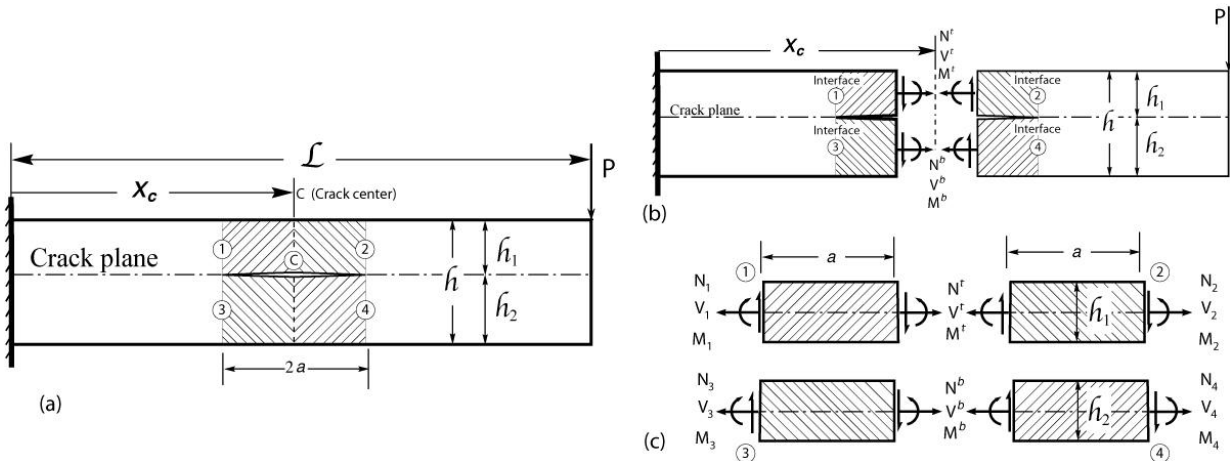


Fig. 5. Schematics used in the development of the analytical model capturing the mechanics of the beams above and below the crack, i.e., Beams 2 and 3 shown in Fig. 4. (a) The cracked beam with Beams 2 and 3 highlighted along with Interfaces 1-4. (b) A section through the center of the crack exposing the force and moment resultants acting in the “top” and “bottom” beams. (c) Free body diagrams of the left and right half of the “top” and “bottom” beams, exposing the resultants acting at their corresponding Interfaces 1-4.

Consistent with beam theory [36-37], it can be shown that the above differential equations can be expressed in terms of the bending moments acting in each beam at the cross section of interest and the bending stiffness El for each beam, i.e.,

$$\frac{M_t}{El_t} = \frac{M_b}{El_b} = \frac{M_c}{El} \quad (2)$$

where the subscripts t and b denote quantities for the top (Beam 2) and bottom (Beam 3) beams respectively.

The above simple equations for the moment resultants at the center of the crack are general, in that, they yield the moment resultants in the top and bottom beams at the center of the crack as a function of the bending moment experienced by the healthy beam at the same location, i.e.,

$$M_t = \frac{l_t}{l} M_c \text{ and } M_b = \frac{l_b}{l} M_c \quad (3)$$

where for a downward load P the bending moment at the crack center location in the healthy beam is $M_c = -P(L - x)$. With the bending moments acting in the top and bottom beams known, an expression for the axial forces N_t and N_b is then obtained through a global moment equilibrium enforced over the right half of the beam (see Fig. 5b), such that,

$$\sum M_c = 0 \text{ yields } N_t \frac{h_1}{2} - N_b \frac{h_2}{2} - M_t - M_b + M_c = 0 \quad (4)$$

Force equilibrium in the x direction for either half of the beam shown in Fig. 5b results in the obvious outcome that the axial force in the bottom beam should be equal and opposite to its counterpart acting in the top beam, i.e., $N_b = -N_t$. The latter finding along with Eqns (3) and (4) yield a general expression for the axial forces N_t and N_b as follows,

$$N_b = -N_t = \frac{2M_c}{h} \left\{ 1 - \frac{I_t + I_b}{I} \right\} \quad (5)$$

where l , l_t and l_b are the second moments of inertia with respect to the bending axis of the healthy beam, top beam or Beam-2 and bottom beam or Beam-3 respectively;

h – is the beam height

M_c – as before is the bending moment acting at the crack center location in the healthy beam.

Further enforcing force equilibrium in the y direction for either half of the beam shown in Fig. 5 yields,

$$V_t + V_b = P \quad (6)$$

Now, by enforcing force and moment equilibrium within the top and bottom beams shown in Figs. 5c and 6a, one can easily establish the following relations between the cross sectional resultants acting at the beam interfaces 1, 2, 3 and 4 shown in Fig. 5c,

$$\begin{array}{llll} N_1 = N_t & N_2 = N_t & N_3 = N_b & N_4 = N_b \\ V_1 = V_t & V_2 = V_t & V_3 = V_b & V_4 = V_b \\ M_1 = M_t - V_t a & M_2 = M_t + V_t a & M_3 = M_b - V_b a & M_4 = M_b + V_b a \end{array} \quad (7)$$

The above analysis suggests that in the presence of a horizontal crack, load transfer across the cracked cross section is enabled by the development of a force couple subjecting the beams above and below the crack into compression and tension respectively for an upwardly applied load P . Meanwhile, the same beams experience a linearly varying bending moment between Interfaces 1

and 2 for the upper beam and 3 and 4 for the lower beam. In the same interval, and over the length of each beam which is equal to the length of the horizontal crack, both the axial and shear resultant forces $N(x)$ and $V(x)$ remain constant and equal to the values attained at the crack center cross sections. Thus far, the shear force resultants V_t and V_b dominating the top and bottom beams are the only remaining unknowns in determining the load transfer mechanics across the beam crack region. These quantities are established below along with other problem variables using beam compatibility conditions.

Beam compatibility conditions. Compatibility conditions are required in enforcing displacement and cross sectional rotation conditions at the interfaces between two beams. It is common to cast a beam problem using the second order differential equation of the elastic curve of the beam along with deflection and beam slope boundary and matching conditions. In this study, for simplicity purposes we shall employ the method of linear superposition in addressing the deformation mechanics of the four-beam model presented in Fig. 4. More specifically, in this formulation each beam will be treated as a Timoshenko beam thus accounting in the general formulation for shear effects. The deformation of each beam (deflections, cross sectional rotations and slope of neutral axis, will be accounted for by superimposing the local deformations of a cantilever beam subjected to end transverse force V and moment M shown in Fig. 6b, to the deformations caused by the deflection and rotation of the “fixed” attached to its adjacent deforming beam. In doing so, the deflection δ , cross section rotation φ and slope of the neutral axis θ at the free end of a typical Timoshenko beam shown in Fig. 6b will be used. For a beam of constant cross section, homogeneous material properties and the loading shown in Fig. 6b, the above quantities are given by [37],

$$\begin{aligned}\delta &= -\frac{VL^3}{3EI} - \frac{VL}{kAG} + \frac{ML^2}{2EI}, \text{ - Deflection at Free End} \\ \varphi &= \frac{VL^2}{2EI} + \frac{ML}{EI}, \text{ - Rotation of Cross Section at Free End} \\ \theta &= -\frac{VL^3}{2EI} + \frac{ML}{EI} - \frac{V}{kAG} \text{ - Beam Slope at Free End}\end{aligned}\quad (8)$$

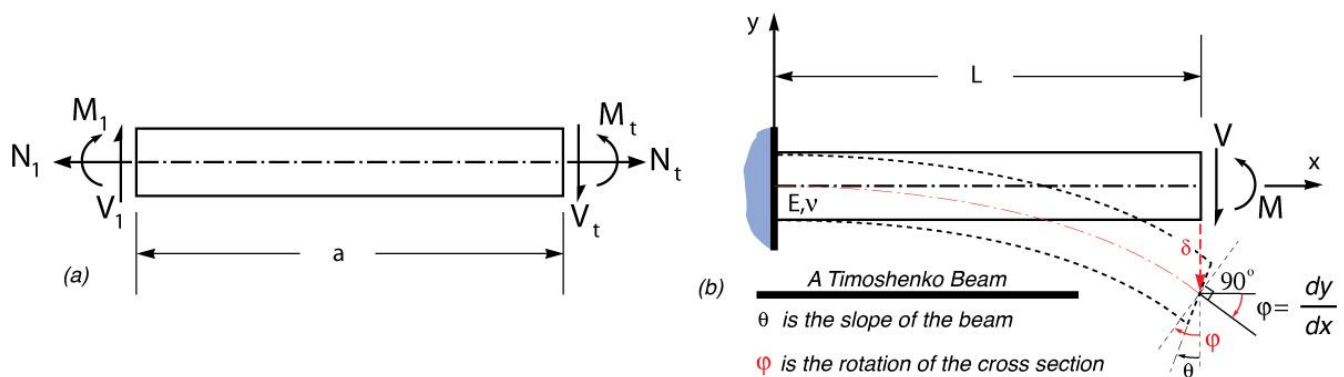


Fig. 6. (a) A free body diagram of the left half of the “top” beam or Beam-2 showing the force and moment resultants acting at interface 1 and mid-section at the crack center. The above schematic along with similar schematics shown in Fig. 5 were used in obtaining the equilibrium equation (7). (b) A Timoshenko cantilever beam subjected to end transverse force V and moment M loading. The

deformed configuration is drawn to distinguish between the beam slope ϑ at the free end and the rotation of the cross section denoted by j used in the compatibility equations.

Where the Timoshenko constant κ [38] appears to influence the deflection δ and slope ϑ , but not the rotation of the cross section measured by j . For clarity purposes, it may be important to note that in a Euler-Bernoulli [39] beam, the deformed cross section remains perpendicular to the neutral axis and thus its rotation is equal to the slope of the beam. However, due to shear effects, in a Timoshenko beam the normal to the deformed cross section may not align with the deformed neutral axis and thus φ may not be equal to ϑ as suggested by Eqn. (8) above and shown schematically in Fig. 6b. With the above in mind, the compatibility at beam interfaces put forward below will be enforced on the cross sectional normal φ and not on the beam slope ϑ which may exhibit discontinuities at beam interfaces due to shear effects.

Introduction of “Transition Regions”. Supported by 2D finite element studies [33], a key contribution of this study is the hypothesis that load transfer through Interfaces 1 through 4 shown in Fig. 5b, takes place in a more convoluted manner within relatively confined transition regions at each of the four-beam interfaces as shown schematically in Figs. 4, 7 and 8. In fact, as will be discussed in this section, the load transfer mechanics through the transition region are shown to result in additional rotations of the cross sections at the crack tip which in this study are captured through rotary and Timoshenko shear springs.

For example, as shown in Fig. 7, the right edge of “Transition Region” 1 is subjected to force and moment resultants N_1, V_1, M_1 , which can be calculated in terms of N_t, V_t, M_t as discussed above. Meanwhile, the left edge of the transition region at cross section A located at a distance λa from the left crack tip ought to be subjected to either the deformation or traction conditions obtained through the beam bending theory as shown in Fig. 7. The force and moment resultants acting on the left edge of the transition region can thus be calculated using the normal and shear stress profiles at Section A as follows (see Fig. 7).

$$N_A^t = w \int_{y=\left(\frac{h}{2}-h_t\right)}^{y=\frac{h}{2}} \sigma_x(y) dy = -\frac{M_A}{2I} (h - h_t) w h_t, \quad (9a)$$

$$V_A^t = w \int_{y=\left(\frac{h}{2}-h_t\right)}^{y=\frac{h}{2}} \tau_{xy}(y) dy = -\frac{V_A I_t}{2I} \left(6 \frac{h}{h_t} - 4 \right), \quad (9b)$$

$$M_A^t = w \int_{y=\left(\frac{h}{2}-h_t\right)}^{y=\frac{h}{2}} y \sigma_x(y) dy = \frac{I_t}{I} M_A. \quad (9c)$$

When comparing the above results to those given by Eqns (3), (5) and (7), one realizes that appreciable gradients in the axial, shear and bending moment resultants must exist in the transition region. For example, the bending moment at A can be expressed in terms of the bending moment at

the crack center location M_C , the applied force P and the distance from the crack center (see Figs. 7 and 8) such that,

$$M_A = M_C - Pa(1 + \lambda) \quad (10)$$

where as before M_C is the bending moment acting at the crack center location in the healthy beam;

P – is a downward transverse load as shown in Fig. 4;

a – is half the crack length;

λa – is the length of a transition region as shown in Figs. 7 and 8.

With the aid of Eqns (5), (7) and (9), one can show that

$$\begin{aligned} N_A^t - N_1 &= M_C \left\{ \frac{2}{h} \left(1 - \frac{I_t}{I} - \frac{I_b}{I} \right) - \frac{h_t h_b}{2I} \right\} + 6P \frac{a}{h} (1 + \lambda) \frac{h_t h_b}{h} \quad \text{and} \\ M_A^t - M_1 &= -Pa(1 + \lambda) \frac{I_t}{I} + V_t a \end{aligned} \quad (11)$$

In the case when the horizontal crack is located on the mid-plane of the healthy beam, i.e., $h_t = h_b = h/2$ it can be shown that $V_t = V_b = P/2$ and thus the axial force and bending moment differences between the quantities at cross section A and Interface 1 are calculated through Eqn. (11) to be,

$$N_A^t - N_1 = \frac{3}{2} P \frac{a}{h} (1 + \lambda) \text{ and } M_A^t - M_1 = \frac{Pa}{8} (3 - \lambda) \quad (12)$$

In the case of $\lambda \rightarrow 0$, the above equations suggest that both the force and moment resultants transferred through the mid-plane of the beams above and below the crack plane would exhibit inadmissible discontinuities in the absence of any external load changes. In fact, in accordance with Eqn. (12) under the condition of $\lambda = 0$, i.e., absence of any transition region, the force and moment discontinuities also shown schematically in Fig. 7, are predicted to be $N_A^t - N_1 = 3Pa/2h$ and $M_A^t - M_1 = 3Pa/8$. These findings form the foundation for the introduction of the transition regions shown in Figs. 7-9.

While the presence of the transition regions would allow the smooth transition of the force and moment resultants from the healthy beam response at section A to the cracked beam mechanics predicted in the crack region, their presence also has a profound effect on the deformation and fracture mechanics of the cracked beam.

In order to better understand the effects of the transition region on the overall beam deformation mechanics, let's consider the axial force and bending moment profiles presented in Fig. 7. The bottom half of the above figure shows a section of the beam in the crack region above the neutral axis of the healthy structure. It includes the left half of the top beam above the crack, or Beam-2 as well as its adjacent transition region labeled as “Transition Region 1”. The transition region is of length a with a being the half crack length. At Interface 1, the resultant forces and moment applied at the mid-plane of the top beam are N_1, V_1 and M_1 . At the left edge of Transition Region 1,

the resultant forces and moment N_A^t, V_A^t and M_A^t are obtained with the aid of Eqn. (9). Profiles of the axial force and bending moment predicted by Eqns (9) through (12) are sketched on the top half of Fig. 7. The profiles shown in solid black lines are predicted using Eqn. (9) for the healthy beam whereas the solid blue line profiles are those obtained with the aid of Eqns (3) through (7) for the crack region. As shown, at Interface 1, the moment and axial force predicted at the left edge of Transition Region 1, i.e., as $\lambda \rightarrow 0$, do not match those predicted by the crack beam model at Interface 1. As discussed earlier, the existence of the transition region is required for the smooth force and moment transition between Section A and Interface 1.

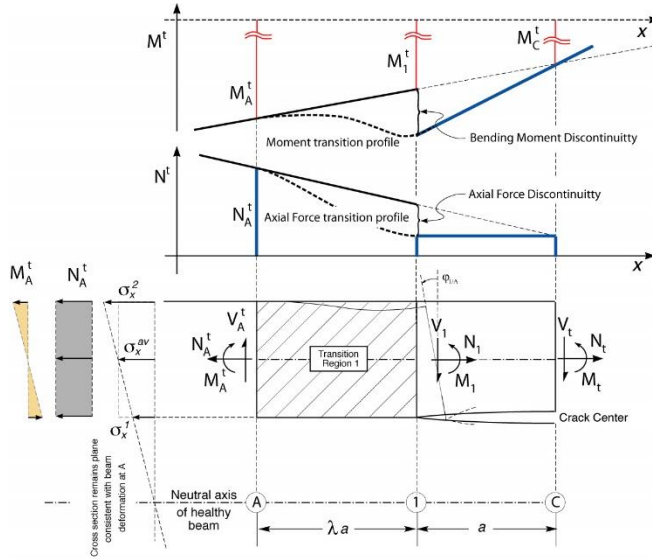


Fig. 7. Schematics showing the profiles of the bending moment and axial force transmitted through the mid-plane of the beam region above the crack plane. The linear profiles on the top left are consistent with the beam theory for the “healthy” beam. The heavy blue lines on the top right represent the profiles predicted by the model developed in this study (see Eqns (3) and (5)). The two results do not match at interface 1 leading to the conclusion that transient profiles are required for the smooth transition between the two profiles. In this study it is postulated that the discrepancy between the two profiles leads to the development of “extra rotations” in the transition region accounted for through rotary springs employed in this study.

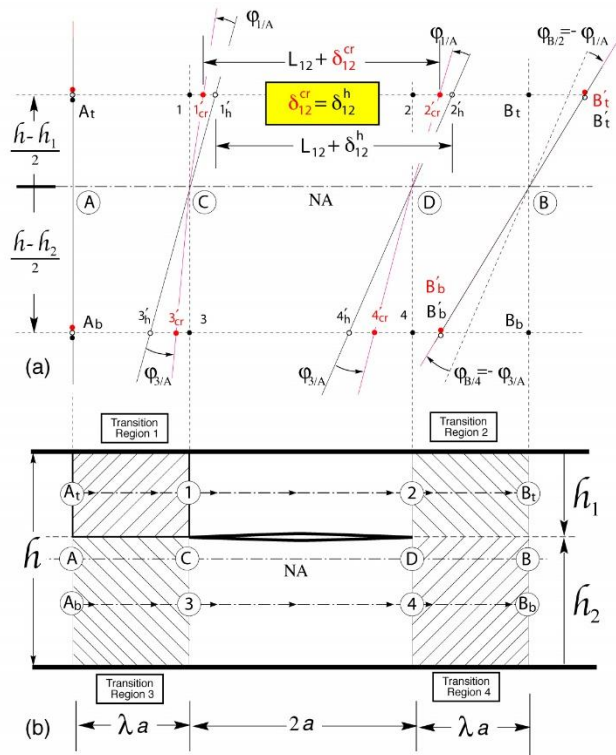


Fig. 8. Schematics showing the relative axial deformations and cross sectional rotations of reference points along the mid-planes of the “top” and “bottom” beams including their adjacent transition regions. Points $A_t \rightarrow 1 \rightarrow 2 \rightarrow B_t$ shown in (b) deformed to locations $A_t \rightarrow 1'_h \rightarrow 2'_h \rightarrow B'_t$ in the “healthy” beam whereas in the “cracked” beam they deformed to locations $A_t \rightarrow 1'_{cr} \rightarrow 2'_{cr} \rightarrow B'_{cr}$ as shown in (a). Similarly, points $A_b \rightarrow 3 \rightarrow 4 \rightarrow B_b$ deformed to $A_b \rightarrow 3'_h \rightarrow 4'_h \rightarrow B'_b$ in the “healthy” and to $A_b \rightarrow 3'_{cr} \rightarrow 4'_{cr} \rightarrow B'_b$ in the “cracked” beams respectively. The above schematics also highlights the accumulation of “extra” rotations $\varphi_{1/A}$ and $\varphi_{3/A}$ in the left transition regions which are offset by “extra rotations” $\varphi_{B/2}$ and $\varphi_{B/4}$ in the right transition regions.

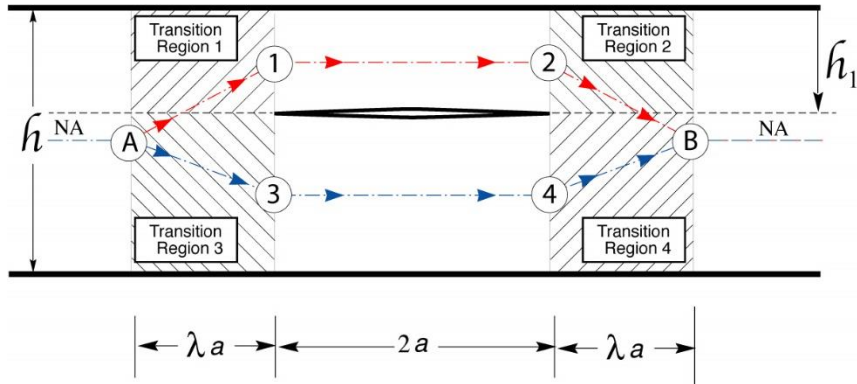


Fig. 9. The compatibility paths followed through the “top” and “bottom” beams in establishing angle of rotation and deflection compatibility conditions from reference section A to reference section B. Also shown are Transition Regions 1-4.

It is reasonable to assume that both the force and moment transitional profiles would be of the general type shown by the transitional profiles in dash black lines in Fig. 7. Under such conditions, reduction in both the force and moment resultants relative to the healthy beam, would result in lower axial strains along the mid-plane of the transition region and thus a comparatively lower extension of the transition region mid-plane relative to its healthy counterpart. This would appear in the cracked beam as a change in the rotary compliance giving rise to an additional angle of rotation $\varphi_{1/A}$ at Interface 1 as shown schematically in Figs. 7 and 8. A similar load transfer and deformation mechanism would exist in Transition Region 3 connecting Section A to the left end of the bottom beam at Interface 3. However, the axial force in the bottom beam being the opposite of that dominating the top beam would result in an added rotation in the same sense as that for Interface 1. The actual amount of added rotations should depend on the extent and thickness of the transition region and should be proportional to the cross sectional resultants N_1, V_1 and M_1 . Since the axial force $N_1 = N_t$ with N_t linearly depending on M_t through Eqn. (5), while M_1 and M_t are linearly related through V_t and a in Eqn. (7), the following rotary and shear deformation equations are proposed for each transition region,

$$\varphi_{1/A} = \frac{M_1 \lambda a}{\kappa_1^m EI_t} \quad \text{and} \quad \delta_{1/A} = \frac{V_1 \lambda a}{k_t G A_t} \quad \text{For Transition Region 1} \quad (13a)$$

$$\varphi_{2/B} = \frac{M_2 \lambda a}{\kappa_1^m EI_t} \quad \text{and} \quad \delta_{2/B} = \frac{V_2 \lambda a}{k_t G A_t} \quad \text{For Transition Region 2} \quad (13b)$$

$$\varphi_{3/A} = \frac{M_3 \lambda a}{\kappa_3^m EI_b} \quad \text{and} \quad \delta_{3/A} = \frac{V_3 \lambda a}{k_b G A_b} \quad \text{For Transition Region 3} \quad (13c)$$

$$\varphi_{4/B} = \frac{M_4 \lambda a}{\kappa_3^m EI_b} \quad \text{and} \quad \delta_{2/B} = \frac{V_4 \lambda a}{k_b GA_b} \quad \text{For Transition Region 4} \quad (13d)$$

where κ_1^m and κ_3^m are the normalized rotary spring stiffness constants to be determined through compatibility conditions;

k_t and k_b are Timoshenko shear constants for the top and bottom beams respectively.

In postulating the above relations, it was assumed that the rotary and shear spring constants for Interfaces 1 and 2 are the same as well as those of Interfaces 3 and 4. It may be of importance to note that due to the anti-symmetry of the force and moment resultants jumps between Sections *A* and Interface 1 at the left crack tip and Interface 2 and Section *B* at the right crack tip as shown in Fig. 8, the added rotations capture by the above equations and occurring in Transition Region 1 would be offset by the added rotations at Interface 2 induced by the load and deformation mechanics in Transition Region 2. In fact, this observation has been validated using 2D finite elements and will be used as one of the compatibility conditions needed to determine the rotary and shear spring constants.

The above observation is further clarified with the aid of Figs. 8 and 9. In the above figures, emphasis is placed on the axial deformation of two reference lines, i.e., the mid-plane line segment of the top beam passing through the reference points $A_t \rightarrow 1 \rightarrow 2 \rightarrow B_t$ and its bottom beam counterpart passing through points $A_b \rightarrow 3 \rightarrow 4 \rightarrow B_b$. The red solid symbols represent the deformed position of the respective points in the cracked beam if the reference line was to stay straight whereas the open white symbols represent the corresponding deformed location of the same reference points in the healthy beam. In Fig. 8, all deformations are sketched relative to those at a reference cross section at *A*. For a downward applied load *P* the “beam” above the crack is subjected to tension whereas the one below the crack is subjected to compression. Consistent with the gradient force and moment profiles shown in Fig. 7 and discussed above, the line segment $A_t \rightarrow 1$ in Transition Region 1, would stretch less than its healthy beam counterpart. Thus the relative cracked beam and healthy beam deformed states are different as denoted by the $1'_{cr}$ and $1'_h$ positions with the latter being further to the right. Since no overall tension is applied to the beam structure, the neutral axis of the healthy beam would remain inextensible. When connecting the deformed reference points of the cracked beam and the healthy beam to their neutral axis counterpart a differential $\varphi_{1/A}$ angle of rotation is obtained when comparing the cracked and healthy beam systems. As discussed above, this rotation is postulated in this study to depend linearly on the cross sectional moment resultant M_1 , the transition region length λa , while inversely proportional to an effective bending stiffness EI_t multiplied by a proportionality constant κ_1^m given by Eqn. (13a). Interestingly enough, a similar effect appears at Interface 3 through the compression and reduction of length arguments for line segment $A_b \rightarrow 3$ in Transition Region 3. In both instances, changes in the effective rotation of Interfaces 1 and 3 relative to the rotation of the healthy beam are predicted. At this stage, it is not apparent as to whether the predicted extra rotations $\varphi_{1/A}$ and $\varphi_{3/A}$ are related to each other and what that relationship is. As such, $\varphi_{3/A}$ is postulated to be proportional to the moment resultant M_3 at Interface 3 and inversely proportional to the effective bending stiffness $\kappa_3^m EI_b$.

While a differential rotation between the healthy and the cracked beam is predicted at Interfaces 1 and 3, it can be shown that the line segments 1 → 2 in the beam above the crack (top beam) and 3 → 4 in the beam below the crack (bottom beam) experience identical stretching or shrinkage in the cracked and healthy beams. This can be proven by integrating the axial strain $\varepsilon_x(x, y)$ along the respective paths in the cracked and healthy beams such that,

$$\int_{x=x_1}^{x=x_2} \varepsilon_x^{cr} \left(x, y = \frac{h-h_t}{2} \right) dx = \int_{x=x_1}^{x=x_2} \varepsilon_x^h \left(x, y = \frac{h-h_t}{2} \right) dx \quad (14)$$

In light of the above, the differential rotations between the cracked and healthy beam associated with Interfaces 1 and 3 remain as such at Interfaces 2 and 4. However, given the anti-symmetry of the force and moment resultant difference between the healthy and cracked beams relative to the crack center, differential rotations take place in Transition Regions 2 and 4 in the opposite sense of those occurring in Transition Regions 1 and 3 fully offsetting one another at reference point B as suggested by the 2D Finite Element results reported elsewhere [33] and in Fig. 2. In this study, the transition crack lengths in all four transition regions are assumed to be equal while making the added rotations to be linearly dependent on the respective bending moment resultants as reflected by Eqn. (13). All rotary spring stiffness proportionality constants, i.e., κ_1^m and κ_3^m along with the transition region length parameter l are to be determined through the compatibility conditions which shall be implemented next.

Compatibility of cross-sectional rotations. Cross sectional rotation and neutral axis deflection compatibility shall be enforced between Sections A and B following two separated paths along the top ($A \rightarrow 1 \rightarrow 2 \rightarrow B$) and bottom ($A \rightarrow 3 \rightarrow 4 \rightarrow B$) beams as shown in Fig. 9. More specifically, for compatibility purposes, it is required that,

$$\varphi_B = \varphi_A + \varphi_{1/A} + \varphi_{2/1} + \varphi_{B/2} = \varphi_A + \varphi_{3/A} + \varphi_{4/3} + \varphi_{B/4} \quad (15)$$

where φ_A and φ_B are the rotations of Sections A and B respectively while $\varphi_{1/A}$, $\varphi_{2/1}$ and $\varphi_{B/2}$ represent the relative rotations between Sections 1 and A, 2 and 1, and B and 2 respectively as shown schematically in Fig. 10.

The above equation is equivalent to state that $\varphi_{B/A}^t = \varphi_{B/A}^b$, or the change of the cross sectional rotation from A and B calculated through the mechanics of Transition Region 1, Beam-2 and Transition Region 2 should be identical to that calculated through the mechanics of Transition Region 3, Beam-3, and Transition Region 4. Thus, after eliminating φ_A appearing at both sides of Eqn. (15) the above compatibility equation simplifies to,

$$\varphi_{1/A} + \varphi_{2/1} + \varphi_{B/2} = \varphi_{3/A} + \varphi_{4/3} + \varphi_{B/4} \quad (16)$$

As discussed earlier in this study, when a Timoshenko beam is used, the rotational compatibility condition is imposed on the rotation of the cross section and not the slope of the beam consistent

with Eqn. (8). The individual terms appearing in Eqn. (16) can be obtained using the postulated transition region equation (13) and the Timoshenko beam equation (8) as follows,

$$\begin{aligned}
 \varphi_{1/A} &= \frac{M_1 \lambda a}{\kappa_1^m EI_t} & \varphi_{3/A} &= \frac{M_3 \lambda a}{\kappa_3^m EI_b} \\
 \varphi_{2/1} &= -\frac{V_2 (2a)^2}{2EI_t} + \frac{M_2 (2a)}{EI_t} & \text{and} & \varphi_{4/3} &= -\frac{V_4 (2a)^2}{2EI_b} + \frac{M_4 (2a)}{EI_b} \\
 \varphi_{B/2} &= \frac{M_2 \lambda a}{\kappa_1^m EI_t} & \varphi_{B/4} &= \frac{M_4 \lambda a}{\kappa_3^m EI_b} & (17)
 \end{aligned}$$

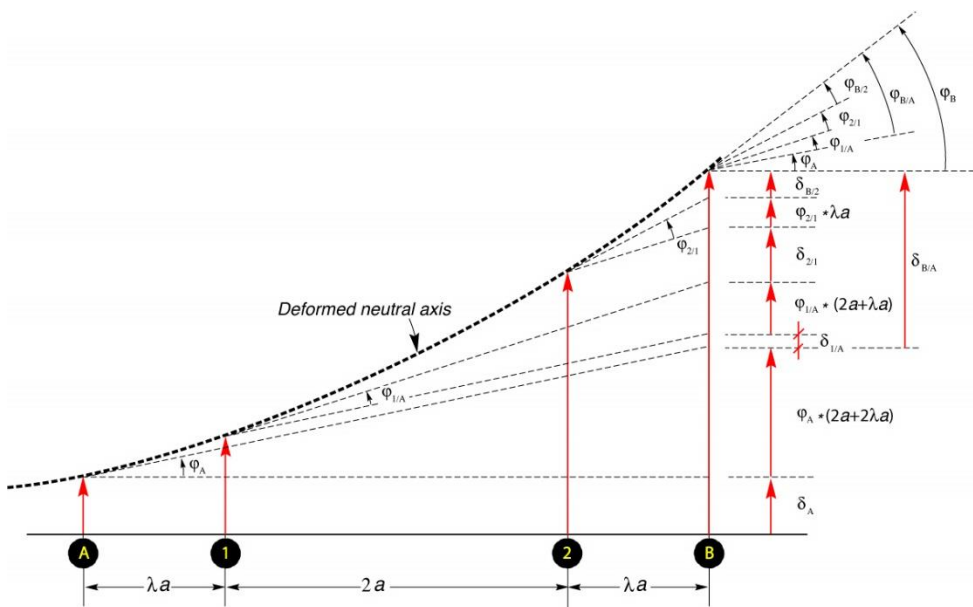


Fig. 10. The deformed neutral axis of a “continuous” beam from the reference cross section A to the reference cross section B highlighting the relations between cross sectional rotations and deflections along the compatibility path A_t → 1 → 2 → B_t shown in Figs. 8 and 9.

In the above equations, the assumption was made that $\kappa_1^m = \kappa_2^m$ and $\kappa_3^m = \kappa_4^m$. When substituting Eqn. (17) into (16), the following relationship is obtained,

$$\frac{M_t 2a}{EI_t} \left(\frac{\lambda}{\kappa_1^m} + 1 \right) = \frac{M_b 2a}{EI_b} \left(\frac{\lambda}{\kappa_3^m} + 1 \right) \quad (18)$$

Now utilizing Eqn. (2), i.e., $M_t / I_t = M_b / I_b = M_C / I$, the above relation yields,

$$\kappa_1^m = \kappa_3^m \quad (19)$$

Compatibility of deflections. Assisted by the deformation schematic shown in Fig. 10, the deflection at section *B* of the cracked beam can be obtained using the principle of linear superposition as follows,

$$\delta_B = \delta_A + \delta_{1/A} + \varphi_{1/A}(2 + \lambda)a + \delta_{2/1} + \varphi_{2/1}\lambda a + \delta_{B/2} \text{ using the } A \rightarrow 1 \rightarrow 2 \rightarrow B \text{ path} \quad (20)$$

or

$$\delta_B = \delta_A + \delta_{3/A} + \varphi_{3/A}(2 + \lambda)a + \delta_{4/3} + \varphi_{4/3}\lambda a + \delta_{B/4} \text{ using the } A \rightarrow 3 \rightarrow 4 \rightarrow B \text{ path}$$

The relative deflections $\delta_{1/A}, \delta_{3/A}, \delta_{B/2}$ and $\delta_{B/4}$ are related to the load transfer and deformation mechanics within the four transition regions. As discussed earlier in this work, the axial force and bending moment transition region effects lead to a postulated change in the angle of rotation at Interfaces 1 through 4. As such, the relative deflection due to shear in the same transition region should be related to the application of the total resultant shear force which in the system under study equals the applied load P . Thus, the relative deflections at the mid-plane at Interfaces 1 and 3 at the left tip and Interfaces 2 and 4 at the right crack tip ought to be equal and most likely given by the Timoshenko shear term. In any case, since $\delta_{1/A} = \delta_{3/A}$ and $\delta_{B/2} = \delta_{B/4}$, the deflection compatibility condition must take the form,

$$\delta_{B/A}^t = \delta_{B/A}^b \quad (21)$$

which can be expressed as follows,

$$\varphi_{1/A}(\lambda + 2)a + \delta_{2/1} + \varphi_{2/1}\lambda a = \varphi_{3/A}(\lambda + 2)a + \delta_{4/3} + \varphi_{4/3}\lambda a \quad (22)$$

Again using the Timoshenko formulas given in Eqn. (8), the individual terms appearing in Eqn. (22) are given in terms of the cross sectional resultants and beam geometry and structural stiffnesses as follows,

$$\varphi_{1/A} = \frac{M_1 \lambda a}{\kappa_1^m EI_t}$$

$$\varphi_{3/A} = \frac{M_3 \lambda a}{\kappa_3^m EI_b}$$

$$\delta_{2/1} = -\frac{V_2(2a)^3}{3EI_t} + \frac{M_2(2a)^2}{2EI_t} - \frac{V_t 2a}{k_t GA_t} \quad \text{and} \quad \delta_{2/1} = -\frac{V_4(2a)^3}{3EI_b} + \frac{M_4(2a)^2}{2EI_b} - \frac{V_b 2a}{k_b GA_b} \quad (23)$$

$$\varphi_{2/1} = -\frac{V_2(2a)^2}{2EI_t} + \frac{M_2(2a)}{EI_t} \quad \varphi_{2/1} = -\frac{V_4(2a)^2}{2EI_b} + \frac{M_4(2a)}{EI_b}$$

where k_t and k_b – are the Timoshenko constants for Beam-2 and Beam-3 respectively.

By substituting the rotations and deflections given by Eqn. (23) into their respective equivalents in (22) and by making use the moment relations given in Eqn. (7), we arrive at the following deflection compatibility equation,

$$\begin{aligned} \frac{M_t a^2}{EI_t} \left[\frac{1}{\kappa_1^m} \lambda(2 + \lambda) + 2(1 + \lambda) \right] - \frac{V_t a^3}{EI_t} \left[\frac{1}{\kappa_1^m} \lambda(2 + \lambda) + \frac{2}{3} \right] - \frac{V_t 2a}{k_t GA_t} = \\ = \frac{M_b a^2}{EI_b} \left[\frac{1}{\kappa_3^m} \lambda(2 + \lambda) + 2(1 + \lambda) \right] - \frac{V_b a^3}{EI_b} \left[\frac{1}{\kappa_3^m} \lambda(2 + \lambda) + \frac{2}{3} \right] - \frac{V_b 2a}{k_b GA_b} \end{aligned} \quad (24)$$

It has already been established that $\kappa_1^m = \kappa_3^m$ (see Eqn. (19)), and given the fact that $M_t / I_t = M_b / I_b = M_C / I$, the above equation further simplifies to the following shear force ratio equation.

$$\frac{V_t}{V_b} = \frac{I_t}{I_b} \frac{\frac{1}{\kappa_1^m} \lambda(2 + \lambda) + 2(1 + \lambda) + \frac{2}{k_b} \frac{I_b}{A_b a^2} \frac{E}{G}}{\frac{1}{\kappa_1^m} \lambda(2 + \lambda) + 2(1 + \lambda) + \frac{2}{k_t} \frac{I_t}{A_t a^2} \frac{E}{G}} \quad (25)$$

It is obvious that in order to establish the above shear force ratio, κ_1^m and $/$ need to be determined through additional conditions as will be discussed below. However, it is worth noting that when ignoring the Timoshenko shear effects, i.e., letting k_t and $k_b \rightarrow \infty$, then the following simple form for the shear force ratio is obtained,

$$\frac{V_t}{V_b} = \frac{I_t}{I_b} \quad (26)$$

It is also noteworthy to observe for systems in which the crack is on the beam neutral axis (i.e., $h_1 = h_2$), both Eqns. (25) and (26) predict that the shear force ratio between the shear resultants in the top and bottom beam is $V_t/V_b = 1$ and thus from the global equilibrium enforced by Eqn. (6), it can be shown that $V_t = V_b = P/2$. As will be discussed later, shear force predictions obtained by the present model were found to compare very well with 2D finite element results.

Calculating the normalized

rotary spring stiffness. Of the two remaining unknowns, i.e., k_1^m and I , the normalized rotary spring stiffness k_1^m can be estimated using the second key observation from 2D finite elements (see Fig. 2), i.e., *the neutral axis rotation (slope) of the cracked beam in the region between the applied load and the nearest crack tip matches the corresponding slope of the healthy beam*. The above observation leads to the following condition,

$$\varphi_{B/A}^{cr} = \varphi_{B/A}^h \quad (27)$$

where the superscripts cr and h denote quantities for the cracked and healthy beams respectively. The left hand side of the above equation is equal to the left hand side of Eqn. (18). Thus, the above relation can be written in terms of the moment and shear force resultants as follows,

$$\varphi_{B/A}^{cr} = \frac{M_t 2a}{EI_t} \left(\frac{\lambda}{\kappa_1^m} + 1 \right) = \varphi_{B/A}^h = -\frac{V_B (2a(1+\lambda))^2}{2EI} + \frac{M_B 2a(1+\lambda)}{EI} \quad (28)$$

where $V_B = P$ and $M_B = M_C + Pa(1+\lambda)$.

In light of the above, Eqn. (28) above takes the form,

$$\frac{M_t 2a}{EI_t} \left(\frac{\lambda}{\kappa_1^m} + 1 \right) = \frac{M_C 2a}{EI} (1 + \lambda) \quad (29)$$

Again utilizing Eqn. (2), i.e., $M_t/I_t = M_b/Ib = M_C/I$, the above equation reduces to

$$\frac{M_C 2a}{EI} \left(\frac{\lambda}{\kappa_1^m} - \lambda \right) = 0 \quad \text{which leads to } \kappa_1^m = 1 \quad (30)$$

The above finding along with Eqn. (19) suggest that $k_1^m = k_3^m = 1$ and thus the rotary spring stiffnesses are as follows,

$$\begin{aligned}\kappa_1 &= M_1 / \varphi_{1/A} = EI_t / \lambda a, & \kappa_2 &= M_2 / \varphi_{B/2} = EI_t / \lambda a \\ \kappa_3 &= M_3 / \varphi_{3/A} = EI_b / \lambda a, & \kappa_4 &= M_4 / \varphi_{B/4} = EI_b / \lambda a\end{aligned}\quad (31)$$

where λa is the extent of the transition regions to be determined next.

On the transition region. The above findings reflected through Eqn. (31), highlight the importance of the transition regions in understanding the load transfer and deformation mechanics in a beam with a horizontal sharp crack. The postulated rotations at Interfaces 1 through 4 at the left and right crack tips are found to depend on the extent or length of the transition region $/ a$. Thus, the full development of the four-beam model proposed in this study requires the determination of the transition region length $/ a$. As will be presented later on in this section, in this study we make use of an independent beam deflection estimate at the free end obtained numerically via the method of finite elements. Thus by matching the beam deflection estimated through the beam model to that obtained through finite elements, a non-linear equation in $/$ is obtained through which estimates for the normalized transition region length. However, before developing the consistency equation in $/$, it may be of value to this and subsequent studies to consider the load transfer and deformation mechanics in the transition regions. For example, let us consider the mechanics of Transition Region 1, shown in Fig. 11. As shown in the above figure, on the left edge of the above transition region, the force and moment resultants would be those obtained from the bending theory consistent with Eqn. (9) as discussed earlier. On the right edge, different moment and force resultants are applied consistent with the mechanics of the cracked beam presented earlier in this study. As discussed earlier, the rotary beam changes relative to the healthy.

can be attributed to the load transfer through the transition region in which the resultants obtained on the left edge must transition to the resultants estimated for the right edge. At this point one has to also account for the singular stress field dominating the crack tip region. For example, based on the crack tip region reference system x', y' shown in Fig. 11, the normal stress $\sigma_x(y)$ acting on the vertical interface 1 in the crack tip region can be obtained by evaluating the respective crack tip stress at $\theta' = -90^\circ$, i.e.,

$$\begin{aligned}\sigma_x(y) &= \sigma_{x'} \left(r', \theta' = -\frac{\pi}{2} \right) = \frac{K_I}{\sqrt{2\pi r}} \cos\left(\frac{\theta'}{2}\right) \left(1 - \sin\left(\frac{\theta'}{2}\right) \sin\left(\frac{3\theta'}{2}\right) \right)_{\theta'=-\frac{\pi}{2}} \\ &+ \frac{K_{II}}{\sqrt{2\pi r}} \left(-\sin\left(\frac{\theta'}{2}\right) \right) \left(2 + \cos\left(\frac{\theta'}{2}\right) \cos\left(\frac{3\theta'}{2}\right) \right)_{\theta'=-\frac{\pi}{2}} = \frac{1}{4\sqrt{\pi}} (K_I + 3K_{II}) y^{-1/2}\end{aligned}\quad (32)$$

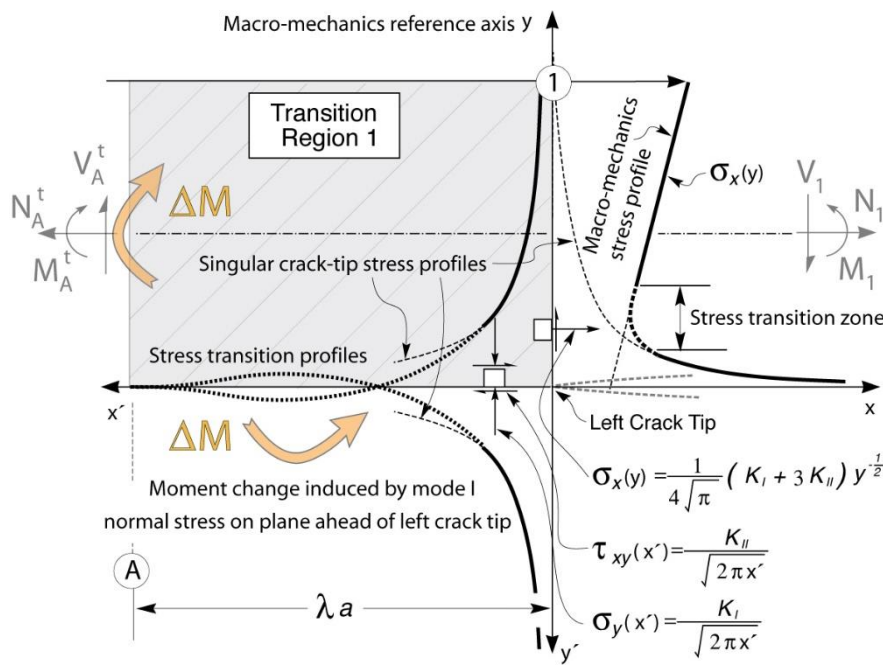


Fig. 11. Schematics of potential transition region stress fields that are superimposed onto those of the healthy beam. These fields are shown to conform to the near-tip mixed mode fields near the crack tip region and to the macro-mechanical field differences sufficiently away from the crack tip. As shown, a change of moment ΔM is induced by the mode I component of the stress intensity factor on the crack plane ahead of the left crack tip. An equal and opposite moment change then must occur on the left vertical plane of the transition region thus causing a slight “bump” on the moment and associated curvature profile at the start of the transition region as shown in Fig. 3.

The above singular stress profile is shown in Fig. 11 with a heavy solid line in the proximity of the crack tip continuing with a light dash line away from the singular region. Meanwhile, sufficiently away from the crack tip region, the same stress component must follow the linear mechanics of material profile predicted by the system macro mechanics. As shown in Fig. 11, a stress transition region must also exist as needed for the smooth transition of the $\sigma_x(y)$ component between the two fields. It is reasonable to expect that such a stress profile that accounts for both the finite macro mechanics profile as well as the singular near-tip profile would cause a shift of the plane on which the force resultant is effectively acting. A similar argument can be made for the shear stress acting on the same vertical plane (i.e., Interface 1) as well as for the normal $\sigma_x(y)$ and shear $\tau_{xy}(x)$ profiles acting on the horizontal transition region edge ahead of the crack tip. Such observations would naturally lead to the conclusion that a rather convoluted stress field dominates the transition region and that its structure and intensity should also depend on the stress intensity factors K_I , K_{II} associated with the related crack tip. With this in mind, it is expected that the extent of the transition region λa should include information related to the crack-tip domain and thus could depend on the structure of the mixed mode [40-45] singular fields and possibly the magnitude of the related stress intensity factor.

Another relevant observation is that the presence of even a slight mode I component would induce a tensile normal stress if $K_I > 0$ associated with crack tip opening, or compressive if $K_I < 0$ associated with crack surface contact as shown schematically in Fig. 11. The presence of such a stress close to the crack tip will need to be offset by an opposite stress resultant away from the crack tip in the transition region. Such a stress profile would then induce a net moment ΔM on the plane

ahead of the crack tip in the transition region which ought to be counter-balanced by an equal and opposite moment on the vertical left edge of the transition region. Such a moment change could explain the free surface curvature “bump” observed via finite elements as shown in Fig. 3. Thus, the presence of such a curvature “bump” could indicate the existence of crack damage in the vicinity of such a measurement used in non-model damage detection methods [46-49].

Given the above qualitative considerations regarding the mechanics of the transition region, several methods can be employed in calculating the relationship between δ and the various problem variables that may affect the local stress intensities. One such method is to evaluate the crack-tip stress intensities and or associated energy release rate using either a compliance method [28-31, 50] or a J -integral approach [40] based on the model findings of this study. Those estimates can then be compared to independent estimates obtained for example using the method of finite elements which will then yield a consistency equation in δ . Yet, another possible approach is to extract the transition domain and conduct rigorous numerical and possibly theoretical studies in solving the requisite boundary value problem thus required to establish the load transfer and deformation mechanics of the transition region. Such an approach would allow for parametric studies needed to establish the relative deformation of the right edge of the transition region relative to the left. Such estimates would be used in determining the differential deformation between the cracked and healthy structures thus giving estimates of the rotary changes induced by the introduction of the crack and thus obtained estimates of the rotary spring stiffnesses which can then be used to obtain the transition length constant λ through Eqn. (31). Such studies are currently being pursued which are expected to be presented in future works. In this work however, we employ a beam deflection matching alternative in determining the transition length constant λ as discussed below.

Beam deflection matching. The global mechanics of a beam with a crack includes the effects of the crack tip regions. Thus, the beam deformations anywhere in its domain including the deflection at its free end include the effects of the dominant stress intensity factors at both crack tips. Thus, one can use a known solution obtained by any other method including experimental techniques and numerical approaches such as the method of finite elements, to calibrate the four-beam model developed in this study as an effective way to calculating the transition length constant λ .

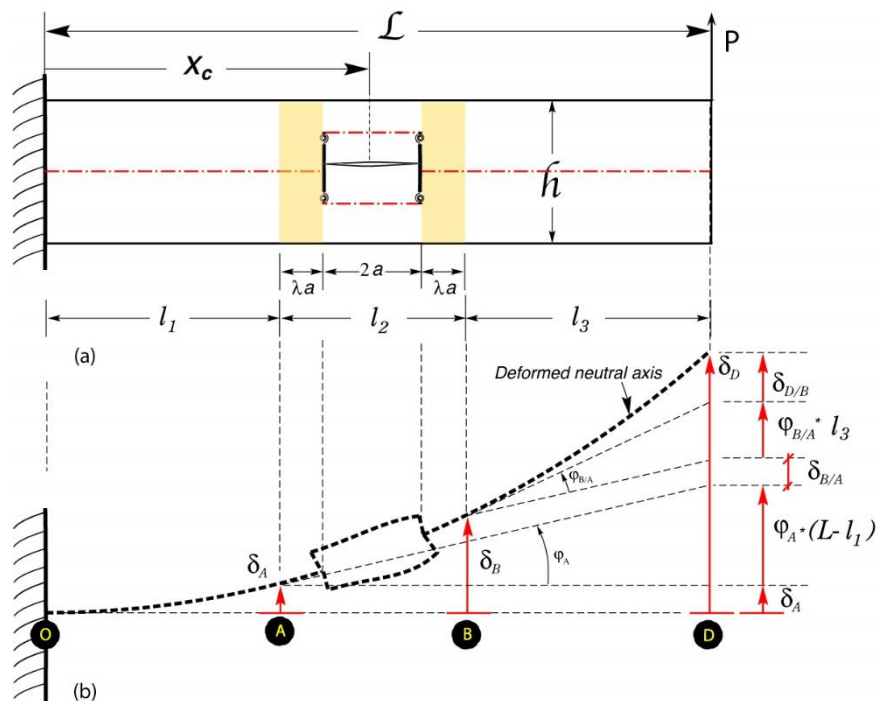


Fig. 12. A schematics showing (a) the original cracked beam with its un-deformed neutral axis and (b) the deformed neutral axis configuration of the four beam model. The relationship between the deflections and rotations at key reference points of the beam are also shown in (b). The deformations and rotations between Sections A and B include the transition region effects captured by the rotary spring and Timoshenko shear effects.

With the aid of Fig. 12, the deflection of the beam at its free end at D is given by,

$$\delta_D = \delta_A + \varphi_A(L - l_1) + \delta_{B/A} + \varphi_{B/A}l_3 + \delta_{D/B} \quad (33)$$

where $\delta_{B/A}$ and φ_A – are the deflection and angle of rotation at the cross section A at the start of the transition region at the left crack tip;

$\delta_{B/A}$ and $\varphi_{B/A}$ – are the deflection and angle of rotation respectively of Section B at the end of the transition region at the right crack tip relative to A ;

and $\delta_{D/B}$ – is the deflection of the free end at D relative to B .

It is important to note that in this analysis, the effects of the transition regions are included in the relative terms $\delta_{B/A}$ and $\varphi_{B/A}$, and thus do not appear directly in Eqn. (33) above. Using the Timoshenko formulas for the deflection and rotations of a cantilever beam given in Eqn. (8) along with the outcomes on the relative deformations of Section B relative to A used earlier in this study the individual terms appearing in Eqn. (33) take the form,

$$\delta_A = -\frac{Pl_1^3}{3EI} - \frac{P(L-l_1)l_1^2}{2EI} - \frac{Pl_1}{kGA} \text{ and } \varphi_A = -\frac{Pl_1^2}{2EI} - \frac{P(L-l_1)l_1}{EI} \quad (34a)$$

$$\delta_{B/A} = \frac{M_t a^2}{EI_t} \left[\frac{1}{\kappa_1^m} \lambda(2 + \lambda) + 2(1 + \lambda) \right] - \frac{V_t a^3}{EI_t} \left[\frac{1}{\kappa_1^m} \lambda(2 + \lambda) + \frac{2}{3} \right] - \frac{V_t 2a}{k_t G A_t} - \frac{P 2 \lambda a}{kGA} \quad (34b)$$

$$\varphi_{B/A} = \frac{M_t 2a}{EI_t} \left(\frac{\lambda}{\kappa_1^m} + 1 \right) \quad (34c)$$

$$\delta_{D/B} = -\frac{Pl_3^3}{3EI} - \frac{Pl_3}{kGA} \quad (34d)$$

where $l_1 = x_C - a(1 + \lambda)$, $l_2 = 2a(1 + \lambda)$, $l_3 = L - (x_C + a(1 + \lambda))$, $M_t/I_t = M_C/I$, and $M_C = -P(L - x_C)$. Also in the above formulas, $\kappa_1^m = 1$ consistent with Eqn. (30) while V_t can be expressed in terms of the load P and the shear force ratio V_t/V_b given by Eqn. (25). Furthermore, in Eqn. (34), the constants k and k_t are the Timoshenko shear constants for the healthy beam and Beam-2 above the crack respectively. Thus using the above equations and after normalizing each term with respect to a characteristic deflection $\Delta = PL^3/EI$, the following consistency condition in which the only unknown is the transition region length constant λ is obtained,

$$\delta_D = -\frac{PL^3}{EI} \left\{ \hat{\delta}_A + \hat{\phi}_A(1 - \hat{l}_1) + \hat{\delta}_{B/A} + \hat{\phi}_{B/A} \hat{l}_3 + \hat{\delta}_{D/B} \right\} = -\frac{PL^3}{EI} \left\{ \frac{1}{12} \left(\frac{h}{L} \right)^3 \hat{\delta}^{FE}_D \right\} \quad (35)$$

Where the $\hat{\cdot}$ symbol denotes normalized quantities with all length quantities normalized with respect to the beam length L and $E' = E/(1-\nu^2)$ is used to convert the beam plane stress to its plane strain equivalent solution. Also in the above consistency equation, $\hat{\delta}_D^{FE}$ is the absolute value of the deflection of the cracked beam at its free end obtained through non-dimensional FE simulations as will be discussed later in the study. In light of the above normalization, the following expanded form of the consistency equation in $/$ is obtained,

$$\begin{aligned} \delta_D^{MM} = & -\frac{(1-\nu^2)PL^3}{EI} \left\{ \frac{1}{3} \hat{l}_1^3 + \frac{1}{2} (1 - \hat{l}_1) \hat{l}_1^2 + \frac{(\hat{l}_1 + \hat{l}_3)(1 + \nu)}{6k} \left(\frac{h}{L} \right)^2 + \left(\frac{1}{2} \hat{l}_1^2 + (1 - \hat{l}_1) \hat{l}_1 \right) (1 - \hat{l}_1) \right. \\ & \left. + (1 - \hat{x}_C) \hat{a}^2 (2 + 4\lambda + \lambda^2) + \frac{V_t}{P} \frac{I}{I_t} \hat{a}^3 \left(\frac{2}{3} + \lambda(2 + \lambda) \right) + \frac{V_t}{P} \frac{\hat{a}(1 + \nu)}{3k_t} \left(\frac{h}{L} \right)^2 \frac{h}{h_1} \right. \\ & \left. + \frac{\lambda \hat{a}(1 + \nu)}{6k} \left(\frac{h}{L} \right)^2 + (1 - \hat{x}_C) 2\hat{a}(1 + \lambda) \hat{l}_3 + \frac{1}{3} \hat{l}_3^3 \right\} = -\frac{PL^3}{EI} \left\{ \frac{1}{12} \left(\frac{h}{L} \right)^3 \hat{\delta}^{FE}_D \right\} \end{aligned} \quad (36)$$

As established earlier (see Eqn. (25), the shear force ratio can be expressed as follows,

$$\frac{V_t}{V_b} = \frac{I_t}{I_b} \gamma(\lambda) \quad (37)$$

where

$$\gamma(\lambda) = \frac{2 + 4\lambda + \lambda^2 + \frac{(1 + \nu)}{3k_b} \left(\frac{h_2}{a} \right)^2}{2 + 4\lambda + \lambda^2 + \frac{(1 + \nu)}{3k_t} \left(\frac{h_1}{a} \right)^2} \quad (38)$$

Clearly, when $h_1 = h_2$, and the Timoshenko constants $k_t = k_b$, the factor $\gamma = 1$ and thus $V_t/V_b = 1$ which yields $V_t/P = 1/2$. It is also worth noting that when ignoring the Timoshenko shear effects, i.e., $k_t, k_b \rightarrow \infty$, then $\gamma = 1$ and the ratio V_t/V_b and thus V_t/P become independent of $/$. Regardless, the consistency equation given by (36) takes on the following form in $/$,

$$a(/)^2 + b(/) + h(/) = 0 \quad (39)$$

where the equation coefficients are functions of λ either explicitly as shown below or implicitly through the beam lengths $\hat{l}_1(\lambda)$, $\hat{l}_2(\lambda)$, $\hat{l}_3(\lambda)$ and are given by,

$$\begin{aligned}
 \alpha(\lambda) &= (1 - \hat{x}_C) \hat{a}^2 + \frac{\mathcal{I}}{I_b + \mathcal{I}_t} \hat{a}^3, \\
 \beta(\lambda) &= 4(1 - \hat{x}_C) \hat{a}^2 + 2 \frac{\mathcal{I}}{I_b + \mathcal{I}_t} \hat{a}^3 + 2(1 - \hat{x}_C) \hat{a} \hat{l}_3 + \frac{\hat{a}(1 + \nu)}{6k} \left(\frac{h}{L} \right)^2, \\
 \eta(\lambda) &= \frac{1}{3} (\hat{l}_1^3 + \hat{l}_3^3) + (1 - \hat{l}_1) \hat{l}_1^2 + \hat{l}_1 (1 - \hat{l}_1)^2 + 2\hat{a}(1 - \hat{x}_C)(\hat{a} + \hat{l}_3) \\
 &+ \frac{V_t}{P} \left[\frac{2}{3} \frac{I}{I_t} \hat{a}^3 + \frac{(1 + \nu)}{3k_t} \hat{a} \left(\frac{h}{L} \right)^2 \frac{h}{h_1} \right] + \frac{(1 + \nu)(\hat{l}_1 + \hat{l}_3)}{6k} \left(\frac{h}{L} \right)^2 \\
 &- \frac{1}{12(1 - \nu^2)} \left(\frac{h}{L} \right)^3 \hat{\delta}_D^{FE}
 \end{aligned} \tag{40}$$

In the above equation, the finite element term is divided by the $(1 - \nu^2)$ factor as needed to match the beam plane stress and the 2D FE plane strain solutions. The above consistency equation in λ will be solved for several cases wherein the horizontal crack is placed at different locations along the length and height of the beam. However, in order to carry out this task, finite element solutions for the non-dimensional deflection of the beam at the free end will need to be obtained. Thus, a brief description of the finite element models used in these simulations would be discussed in the second part, i.e., Part B of this report.

Summary. This study represents the first part of a two-part study aimed at modeling the mechanical response of a cantilever beam containing an embedded horizontal crack and subjected to end transverse force condition. Informed by 2D finite element findings reported elsewhere [33] and summarized in this work, a four-beam mechanics of materials model has been developed capable of predicting the load transfer and deformation mechanics of a cracked cantilever beam discussed above. The model employs the transition regions associated with four rotary springs as a means of accounting for the load transfer through the regions adjacent to the crack tips. The rotary springs account for relative cross sectional rotations in the transition region induced by changes in the axial force and bending moments through the crack region.

Initially, the load transfer through the crack region was addressed. Finite element observations reported elsewhere [33] of matching curvatures enabled the development of analytical models capable of predicting the bending moment and axial force transmitted through the beams above and below the crack. The above quantities were then incorporated into the four-beam model which was used to obtain estimates of the transition region length as well as estimates of the shear force distribution in the beams above and below the crack. Deflection and cross-sectional rotation compatibility conditions were used in establishing the effective rotary spring stiffnesses, which capture the effects of the transition region. The transition region length is obtained via non-linear

equation derived by matching the free end deflection of the cracked beam predicted by the current model to independent estimates obtained via the method of finite elements. The finite element model formulation along with the results obtained through broad parametric studies and related discussion is presented in a Part-B companion paper.

References

- [1] Thomson, T.W. & Dahleh, M.D. (1993). Theory of Vibration with Applications, 5th Ed. Prentice Hall.
- [2] Stanbridge, A.B., Martarelli, M. & Ewins, D.J. (1999). Measuring Area Mode Shapes with a Scanning Laser Doppler Vibrometer. *Proceedings of International Modal Analysis Conference*, 1999, Kissimmee, FL.
- [3] Ewins, D.J. (2000). Modal Testing: Theory, Practice and Application, 2nd edition. Research Studies Press Ltd., Baldock, Hertfordshire, England: 422-427. 37.
- [4] Stanbridge, A.B., Ewins, D.J. & Khan, A.Z. (2000). Modal Testing Using Impact Excitation and a Scanning LDV. *Shock and Vibration*, 7, 91-100.
- [5] Vignola, J.F., Judge, J.A. & Kurdila, A.J. (2009). Shaping of a System's Frequency Response Using an Array of Subordinate Oscillators. *Journal of the Acoustical Society of America*, 126(1), 129-139.
- [6] Rizos, P.F., Aspragathos, N. & Dimarogonas, A.D. (1990). Identification of Crack Locations and Magnitude in a Cantilever Beam from Vibration Modes. *J. of Sound and Vibration*, 138(3), 381-388.
- [7] Wong, C.N., Zhu, W.D. & Xu, G.Y. (2004). On an Iterative General-Order Perturbation Method for Multiple Structural Damage Detection. *J. Sound and Vibration*, 273, 363-386.
- [8] Xu, G.Y., Zhu, W.D. & Emory, B.H. (2007). Experimental and Numerical Investigation of Structural Damage Detection Using Changes in Natural Frequencies. *J. Vibration and Acoustics*, 129(6), 686-700.
- [9] He, K. & Zhu, W.D. (2011). A Vibration-based Structural Damage Detection Method and Its Applications to Engineering Structures. *International Journal of Smart and Nano Materials*, 2(3), 194-218, doi: 10.1080/19475411.2011.594105
- [10] Xu, Y.F. & Zhu, W.D. (2011). Operational Modal Analysis of a Rectangular Plate Using Noncontact Acoustic Excitation. *Proceedings of the International Modal Analysis Conference*, 2011, Jacksonville, FL, doi: 10.1007/978-1-4419-9428-8_30
- [11] He, K. & Zhu, W.D. (2010). Detection of Damage and Loosening of Bolted Joints in Structures Using Changes in Natural Frequencies. *ASNT Material Evaluation*, June, 2010, 721-732, doi: 10.1088/1742-6596/305/1/012054
- [12] He, K. & Zhu, W.D. (2011). Damage Detection of Space Frame Structures with L-shaped Beams and Bolted Joints Using Changes in Natural Frequencies. *Proceedings of the 23rd ASME Biennial Conference on Mechanical Vibration and Noise*, Washington, DC, Aug. 28-31, 2011, doi:10.1115/DETC2011-48982
- [13] He, K. & Zhu, W.D. (2011). Detecting Loosening of Bolted Connections in a Pipeline Using Changes in Natural Frequencies. *Proceedings of the 23rd ASME Biennial Conference on Mechanical Vibration and Noise*, Washington, DC, Aug. 28-31, 2011.
- [14] He, K. & Zhu, W.D. (2011). Finite element modeling of structures with L-shaped beams and bolted joints. *ASME Journal of Vibration and Acoustics*, Vol. 133(1), doi:10.1115/1.4001840
- [15] He, K. & Zhu, W.D. (2009). Modeling of Fillets in Thin-walled Beams Using Shell/Plate and

Beam Finite Elements. *ASME Journal of Vibration and Acoustics*, 131, 051002 (16 pages), doi:10.1115/1.3142879

- [16] Lin, R.J. & Cheng, F.P. (2008). Multiple crack Identification of a Free-free Beam with Uniform Material Property Variation and Varied Noised Frequency. *Engineering Structures*, 30, 909-929.
- [17] Ganeriwala, S.N., Yang, J. & Richardson, M. (2011). Using Modal Analysis for Detecting Cracks in Wind Turbine Blades. *Sound and Vibration.*, 45(5), 10-13.
- [18] Das, P. (2012). Detection of Cracks in Beam Structures Using Modal Analysis. *Applied Mechanics and Materials*, 105-107, 689-694.
- [19] Swamidas, A.S., Yang, X. & Seshadri, R. (2004). Identification of cracking in beam structures using Timoshenko and Euler formulations. *J. Eng. Mech.*, 130(11), 1297–1308.
- [20] Caddemi, S. & Calio, I. (2009). Exact closed-form solution for the vibration modes of the Euler-Bernoulli Beam with multiple open cracks. *J. Sound and Vibration*, 327, 473-489.
- [21] Rubio, L. (2011). An Efficient Method for Crack Identification in Simply Supported Euler-Bernoulli Beams. *Journal of Vibrations and Acoustics*, 131, 051001-1 to 051001-6.
- [22] Krawczuk, M. & Ostachowicz, W.M. (1995). Modeling and Vibration Analysis of a Cantilever Composite Beam with a Transverse open crack. *J. Sound and Vibration*, 183(1), 69-89.
- [23] Dimarogonas, A.D. (1996). Vibration of Cracked Structures: A State of the Art Review. *Engineering Fracture Mechanics*, 55(5), 831-857.
- [24] Wang, K., Inman, D.J. & Farrar, C.R. (2005). Modeling and Analysis of a Cracked Composite Beam Vibrating in Coupled Bending and Torsion. *J. Sound and Vibration*, 284, 23-49.
- [25] Zhang, X.Q., Han, Q. & Li, F. (2010). Analytical Approach for Detection of Multiple Cracks in a Beam. *J. Eng. Mech.*, 136(3), 345-357.
- [26] Chatterjee, A. (2011). Nonlinear Dynamics and Damage Assessment of a Cantilever Beam with Breathing Edge Crack. *J. Vibration and Acoustics*, 133(5), 051004-1 to 051004-6, doi:10.1115/1.4003934
- [27] Liu, J., Zhu, W.D., Charalambides, P.G., *et al.* (2016). Four-beam Model for Vibration Analysis of a Cantilever Beam with an Embedded Horizontal Crack. *Chinese Journal of Mechanical Engineering*, 29(1), 163-179. doi: 10.3901/CJME.2015.0901.108
- [28] Broek, D. (1974). Elementary Engineering Fracture Mechanics. Springer Press.
- [29] Kanninen, M.F. & Popelar, C.H. (1986). Advanced Fracture Mechanics. Oxford Press.
- [30] Anderson, T.L. (1991). Fracture Mechanics: Fundamentals and Applications, Second Editions. CRC Press Inc.
- [31] Data, H., Paris, P.C. & Irwin, G.R. (2000). The Stress Analysis of Cracks Handbook, 3rd Edition. American Society of Mechanical Engineers Press.
- [32] Erdogan, E. (2000). Fracture Mechanics. *International Journal of Solids and Structures*, 27, 171-183.
- [33] Fang, X. (2013). The Mechanics of an Elastically Deforming Cantilever Beam with an Embedded Sharp Crack Subjected to an End Transverse Load. Ph.D. Dissertation. Department of Mechanical Engineering, The University of Maryland, Baltimore County. December 2013.
- [34] Fang, X. & Charalambides, P.G. (2015). The Fracture Mechanics of Cantilever Beams with an Embedded Sharp Crack under End Force Loading. *Engineering Fracture Mechanics*, Vol. 149, 1-17, doi:10.1016/j.engfracmech.2015.09.039

[35] Aladzyeu, V. (2013). The Dynamic Response of an Elastic Structure with an Embedded Sharp Crack for Damage Detection. Ph.D. Dissertation. Department of Mechanical Engineering, The University of Maryland, Baltimore County. December 2013.

[36] Sokolnikoff, I.S. (1956). Mathematical Theory of Elasticity, 2nd Edition. McGraw-Hill Press.

[37] Timoshenko, S.P. (1921). On the correction factor for shear of the differential equation for transverse vibrations of bars of uniform cross-section. *Philosophical Magazine*, p. 744.

[38] Cowper, G.R. (1966). The Shear Coefficient in Timoshenko's Beam Theory. *ASME, J. Appl. Mech.*, 33, 335-340.

[39] Riley, W.F., Sturges, L.D. & Morris, D.H. (2008). Mechanics of Materials, Sixth Edition. John Wiley & Sons, Inc.

[40] Rice, J.R. (1968). A Path Independent Integral and the Approximate Analysis of Strain Concentration by Notches and Cracks. *J. Appl. Mech.*, 35, 379-386.

[41] Rice, J.R. (1988). Elastic Fracture Mechanics Concepts for Interfacial Cracks. *J. Appl. Mech.*, 55, 98-103.

[42] Charalambides, P.G. (1990). Fiber Debonding in Residually Stressed Brittle Matrix Composites. *J. Am. Ceram. Soc.*, 73(6), 1674-1680.

[43] Charalambides, P.G., Lund, J., Evans, A.G. & McMeeking, R.M. (1989). A Test Specimen for Determining the Fracture Resistance of Bimaterial Interfaces. *J. Appl. Mech.*, 56(1), 77-82.

[44] Charalambides, P.G. (1991). Steady-State Delamination Cracking in Laminated Ceramic Matrix Composites. *J. Am. Ceram. Soc.*, 74(12), 3066-3080.

[45] Hutchinson, J.W. & Suo, Z. (1992). Mixed-mode cracking in layered materials. *Advances in Applied Mechanics*, 29, 63-191.

[46] Pandey, A.K., Biswas, M. & Samman, M.M. (1991). Damage Detection from Changes in Curvature Mode Shapes. *J. Sound and Vibration*, 145(2), 321-332.

[47] Ratcliffe, C.P. (2000). A Frequency and Curvature Based Experimental Method for Locating Damage in Structures. *J. Vibration and Acoustics*, 122(3), 324-329.

[48] Ratcliffe, C.P. & Crane, R.M. (2005). Structural Irregularity and Damage Evaluation Routine (SIDER) for Testing of the ½-Scale Corvette Hull Section Subjected to UNDEX Testing. *NSWCCD-65-TR-2005/24*.

[49] Crane, R.M., Ratcliffe, C.P., Gould, R. & Forsyth, D.S. (2006). Comparison Of The Structural Irregularity And Damage Evaluation Routine (SIDER) Inspection Method With Ultrasonic And Thermographic Inspections To Locate Impact Damage On An A-320 Vertical Stabilizer. *Proceedings of the 33rd Annual Review of Progress in Quantitative Nondestructive Evaluation*, July 30 - Aug 4, 2006, Portland, OR.

[50] Irwin, G. (1957). Analysis of Stresses and Strains Near the End of a Crack Traversing a Plate. *J. Appl. Mech.*, 24, 361-364.

The Mechanics of a Cantilever Beam with an Embedded Horizontal Crack Subjected to an End Transverse Force, Part B: Results and Discussion

Panos G. Charalambides¹ and Xiaomin Fang¹

1 – Department of Mechanical Engineering, The University of Maryland, Baltimore County, 1000 Hilltop Circle, Baltimore, MD 21250, USA



DOI [10.13140/RG.2.1.3454.1046](https://doi.org/10.13140/RG.2.1.3454.1046)

Keywords: mechanics of materials, cantilever, beam, embedded crack, horizontal, finite elements, modeling, results.

ABSTRACT. This is the second part of a two-part study aimed at establishing the mechanics of a cracked cantilever beam subjected to a transverse force applied at its free end. Following the development of a four-beam model in Part A, in this Part B of a two Part series of papers, a two dimensional (2D) Finite Element (FE) model is developed and used to obtain independent numerical estimates of the cross sectional resultants dominating the beams above and below the fully embedded horizontal crack in a cantilever beam subjected to an end transverse force. The FE model is also used to obtain numerical estimates of the required deformation of the cantilever free end as needed to establish the effective of the transition regions adjacent to the crack tips. The FE model results are then compared to the four-beam model predictions. The four-beam model predictions are found to be in excellent agreement with their FE counterparts. Related discussion is presented wherein the relevance of the model developed in Part A to damage and crack detection as well as to fundamental fracture mechanics studies on homogeneous and heterogeneous layer systems containing delamination cracks is addressed.

Introduction. The background and motivation of this study are presented in Part A [1] of this two-part series of papers. As discussed in [1], the development of a simple but robust mechanics of materials model for the cracked system considered in this study is motivated by the need to develop robust damage and crack detection [2-19] diagnostic tools and capabilities that are needed in assessing the structural integrity of components and structures. While ample research has been undertaken in the above areas, simple to use and implement models and methods are still required for the timely detection of both diffused damage as well as the presence of cracks in such systems. In light of the above, this study is expected to contribute in the development of such tools that are based both on physics based models as well as on non-model based methods primarily based on damage and crack induced free surface curvature changes as discussed elsewhere [20-23]. The focus of this Part B of the two-part series of papers is to conduct parametric studies using the model developed in [1] while also developing independent 2D FE model predictions needed to calibrate the model developed in [1] and present comparisons between the four-beam model predictions and the 2D FE estimates.

In Part A [1] of this two-part series of papers, a four-beam model was developed capable of capturing the load transfer mechanics through the near-tip Transition regions for a cantilever beam containing a horizontal crack and subjected to an end loading force. As discussed above, the model

⁶ This research was partially supported through a University of Maryland, Baltimore County DRIF award and Graduate Assistantship in the Department of Mechanical Engineering.

⁷ Professor Charalambides would like to acknowledge many useful discussions with Mechanical Engineering Professor Weidong Zhu and Professor Emeritus Christian von Kerczek.

developed in [1] will be employed in this study in obtaining cross-sectional resultants dominating the beam area in the crack region while also using the model findings to better understand the load transfer mechanics through the same crack region for the system under consideration. In doing so, a summary of the key findings of the four-beam model developed in [1] shall be presented next.

Key findings of the four-beam model. The four-beam model reported in [1] was developed for the cracked cantilever beam shown in Fig. 1a. Overall, the beam has a length L , height h while containing a horizontal sharp crack of length $l = 2a$ located at position x_c from the fixed end at depth h_l from the top surface. Consistent with the four-beam model developed in [1], the above domain was divided into four sub-domains, each forming a beam as shown in Fig. 1a labeled Beam-1, Beam-2, Beam-3 and Beam-4. Transition regions 1 through 4 were introduced, the effective deformation of which was assumed to be captured by rotary springs placed at Beam Interfaces 1 through 4 shown in Figs. 1 and 2. The model developed in [1] employed the following beam deformation findings established via the method of finite elements in [18]:

(a) *The free surface and neutral axis curvatures of the cracked beam at the crack center location match the curvature of a healthy beam, i.e., an identical beam without a crack under an end force condition;*

(b) *The neutral axis rotations (slope) of the cracked beam in the region between the applied load and the nearest crack tip matches the corresponding slope of the healthy beam.*

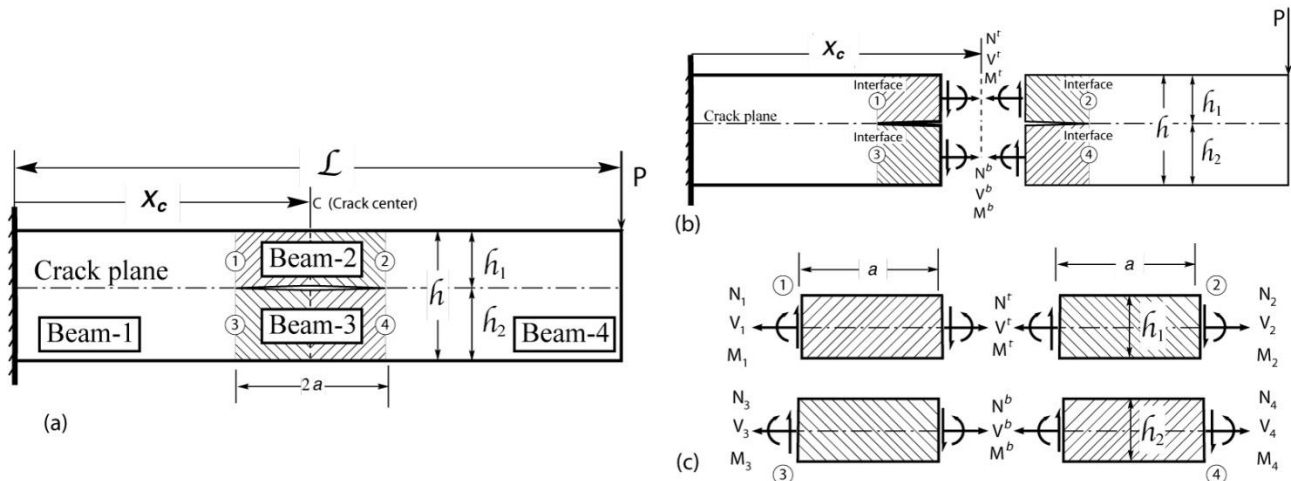


Fig. 1. Schematics used in the development of the analytical model capturing the mechanics of the beams above and below the crack, i.e., Beams 2 and 3 shown above. (a) The cracked beam with Beams 2 and 3 highlighted along with Interfaces 1-4. (b) A section through the center of the crack exposing the force and moment resultants acting in the “top” and “bottom” beams. (c) Free body diagrams of the left and right half of the “top” and “bottom” beams, exposing the resultants acting at their corresponding Interfaces 1-4.

Based on the finding (a) above, curvature matching of Beams 2 and 3, i.e., the beams above and below the horizontal crack also referred to as the top and bottom beams respectively, with that of the healthy beam yields the following beam resultant moment equations:

$$M^t = \frac{l_t}{l} M_C \text{ and } M^b = \frac{l_b}{l} M_C \quad (1)$$

where M^t is the moment resultant at the crack center cross section dominating the “top” beam or Beam-2;

M^b is its counterpart dominating the “bottom” beam or Beam-3 as shown in Fig. 1b;

M_C is the resultant bending moment transferred through the cross section at the crack center location in the healthy beam, i.e., an identically loaded and supported beam without a crack.

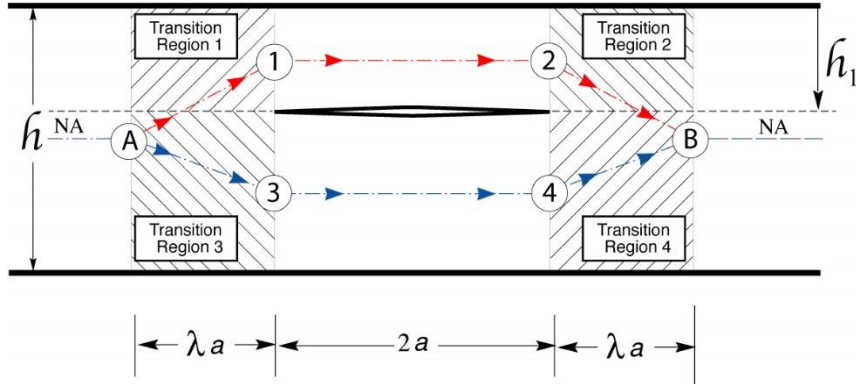


Fig. 2. The compatibility paths followed through the “top” and “bottom” beams in establishing angle of rotation and deflection compatibility conditions from reference section A to reference section B. Also shown are Transition Regions 1-4.

For a downward load P the bending moment at the crack center location in the healthy beam is $M_c = -P(L - x)$. The quantities I_t , I_b , and I are the second moments of inertia for the top, bottom, and healthy beams respectively. With the bending moments acting in the top and bottom beams known, an expression for the axial forces N^t and N^b is then obtained through a global moment equilibrium enforced over the right half of the beam as discussed in [1] (see Fig. 1), such that,

$$N^b = -N^t = \frac{2M_C}{h} \left\{ 1 - \frac{I_t + I_b}{I} \right\} \quad (2)$$

As shown in Fig. 1, at the crack center cross sections, Beam-2, i.e., the beam above the crack plane, is subjected to an axial force resultant N^t , shear force resultant V^t and bending moment resultant M^t . Similarly, Beam-3 also referred to in this study as the bottom beam denoted by a superscript $(\cdot)^b$ or subscript $(\cdot)_b$, is subjected to force and moment resultants N^b , V^b and M^b respectively. Meanwhile, Section/Interface 1 which is the left end of the top beam is subjected to the force and moment resultants N_1 , V_1 and M_1 whereas the right end of the same beam is subjected to N_2 , V_2 and M_2 at Interface 2. Similarly, the bottom beam or Beam-3 is subjected to end forces and moments N_3 , V_3 and M_3 at Section/Interface 3 and N_4 , V_4 and M_4 at Section 4 as shown in Fig. 1c.

As presented in [1], beam deflection and beam slope compatibility conditions along with the finding (b) above, (i.e., slope matching of the cracked and healthy beams at the end of the Transition region to the right of the right crack tip), yield the following shear force equation,

$$\frac{V_t}{V_b} = \frac{l_t}{l_b} \frac{\lambda(2+\lambda) + 2(1+\lambda) + \frac{2}{k_b} \frac{l_b}{A_b a^2} \frac{E}{G}}{\lambda(2+\lambda) + 2(1+\lambda) + \frac{2}{k_t} \frac{l_t}{A_t a^2} \frac{E}{G}} \quad (3)$$

where λa is the length of the transition regions (see Fig. 2);

$2a$ is the crack length.

Also in the above equation, I represents the second moment of inertia, A is the related cross sectional area, E is the modulus of elasticity, G is the shear modulus and k is the Timoshenko shear constant [17]. The subscripts $()_t$ and $()_b$ denote quantities for the beams above (top beam or Beam-2) and below (bottom beam or Beam-3) the crack. As discussed in [1], it is worth noting that when ignoring the Timoshenko shear effects, i.e., letting k_t and $k_b \rightarrow \infty$ then the following simple form for the shear force ratio which becomes independent of the transition region length proportionality constant λ , is obtained, i.e.,

$$\frac{V_t}{V_b} = \frac{I_t}{I_b} \quad (4)$$

It is also noteworthy to observe for systems in which the crack is on the beam neutral axis (i.e., $h_1 = h_2$), both Eqns. (3) and (4) predict that the shear force ratio between the shear resultants in the top and bottom beam is $V_t/V_b = 1$ and thus from global equilibrium it can be shown that $V_t = V_b = P/2$. As will be discussed later in this study, shear force predictions obtained by the present model were found to compare very well with 2D finite element results.

In [1], the transition region length proportionality constant λ , is obtained by matching the deflection at the free end of the cracked beam predicted by the four-beam model to its counterpart obtained independently using a 2D FE model. This consistency condition gives rise to a non-linear equation in λ which can then be solved for admissible values of λ . The above consistency equation is fully derived in [1] and is summarized below.

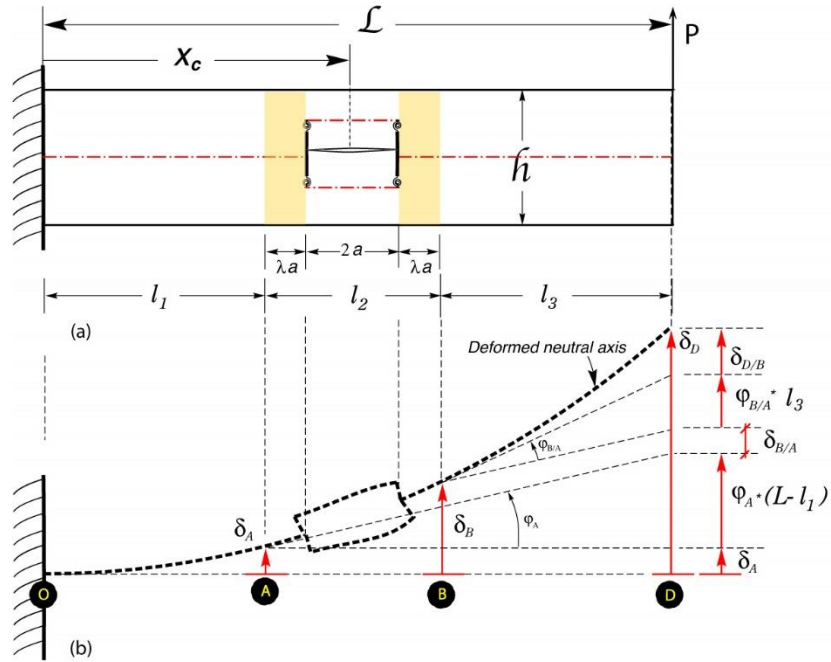


Fig. 3. A schematics showing (a) the original cracked beam with its un-deformed neutral axis and (b) the deformed neutral axis configuration of the four-beam model. The relationship between the deflections and rotations at key reference points of the beam are also shown in (b). The deformations and rotations between A and B include the transition region effects captured by the rotary spring and Timoshenko shear effects.

With the aid of the schematic shown in Fig. 3 and as presented in [1], the following consistency equation applies,

$$\begin{aligned}
 \delta_D^{MM} = & -\frac{(1-\nu^2)PL^3}{EI} \left\{ \frac{1}{3}\hat{l}_1^3 + \frac{1}{2}(1-\hat{l}_1)\hat{l}_1^2 + \frac{(\hat{l}_1 + \hat{l}_3)(1+\nu)}{6k} \left(\frac{h}{L} \right)^2 + \left(\frac{1}{2}\hat{l}_1^2 + (1-\hat{l}_1)\hat{l}_1 \right)(1-\hat{l}_1) \right. \\
 & \left. + (1-\hat{x}_C)\hat{a}^2(2+4\lambda+\lambda^2) + \frac{V_t}{P} \frac{I}{I_t} \hat{a}^3 \left(\frac{2}{3} + \lambda(2+\lambda) \right) + \frac{V_t}{P} \frac{\hat{a}(1+\nu)}{3k_t} \left(\frac{h}{L} \right)^2 \frac{h}{h_1} \right. \\
 & \left. + \frac{\lambda\hat{a}(1+\nu)}{6k} \left(\frac{h}{L} \right)^2 + (1-\hat{x}_C)2\hat{a}(1+\lambda)\hat{l}_3 + \frac{1}{3}\hat{l}_3^3 \right\} = -\frac{PL^3}{EI} \left\{ \frac{1}{12} \left(\frac{h}{L} \right)^3 \hat{\delta}_D^{FE} \right\}
 \end{aligned} \quad (5)$$

where δ_D^M is the beam deflection at its free end at D as shown in Fig. 3;

δ_D^{FE} is its 2D FE counterpart.

In the above equation, the $\hat{\cdot}$ symbol denotes non-dimensional values with all length quantities normalized with respect to the beam length L and $E' = E/(1-\nu^2)$ is used to convert the beam plane stress to its plane strain equivalent solution. Also in the above consistency equation, $\hat{\delta}_D^{FE}$ is the absolute value of the deflection of the cracked beam at its free end obtained through non-

dimensional FE simulations as will be discussed later in the study. Also in Eqn. (5), $I_1 = L - (x_c - a(1 + \lambda))$, $l_2 = 2a(1 + \lambda)$ and $I_3 = L - (x_c + a(1 + \lambda))$, $M_t / I_t = M_c / I$ and $M_c = -P(L - x_c)$. Furthermore, V_t can be expressed in terms of the load P and the shear force ratio V_t / V_b given by Eqn. (3). In Eqn. (5), the constants k and k_t are the Timoshenko shear constants for the healthy beam and Beam-2 above the crack respectively. Thus using the above equations and after normalizing each term with respect to a characteristic deflection $\Delta = PL^3/EI$, the following consistency condition in which the only unknown is the transition region length constant λ is obtained,

$$\alpha(\lambda)\lambda^2 + \beta(\lambda)\lambda + \eta(\lambda) = 0 \quad (6)$$

where the equation coefficients are functions of λ either explicitly as shown below or implicitly through the beam lengths $\hat{l}_1(\lambda), \hat{l}_2(\lambda), \hat{l}_3(\lambda)$ and are given by,

$$\begin{aligned} \alpha(\lambda) &= (1 - \hat{x}_C)\hat{a}^2 + \frac{\gamma}{I_b + \gamma_t}\hat{a}^3 \\ \beta(\lambda) &= 4(1 - \hat{x}_C)\hat{a}^2 + 2\frac{\gamma}{I_b + \gamma_t}\hat{a}^3 + 2(1 - \hat{x}_C)\hat{a}\hat{l}_3 + \frac{\hat{a}(1 + \nu)}{6k}\left(\frac{h}{L}\right)^2 \\ \eta(\lambda) &= \frac{1}{3}(\hat{l}_1^3 + \hat{l}_3^3) + (1 - \hat{l}_1)\hat{l}_1^2 + \hat{l}_1(1 - \hat{l}_1)^2 + 2\hat{a}(1 - \hat{x}_C)(\hat{a} + \hat{l}_3) \\ &+ \frac{V_t}{P}\left[\frac{2}{3}\frac{I}{I_t}\hat{a}^3 + \frac{(1 + \nu)\hat{a}}{3k_t}\left(\frac{h}{L}\right)^2\frac{h}{h_1}\right] + \frac{(1 + \nu)(\hat{l}_1 + \hat{l}_3)}{6k}\left(\frac{h}{L}\right)^2 \\ &- \frac{1}{12(1 - \nu^2)}\left(\frac{h}{L}\right)^3\hat{\delta}_D^{FE} \end{aligned} \quad (7)$$

where $\gamma(\lambda)$ is a subset of Eqn. (3) and is given by,

$$g(\lambda) = \frac{\lambda(2 + \lambda) + 2(1 + \lambda) + \frac{2}{k_b}\frac{I_b}{A_b a^2}\frac{E}{G}}{\lambda(2 + \lambda) + 2(1 + \lambda) + \frac{2}{k_t}\frac{I_t}{A_t a^2}\frac{E}{G}} \quad (8)$$

In the above equation, the finite element term is divided by the $(1-\nu^2)$ factor as needed to match the beam plane stress and the 2D FE plane strain solutions. The above consistency equation in λ will be solved for several cases wherein the horizontal crack is placed at different locations along the length and height of the beam. However, in order to carry out this task, finite element solutions for the non-dimensional deflection of the beam at the free end will need to be obtained. Thus, a brief description of the finite element models used in these simulations shall be discussed next.

Finite Element modeling of a beam with a horizontal crack. Broad finite element studies of a cantilever beam containing a fully embedded sharp crack and subjected to end transverse loading and bending moment have been carried out as reported in [18,19]. In those studies, cracks of varying length and orientation were systematically placed at various geometrically admissible locations within the beam. The near tip mechanics both at the left and right crack tips were established while neutral axis, as well as top and bottom surface deflections, slopes and curvatures were also established. The finite element results reported in this study compliment those reported in [18] and [19] in that they help in the development of a better understanding of the load transfer mechanism across the crack region in the areas above and below the crack as well as within the transition regions near the crack tip regions. For completeness, specifics of the finite element modeling used in deriving the results reported in this study shall be presented next.

As shown in Fig. 4, a 2D rectangular domain of length L and height h with a horizontal sharp crack of length $l = 2a$ with its center located at position x_C from the left fixed end and at depth h_l from the top surface was discretized using 4-noded isoparametric elements under plane strain conditions. A generalized mesh generator developed in [18] was used. Care was given to the meshing of the near-tip regions using a converging “spider web” with a minimum of 16 rings of elements all placed within a small region as needed to capture sufficient details of the near-tip singular fields. A vertical transverse load P was applied at the top left corner of the mesh as shown in Fig. 4. The finite element simulations were carried out in a non-dimensional environment as discussed in [18,19], where the length of the beam L was taken to be the characteristic length, its elastic modulus was taken to be the characteristic modulus with a Poisson’s ratio $\nu = 0.3$ and the intensity of the applied load P was taken to be the characteristic line force. Fig. 4 shows five FE models in which a crack of length $2a = 0.2L$ is shown to be placed at $x_C = 0.4L$ and at various depths as measured by the parameter h_l/h . For example, the top FE model corresponds to $h_l/h = 0.7$ whereas the bottom mesh represents a beam containing a shallow crack relative to the top surface with $h_l/h = 0.3$. All FE simulations reported in this study were carried out for a beam with an $h/L = 0.1$ aspect ratio.

As a means of comparing the four-beam model predictions to the 2D finite element results, the normalized axial force resultants N^t/P and N^b/P along with the shear counterparts V^t/P and V^b/P as well as the equivalent bending moment acting at the mid-plane of the regions above and below the crack surface, M^t/PL and M^b/PL respectively were calculated using finite element stress estimates. In doing so, finite element stresses were extracted at the Gauss integration stations nearest to the vertical plane passing through the crack center using elements from both sites of the above vertical plane. Finite element stress estimates from adjacent stations were then averaged and were then numerically integrated along the height of the individual beam (Beams 2 and 3 above the below the crack plane respectively as shown in Fig. 2) as needed to obtain the stress resultants reported herein.

In addition to obtaining finite element estimates of the force and moment resultants, the deflection at the free end of the cracked beam for each model was also extracted. Those results were reported in [18]. As discussed above, an independent finite element estimate of the beam deflection is needed in calibrating the four-beam model developed in this study. Furthermore, deflection, slope and curvature results along the top free surface of a cracked beam reported in [18] provide evidence of the two critical observations employed in the model development. The above finite element results along with the model predictions shall be presented next.

Results. Cross sectional force and moment resultants as well as effective transition region length predictions obtained using the four-beam model are reported in Figs. 5 through 8 where their finite element counterparts are also reported.

For example, Fig. 5 shows the normalized moment resultants M^t / PL and M^b / PL as a function of the normalized crack depth h_1/h in the 0.25 to 0.75 range. The analytical predictions obtained through Eqn. (3) are shown using solid lines whereas the finite element results are shown using discrete symbols. Three sets of data obtained for $x_C/L = 0.3, 0.4$ and 0.5 are reported. It may be of importance to recall that the model developed in [1] and summarized in this study is based on the fundamental observation of matching curvatures at the cross sections located at the crack center. That observation led to the development of the moment equation given by Eqn. (1) which was used to obtain the analytical moment predictions reported in Fig. 5. As shown, the analytically predicted moment resultants are in excellent agreement with those obtained using finite elements. This finding validates the fundamental assumption made in the model development and further reinforces the notion that simple but robust models can be developed in understanding the seemingly complex behavior of cracked structures. As expected, the beams above and below the crack are shown to experience equal amounts of bending moments predicted to be $1/8$ of the bending moment experienced by the healthy beam at the crack center location when $h_1/h = 0.5$, while a higher portion of the moment is predicted to be transferred through the thicker of the two beams when $h_1 \neq h_2$.

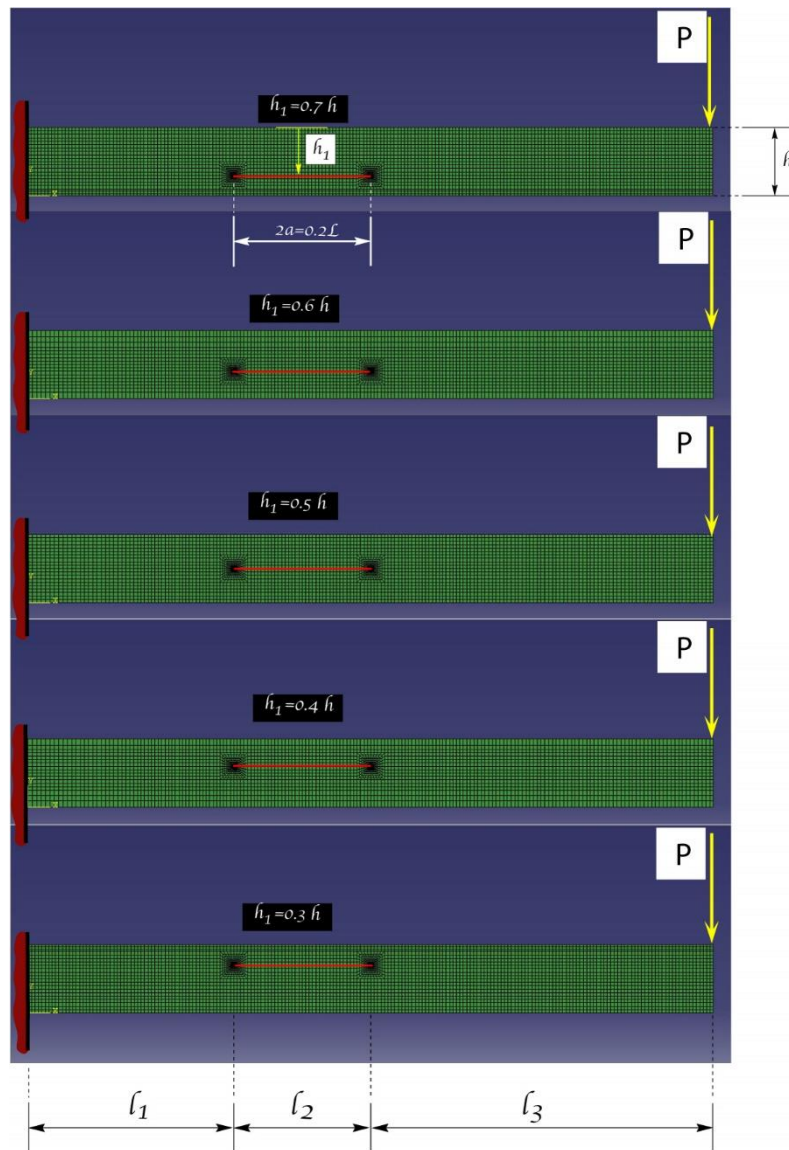


Fig. 4. Two dimensional finite element models used in extracting force and moment resultants as well as the free-end deflections used in model calibration and comparison studies reported in Figs. 5-10 below. As shown, the fixed conditions were imposed on the left edge of the beam whereas a downward transverse load P was applied at the top right corner of each mesh. The various models shown represent beams containing horizontal cracks of length $2a = 0.2L$ at various depths, with a beam aspect ratio $h/L = 0.1$ as reported in [18].

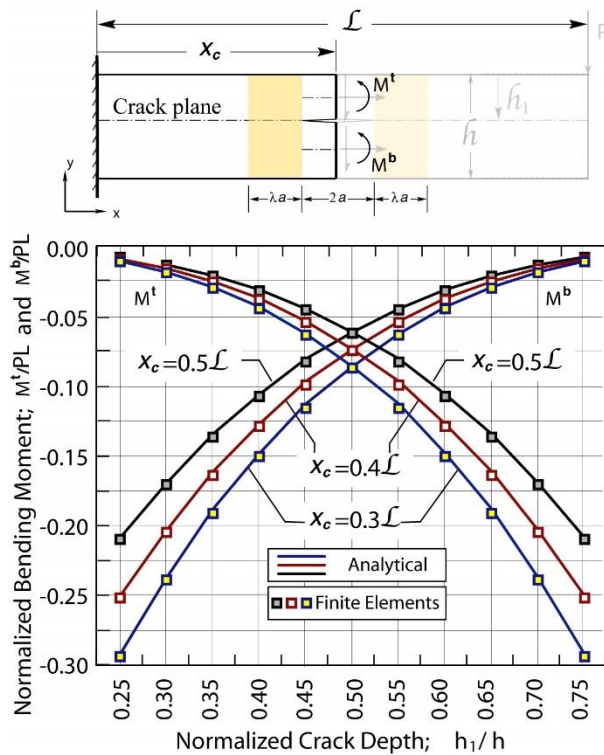


Fig. 5. Normalized bending moment resultants plotted against the crack depth ratio h_1/h predicted for the “top” and “bottom” beams in the crack region. The discrete points were obtained via 2D finite element simulations using model similar to those presented in Fig. 4. The solid lines were obtained using Eqn. (1). The results correspond to a downward load P . Results for three different crack center locations, i.e., $x_c/L=0.3, 0.4$ and 0.5 are presented. The curves with the upward trend correspond to the moment M^b in the bottom beam, whereas the results with the downward trend correspond to the moment M^t in the top beam.

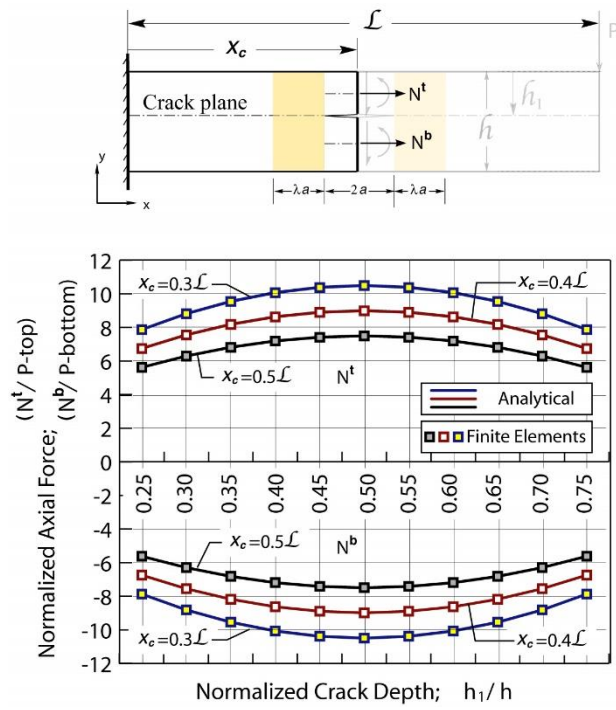


Fig. 6. Normalized axial force resultants plotted against the crack depth ratio h_1/h predicted for the “top” and “bottom” beams in the crack region. The discrete points represent 2D finite element predictions whereas the solid lines were obtained using Eqn. (2). The results correspond to a downward load P . The “top” beam is predicted to be in tension while the “bottom” beam is predicted to be in compression with a force of equal magnitude as that of the top beam. The curves with negative values correspond to the axial force N^b in the bottom beam, whereas the results with the positive values correspond to the axial force N^t in the top beam.

Fig. 6 shows the normalized axial force resultants N^t/P and N^b/P as a function of the normalized crack depth h_1/h again in the 0.25 to 0.75 range. The analytical predictions obtained through Eqn. (5) are shown using solid lines whereas the finite element results are shown using discrete symbols. As before, three sets of data obtained for $x_c/L=0.3, 0.4$ and 0.5 are reported. The top set of curves correspond to the axial force N^t/P acting at the mid-plane of Beam-2 above the crack plane. The bottom set of curves correspond to the normalized resultant N^b/P acting at the mid-plane of Beam-3 below the crack plane. A remarkable agreement is shown to exist between the axial force predicted through Eqn. (2) and the finite element results for all instances considered. As expected, for a downward load P , Beam-2 above the crack plane is subjected to a tensile force whose magnitude scales with the distance of the crack center from the applied load P while inversely proportional to the beam height h consistent with Eqn. (5). Again, as expected, an equal

and opposite axial force is applied at the mid-plane of Beam-3 below the crack plane thus forming a couple with its counterpart acting in Beam-2 above the crack plane. When considering the results reported in Figs. 5 and 6, one recognizes that in the crack region the bending moment transfer through the cracked beam region takes place primarily through a couple with a pair of tensile and compressive forces acting at the mid-plane of the beams above and below the crack plane. It may also be important to note that once the resultant forces and moment N^t and M^t are known, their counterparts in the lower beam are established, through Eqns. (1) and (2).

The shear force resultants predicted both using the model developed in this study and through the method of finite elements are presented in Fig. 7. It is important to note that in order to establish the shear forces V^t and V^b acting in Beams 2 and 3 respectively, one needs to solve for the transition region length parameter λ first using the consistency condition given by Eqn. (5). Once λ is established, then the shear force ratio can be obtained through Eqn. (3) and then use global force equilibrium as needed to obtain the individual shear forces V^t and V^b . So, for each case considered, the corresponding value for the deflection at the free end of the cracked beam was used to solve a non-linear equation in λ given by Eqn. (6). For the systems considered, the λ values obtained with the aid of Eqn. (6) are reported in Fig. 8. However, the λ trends will be discussed later on in this section while now focusing on the shear resultants shown in Fig. 7.

The shear force profiles plotted against the crack depth ratio h_1/h and predicted using the analytical model are shown in solid blue lines in Fig. 7. The finite element results are shown using the discrete symbols as marked on the same figure. As shown, the model predictions and finite element results exhibit the same overall trends. The results appear to be in excellent agreement for cracks located at or close to the mid-plane of the healthy beam. However, the analytical predictions appear to be slightly larger when compared to the finite element predictions for the shear force in the thicker beam while slightly underestimating its FE counterpart in the thinner of the two beams when $h_1 \neq h_2$. Maximum deviation of less than 8% in the thicker beams appears for systems in which $0.3 \leq h_1/h \leq 0.4$ or $0.6 \leq h_1/h \leq 0.7$. It may be of importance to note that the λ and related shear force resultant results reported in this study were obtained using a Timoshenko constant $k_t = k_b = k = 0.856$ for the top, bottom and healthy beam respectively consistent with reported values for beams with a rectangular cross section [24, 25].

The λ curves obtained by solving Eqn. (6) and reported in [18] are plotted in Fig. 8. Some interesting observations can be made. For example, the normalized transition region length parameter λ is predicted to increase with the normalized crack depth h_1/h , acquiring a maximum at $h_1/h = 0.5$. A symmetric profile is predicted for cracks located at equal distance above or below the mid-plane of the healthy beam. The results also suggest that the transition region length does depend on the location of the crack center along the axis of the beam. Perhaps somewhat counter-intuitive is the model prediction that a shorter transition region is predicted for cracks located close to the fixed end of the beam as shown by the $x_C/L = 0.5, 0.4$ and 0.3 curves. It may also be important to note that for the case of $h_1/h = 0.5$, although for a slightly higher beam aspect ratio, i.e., $h/L = 0.2$, available finite element results reported in [18] suggest a value for $\lambda = 1.67$. As reported in [18] and shown in Fig. 8, the model prediction for the case of $x_C/L = 0.5$ and $h/L = 0.1$ is $\lambda = 1.615$ which is remarkably close to the value obtained through finite elements. The above results and general findings of this study are critically analyzed and discussed in the next section.

In order to further understand the transition region mechanics, profiles of the normalized bending moment transferred through the top portion of the beam along with the % difference between the moment carried by the crack beam and its “healthy” counterpart are plotted in Fig. 9.

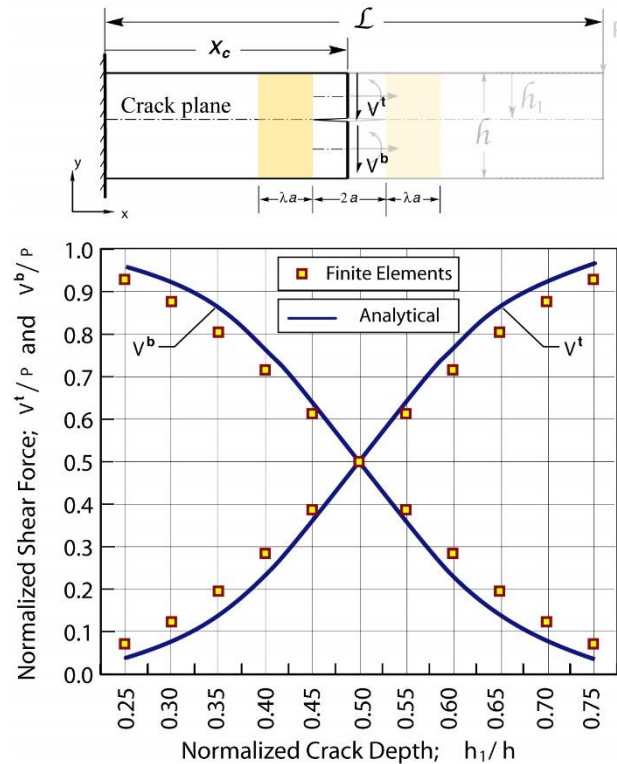


Fig. 7. Normalized shear force resultants plotted against the crack depth ratio h_1/h predicted for the “top” and “bottom” beams in the crack region. The discrete points represent 2D finite element results whereas the solid lines were obtained via Eqn. (3) and global force equilibrium. Both the finite element and analytical model simulations reproduced the same profiles for all crack center locations considered indicating that the shear forces depend only on the normalized crack depth h_1/h .

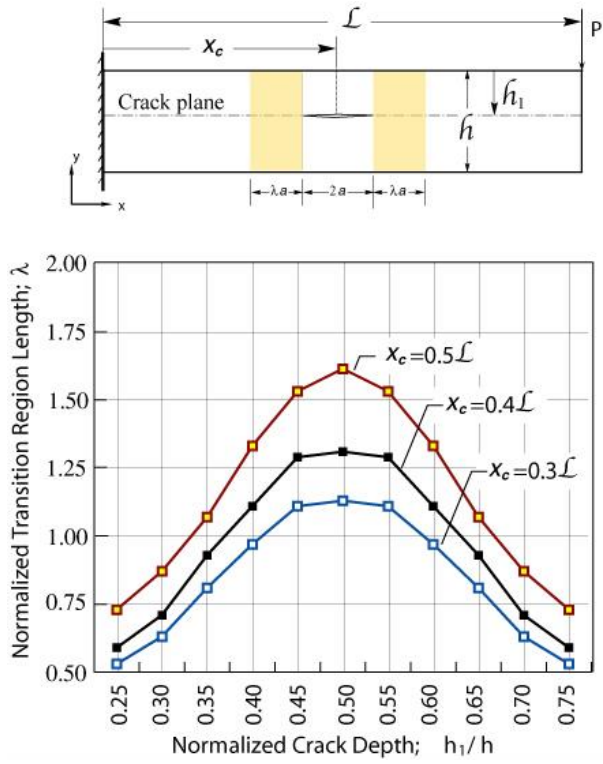


Fig. 8. The non-dimensional transition region length parameter λ plotted against the normalized crack depth h_1/h . Results obtained through the four-beam model for three different crack locations, i.e., $x_c/L=0.3, 0.4$ and 0.5 are presented. The discrete symbols represent the cases for which finite element deflections at the free end of the beam were used to solve for the crack length parameter λ .

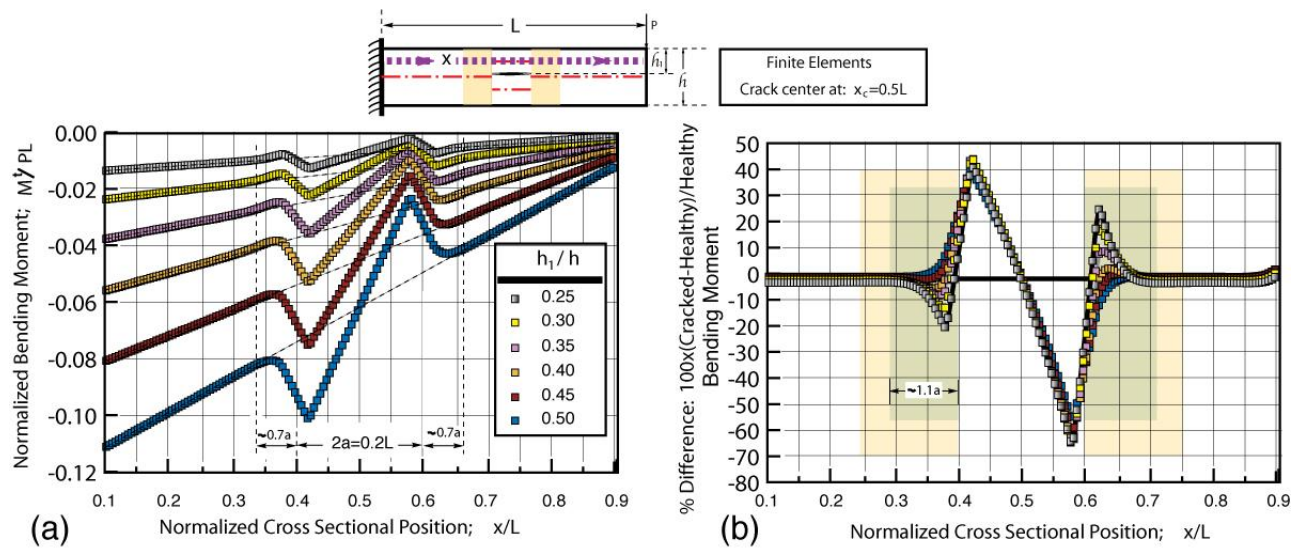


Fig. 9. (a) Profiles of the normalized bending moment carried by the “top” portion of the beam extracted from the FE models discussed in this study. Different curves correspond to beams with cracks placed at different h_1/h depths as indicated in the figure. (b) Profiles of the % difference of the bending moment carried by the top portion of the cracked beam to its “healthy” counterpart.

The results reported in Fig. 9a were extracted from the 2D FE models discussed earlier in this work. In obtaining these results, the normal stresses to cross sections along the path x indicated in the figure were first extracted from the FE model. Their contribution to the bending moment with respect to the neutral axis of the top beam was then integrated to obtain the moment resultant carried by the top beam, i.e., the beam above the embedded horizontal crack. A % difference between the moment carried by the cracked beam and its “healthy” counterpart was also calculated for each of the models considered in this study. The latter results are reported in Fig. 9b. In Fig. 9a, the straight dash lines represent the bending moment carried by the “healthy” beam. It is of interest to observe that the presence of the crack appears to cause a local change in the bending moment, and thus the beam curvature in the vicinity of the crack. The predicted moment change appears to extend at the most extreme case to approximately 0.7a to 1.1a (see Fig. 9a and 9b respectively) on either side of the crack. Similar results related to the axial and shear force profiles (see Fig. 10) suggest that the changes in the associate axial and shear force resultants may persist over somewhat greater extent to approximately 1.5a to 1.7a as shown in Fig. 10. The latter results would indeed be consistent with model transition region estimates reported herein. As shown, in Fig. 10, finite element profiles of the normalized axial force N^t/P and shear force V^t/P , transmitted through the top portion (i.e., beam above the crack plane) of the cracked beam are reported. Like in Fig. 9, the force resultants reported in Fig. 10 were extracted from FE models by integrating the normal and shear stresses acting on cross sections along the designated path x . The different curves correspond to beam systems containing a horizontal crack at different depths h_1/h as indicated in the figure. It may be of interest to observe that when comparing the profiles reported in Figs. 9 and 10, the shear force resultant appears to exhibit larger transition profiles when compared to either the bending moment or the axial force profiles.

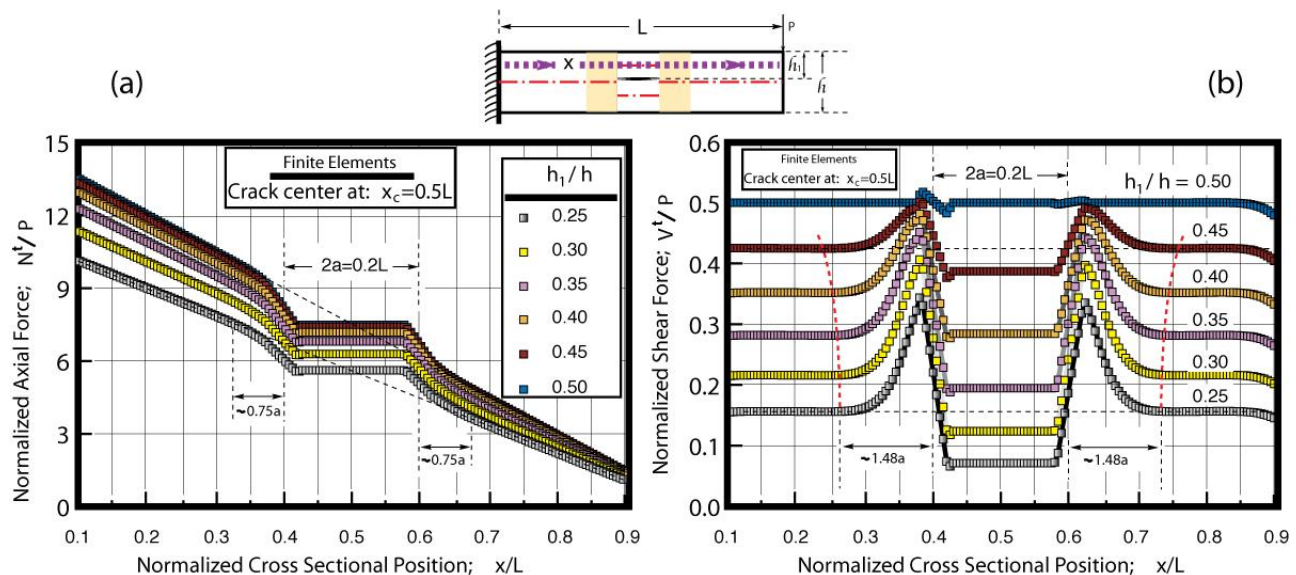


Fig. 10. Finite element profiles of the normalized axial force (a) and shear force (b), transmitted through the top portion (i.e., beam above the crack plane) of the cracked beam. The different curves correspond to beam systems containing a horizontal crack at different depths h_1/h as indicated in the figure.

The results reported in Fig. 9, may also have profound implications on the development of non-model crack detection methods [20-23], since, the predicted crack induced changes in the bending moment would cause reciprocal and measurable changes in the beam's surface curvatures.

Discussion. The four-beam mechanics of materials model developed in [1] is founded on two fundamental observations made possible through the method of finite elements, i.e., (a) *the matching of the curvatures of the beams above and below the crack to the curvature of the healthy beam at the crack center location*, and (b) *the matching of the beam slope of the crack beam to that of the healthy beam at the end of the transition region closest to the applied loading*. While the matching of the beam slopes has been discussed as part of the transition region load transfer and deformation mechanism in an earlier section of this study, no such consideration has thus far been given to the first fundamental observation of matching curvatures. In an effort to do so, let's consider the mechanics of the beams above and below the crack plane, i.e., Beams 2 and 3 respectively.

As suggested both by the model and finite elements, the cross sectional force and moment resultants acting at the mid-plane of Beams 2 and 3 at the crack center cross section are fixed and depend on the bending moment $M_C = -P(L - x_C)$ acting at the crack center location in the healthy beam as well as on the beam height h and crack depth h_1/h . As discussed above, the shear forces also may depend on the mechanics of the transition region. Regardless, once those quantities are established, it is of importance to recognize that both the shear and axial force resultants acting in Beams 2 and 3 remain constant throughout the crack region. On the other hand, the bending moment would vary linearly consistent as discussed in [1]. Given the fact that no net axial force is present in the healthy beam while the shear force is also constant under the loading considered in this study, moment equilibrium at the crack tip cross section would suggest that the moment M_1 acting at Interface 1 would not be equal to its healthy beam counterpart and thus would exhibit a discontinuity through a finite jump. At the same time, similar arguments made for the cross section at the right crack tip, i.e., Interface 2 would lead to the conclusion that a similar moment discontinuity between M_2 and its healthy beam counterpart of an equal and opposite amount exist at the right crack tip at Interface 2. In light of the linear moment profile within Beams 2 and 3, the moments dominating the latter beams will have to intersect with their healthy beam counterparts at the crack center location. Since these moments are given in terms of the moment of inertia ratio as expressed in Eqn. (1), it can be concluded that at least for homogeneous systems the moment matching is equivalent to the matching of curvatures of Beams 2 and 3 in the cracked region, to the curvature of the healthy beam at the crack center location. With the above in mind, one could make similar arguments in understanding the mechanics of cracked beams under other type of loadings or even heterogeneous biomaterial or multilayered beams including composite laminates.

Another issue of relevance for discussion is the introduction of a transition region in the model development along with the predicted trends in the normalized transition region length parameter λ . The transition regions were introduced in this beam model development as a means of accounting for the complex load transfer and deformation mechanics in the vicinity of the singular fields in the crack tip region. As discussed earlier, evidence from finite element studies do support the existence of such transition regions [18]. It is encouraging to see that the model predictions, at least in the $h_1/h_2 = 1$ case, are very close to results obtained using 2D finite elements. Additional finite element results may in fact be needed in establishing higher confidence in the λ model predictions over a wide range of h_1/h_2 ratios and crack center locations x_C/L . However, such broad comparisons are

beyond the scope of this study and are expected to be reported in future works. For relatively long cracks, i.e., $a > \min(h_1, h_2)$ one could explain the transition region dependency on the crack depth (see Fig. 8) as being driven by the characteristic length ratio h_1/h . However, it is not quite obvious, at least to the authors, why smaller transition region lengths are predicted for cracks located closer to the fixed end. One possible explanation is the fact that such cracks are subjected to higher bending moments at the crack center location which results in higher axial force and bending moments acting at the crack tip edge of the transition region. In this model development, the mechanics of the transition region are captured through rotary spring and Timoshenko shear equations consistent with Eqn. (13). The important aspect of this modeling approach is that the rotations resulting from the deformation mechanics in the transition region are taken to be proportional to the respective moments M_1, M_2, M_3 and M_4 which increase with decreasing x_C/L . Thus, for a fixed h_1/h_2 and otherwise similar cracked beam geometries, the current model would yield larger rotational angles in the transition region for cracks located closer to the fixed end. Thus, as result of rigid body motions, smaller transition region lengths may be required to match the free end deflections. This finding is possibly an artifact of the model used. An improved model may in fact be needed wherein the transition region rotations are set to be related to the moment change in the crack region rather than the total moments acting at each of the four transition region interfaces.

Although the / predictions may need to be better understood through further studies, the same model has provided useful insights regarding both the global mechanics of the cracked beam as well as the local transition region and crack region mechanics. It is of interest to know that a predictive model now exists in calculating the force and moment resultants N_i, V_i and M_i , $i = 1, \dots, 4$ acting at Interfaces 1-4. With the above resultants and those acting on the opposite vertical edge of the transition region known, one can proceed to develop a better understanding of the transition fields and their local and global mechanical effects. For example, when focusing on the bottom edge of the transition region, one could start developing useful qualitative arguments regarding the profiles of the normal and shear stress and how they can be related to the singular crack tip fields. A simple schematic showing such potential profiles is presented in Fig. 11. As shown, and due to the fact that the axial force acting on the left edge of the referenced transition region is not equal to that acting on the right edge, i.e., $N_A^t \neq N_1$, force equilibrium in the x -direction would suggest that a shear stress must exist on the bottom edge of the transition region which is the crack plane ahead of the left crack tip. The shear stress induced by the transverse shear force P on the horizontal plane ahead of the left crack tip is known to equilibrate the axial force difference acting at the left and right edges of the transition region in the healthy beam. Since N_1 is not equal to its counterpart acting in the healthy beam, an additional shear stress must exist on the crack plane ahead of the left crack tip as needed for global equilibrium. Since no change in the transverse force acting in the beam takes place, this added shear must be induced by the mode II [26,27] singular stress field dominating the crack tip region since mode I induces no shear on the crack plane. This observation provides useful insights in how one can integrate the macro-mechanics of the crack region to the singular fracture fields induced in the crack-tip regions. For example, force equilibrium in the x -direction would take the form,

$$\Delta N_{A-1}^{healthy} - \Delta N_{A-1}^{cracked} = w \int_0^{\lambda a} \Delta \tau_{xy}(x) dx \quad (9)$$

where $\Delta N_{A-1}^{healthy}$ is the change of the axial force between Sections A and 1 in the healthy beam (see Fig. 2);

$\Delta N_{A-1}^{cracked}$ is its counterpart in the cracked beam;

w is the beam width;

$\Delta \tau_{xy}$ is the change in the shear stress on the crack plane ahead of the crack tip required for equilibrium.

Qualitative arguments can lead to the development of viable stress profiles. For example, as shown in Fig. 11, the profile of $\Delta \tau_{xy}$ in the transition region ahead of the crack tip should conform to the mode *II* driven shear stress close to the crack tip. At a critical distance from the crack tip, the stress profile must go through a stress transition region as needed to bridge the stress profile away from the crack tip to that close to the crack tip. While plausible transition stress profiles can be postulated for all stress components, the importance of this argument is to note that a relationship between the transition length λ and the mode *I* and mode *II* stress intensity factors may exist and could be established through the structure of the transition fields.

As discussed earlier in this study, another relevant observation is that the presence of even a slight mode *I* component would induce a tensile normal stress if $K_I > 0$ associated with crack tip opening, or compressive if $K_I < 0$ associated with crack surface contact as shown schematically in Fig. 11. The presence of such a stress close to the crack tip will need to be offset by an opposite stress resultant away from the crack tip in the transition region. Such a stress profile would then induce a net moment ΔM on the plane ahead of the crack tip in the transition region which ought to be counter-balanced by an equal and opposite moment on the vertical left edge of the transition region. Such a moment change could explain the free surface curvature “bump” at the end of each transition region as predicted via finite elements and reported in [18]. Thus, the presence of such a curvature “bump” could indicate the existence of crack damage in the vicinity of such a measurement used in non-model damage detection methods [20-23].

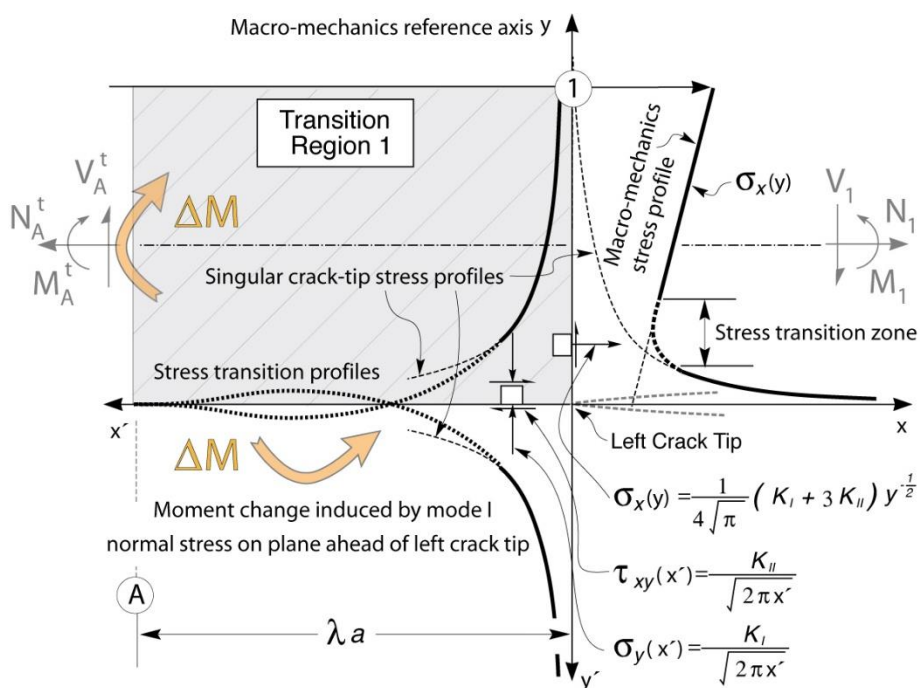


Fig. 11. Schematics of potential transition region stress fields that are superimposed onto those of the healthy beam. These fields are shown to conform to the near-tip mixed mode fields near the crack tip region and to the macro-mechanical field differences sufficiently away from the crack tip. As shown, a change of moment ΔM is induced by the mode I component of the stress intensity factor on the crack plane ahead of the left crack tip. An equal and opposite moment change then must occur on the left vertical plane of the transition region thus causing a slight “bump” on the moment and associated curvature profile at the start of the transition region as discussed in [1].

Finally in this section, it may also be important to note that this work is expected to have broader impact in advancing damage detection studies as well as studies on the fracture mechanics of structures with fully embedded cracks. For example, the macro-mechanics of the cracked beam established via the current model yield valuable information regarding the predicted free surface curvatures along the length of the beam. Enabled by the findings of this work, curvature deviations from an otherwise smooth profile measured experimentally, could be used to diagnose the presence of crack damage in structures as discussed elsewhere. Meanwhile, the near-tip mechanics can now be more thoroughly explored using analytical techniques such as the compliance method or the J -integral approach [26] in establishing the near-tip energy release rates and associated mode I and mode II stress intensity factors. Such studies have the potential to substantially enhance our understanding of mixed mode [28-30] and predominately mode II fractures while guiding improved designs of composites and composite laminate systems [29].

Summary. Informed by 2D finite element findings, a four-beam mechanics of materials model was developed in Part A [1] of this two-part series of papers. In this work, key findings of the four-beam model were first summarized. The development of related 2D FE models was then discussed and used to conduct parametric studies through which the cross sectional resultants acting in the beams above and below the crack were obtained. In addition, FE estimates of the cracked beam deflection at its free end were used to obtain the effective transition region length introduced in the development of the four beam model. Force and moment predictions were also obtained using the four-beam model which were then compared to their FE counterparts. The model and FE results were shown to be in excellent agreement over a wide range of crack location, i.e., depth from the top beam surface, and crack center location along the longitudinal axis of the beam.

The reported results show that the four-beam model is capable of predicting the load transfer and deformation mechanics of a cantilever beam containing a fully embedded horizontal crack under the application of an end transverse force. Discussion on the limitations of the model as well as its potential impact on damage detection and fracture of structures with embedded cracks is also included in this work.

References

- [1] Charalambides, P.G. & Fang, X., The Mechanics of a Cantilever Beam with an Embedded Horizontal Crack Subjected to an end Transverse Force, Part A: Modeling, Mechanics, Materials Science & Engineering Journal ISSN 2412-5954, Vol.5, 2016, doi: 10.13140/RG.2.1.3874.4560
- [2] Rizos, P.F., Aspragathos, N. & Dimarogonas, A.D. (1990). Identification of Crack Locations and Magnitude in a Cantilever Beam from Vibration Modes. *J. of Sound and Vibration*, 138(3), 381-388.
- [3] Wong, C.N., Zhu, W.D. & Xu, G.Y. (2004). On an Iterative General-Order Perturbation Method for Multiple Structural Damage Detection. *Journal of Sound and Vibration*, 273, 363-386, doi: 10.1016/S0022-460X(03)00543-1

[4] Xu, G.Y., Zhu, W.D. & Emory, B.H. (2007). Experimental and Numerical Investigation of Structural Damage Detection Using Changes in Natural Frequencies. *J. Vibration and Acoustics*, 129(6), 686-700, doi:10.1115/1.2731409

[5] He, K. & Zhu, W.D. (2011). A Vibration-based Structural Damage Detection Method and Its Applications to Engineering Structures. *International Journal of Smart and Nano Materials*, 2(3), 194-218, doi: 10.1080/19475411.2011.594105

[6] He, K. & Zhu, W.D. (2011). Damage Detection of Space Frame Structures with L-shaped Beams and Bolted Joints Using Changes in Natural Frequencies. *Proceedings of the 23rd ASME Biennial Conference on Mechanical Vibration and Noise*, Washington, DC, Aug. 28-31, 2011, doi:10.1115/DETC2011-48982

[7] He, K. & Zhu, W.D. (2011). Detecting Loosening of Bolted Connections in a Pipeline Using Changes in Natural Frequencies. *Proceedings of the 23rd ASME Biennial Conference on Mechanical Vibration and Noise*, Washington, DC, Aug. 28-31, 2011.

[8] Lin, R.J. & Cheng, F.P. (2008). Multiple crack Identification of a Free-free Beam with Uniform Material Property Variation and Varied Noised Frequency. *Engineering Structures*, 30, 909-929.

[9] Ganeriwala, S.N., Yang, J. & Richardson, M. (2011). Using Modal Analysis for Detecting Cracks in Wind Turbine Blades. *Sound and Vibration.*, 45(5), 10-13.

[10] Das, P. (2012). Detection of Cracks in Beam Structures Using Modal Analysis. *Applied Mechanics and Materials*, 105-107, 689-694, doi: 10.4028/www.scientific.net/AMM.105-107.689

[11] Swamidas, A.S., Yang, X. & Seshadri, R. (2004). Identification of cracking in beam structures using Timoshenko and Euler formulations. *J. Eng. Mech.*, 130(11), 1297–1308, doi: 10.1061/(ASCE)0733-9399(2004)130:11(1297)

[12] Caddemi, S. & Calio, I. (2009). Exact closed-form solution for the vibration modes of the Euler-Bernoulli Beam with multiple open cracks. *J. Sound and Vibration*, 327, 473-489, doi:10.1016/j.jsv.2009.07.008

[13] Rubio, L. (2011). An Efficient Method for Crack Identification in Simply Supported Euler-Bernoulli Beams. *Journal of Vibrations and Acoustics*, 131, 051001-1 to 051001-6.

[14] Krawczuk, M. & Ostachowicz, W.M. (1995). Modeling and Vibration Analysis of a Cantilever Composite Beam with a Transverse open crack. *J. Sound and Vibration*, 183(1), 69-89.

[15] Dimarogonas, A.D. (1996). Vibration of Cracked Structures: A State of the Art Review. *Engineering Fracture Mechanics*, 55(5), 831-857.

[16] Chatterjee, A. (2011). Nonlinear Dynamics and Damage Assessment of a Cantilever Beam with Breathing Edge Crack. *J. Vibration and Acoustics*, 133(5), 051004-1 to 051004-6.

[17] Liu, J., Zhu, W.D., Charalambides, P.G., *et al.* (2016). Four-beam Model for Vibration Analysis of a Cantilever Beam with an Embedded Horizontal Crack. *Chinese Journal of Mechanical Engineering*, 29(1), 163-179. DOI: 10.3901 / CJME.2015.0901.108.

[18] Fang, X. (2013). The Mechanics of an Elastically Deforming Cantilever Beam with an Embedded Sharp Crack Subjected to an End Transverse Load. Ph.D. Dissertation. Department of Mechanical Engineering, The University of Maryland, Baltimore County. December 2013.

[19] Fang, X. & Charalambides, P.G. (2015). The Fracture Mechanics of Cantilever Beams with an Embedded Sharp Crack under End Force Loading. *Engineering Fracture Mechanics*, 149, 1-17, doi: 10.1016/j.engfracmech.2015.09.039

[20] Pandey, A.K., Biswas, M. & Samman, M.M. (1991). Damage Detection from Changes in Curvature Mode Shapes. *J. Sound and Vibration*, 145(2), 321-332.

[21] Ratcliffe, C.P. (2000). A Frequency and Curvature Based Experimental Method for Locating Damage in Structures. *J. Vibration and Acoustics*, 122(3), 324-329.

[22] Ratcliffe, C.P. & Crane, R.M. (2005). Structural Irregularity and Damage Evaluation Routine (SIDER) for Testing of the ½-Scale Corvette Hull Section Subjected to UNDEX Testing. *NSWCCD-65-TR-2005/24*.

[23] Crane, R.M., Ratcliffe, C.P., Gould, R. & Forsyth, D.S. (2006). Comparison Of The Structural Irregularity And Damage Evaluation Routine (SIDER) Inspection Method With Ultrasonic And Thermographic Inspections To Locate Impact Damage On An A-320 Vertical Stabilizer. *Proceedings of the 33rd Annual Review of Progress in Quantitative Nondestructive Evaluation*, July 30 – Aug 4, 2006, Portland, OR .

[24] Timoshenko, S.P. (1921). On the correction factor for shear of the differential equation for transverse vibrations of bars of uniform cross-section. *Philosophical Magazine*, p. 744.

[25] Cowper, G.R. (1966). The Shear Coefficient in Timoshenko's Beam Theory. *ASME, J. Appl. Mech.*, 33, 335-340.

[26] Rice, J.R. (1968). A Path Independent Integral and the Approximate Analysis of Strain Concentration by Notches and Cracks. *J. Appl. Mech.*, 35, 379-386.

[27] Rice, J.R. (1988). Elastic Fracture Mechanics Concepts for Interfacial Cracks. *J. Appl. Mech.*, 55, 98-103.

[28] Charalambides, P.G., Lund, J., Evans, A.G. & McMeeking, R.M. (1989). A Test Specimen for Determining the Fracture Resistance of Bimaterial Interfaces. *J. Appl. Mech.*, 56(1), 77-82.

[29] Charalambides, P.G. (1991). Steady-State Delamination Cracking in Laminated Ceramic Matrix Composites. *J. Am. Ceram. Soc.*, 74(12), 3066-3080.

[30] Hutchinson, J.W. & Suo, Z. (1992). Mixed-mode cracking in layered materials. *Advances in Applied Mechanics*, 29, 63-191.

Lagrangian Representations and Solutions of Modified Emden-Type Equations

Aparna Saha¹ and Benoy Talukdar¹

1 – Department of Physics, Visva-Bharati University, Santiniketan 731235, India



DOI [10.13140/RG.2.1.2683.0323](https://doi.org/10.13140/RG.2.1.2683.0323)

Keywords: variation of parameters, factorization method, modified Emden-type equations, solutions, Lagrangian representation.

ABSTRACT. We derive two novel methods to construct solutions of the physically important modified Emden-type equations (MEEs). Following the basic philosophy implied in the Lagrange's method of variation of parameters, we make use of a trivial particular solution of the problem to construct expressions for the nontrivial general solutions. Secondly, we judiciously adapt the factorization method of differential operators to present solutions of certain oscillator equations obtained by adding a linear term to the MEEs. We provide Lagrangian and Hamiltonian formulations of these equations in order to look for another useful theoretical model for solving MEEs.

PACS numbers: 02.30.Hq, 02.30.Ik, 05.45.-a

1. Introduction. The modified Emden-type equation [1] is given by:

$$\ddot{x} + \alpha x \dot{x} + \beta x^3 = 0, \quad x = x(t), \quad (1)$$

where α and β – are arbitrary parameters, and overdots denote differentiation with respect to time t .

This equation plays a role in several applicative contexts including the study of equilibrium configurations of a spherical gas cloud with mutual interaction between the molecules subject to laws of thermodynamics [2]. An important mathematical observation on (1) is that only for $\beta = \alpha^2/9$ it possess eight parameter Lie point symmetries [3] and is exactly solvable. In the recent past Chandrasekar, Senthilvelan and Lakshmanan [4] made use of an extension of the semi-decision algorithmic method [5] supplemented by a suitable Hamiltonian theory to demonstrate that (1) is integrable for arbitrary values of α and β . Iacono [6] proved the integrability of (1) by mapping it into the separable Abel's equation. It is true that one can look for alternative methods to solve nonlinear differential equations once their forms are found by a specific method [7]. However, we note that, as opposed to the theory of linear differential equations, the nonlinear theory is highly fragmented. Thus the identification of a new mathematical procedure and demonstration of its usefulness in solving nonlinear equations will always remain interesting provided the method of solution is uncomplicated enough to be appreciated by a wide variety of audience. The present work is an effort in this direction. In particular, we shall present two independent methods to solve MEEs – one based on the Lagrange's method of variation of parameters and the other based on a suitable factorization of the differential operators [1] that give the equations. To the best of our knowledge these methods have not hitherto been discussed in the literature. In addition, we provide

for these equations a suitable Lagrangian and Hamiltonian formulation which paves the path to introduce still another uncomplicated method for their solution.

In section 2 we apply the first method to solve (1) for $\beta = \alpha^2/9$ and $\beta = \alpha^2/8$ with a view to compare our solutions with other available results [3, 4]. In section 3 we provide a solution of the nonlinear oscillator equation

$$\ddot{x} + \alpha x \dot{x} + \beta x^3 + \lambda x = 0, \quad (2)$$

where $\beta = \alpha^2/9$ by the second method.

We consider (2) as a Liénard-type differential equation of the form:

$$\ddot{x} + g(x) \dot{x} + F(x) = 0. \quad (3)$$

With

$$g(x) = \alpha x \text{ and } F(x) = \beta x^3 + \lambda x. \quad (4)$$

We shall see in the course of our study that form in (3) is very suitable to develop the second method. It is interesting to note that the second method is also applicable to (1). The system (3) has been found to exhibit unusual nonlinear dynamical properties [8] in that for $\lambda > 0$ the frequency of oscillation is completely independent of its amplitude as found in the case of a linear harmonic oscillator. We devote section 4 to study the Lagrangian and Hamiltonian representations of our equations and demonstrate that the Jacobi integrals [9] can be used to solve the equations for $\beta = \alpha^2/9$ only. The equation with $\beta = \alpha^2/8$ needs altogether a separate consideration. Here we also introduce a family of Emden-type equations and study their Hamiltonian structure. Finally, in section 5 we make some concluding remarks with a view to summarize our outlook on the present work.

2. Modified Emden-type equations (MEEs). For simplicity of presentation we write two different forms of (1) as follows:

$$\ddot{x} + 3kx \dot{x} + k^2 x^3 = 0. \quad (5)$$

And

$$\ddot{x} + 4kx \dot{x} + 2k^2 x^3 = 0. \quad (6)$$

Comparing (5) and (6) with (1) it is evident that these equations refer to the cases $\beta = \alpha^2/9$ and $\beta = \alpha^2/8$ respectively. It is interesting to note that

$$x = 1/(kt - c), \quad (7)$$

where c – an arbitrary constant represents a particular solution of both (5) and (6).

We postulate that the general solutions of these equations are given by:

$$x = 1/(kt - f(t)), \quad (8)$$

where the constant c in (7) has been replaced by a function of t , namely, $f(t)$.

The replacement sought by us forms the basic philosophy of Lagrange's method of variation of parameters [1] for finding general solution of second-order linear differential equations from the particular solutions. We now use the following steps to solve the above MEEs.

- (i) We substitute (8) either in (5) or (6) to obtain an ordinary differential equation for $f(t)$ and then
- (ii) Use the solution of it in (8) to find a general solution of the chosen MEE.
- (a) **Equation (5).** Substituting (8) in (5) we obtain the differential equation for $f(t)$ as

$$(kt - c)\ddot{f} + 2\dot{f}^2 - k\dot{f} = 0. \quad (9)$$

Albeit nonlinear, (9) can be solved analytically to get

$$f(t) = \frac{e^{-4\alpha_1}(kt^2 - k^2\alpha_2^2 - e^{-2\alpha_1})}{2(t - \alpha_2)}, \quad (10)$$

where α_1 and α_2 – are constants of integration.

For $\alpha_1 = \alpha_2 = 0$ we have

$$f(t) = \frac{kt^2 - 1}{2t} \quad (11)$$

Which in conjunction with (8) leads to the well-known general solution

$$x = \frac{2t}{1 + kt^2}, \quad (12)$$

as given in [3].

(b) **Equation 6.** In this case an equation analogous to that of (9) reads

$$(c - kt)\ddot{f} - 2\dot{f}^2 + 8k\dot{f} - 8k^2 = 0. \quad (13)$$

Unlike (9), (13) cannot be integrated analytically. We thus try to find a solution of it by introducing a change of variable written as

$$f(t) = g(t) + kt. \quad (14)$$

From (13) and (14) we get

$$g\ddot{g} - 2\dot{g}^2 + 4k\dot{g} - 2k^2 = 0, \quad (15)$$

which is again almost of the same form as that in (13). However, if we choose to work with $\dot{g} = 0$, (15) can be solved to get

$$g(t) = e^{\frac{1}{4} \left(-\frac{c_1}{k^2} - 4\operatorname{erf}^{-1} \left(\frac{2i\sqrt{\frac{c_1}{e^{2k^2}}(t+c_2)}}{\pi} \right) \right)}, \quad (16)$$

where, as before, c_1 and c_2 – are arbitrary constants of integration;

erf^{-1} – stands for the inverse error function.

Since $\dot{g} = 0$ implies, that $\dot{c} = k$, the reciprocal of the result in (16) refers to a solution of (6) which is not the most general one.

In [4] Chandrasekar et. al solved (6) by treating it as a Hamiltonian system and then taking recourse to the use of a canonical transformation. Interestingly, our solution of (6) for $c_1 = 1$ and $c_2 = -it_0$ is in exact agreement with that of (16) in their work where it was also taken not as a general solution. The general solution was found by substituting the result in the equation for the canonical transformation of $x(t)$. We follow a different viewpoint to find the general solution.

The function $\frac{1}{g(t)}$ represents the solution of (6) only when the first derivative of the variable parameter is fixed at k . The question is how can one relax this condition and find a general solution of the equation. In this context we note, that the transformation:

$$x(t) = \frac{1}{k} \ln(y(t)), \quad (17)$$

reduces (5) to the linear form

$$\ddot{y} = 0, \quad (18)$$

and the solution of (18) when substituted in (17) gives the exact solution of (5). Unfortunately, no such transformation can be found to reduce (6) to the linear form. In this situation we suggest that the choice:

$$y(t) = \frac{1}{g(t)} \quad (19)$$

together with (17) will at least lead to an approximate general solution of (6). Following this viewpoint we obtain:

$$x(t) = 2i \operatorname{erf}^{-1}(z) \exp\left[\frac{1}{2} \left(\frac{1}{2k^2} + 2\{\operatorname{erf}^{-1}(z)\}^2\right)\right] \quad (20)$$

where:

$$z = \frac{2ikt}{\sqrt{\pi}} \exp\left(\frac{1}{2k^2}\right). \quad (21)$$

The solution (21) of (6) as obtained by us is in exact agreement with that found in [4] where the authors claimed that their result is exact.

3. Nonlinear oscillator equation. As given in (7) we could write a simple form for the particular solution of (5) or (6) only by inspection. For the oscillator equation (2) written as

$$\ddot{x} + 3x\dot{x} + k^2x^3 + \lambda x = 0 \quad (22)$$

it is, however, not possible to write a similar particular solution. As a result we take recourse to the use of a method of factorization applicable for Liénard-type equations to construct the general solution of (22). Equation (3) can be written in the factored form

$$(D - \phi_2(x))(D - \phi_1(x))x = 0, D = \frac{d}{dt}. \quad (23)$$

It is rather straightforward to deduce that

$$g(x) = -(\phi_1 + \phi_2 + \frac{d\phi_1}{dx} x) . \quad (24)$$

and

$$F(x) = \phi_1 \phi_2 x . \quad (25)$$

Since (3) has been factored as (23), a particular solution of the equation can be found from the first-order equation

$$(D - \phi_1(x))x = 0, D = \frac{d}{dt} . \quad (26)$$

In applying the factorization method to problems of physical interest one proceeds by writing ϕ_1 and ϕ_2 with some pre-factors so as to satisfy (25). Understandably, if the pre-factor for ϕ_1 is taken as a , that for ϕ_2 should be a^{-1} . The chosen results for ϕ_1 and ϕ_2 when substituted in (24) leads to an equation for a . One can assume that a is a c-number. Alternatively, one can regard a as a function of x say $b(x)$. It is straightforward to see that (i) a satisfies an algebraic equation while (ii) $b(x)$ satisfies a first-order differential equation. In two interesting publications Rosu and Cornejo-Peréz [10], and Cornejo-Peréz and Rosu [11] have chosen to work with a as a c number and found that the above factorization method provides an efficient tool to obtain particular solutions of many physically important equations which can be written in the Liénard form. We postulate that the solution of the differential equation for $b(x)$ in conjunction with (26) gives the general solution of (3). We first verify the conjecture with attention to (5) which is also of the Liénard form with $g(x) = 3kx$ and $F(x) = k^2 x^3$. Thus we introduce:

$$\phi_1 = b(x) \text{ and } \phi_2 = k^2 x^2 / b(x) . \quad (27)$$

to write (24) as

$$x \frac{db}{dx} + b + 3kx + \frac{k^2 x^2}{b} = 0 . \quad (28)$$

The solution of (28) can be found as

$$b = \phi_1 = \frac{-1 + kx^2 + \sqrt{1 - kx^2}}{x}. \quad (29)$$

It is now straightforward to substitute the expression for ϕ_1 in (26) and solve the resulting equation to get the general solution of (5) as given in (12).

For the nonlinear equation in (22) the value of $g(x)$ is same as that in (5) but $F(x) = k^2 x^3 + \lambda x$. Thus we take ϕ_1 as given in (27). Here $\phi_2 = (k^2 x^2 + \lambda)/b(x)$. In this case an equation similar to that in (28) is only slightly different and is given by

$$x \frac{db}{dx} + b + 3kx + \frac{k^2 x^2 + \lambda}{b} = 0. \quad (30)$$

We obtained the solution of (30) as:

$$b = \phi_1 = \frac{1 - 3\lambda - 3k^2 x^2 + \sqrt{1 - 3\lambda - 3k^2 x^2}}{3kx}. \quad (31)$$

For $\lambda = 0$, (30) coincides with (28). But on the same limit (31) does not go over to (29). Thus before proceeding further to use (31) to deal with the oscillator equation one would like to check if

$$\phi_1 = \frac{1 - 3k^2 x^2 + \sqrt{1 - 3k^2 x^2}}{3kx} \quad (32)$$

When used in (26) leads to the solution of (5). We found that this is indeed the case. The factorization method also works for (6) for which $\beta = \alpha^2/8$. In this case we, however, need to invoke the set of approximations as used in deriving the result in (20). Coming back to the oscillator equation we now substitute (31) in (26) and solve the resulting linear first-order differential equation to get

$$x(t) = \frac{n_1 + in_2}{kd} \quad (33)$$

Where:

$$n_1 = 2\sqrt{\lambda}(1 - 3\lambda) \sin(2\sqrt{\lambda}t), \quad (34a)$$

$$n_2 = -2\sqrt{3\lambda^2 - \lambda} \sin(\sqrt{\lambda}t). \quad (34b)$$

And

$$d = \frac{3\lambda+1}{2} + \frac{3\lambda-1}{2} \cos(2\sqrt{\lambda}t). \quad (34c)$$

It is of interest to note, that the real part of $x(t)$ corresponds to the solution of (22) given in [8].

4. Lagrangian and Hamiltonian formulations and MEEs. Traditionally, a Lagrangian function L is called natural (mechanical type) when it is of the form $L = T - V$ where T is a quadratic kinetic term and V is a potential function. For the equation of motion $\ddot{x} = 0$ of a free particle moving in the x direction the natural or standard Lagrangian is given by $L = \frac{1}{2}\dot{x}^2$. However, one can verify that

$L_1 = \frac{1}{\dot{x}}$ and $L_2 = \ln x$ via the Euler-Lagrange equations reproduce the equation of motion of the free particle. Thus, these two also equations represent admissible Lagrangians for the motion of a free particle. Following this viewpoint we introduce:

$$L_1 = \frac{1}{k\dot{x} + k^2x^2} \quad (35)$$

And

$$L_2 = \ln(k\dot{x} + k^2x^2), \quad (36)$$

and verify that (35) and (36) when substituted in the appropriate Euler-Lagrange equation lead to (5) and (6). A Lagrangian for (22) similar to that in (35) reads

$$L_3 = \frac{1}{k\dot{x} + k^2x^2 + \lambda}. \quad (37)$$

One can check that

$$L_4 = \ln(k\dot{x} + k^2x^2 + \frac{\lambda}{2}) \quad (38)$$

Is associated with the oscillator equation:

$$\ddot{x} + 4kx\dot{x} + 2k^2x^3 + \lambda = 0. \quad (39)$$

From the expressions for L_s presented here it is clear that Emden-type equations for $\beta = \alpha^2/9$ follow from the inverse type of Lagrangians while those for $\beta = \alpha^2/8$ follow from a logarithmic class. Both inverse and logarithmic class of Lagrangians do involve neither the kinetic energy term nor the potential function. As a result they were qualified as nonstandard [12].

The Jacobi integral for the one-dimensional motion can be written as [9]

$$J = \dot{x} \frac{\partial L}{\partial \dot{x}} - L. \quad (40)$$

For the equations in (5) and (6) the expressions for J obtained from (35), (36) and (40) can be written as

$$J_1 = -\frac{kx^2 + 2\dot{x}}{(kx^2 + \dot{x})^2} \quad (41)$$

And

$$J_2 = \frac{\dot{x}}{kx^2 + \dot{x}} - \ln(kx^2 + \dot{x}). \quad (42)$$

For (41) we can express \dot{x} as a function of x and J_1 and solve the resulting equation to get the solution of (5), which agrees with that given in (12). On the other hand \dot{x} in (42) occurs in essentially non-algebraic way and does not permit one to write \dot{x} as a function of x and J_2 . This is precisely the reason why the MEE for $\beta = \alpha^2/8$ poses inordinate complications to find its solution.

Let us generalize (35) and (36) to write

$$L_1^g = \frac{1}{k\dot{x} + k^2 x^n} \quad (43)$$

And

$$L_2^g = \ln(k\dot{x} + k^2 x^n). \quad (44)$$

The equations of motion corresponding to (43) and (44) are:

$$\ddot{x} + \frac{3}{2} knx^{n-1}\dot{x} + \frac{1}{2} nk^2 x^{2n-1} = 0 \quad (45)$$

and

$$\ddot{x} + 2knx^{n-1}\dot{x} + nk^2x^{2n-1} = 0 \quad (46)$$

respectively. Equations (45) and (46) give the equations of motion for the over-damped and critically damped harmonic oscillators for $n=1$ with appropriate non-standard Lagrangians obtained from (43) and (45) respectively. This provides an example of the non-standard Lagrangian representation for a system which follows from an explicitly time-dependent standard Lagrangian [13].

The non-standard Lagrangians are explicitly time independent by choice although the associated equations of motion involve velocity terms. Thus the Hamiltonians corresponding to both will refer to the total energies of the systems represented by (45) and (46). Using the Legendre transformation between the Hamiltonian H and Lagrangian L

$$H = (\dot{x}p_x - L)_{\dot{x}=f(x, p_x)}, \quad p_x = \frac{\partial L}{\partial \dot{x}} \quad (47)$$

we obtain the Hamiltonian functions

$$H_1^g = \frac{2\sqrt{p_1}}{\sqrt{k}} - kp_1x^n \quad (48)$$

And

$$H_2^g = 1 - \ln\left(\frac{k}{p_2}\right) - kp_2x^n \quad (49)$$

For (45) and (46). Here p_1 and p_2 are given by

$$p_1 = \frac{k}{(k\dot{x} + k^2x^n)^2} \quad (50)$$

And

$$p_2 = \frac{k}{k\dot{x} + k^2x^n} \quad (51)$$

If we substitute back the values of p_1 and p_2 in (50) and (51) in (48) and (49) we shall get respectively the Jacobi integrals J_1^g and J_2^g for the equations of motion in (45) and (46). Written explicitly

$$J_1^g = \frac{kx^n + 2\dot{x}}{k(kx^n + \dot{x})^2} \quad (52)$$

And

$$J_2^g = \frac{\dot{x}}{kx^n + \dot{x}} - \ln(k^2 x^n + k\dot{x}). \quad (53)$$

For $n = 2$ (52) and (53) reduce to the results in (41) and (42).

Summary. We introduced, in this paper, two methods to solve modified Emden-type equations. The merit of the approaches developed by us lies in their simplicity and effectiveness to deal with the problem. The first method, where we obtained the general solutions from a particular solution satisfying the asymptotic boundary condition only has a deep root in the scientific literature. For example, Sommerfeld [14] used the exact particular solution $144/x^3$ to construct a beautiful well behaved analytic solution for the famous Thomas-Fermi equation (TF). The method of Majorana [15] for constructing semi-analytical solution of the TF equation also provides another example in respect of this. In the second method we modified a factorization technique of differential operators applicable to Liénard-type equations for finding particular solutions. The modification used by us automatically led to general solutions not only of MEEs but also of an unusual Liénard-type oscillator.

References

- [1] E. L. Ince, *Ordinary Differential Equations* (Dover, New York, 1956).
- [2] S. Chandrasekher, *An Introduction to the study of Stellar Structure* (Dover Pub., New York, 1957).
- [3] P. G. Leach, *J. Math. Phys.* Vol. 26, 2310 (1985).
- [4] V. K. Chandrasekar, M. Senthilvelan and M. Lakshmanan, On the general solution for the modified Emden-type equation, *J. Phys. A : Math. Theor.* 40, 4717 (2007).
- [5] M. J. Prelle and M. F. Singer, Elementary first integrals of differential equations, *Trans. Amer. Math. Soc.* 279, 215 (1983).
- [6] R. Iacono 2008, Comment on 'On the general solution for the modified Emden-type equation, *J. Phys. A : Math. Theor.* 41, 068001(2008).
- [7] V. K. Chandrasekar, M. Senthilvelan and M. Lakshmanan, Reply to 'Comment on "On the general solution for the modified Emden type equation, *J. Phys. A : Math. Theor.* 41, 0680002(2008).
- [8] V. K. Chandrasekar, M. Senthilvelan and M. Lakshmanan, Unusual Liénard-type nonlinear oscillator, *Phys. Rev. E* 72, 066203(2005).

- [9] H. Goldstein *Classical Mechanics*, 7th reprint (Narosa Pub. House, New Delhi, India, 1998).
- [10] H. C. Rosu and O. Cornejo-Pérez, Supersymmetric pairing of kinks for polynomial nonlinearities, *Phys. Rev. E* 71, 046607(2005).
- [11] O. Cornejo-Pérez and H. C. Rosu, Nonlinear second order ODE's: Factorizations and particular solutions, *Prog. Theor. Phys.* 114, 533 (2005).
- [12] J. F. Cariñena, M. F. Rañada and F. Santander, Lagrangian formalism for nonlinear second-order Riccati systems: one-dimensional integrability and two-dimensional superintegrability, *J. Math. Phys.* 46, 062703 (2005).
- [13] P. Caldirola *Nuovo. Cim.* 18. 393 (1941); E. Kanai *Prog. Theor. Phys.* 20, 440(1948).
- [14] A. Sommerfeld, 1932 *Z. Phys.* 78, 19 (1932).
- [15] S. Esposito, Majorana solution of the Thomas-Fermi equation, arXiv : physics/0111167v1(2001) [physics. atom-ph]

Improvement of Fourier Series Convergence on the Basis of Splines and Its Application for Numerical Inversion of Laplace Transform

Tanya Solyar ^{1,a}

1 – Pidstryhach Institute for Applied Problems of Mechanics and Mathematics, National Academy of Sciences of Ukraine, 3-B Naukova St., 79060 Lviv, Ukraine

a – tanya@iapmm.lviv.ua



DOI [10.13140/RG.2.1.4069.2727](https://doi.org/10.13140/RG.2.1.4069.2727)

Keywords: Fourier series, improvement of series convergence, piecewise-continuous polynomials, conformal mapping, numerical inversion of Laplace transform.

ABSTRACT. The method of approximation of functions by piecewise continuous polynomials of second degree by means of least squares method is proposed. At that, the finding of functions in the nodal points is reduced to solving the system of linear algebraic equations. The developed approach is used for functions given by Fourier series for which this system is solved in closed form. Thus, the formula for finding the functions in nodal points through modified Fourier series is obtained. There is illustrated the effectiveness of proposed formulas for numerically-analytical finding the original based on an improved approach of Prudnikov, which in general is reduced to calculation of the slowly convergent Fourier series.

1. Introduction. The solution of a wide class of applied problems of mathematical physics is written in the form of Fourier series. In addition, on solving a system of differential equations in partial derivatives the method of Fourier series is used jointly with other approaches. In particular, on additional applying the method of boundary elements the series coefficients are found by means of solution the one-or two-dimensional integral equations by numerical method [1-6]. In addition, determination of the series coefficients demands a lot of calculations and these coefficients are found with some errors what, in turn, can cause the loss of calculation accuracy. Due to this fact, at the studying these problems actual will be the problem of development the approaches to improve the series convergence which would enable one to sum these series with controlled accuracy on the basis of relatively small number of terms.

To improve the series convergence in literature [7] are used widely the approaches, obtained on the basis of consideration the problem of series summation, which is incorrect problem [8]. Since the functions, which are described by the series with improved convergence, are found at that as some averaging of the initial [7], then the fast-charging values in the vicinity of localized actions will be found with the largest error. Other methods of improving the series convergence [7, 8] are also efficient only for separate classes of functions.

The article offers a way to improve the Fourier series convergence for the functions in the assumption that they can be approximated with given accuracy by piecewise-continuous polynomials of the second degree. The constructed formula is applied to increase the accuracy of numerical inversion of Laplace transform.

Note that in [9] way of improving the Fourier series convergence is given for the functions in the assumption that they can be approximated with given accuracy by piecewise-continuous polynomials of the first degree.

2. Basic Ratio. First present the formulas for approximation the functions by piecewise continuous polynomials using the least squares method. Consider the function $f(x)$ continuous on the interval $c \leq x \leq d$. We will describe it on this interval approximately by the function of the form

$$f(x) \equiv \tilde{f}(x) = \sum_{j=0}^J A_j g_j(x), \quad (1)$$

where $g_j(x)$ – are the linearly independent functions.

We find coefficients A_j by the least square method minimizing the expression

$$I = \int_c^d \varphi(x) \left[f(x) - \sum_{j=1}^J A_j g_j(x) \right]^2 dx,$$

where $\varphi(x)$ is – the given weight function. From this we obtain a system of equations to determine the coefficients A_j

$$\sum_{j=0}^N \alpha_{ij} A_j = \beta_i, \quad i = 0, \dots, N. \quad (2)$$

Here

$$\alpha_{ij} = \int_c^d \varphi g_i g_j dx, \quad \beta_i = \int_c^d \varphi f g_i dx.$$

Divide the segment $[c, d]$ into $2N$ intervals with a step $h = \frac{d-c}{2N}$ with nodes $x_j = c + jh$, $j = 0, \dots, 2N$. Approximate the function $f(x)$ by the second order piecewise-continuous polynomials. On the intervals $x_{2n} < x < x_{2n+2}$ we write the interpolation polynomial with nodes $x_{2n}, x_{2n+1}, x_{2n+2}$ as

$$f(x) = A_{2n} \frac{(x-x_{2n+1})(x-x_{2n+2})}{2h^2} + A_{2n+1} \frac{(x-x_{2n})(x-x_{2n+2})}{-h^2} + A_{2n+2} \frac{(x-x_{2n})(x-x_{2n+1})}{2h^2},$$

where A_j – are the values (unknowns) of function $f(x)$ at the points $x = x_j$.

The functions $g_j(x)$ in (1) can be written as

$$g_{2n+1} = -\frac{(x-x_{2n})(x-x_{2n+2})}{h^2} \text{ for } x_{2n} < x < x_{2n+2},$$

$$g_{2n} = \left(1 - \frac{|x - x_{2n}|}{2h}\right) \left(1 - \frac{|x - x_{2n}|}{h}\right) \text{ for } x_{2n-2} < x < x_{2n+2},$$

$$g_0 = \left(1 - \frac{x}{2h}\right) \left(1 - \frac{x}{h}\right), \quad g_{2N} = \left(1 + \frac{x - x_{2N}}{2h}\right) \left(1 + \frac{x - x_{2N}}{h}\right).$$

Then we write a system of equations (2) in the form

$$0,5\alpha_0 A_0 + \alpha_1 A_1 + \alpha_2 A_2 = \beta_0,$$

$$\alpha_2 A_{2N-2} + \alpha_1 A_{2N-1} + 0,5\alpha_0 A_{2N} = \beta_{2N},$$

$$\alpha_2 A_{j+2} + \alpha_1 A_{j+1} + \alpha_0 A_j + \alpha_1 A_{j-1} + \alpha_2 A_{j-2} = \beta_j, \quad j = 2, 4, \dots, 2N-2,$$

$$\alpha_1 A_{j+1} + 2\alpha_0 A_j + \alpha_1 A_{j-1} = \beta_j, \quad j = 1, 3, \dots, 2N-1, \quad (3)$$

where:

$$a_0 = \frac{8}{15}h, \quad a_1 = \frac{2}{15}h, \quad a_2 = -\frac{1}{15}h,$$

$$\beta_{2n} = \int_{-2h}^{2h} f(x + x_{2n}) \left(1 - \frac{|x|}{2h}\right) \left(1 - \frac{|x|}{h}\right) dx = h \int_{-2}^2 f(ht + x_{2n}) \left(1 - \frac{|t|}{2}\right) (1 - |t|) dt,$$

$$\beta_{2n+1} = -\frac{1}{h^2} \int_{-2h}^{2h} f(x + x_{2n+1}) (x^2 - h^2) dx = -h \int_{-1}^1 f(ht + x_{2n+1}) (t^2 - 1) dt,$$

$$\beta_{2N} = \int_{-2h}^0 f(x + x_{2N}) \left(1 + \frac{x}{2h}\right) \left(1 + \frac{x}{h}\right) dx = h \int_{-2}^0 f(ht + x_{2N}) \left(1 + \frac{t}{2}\right) (1 + t) dt,$$

$$\beta_0 = \int_0^{2h} f(x) \left(1 - \frac{x}{2h}\right) \left(1 - \frac{x}{h}\right) dx = h \int_0^2 f(ht) \left(1 - \frac{t}{2}\right) (1 - t) dt.$$

3. Improvement of Fourier Series Convergence. Consider the function given by the series

$$f(x) = \sum_{k=-\infty}^{\infty} a_k e^{i\lambda_k x} \quad (4)$$

for $\lambda_k = \frac{2\pi k}{L}$, $c=0$, $d=L$, $L=\text{const.}$

The coefficients β_j will be

$$\beta_{2n} = h \sum_k a_k \exp(i\lambda_k x_{2n}) \varphi_{2k}, \quad n=1, \dots, N-1,$$

$$\beta_{2n+1} = h \sum_k a_k \exp(i\lambda_k x_{2n+1}) \varphi_{1k}, \quad n=0, \dots, N-1,$$

$$\beta_0 = h \sum_k a_k \varphi_{0k} \exp(i\lambda_k h), \quad \beta_{2N} = h \sum_k a_k \overline{\varphi_{0k}} \exp(-i\lambda_k h), \quad (5)$$

where

$$\begin{aligned} \varphi_{2,k} &= \int_{-2}^2 \exp(i\gamma_k t) \left(1 - \frac{|t|}{2}\right) \left(1 - \frac{|t|}{h}\right) dt, \quad \varphi_{1,k} = - \int_{-1}^1 \exp(i\gamma_k t) (t^2 - 1) dt, \\ \varphi_{0,k} &= 0,5 \int_{-1}^1 \exp(i\gamma_k t) (t - 1) t dt, \quad \gamma_k = \lambda_k h. \end{aligned}$$

This implies, that

$$\begin{aligned} \varphi_{2,k} &= \varphi_2(\gamma_k), \quad \varphi_{1,k} = \varphi_1(\gamma_k), \quad \varphi_{0,k} = \varphi_0(\gamma_k), \\ \varphi_2(\lambda) &= \frac{2}{\lambda^2} \left(1 + \cos^2 \lambda - \frac{\sin 2\lambda}{\lambda}\right), \quad \varphi_1(\lambda) = \frac{4}{\lambda^2} \left(\frac{\sin \lambda}{\lambda} - \cos \lambda\right), \\ \varphi_0(\lambda) &= \frac{\sin \lambda}{\lambda} - 0,5 \varphi_1(\lambda) (1 + 0,5\lambda i). \end{aligned}$$

We note, that $\varphi_2(0) = 2/3$, $\varphi_1(0) = 4/3$, $\varphi_0(0) = 1/3$.

4. Periodic Continuous Function $f(x)$. Assume that the function $f(x)$ is continuous for $0 < x < L$ and $f(0) = f(L)$. In this case the function $f(x)$ is continuous and periodic with a period L . Denote the coefficients A_j by Φ_j for this case. Then a system of equations (3) will have the form:

$$\begin{aligned} -\Phi_{j+2} + 2\Phi_{j+1} + 8\Phi_j + 2\Phi_{j-1} - \Phi_{j-2} &= \beta_j \frac{15}{h}, \quad j=0, 2, \dots, 2N-2, \\ 2\Phi_{j+1} + 16\Phi_j + 2\Phi_{j-1} &= \beta_j \frac{15}{h}, \quad j=0, 3, \dots, 2N-1, \\ -\Phi_{2N+2} + 2\Phi_{2N+1} + 8\Phi_{2N} + 2\Phi_{2N-1} - \Phi_{2N-2} &= \beta_{2N}^* \frac{15}{h}, \end{aligned} \quad (6)$$

where

$$\beta_{2N}^* = h \int_{-2}^2 f(ht + x_{2N}) \left(1 - \frac{|t|}{2}\right) (1 - |t|) dt = \beta_0 + \beta_{2N} = h \sum_k a_k \exp(i\lambda_k x_{2N}) \varphi_{2k}.$$

In view of the expressions for the coefficients β_j we find first the solution of a system of equations (6) at $\beta_{2k} = s_2 c^{2k}$, $\beta_{2k+1} = s_1 c^{2k+1}$, where $s_{1,2}$ are the given constants, $c = \exp(i\lambda)$. Represent

$$\Phi_{2k} = S_2 c^{2k}, \Phi_{2k+1} = S_1 c^{2k+1},$$

where $S_{1,2}$ – are the unknown constants.

Substituting these constants into a system of equations (6), we obtain a system to determine $S_{1,2}$ of the form:

$$\begin{cases} S_2(-c^2 - c^{-2} + 8) + 2S_1(c + c^{-1}) = 15s_2, \\ 2S_2(c + c^{-1}) + 16S_1 = 15s_1. \end{cases}$$

Rewrite it in the form:

$$\begin{cases} S_2(-2\cos 2\lambda + 8) + 4S_1 \cos \lambda = 15s_2, \\ 4S_2 \cos \lambda + 16S_1 = 15s_1. \end{cases}$$

This implies, that

$$S_2 = \frac{4s_2 - s_1 \cos \lambda}{8 - 2\cos 2\lambda - \cos^2 \lambda} \frac{15}{4}, \quad S_1 = -\frac{s_2 \cos \lambda - s_1(2 - 0,5 \cos 2\lambda)}{8 - 2\cos 2\lambda - \cos^2 \lambda} \frac{15}{4}.$$

On the basis of obtained formulas from a system of equations (6) we find

$$\Phi_{2n} = \sum_{k=-\infty}^{\infty} a_k \Gamma_{2,k} \exp(i\lambda_k x_{2n}), \quad \Phi_{2n+1} = \sum_{k=-\infty}^{\infty} a_k \Gamma_{1,k} \exp(i\lambda_k x_{2n+1}), \quad (7)$$

where

$$\Gamma_{2,n} = \frac{15}{4} \frac{4\varphi_2(\gamma_n) - \varphi_1(\gamma_n) \cos \gamma_n}{\Delta(\gamma_n)} = g_2(\gamma_n),$$

$$\Gamma_{1,n} = \frac{15}{4} \frac{-\varphi_2(\gamma_n) \cos \gamma_n + (2 - 0,5 \cos 2\gamma_n) \varphi_1(\gamma_n)}{\Delta(\gamma_n)} = g_1(\gamma_n). \quad (8)$$

Here

$$g_1(\lambda) = 15 \frac{-5 \cos \lambda - \cos \lambda \sin^2 \lambda + 5 \sin \lambda / \lambda}{2 \Delta \lambda^2}, \quad \Delta(\lambda) = 8 - 2 \cos 2\lambda - \cos^2 \lambda.$$

$$g_2(\lambda) = 15 \frac{2 + 3 \cos^2 \lambda - 2,5 \sin 2\lambda / \lambda}{\Delta \lambda^2}.$$

For large values n the coefficients $\Gamma_{j,k} = O(k^{-2})$. For this reason the formulas (7) make it possible to find the values of function f at the nodes in terms of the series the convergence of which is much higher than that of initial series (5).

The graphs of function as $g_{1,2}(\lambda)$ are given in Fig. 1.

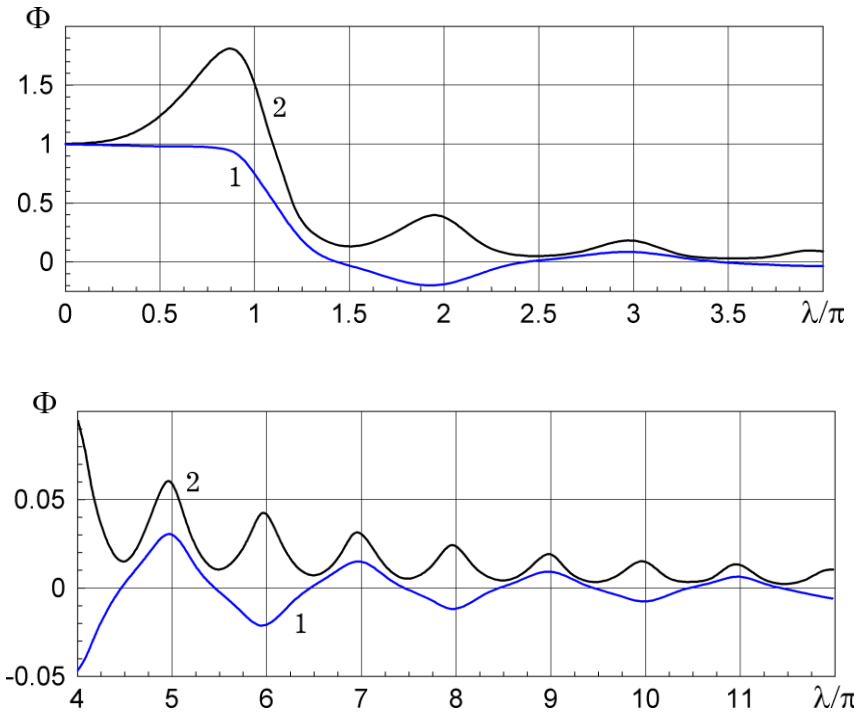


Figure 1. The graphs of auxiliary function $g_{1,2}(\lambda)$.

From the graph we see that to improve the convergence of slowly convergent series it is advisable to confine ourselves in the series M by the terms choosing them so that $\lambda_M h \approx (m+0,5)\pi$, $m=2,3,\dots$. That is it is advisable to assume $M \approx (m+0,5)N$. In addition the first not considered forms of the series will be small because of near to zero values of multipliers $\Gamma_{n,k}$.

5. The Case of Nonperiodic Functions. Consider now a general case when $f(0) \neq f(L)$. We present solutions of the system (3) as

$$A_j = \Phi_j + D_j.$$

Substituting it into (3), we obtain a system of equations to determine the values D_j

$$\begin{aligned} -D_{j+2} + 2D_{j+1} + 8D_j + 2D_{j-1} - D_{j-2} &= 0, \quad j = 1, 2, \dots, 2N-2. \\ 2D_{j+1} + 16D_j + 2D_{j-1} &= 0, \quad j = 0, 3, \dots, 2N-1, \\ 4D_0 + 2D_1 - D_2 &= \delta_0, \\ -D_{2N-2} + 2D_{2N-1} + 4D_{2N} &= \delta_{2N}, \end{aligned} \tag{9}$$

where

$$\delta_0 = \frac{15}{h} \beta_0 - (4\Phi_0 + 2\Phi_1 - \Phi_2), \quad \delta_{2N} = \frac{15}{h} \beta_{2N} - (-\Phi_{2n-2} + 2\Phi_{2n-1} + 4\Phi_{2N}).$$

On the basis of the last of equations of the system (6) we have $\delta_0 + \delta_{2N} = 0$. That is $\delta_{2N} = -\delta_0$.

A solution of this system we shall seek in the form

$$D_{2k} = Dq^{2k}, \quad k = 0, \dots, N; \quad D_{2k+1} = Dpq^{2k+1}, \quad k = 0, \dots, N-1,$$

where D, q, p – are the unknown values.

Substituting it into the homogeneous equations of the system (9) we obtain the equation

$$\begin{cases} -(q^2 + q^{-2}) + 2p(q + q^{-1}) + 8 = 0, \\ q + q^{-1} + 8p = 0. \end{cases}$$

Denote $q + q^{-1} = z$. Then these equations become

$$\begin{cases} -z^2 + 2pz + 10 = 0, \\ z + 8p = 0. \end{cases}$$

Solving this system we obtain

$$z_{1,2} = \pm 2\sqrt{2}, \quad p_{1,2} = \mp \frac{\sqrt{2}}{4}.$$

Then from equation $q + q^{-1} = z_{1,2}$ we find the roots $q_1 = -\sqrt{2} + 1, \quad p_1 = \frac{\sqrt{2}}{4}; \quad q_2 = -\sqrt{2} - 1 = \frac{1}{q_1}, \quad p_2 = p_1; \quad q_3 = -q_1, \quad p_3 = -p_1; \quad q_4 = -q_2, \quad p_4 = -p_2.$

Thus the general solution for homogeneous equations of the system (9) will read

$$\begin{aligned} D_{2k} &= B_1 q_1^{2k} + B_2 q_2^{2k} + B_3 q_3^{2k} + B_4 q_4^{2k} = (B_1 + B_3) q_1^{2k} + (B_2 + B_4) q_2^{2k}, \quad k = 0, \dots, N \\ D_{2k+1} &= B_1 p_1 q_1^{2k} + B_2 p_2 q_2^{2k} + B_3 p_3 q_3^{2k} + B_4 p_4 q_4^{2k} = \\ &= p_1 \left[(B_1 + B_3) q_1^{2k+1} + (B_2 + B_4) q_2^{2k+1} \right], \quad k = 0, \dots, N-1. \end{aligned}$$

where $B_{1, \dots, 4}$ – are arbitrary constants.

That is, the general solution will have the form

$$\begin{aligned} D_{2k} &= A q_1^{2k} + \frac{B}{q_2^{2N}} q_2^{2k}, \quad k = 0, \dots, N, \\ D_{2k+1} &= p_1 \left[A q_1^{2k+1} + \frac{B}{q_2^{2N}} q_2^{2k+1} \right], \quad k = 0, \dots, N-1. \end{aligned}$$

where A, B – are the arbitrary constants.

Substituting the obtained solution into non homogeneous equations of the system (8), we obtain

$$\begin{cases} d_1 A + d_2 q_1^{2N} B = \delta_0, \\ d_2 q_1^{2N} A + d_1 B = \delta_{2N}, \end{cases}$$

where $d_{1,2} = 4 + 2p_1 q_{1,2} - q_{1,2}^2 = \pm 5/\sqrt{2}.$

From this we obtain

$$A = \frac{d_1 \delta_0 - d_2 q_1^{2N} \delta_{2N}}{d_1^2 - q_1^{4N} d_2^2} = \frac{\delta_0}{d_1} \frac{1}{1 + q_1^{2N}}, \quad B = \frac{d_1 \delta_{2N} - d_2 q_1^{2N} \delta_0}{d_1^2 - q_1^{4N} d_2^2} = -A. \quad (10)$$

That is

$$D_{2n} = Aq_1^{2n} + \frac{B}{q_2^{2N}} q_2^{2n} = A(q_1^{2n} - q_1^{2N-2n}), \quad n = 0, \dots, N;$$

$$D_{2n+1} = p_1 A (q_1^{2n+1} - q_1^{2N-2n-1}), \quad n = 0, \dots, N-1.$$

Thus to determine the functions at the nodes we have

$$f(x_{2n}) = \Phi_{2n} + D_{2n} = \sum_{k=-\infty}^{\infty} a_k \Gamma_{2,k} \exp(i\lambda_k x_{2n}) + \frac{\sqrt{2}}{5} \delta_0 \frac{q_1^{2n} - q_1^{2N-2n}}{1+q_1^{2N}}, \quad n = 0, \dots, N,$$

$$f(x_{2n+1}) = \Phi_{2n+1} + D_{2n+1} = \sum_{k=-\infty}^{\infty} a_k \Gamma_{1,k} \exp(i\lambda_k x_{2n+1}) + \frac{\delta_0}{20} \frac{q_1^{2n+1} - q_1^{2N-2n-1}}{1+q_1^{2N}}, \quad n = 0, \dots, N-1. \quad (11)$$

The multipliers q_1^n for $n=1, \dots, 6$ are equal to: 0,414; 0,172; 0,071; 0,029; 0,012; 0,005. That is these multipliers decay rapidly, therefore at the internal points x_k for $k > 5$ we can reject the components D_n in (11). Analogously, at the points far from the boundary point $x=L$ we can also reject the components D_n .

6. Optimization of the Algorithm. When applying the above approach the values Φ_n , $n=0, \dots, 2N$ are determined in terms of quickly convergent series, the initial coefficients in which are multiplied by the multipliers of the order $O(k^{-2})$ as $k \rightarrow \infty$. At the same time when determining the coefficients A, B in (10) it is necessary to determine the constants β_0, β_{2N} expressed in terms of the series the coefficients in which have additional multipliers of the order $\varphi_0(\lambda_k h) O(k^{-1})$ as $k \rightarrow \infty$. The graphs of the curves $\text{Re } \varphi_0, \text{Im } \varphi_0$ are given in Fig. 2 by the curves 1 and 2.

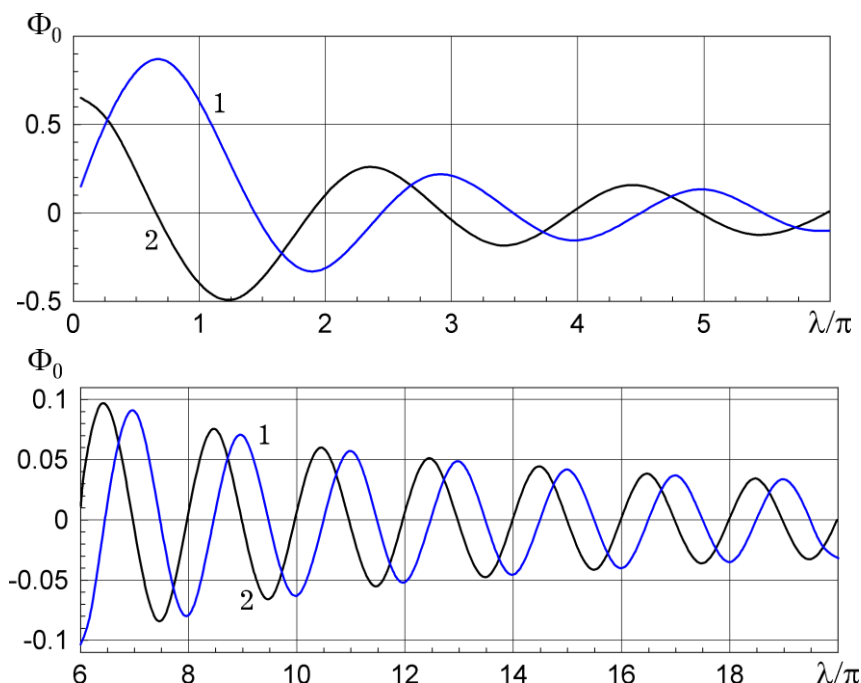


Figure 2. The graph of auxiliary function $\operatorname{Re} \varphi_0, \operatorname{Im} \varphi_0$.

From Fig. 2 we see that to calculate these constants it is necessary to hold a greater number of the series terms than to find the coefficients Φ_n ($M \sim 8N$). Besides, the constants β_0, β_{2N} in the system (9) have as a multiplier the number 15 what demands to calculate with larger accuracy.

Consider the case when we can avoid calculating these relatively slowly convergent series. Let the function $f(x)$ be continuous together with derivative and given by the series (4) on the interval $[0, L]$ and $f(0) \neq f(L)$. In this case the series (4) converge slowly and the coefficients in it have the order $a_k = O(1/k)$, $k \rightarrow \infty$.

Really,

$$\begin{aligned} a_k &= \frac{1}{L} \int_0^L f(x) \exp(-i\lambda_k x) dx = \\ &= \frac{f \exp(-i\lambda_k x)}{-i\lambda_k L} \Big|_{x=0}^L + \frac{1}{i\lambda_k L} \int_0^L f' \exp(-i\lambda_k x) dx = \frac{i}{\lambda_k} \delta + O(k^{-2}), \end{aligned}$$

where

$$\delta = \frac{f(L) - f(0)}{L}. \quad (12)$$

Put $f(x) = F(x) + \delta x$, where $F(x) = f(x) - \delta x$.

We present the function $F(x)$ as a series

$$F(x) = \sum_{k=-\infty}^{\infty} (a_k - \delta \gamma_k) \exp(i\lambda_k x), \quad (13)$$

where $\gamma_k = i/\lambda_k$.

Obviously the series (13) for functions $F(x)$ converges more rapidly then for initial function $f(x)$, since the coefficients in it are of the order $O(k^{-2})$ as $k \rightarrow \infty$.

To calculate the function $F(x)$, which is a continuous periodic (with a period L), we apply the relation (7)

$$F(x_n) \approx \sum_{k=-\infty}^{\infty} (a_k - \delta \gamma_k) g_{n,k} \exp(i\lambda_k x) = \Phi_n - \delta Y_n,$$

where

$$Y_n = \sum_{k=-\infty}^{\infty} \gamma_k g_{n,k} \exp(i\lambda_k x_n), \quad g_{2m,k} = \Gamma_{2,k}, g_{2m+1,k} = \Gamma_{1,k}.$$

Then

$$f(x_n) \approx \Phi_n + \delta(x_n - Y_n). \quad (14)$$

Consider the case when the value δ is unknown. To find it we write the expression δ on the basis of (12) and (14)

$$\delta = [f(x_{2N}) - f(x_0)]/L = (\Phi_{2N} - \Phi_0)/L + \delta [1 - (Y_{2N} - Y_0)].$$

Thus we have

$$\delta = \frac{\Phi_{2N} - \Phi_0}{Y_{2N} - Y_0}.$$

Since the value δ can be found in such a way with errors, to determine the function f is advisable to use the formulas

$$f(x_k) \approx (\Phi_k - \delta Y_k) + \delta x_k. \quad (15)$$

The values $(\Phi_k - \delta Y_k)$ it is advisable to determine by the formulas (11) on the basis of (13).

As an example the calculations for function $f(x) = e^{-mx}$ are carried out. The coefficients of the series (4) for this function are

$$a_k = \frac{1}{L} \frac{1 - e^{-mL}}{ki + m}.$$

The calculations are carried out for $m = -2$, $L = 2$, $N = 10$, $M = 35$. The values of function $f(x)$ at the nodes are calculated; the nodes are denoted as: y_t – by the exact formula; y_1 – by the formula (11); y_2 – by the formula (15); y_0 – on the basis of the series (4) containing $M = 100$ and $M = 500$ terms. The calculated values y_t and relative values $y_{1,2} / y_t$ are presented in Table 1.

From the Table we see that in this case the formula (15) enables us to calculate the series with high accuracy on the basis of choice of 11 nodes and 18 terms of the series. Considering 21 nodes and 35 terms of the series, the maximal relative error of finding the series is $\sim 0,1\%$. At the same time when summing up directly the series using 500 terms if the series, the calculation error is much larger, especially near the ends of the interval. Note that sufficiently large error of formula (11) for small values of argument x (values y_1) appeared because of small number of terms when calculating the coefficient β_0 .

Table 1. Approximated and exact values of function $f(x) = e^{-mx}$.

I		$N=10, M=35$		$N=5, M=18$		$M=100$	$M=500$
		x	y_t	y_1 / y_t	y_2 / y_t	y_1 / y_t	y_2 / y_t
	0,0	1,000	1,099	1,000	1,050	1,010	11,1
	0,2	1,492	0,978	0,999	1,009	1,001	1,175
	0,4	2,226	1,001	1,000	0,992	1,004	1,052
	0,6	3,320	0,999	1,000	1,003	0,999	1,018
	0,8	4,953	1,001	1,000	0,999	1,003	1,005
	1,0	7,389	1,000	1,000	0,999	0,999	1,000
	1,2	11,023	1,000	1,000	1,005	1,003	0,997
	1,4	16,445	1,000	1,000	0,999	0,999	0,999
	1,6	24,533	1,000	1,000	1,002	1,001	0,995
	1,8	36,598	1,001	1,000	1,000	1,001	0,993
	2,0	54,598	0,997	0,999	0,995	0,996	9,8
							21,5

7. Determination of Function on the Part of Interval. Consider the case when function given by the series (4) has a peculiarity at some point $x = x_r$. In such cases the series converges slowly and in the vicinity of point x_r it diverges. The proposed way makes possible to calculate the function on the basis of the series on the intervals $[a, b]$ which do not include the point x_r . Then in the given above formulas we assume

$$h = (b - a) / 2N, \quad x_n = a + nh, \quad n = 0, \dots, 2N.$$

As an example consider the function

$$f(x) = 0,5 \ln \frac{1}{2(1 - \cos x)},$$

having algorithmic peculiarity for $x = 0$.

The coefficients of the series (4) for this function are

$$a_k = \frac{1}{2|k|}, \quad k \neq 0; \quad a_0 = 0.$$

The calculations are carried out for $N = 16$, $a = 0,4\pi$, $b = 1,9\pi$, $M = 70$. In Table 2 are presented results of calculations: y_1 – by formula (11); y_0 – on the basis of series (4) containing 200 terms.

Table 2. Approximated and exact values of function $f(x) = 0,5 \ln[2(1-\cos x)]^{-1}$.

x	y_t	y_1 / y_t	y_0 / y_t
1,2566	-0,1618	0,9980	1,0156
1,8064	-0,4515	1,0000	0,9944
2,3562	-0,6140	1,0015	1,0041
2,9060	-0,6862	0,9998	0,9963
3,4558	-0,6808	0,9987	1,0037
4,0055	-0,5968	1,0004	0,9958
4,5553	-0,4192	1,0024	1,0060
5,1051	-0,1054	0,9924	0,9761
5,6549	0,4812	0,9999	0,9947

We see that formula (11) makes possible to calculate the series directly with high accuracy without previous making of logarithmic peculiarity.

8. Improvement of Fourier Series Convergence into Inversion Formula of Laplace Transform on the Basis of Prudnikov Formula. Consider the problem of finding the function $f(t)$ on the

basis of the known integral Laplace image $F(s) = \int_0^\infty f(t) \exp(-st) dt$. Assume $F(s)$ to be an

analytical function for $\operatorname{Re}(s) > d$, where d is a known constant. Then there exists exact formula of presenting the original in terms of its image [10]

$$f(t) = \frac{1}{l} \exp(ct/l) \sum_{n=-\infty}^{\infty} F(s_n) \exp(2\pi n i t/l) - R_1, \quad (14)$$

where $s_n = (c + 2\pi n i)/l$;

c – is the constant, choosing which we can improve convergence of solution ($\operatorname{Re}(c) > 0$);

l – is time constant, $0 < t < l$,

$$R_1 = \sum_{n=1}^{\infty} \exp(-nc) f(t + nl). \quad (15)$$

As a rule, the series in formula (14) converges slowly. This is due to that for a wide class of functions $F(s_n) = O(1/n)$. Therefore, while calculating, using formula (14), to calculate the series it is necessary to hold in it a large number of terms. In this connection it will be problematic to use directly formula (14). In [2-6] for a class of functions with known values of original and its derivative for $t=0$ and at large values of argument, the refined inversion formulas are obtained, these formulas make it possible to calculate the original with controlled accuracy in terms of quickly convergent series.

Consider a widespread case when we know only that the original can be approximated with given accuracy by the second degree piecewise continuous polynomials.

To use formula (14) it is necessary to sum up with given accuracy slowly convergent series

$$S(t) = \sum_{n=-\infty}^{\infty} A_n \exp(2\pi n i t / l), 0 < t < l,$$

where $A_n = F(s_n)$.

We shall show that to this end the formula (7) can be used efficiently. As an example consider the image given by the formula $F(s) = 1/(s\sqrt{s})$, where $a = \text{const}$. Note that function $f(x) = \frac{2}{\sqrt{\pi}}\sqrt{x}$ is the original for this image. In calculations we assumed $c=8$, $l=L=6$ and rejected the residual term R_1 , since at that it will have a small multiplier $e^{-8} \approx 3 \cdot 10^{-4}$.

Table 3 presents the values of exact function $y_T = f(t)$ and relative errors in percent

$$\varepsilon_1 = \frac{y_1 - y_T}{y_T} 100, \quad \varepsilon_2 = \frac{y_2 - y_T}{y_T} 100.$$

Table 3. The error of inversion formula of Laplace transform.

X	$y = 2\sqrt{x}/\pi$			$y = e^{-x}$		
	y_T	ε_1	ε_2	y_T	ε_1	ε_2
0	0,000			1,000	0,131	0,283
0,5	0,798	0,343	-0,056	0,607	-0,062	0,004
1	1,128	-0,045	-0,064	0,368	-0,071	0,013
1,5	1,382	-0,067	-0,074	0,223	-0,055	0,042
2	1,596	-0,066	-0,103	0,135	-0,025	0,137
2,5	1,784	-0,065	-0,172	0,082	0,027	0,445
3	1,954	-0,066	-0,329	0,050	0,120	1,441
3,5	2,111	-0,069	-0,678	0,030	0,297	4,670
4	2,257	-0,080	-1,473	0,018	0,667	15,180
4,5	2,394	-0,107	-3,375	0,011	1,540	49,688

5	2,523	-0,199	-8,504	0,007	4,861	165,965
---	-------	--------	--------	-------	-------	---------

As it is seen from the Table 3, the proposed formula (7) enables to have larger accuracy using 60 terms than direct calculation the series, containing 1000 terms. The largest relative errors of formula (7) are at the points where function $f(x)$ is small in its value.

Table 2 presents as well the results of calculations for functions $f(t) = e^{-t}$ for which the image is $F(s) = 1/(s+1)$. We see that accuracy of finding the original by formula (7) for this function is also high.

Summary. The way to improve the convergence of Fourier series is constructed; it is efficient for functions which can be approximated by the second degree piecewise-continuous polynomials. The obtained formulas are applied to improve the series convergence appearing at numerical inversion of Laplace transform by Prudnikov formula. The presented examples illustrate the efficiency of approach for numerical finding the originals on the basis of their Laplace images.

References

- [1] R. M. Kushnir and T. Ya. Solyar, A numerical-analytical approach to the analysis of nonstationary temperature fields in multiply-connected solids, *Mechanics, Materials Science & Engineering*, March, no. 3, pp. 90-106, 2016. DOI 10.13140/RG.2.1.1167.0165.
- [2] R. M. Kushnir, V. M. Maksymovych, and T. Ya Solyar, Determination of nonstationary temperatures with the help of improved formulas of the inverse Laplace transformation, *Mater. Sci.*, vol. 38, no. 2, pp. 172–184, 2002.
- [3] R. M. Kushnir and T. Ya Solyar, Quasistationary temperature stresses in multiply connected plates in the process of heating, *J. Mater. Sci.*, vol. 46, no. 6, pp. 739–748, 2006.
- [4] R. M. Kushnir and T. Ya Solyar, Unsteady thermal stresses near a curvilinear hole in a plate with heat transfer under its warming by a heat flow, *J. Math. Sci.*, vol. 160, no. 4, pp. 407–415, 2009.
- [5] V. N. Maksimovich and T. Ya Solyar, Refined formulas for determination of the inverse Laplace transform using Fourier series and their use in problems of heat conduction, *J. Eng. Phys. Thermophys.*, vol. 75, no. 3, pp. 648-650, 2002.
- [6] O. V. Maksymovych and T. Ya. Solyar, Determination of three-dimensional temperature fields in multiply connected orthotropic bodies under heating with heat sources and flows, *J. Math. Sci.*, vol. 168, no. 5, pp. 739–745, 2010.
- [7] N. N. Kalitkin, *Numerical Methods*, Nauka, Moscow, 1978.
- [8] A. N. Tikhonov. and V. Y. Arsenin, *Solution of Ill-posed Problems*, John Wiley & Sons Inc., New York, 1977.
- [9] T. Solyar, *Ways to improve Fourier series convergence and its application for Laplace numerical inversion*, *Sci. J. Ternopil National Technical University*, no. 1(81), pp. 136-144, 2016.
- [10] V. A. Ditkin and A. P. Prudnikov, *Integral Transforms and Operational Calculus*, Oxford, New York, 1965.

On the Boltzmann Equation of Thermal Transport for Interacting Phonons and Electrons

Amelia Carolina Sparavigna¹

1 – Department of Applied Science and Technology, Politecnico di Torino, Torino, Italy



DOI 10.13140/RG.2.1.2824.0885

Keywords: Boltzmann Equation, thermal conductivity, phonons and electrons.

ABSTRACT. The thermal transport in a solid can be determined by means of the Boltzmann equations regarding its distributions of phonons and electrons, when the solid is subjected to a thermal gradient. After solving the coupled equations, the related thermal conductivities can be obtained. Here we show how to determine the coupled equations for phonons and electrons.

Introduction. In some previous papers we have considered the thermal transport in a solid when just phonons are present [1-6]. Phonons are the quantization of the vibrations of the ions in crystals. They are the quanta which are carrying the thermal energy in the dielectric solids. Since the phonons are interacting among them and with the crystal defects and boundaries, a finite thermal conductivity is observed. Here, we will consider the presence in the solid of both phonons and electrons, subjected to a thermal gradient. The electrons we consider are those which can freely move in the crystal. In fact, these electrons can give rise to several phenomena connected to charge transport: these phenomena will be the subject of a future paper. Here we concentrate just on the effect of a thermal gradient and on the interaction of electrons with phonons and how it can be described by the Boltzmann equation, aiming to introduce the subject to students of engineering colleges.

As shown in [7-9], the interaction among phonons, in three phonons scattering processes for instance, is coming from the Lagrangian of the lattice. In the case that in the solid there are electrons which can support an energy/charge conductivity, these particles, when moving in the solid, are interacting with the ions of the lattice. The use of a pseudopotential [10] allows us to consider the conducting electrons as electrons described by means of a plane waves basis. In this manner we can analyse the transport with an approach based on a perturbative interaction with phonons, neglecting electron-electron interaction and the scattering of electrons with lattice defects. As we have seen for phonons, we can solve the Boltzmann equation for these electrons and determine their contribution to the thermal conductivity. However, the electron-phonon interaction is also influencing the phonon transport, and therefore the phonon thermal conductivity is changed too.

The Boltzmann equation for phonons in a thermal gradient. A thermal gradient in a solid is exciting electrons and phonons which are present in the crystal; they are gaining energy which are transferring, that is conducting, from one end of the solid to the other, moving from the hotter to the coldest side. In metals, both electrons and phonons are playing a relevant role in the thermal conduction, whereas in dielectrics, only phonons are involved. To find the thermal resistance and then the thermal conductivity of the solid, we need to describe several interactions among phonons, electrons, those of phonons with electrons and of phonons and electrons with defects and impurities of the crystals. Moreover the scattering with the boundaries of the crystal have to be considered too.

The problem of evaluating the thermal conductivity in solids is therefore quite complex. It can be solved, from a microscopic point of view [11], using the relaxation time approximation [5,6,11-18], using some variational [19-21] or iterative methods [1-4], or the Green functions [22,23]. The methods based on relaxation time approximations and on variational and iterative methods are based on the Boltzmann equation, whereas the approach with the Green functions is based on quantum statistics. Here we consider the approach based on the Boltzmann equation.

Let us start from phonons. To derive the Boltzmann equation we need that a distribution function $n_{\mathbf{q}p}(\mathbf{r}, t)$ exists concerning the phonon state (\mathbf{q}, p) about position \mathbf{r} , at time t . The state is described by the wave vector \mathbf{q} and by its polarization p . If a thermal gradient ∇T exists, which is changing the temperature $T = T(\mathbf{r})$ in the sample, we will have a diffusion process in the distribution. In this case we can write:

$$\left. \frac{\partial n_{\mathbf{q}p}}{\partial t} \right|_{\text{diff}} = -k_B T \mathbf{v}_p(\mathbf{q}) \cdot \nabla T \frac{\partial n_{\mathbf{q}p}}{\partial T} \quad (1)$$

In (1), $\mathbf{v}_p(\mathbf{q})$ is the group velocity of phonon (\mathbf{q}, p) . Let us observe that the phonon distribution $n_{\mathbf{q}p}$ is depending on space through the temperature $T = T(\mathbf{r})$.

The scattering processes will give a change of the phonon distribution. In the case of a stationary condition, we must have:

$$\left. -k_B T \mathbf{v}_p(\mathbf{q}) \cdot \nabla T \frac{\partial n_{\mathbf{q}p}}{\partial T} + \frac{\partial n_{\mathbf{q}p}}{\partial t} \right|_{\text{scatt}} = 0 \quad (2)$$

This is the general form of the Boltzmann equation [9, 24]. It is an integral-differential equation. A way to solve this equation is in its linearization, considering only the deviation from equilibrium $n_{\mathbf{q}p} - n_{\mathbf{q}p}^0$, being $n_{\mathbf{q}p}^0$ the equilibrium distribution.

The simplest case of scattering we can discuss is that of an elastic scattering. The phonon process is $(\mathbf{q}, p) \rightarrow (\mathbf{q}', p')$, conserving the energy. In this process, we have a transition from the phonon state (\mathbf{q}, p) to the state (\mathbf{q}', p') . The relative probability of a transition in the unit of time is:

$$P_{\mathbf{q}p}^{\mathbf{q}'p'} = n_{\mathbf{q}p}(n_{\mathbf{q}'p'} + 1) Z_{\mathbf{q}p}^{\mathbf{q}'p'} \quad (3)$$

In (3), $Z_{\mathbf{q}p}^{\mathbf{q}'p'}$ is the intrinsic probability, that is the probability not depending on the occupation of phonon states (\mathbf{q}, p) and (\mathbf{q}', p') . Therefore, the probability of the transition from (\mathbf{q}', p') to (\mathbf{q}, p) is:

$$P_{\mathbf{q}'p'}^{\mathbf{q}p} = n_{\mathbf{q}'p'}(n_{\mathbf{q}p} + 1) Z_{\mathbf{q}'p'}^{\mathbf{q}p} \quad (4)$$

where

$$Z_{\mathbf{q}'p'}^{\mathbf{q}p} = Z_{\mathbf{q}p}^{\mathbf{q}'p'} \quad (5)$$

Because the variation of the phonon distribution is equal to the probability of having a scattering per unit of time, we have:

$$\left. \frac{\partial n_{\mathbf{q}p}}{\partial t} \right|_{\text{scatt}} = \sum_{\mathbf{q}'p'} \left(P_{\mathbf{q}'p'}^{\mathbf{q}p} - P_{\mathbf{q}p}^{\mathbf{q}'p'} \right) = \sum_{\mathbf{q}'p'} \left[n_{\mathbf{q}'p'} (n_{\mathbf{q}p} + 1) - n_{\mathbf{q}p} (n_{\mathbf{q}'p'} + 1) \right] Z_{\mathbf{q}p}^{\mathbf{q}'p'} \quad (6)$$

After simplifying and linearizing we find:

$$\left. \frac{\partial n_{\mathbf{q}p}}{\partial t} \right|_{\text{scatt}} = \sum_{\mathbf{q}'p'} \left[(n_{\mathbf{q}'p'} - n_{\mathbf{q}'p'}^0) - (n_{\mathbf{q}p} - n_{\mathbf{q}p}^0) \right] Z_{\mathbf{q}p}^{\mathbf{q}'p'} \quad (7)$$

In (7), $n_{\mathbf{q}p}^0 = n_{\mathbf{q}'p'}^0$, because $n_{\mathbf{q}p}^0$ is depending just on energy and that in an elastic process:

$$\hbar \omega(\mathbf{q}, p) = \hbar \omega(\mathbf{q}', p') \quad (8)$$

The linearized Boltzmann equation turns out to be:

$$-k_B T \mathbf{v}_p(\mathbf{q}) \cdot \nabla T \frac{\partial n_{\mathbf{q}p}^0}{\partial T} = \sum_{\mathbf{q}'p'} \left[(n_{\mathbf{q}p} - n_{\mathbf{q}p}^0) - (n_{\mathbf{q}'p'} - n_{\mathbf{q}'p'}^0) \right] Z_{\mathbf{q}p}^{\mathbf{q}'p'} \quad (9)$$

In (9), to evaluate $\partial n_{\mathbf{q}p}^0 / \partial T$ we used only the equilibrium distribution $n_{\mathbf{q}p}^0$.

In the general case, to obtain the linearized Boltzmann equation we use the deviation from equilibrium $\Psi_{\mathbf{q}p}$ in the following manner:

$$n_{\mathbf{q}p} = n_{\mathbf{q}p}^0 - \Psi_{\mathbf{q}p} \frac{\partial n_{\mathbf{q}p}^0}{\partial (\hbar \omega_{\mathbf{q}p})} \quad (10')$$

Let us assume $x = \hbar \omega_{\mathbf{q}p} / k_B T$, where k_B is the Boltzmann constant. From (10') we have:

$$\frac{\partial n_{\mathbf{q}p}^0}{\partial(\hbar\omega_{\mathbf{q}p})} = \frac{\partial n_{\mathbf{q}p}^0}{\partial x} \frac{\partial x}{\partial(\hbar\omega_{\mathbf{q}p})} = \frac{1}{k_B T} \frac{\partial}{\partial x} \left\{ \frac{1}{e^x - 1} \right\} = \frac{1}{k_B T} n_{\mathbf{q}p}^0 (n_{\mathbf{q}p}^0 + 1) \quad (10'')$$

Therefore:

$$n_{\mathbf{q}p} = n_{\mathbf{q}p}^0 - \Psi_{\mathbf{q}p} \frac{\partial n_{\mathbf{q}p}^0}{\partial(\hbar\omega_{\mathbf{q}p})} = n_{\mathbf{q}p}^0 + \frac{\Psi_{\mathbf{q}p}}{k_B T} n_{\mathbf{q}p}^0 (n_{\mathbf{q}p}^0 + 1) \quad (10'')$$

For the elastic scattering:

$$-k_B T \mathbf{v}_p(\mathbf{q}) \cdot \nabla T \frac{\partial n_{\mathbf{q}p}^0}{\partial T} = \sum_{\mathbf{q}'p'} [\Psi_{\mathbf{q}p} n_{\mathbf{q}p}^0 (n_{\mathbf{q}p}^0 + 1) - \Psi_{\mathbf{q}'p'} n_{\mathbf{q}'p'}^0 (n_{\mathbf{q}'p'}^0 + 1)] Z_{\mathbf{q}p}^{\mathbf{q}'p'} \quad (11)$$

That is:

$$k_B T \mathbf{v}_p(\mathbf{q}) \cdot \nabla T \frac{\partial n_{\mathbf{q}p}^0}{\partial T} = \sum_{\mathbf{q}'p'} [\Psi_{\mathbf{q}'p'} - \Psi_{\mathbf{q}p}] Q_{\mathbf{q}p}^{\mathbf{q}'p'} \quad (12)$$

$$Q_{\mathbf{q}p}^{\mathbf{q}'p'} = n_{\mathbf{q}p}^0 (n_{\mathbf{q}p}^0 + 1) Z_{\mathbf{q}p}^{\mathbf{q}'p'} \quad (13)$$

With this formalism, in the case that we have three-phonon processes, the linearized Boltzmann equation is:

$$\begin{aligned} k_B T \mathbf{v}_p(\mathbf{q}) \cdot \nabla T \frac{\partial n_{\mathbf{q}p}^0}{\partial T} &= \sum_{\mathbf{q}'p'} \sum_{\mathbf{q}''p''} Q_{\mathbf{q}p, \mathbf{q}'p'}^{\mathbf{q}''p''} [\Psi_{\mathbf{q}''p''} - \Psi_{\mathbf{q}'p'} - \Psi_{\mathbf{q}p}] + \\ &+ \frac{1}{2} \sum_{\mathbf{q}'p'} \sum_{\mathbf{q}''p''} Q_{\mathbf{q}p}^{\mathbf{q}'p', \mathbf{q}''p''} [\Psi_{\mathbf{q}''p''} + \Psi_{\mathbf{q}'p'} - \Psi_{\mathbf{q}p}] \end{aligned} \quad (14)$$

In the linearized Boltzmann equation, we have the additions on phonons \mathbf{q}' and \mathbf{q}'' of the Brillouin Zone. However, sums can be converted into integrals:

$$\sum_{\mathbf{q}'} \rightarrow \frac{\Omega}{(2\pi)^3} \int d^3 \mathbf{q}' = \frac{\Omega}{(2\pi)^3} \left(\frac{2\pi\sqrt{2}}{h_1} \right) \int_0^{2\pi} d\theta' \int_0^{H(\theta')} \eta' d\eta' \int_{-M(\theta', \eta')}^{M(\theta', \eta')} d\zeta' \quad (15)$$

In (15), $\Omega = NV$ is the volume of the crystal, made of N lattice cells each with volume V . H and M are the functions describing the boundary of the Brillouin Zone, and h_1 is the nearest neighbor site distance [1].

Once obtained the deviation of the distribution function, the Boltzmann equation is solved and the thermal current \mathbf{U} can be calculated as:

$$\mathbf{U} = \frac{1}{\Omega} \sum_{\mathbf{q}p} \hbar \omega_{\mathbf{q}p} \mathbf{v}_{\mathbf{q}p} n_{\mathbf{q}p} = - \frac{1}{\Omega} \sum_{\mathbf{q}p} \hbar \omega_{\mathbf{q}p} \mathbf{v}_{\mathbf{q}p} \frac{\partial n_{\mathbf{q}p}^0}{\partial (\hbar \omega_{\mathbf{q}p})} \Psi_{\mathbf{q}p} \quad (16)$$

In a Cartesian frame of reference having unit vectors \mathbf{u}_i , current \mathbf{U} is represented by:

$$U_j = - \sum_i \kappa_{ji} \frac{\partial T}{\partial x_i} \quad (17)$$

In (17) κ_{ij} is a term of the thermal conductivity tensor, which is diagonal ($\kappa_{xx} = \kappa_{yy} = \kappa_{zz} = \kappa$).

Besides the phonon-phonon interaction, a phonon can be subjected to a scattering coming from the lattice defects and from electrons [1-6].

The Boltzmann Equation for electrons Let us use symbol Q when considering a phonon having wave-vector \mathbf{q} , polarization p and frequency $\omega_{\mathbf{q}p}$. And also use simply k for an electron having wave-vector \mathbf{k} , and energy ε_k and spin σ . Supposing a thermal gradient disturbing the distribution of electrons from equilibrium f_k^0 to a distribution f_k , let us assume, as we did for phonons:

$$f_k - f_k^0 = \Phi_k \frac{f_k^0 (1 - f_k^0)}{k_B T} \quad (18)$$

The equilibrium distribution f_k^0 is that of Fermi-Dirac, where each energy level is occupied by an electron. In it, we have the Fermi energy ε_F . This threshold is obtained by the distribution f_k^0 which becomes a step function of energy when the Kelvin temperature is null. For non-null temperature:

$$f_k^0 = \frac{1}{1 + e^{(\varepsilon - \varepsilon_F)/k_B T}} \quad (19)$$

Let us have free electrons described by \mathbf{k} . At null temperature, the energy levels would be occupied till the radius k_F so that:

$$\varepsilon_F = \frac{\hbar^2}{2m_e} k_F^2 \quad (20)$$

In (20), m_e is the mass of the electron. For a non-null temperature, some electrons have $|\mathbf{k}| > k_F$ and then they can be above the Fermi energy.

In (18), the deviation from equilibrium $f_k - f_k^0$, coming from the presence of a thermal gradient, is considered with the same approach we followed to solve the Boltzmann equation for phonons (see Eqs. (10')-(10'''').

Let $\Pi_{k\mathbf{q}}^{k'\mathbf{q}}$, $\Pi_k^{k'\mathbf{q}}$ be the intrinsic probability of an electron-phonon scattering of an electron \mathbf{k} interacting with a phonon \mathbf{q} as shown in the following scheme (Figure 1). After the scattering, the electron has momentum \mathbf{k}' , because it had gained a phonon or lost it [9].

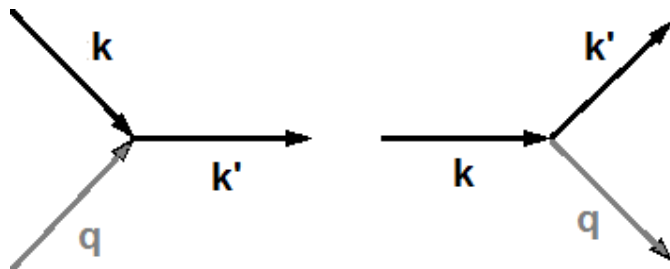


Figure 1: An electron changes its momentum after it has gained or lost a phonon.

Of course, as in the case of phonons, we can have processes involving the \mathbf{g} vectors of the reciprocal lattice. The electron-phonon scatterings are adding new contributions in the scattering term of the Boltzmann equation for phonons. For instance, if we consider the case when just three-phonon scattering processes are present, to them we have to add the scattering from electrons:

$$\left(\frac{\partial n_Q}{\partial t} \right)_{scatt} = \sum_{\mathbf{k}\sigma} \sum_{\mathbf{k}'\sigma'} P_{kQ}^{k'} \delta_{\sigma\sigma'} (\Phi_{k'} - \Psi_Q - \Phi_k) + \sum_{\mathbf{k}\sigma} \sum_{\mathbf{k}'\sigma'} P_k^{k'Q} \delta_{\sigma\sigma'} (\Phi_{k'} + \Psi_Q - \Phi_k) + \frac{1}{2} \sum_{Q'Q''} Q_Q^{Q'Q''} (\Psi_{Q''} - \Psi_Q + \Psi_{Q'}) + \sum_{Q'Q''} Q_{QQ'}^{Q''} (\Psi_{Q''} - \Psi_Q - \Psi_{Q''}) \quad (21')$$

Then, the linearized Boltzmann equation is:

$$k_B T \mathbf{v}_p(\mathbf{q}) \cdot \nabla T \frac{\partial n_{\mathbf{q}p}^0}{\partial T} = \sum_{\mathbf{k}\sigma} \sum_{\mathbf{k}'\sigma'} P_{kQ}^{k'} \delta_{\sigma\sigma'} (\Phi_{k'} - \Psi_Q - \Phi_k) + \sum_{\mathbf{k}\sigma} \sum_{\mathbf{k}'\sigma'} P_k^{k'Q} \delta_{\sigma\sigma'} (\Phi_{k'} + \Psi_Q - \Phi_k) + \frac{1}{2} \sum_{Q'Q''} Q_Q^{Q'Q''} (\Psi_{Q''} - \Psi_Q + \Psi_{Q'}) + \sum_{Q'Q''} Q_{QQ'}^{Q''} (\Psi_{Q''} - \Psi_Q - \Psi_{Q''}) \quad (21'')$$

Symbol σ is indicating electronic spin. Delta $\delta_{\sigma\sigma'}$ is considering the conservation of electronic spin. Probabilities are given by the following expressions:

$$P_{k\mathbf{q}}^{k'} = \Pi_{k\mathbf{q}}^{k'} f_k^0 n_{\mathbf{q}}^0 (1 - f_{k'}^0) \quad (22)$$

$$P_k^{k'\mathbf{q}} = \Pi_k^{k'\mathbf{q}} f_k^0 (1 + n_{\mathbf{q}}^0) (1 - f_{k'}^0) \quad (23)$$

In metals, electrons too are contributing to the thermal transport. In the Boltzmann equation for electrons, we find the scattering with phonons [9]:

$$\left(\frac{\partial f_k}{\partial t} \right)_{scatt} = - \sum_{Q\mathbf{k}'\sigma'} P_{\mathbf{k}Q}^{\mathbf{k}'} \delta_{\sigma\sigma'} (\Phi_k + \Psi_Q - \Phi_{k'}) - \sum_{Q\mathbf{k}'\sigma'} P_{\mathbf{k}}^{\mathbf{k}'Q} \delta_{\sigma\sigma'} (\Phi_k - \Psi_Q - \Phi_{k'}) \quad (24')$$

Then, the linearize Boltzmann equation for electrons is:

$$k_B T \mathbf{v}_k \cdot \nabla T \frac{\partial f_k^0}{\partial T} = - \sum_{Q\mathbf{k}'\sigma'} P_{\mathbf{k}Q}^{\mathbf{k}'} \delta_{\sigma\sigma'} (\Phi_k + \Psi_Q - \Phi_{k'}) - \sum_{Q\mathbf{k}'\sigma'} P_{\mathbf{k}}^{\mathbf{k}'Q} \delta_{\sigma\sigma'} (\Phi_k - \Psi_Q - \Phi_{k'}) \quad (24'')$$

From the theory of electron-phonon scattering [9], the probability $P_{\mathbf{k}Q}^{\mathbf{k}'}$ turns out to be:

$$P_{\mathbf{k}Q}^{\mathbf{k}'} = \Re(\mathbf{k}' - \mathbf{k}) \frac{[\mathbf{e}_{\mathbf{q}p} \cdot (\mathbf{k}' - \mathbf{k})]^2}{\omega_{\mathbf{q}p}} f_k^0 n_{\mathbf{q}}^0 (1 - f_{k'}^0) \delta(\varepsilon_{\mathbf{k}} + \hbar\omega_{\mathbf{q}p} - \varepsilon_{\mathbf{k}'}) \quad (25)$$

$$P_{\mathbf{k}}^{\mathbf{k}'Q} = \Re(\mathbf{k}' - \mathbf{k}) \frac{[\mathbf{e}_{\mathbf{q}p} \cdot (\mathbf{k}' - \mathbf{k})]^2}{\omega_{\mathbf{q}p}} f_k^0 (1 + n_{\mathbf{q}}^0) (1 - f_{k'}^0) \delta(\varepsilon_{\mathbf{k}} - \hbar\omega_{\mathbf{q}} - \varepsilon_{\mathbf{k}'}) \quad (26)$$

In (25) and (26) we find the polarization vectors \mathbf{e} of phonons. The interaction between electron and lattice is described by the function $\Re(\mathbf{k})$. It can be described by means of a pseudopotential for instance.

Let us note that we have to consider the conservation of energy and of the generalized conservation of momentum given by the following expression:

$$\mathbf{k} + \mathbf{q} = \mathbf{k}' + \mathbf{g} ; \mathbf{k} - \mathbf{q} = \mathbf{k}' + \mathbf{g}$$

The coupled Boltzmann linearized equations for phonons and electrons can be solved in an iterative approach for instance. Another question we have to discuss before solving the equation is the description of interaction. This will be shortly analysed in the next section.

Scattering electron-phonon Let us consider the following scheme (Figure 2):

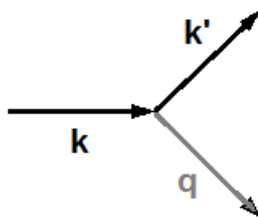


Figure 2: A scattering electron-phonon

In this process we have a phonon having momentum \mathbf{q} and polarization p added to the population n_Q so that population becomes $n_Q + 1$. Then, the initial quantum state is given by $|i\rangle = \psi_k |n_Q\rangle$ and the final quantum state is $|j\rangle = \psi_{k'} |n_Q + 1\rangle$. If we use a pseudopotential approach [24], the electron can be described by plane waves [25-27], so that:

$$\psi_k = \frac{1}{\sqrt{\Omega}} e^{i\mathbf{k}\cdot\mathbf{r}} ; \psi_{k'} = \frac{1}{\sqrt{\Omega}} e^{i\mathbf{k}'\cdot\mathbf{r}} \quad (27)$$

Let us remember that a pseudopotential is an effective potential used as an approximation for the simplified description of complex systems. It is an attempt to consider the effects of the motion of the core, that is of the non-valence electrons of an atom and of the nucleus with an effective potential, so that the Schrödinger equation contains such effective potential instead of the Coulomb terms for the core electrons. In this manner the valence electrons are described by pseudo-wave functions, in which a plane-wave basis is used.

We can write the scattering as the passage from the initial state $|i\rangle$ to the final state $|f\rangle$ through pseudopotential W [25,26]:

$$\begin{aligned} \langle f | W | i \rangle &= \int \Psi_{k'}^*(\mathbf{r}) \langle n_Q + 1 | W(\mathbf{r}) | n_Q \rangle \Psi_k(\mathbf{r}) d^3x = \langle n_Q + 1 | \int \Psi_{k'}^*(\mathbf{r}) W(\mathbf{r}) \Psi_k(\mathbf{r}) d^3x | n_Q \rangle \\ &= \langle n_Q + 1 | \frac{1}{\Omega} \int e^{-i(\mathbf{k}' - \mathbf{k}) \cdot \mathbf{r}} W(\mathbf{r}) d^3x | n_Q \rangle = \langle n_Q + 1 | W_{\mathbf{k}' - \mathbf{k}} | n_Q \rangle \end{aligned} \quad (28)$$

Moreover, we can write [25-27]:

$$W_{\mathbf{k}' - \mathbf{k}} = \frac{N S(\mathbf{k}' - \mathbf{k}) w(\mathbf{k}' - \mathbf{k})}{\epsilon(\mathbf{k}' - \mathbf{k})} \quad (29)$$

In (29), w is the pseudopotential generated by a single ion which is acting on the electron. N is the number of lattice sites. We find also in (29) the static dielectric constant ϵ , which can be written as the following function [25-27] (e is the electron charge):

$$\varepsilon_Q = 1 + \frac{4\pi e^2}{Q^2} \frac{m_e k_F}{2\pi^2 \hbar^2} \left[\frac{1 - (Q/2k_F)^2}{(Q/2k_F)} \ln \left| \frac{1 + (Q/2k_F)}{1 - (Q/2k_F)} \right| + 1 \right] \quad (30)$$

Moreover (l is giving the lattice site described by the position vector \mathbf{l}):

$$\begin{aligned} NS(\mathbf{k}' - \mathbf{k}) &= \sum_l e^{-i(\mathbf{k}' - \mathbf{k}) \cdot (\mathbf{l} + \mathbf{u}_l)} \\ &= \sum_l e^{-i(\mathbf{k}' - \mathbf{k}) \cdot \mathbf{l}} e^{-i(\mathbf{k}' - \mathbf{k}) \cdot \mathbf{u}_l} = \sum_l e^{-i(\mathbf{k}' - \mathbf{k}) \cdot \mathbf{l}} [1 - i(\mathbf{k}' - \mathbf{k}) \cdot \mathbf{u}_l + \dots] \end{aligned}$$

As usual, the phononic function of the displacement of the lattice site given by the position vector \mathbf{l} is [9,10]:

$$\mathbf{u}_l = i \sqrt{\frac{\hbar}{2mN}} \sum_{\mathbf{q}p} \frac{1}{\sqrt{\omega_{\mathbf{q}p}}} \left[\mathbf{e}_{\mathbf{q}p}^* e^{-i\mathbf{q} \cdot \mathbf{l}} a_{\mathbf{q}p} - \mathbf{e}_{\mathbf{q}p} e^{i\mathbf{q} \cdot \mathbf{l}} a_{\mathbf{q}p}^+ \right] \quad (31)$$

In (31), m – is the mass of ions. In this manner we can write the matrix:

$$\langle f | W | i \rangle = \frac{w(\mathbf{k}' - \mathbf{k})}{\varepsilon(\mathbf{k}' - \mathbf{k})} \left\langle n_Q + 1 \left| \sum_l e^{-i(\mathbf{k}' - \mathbf{k}) \cdot \mathbf{l}} [1 - i(\mathbf{k}' - \mathbf{k}) \cdot \mathbf{u}_l] \right| n_Q \right\rangle \quad (32)$$

Then, we can obtain:

$$\begin{aligned} \langle f | W | i \rangle &= \frac{w(\mathbf{k}' - \mathbf{k})}{\varepsilon(\mathbf{k}' - \mathbf{k})} \left\{ \left\langle n_Q + 1 \left| \sum_l e^{-i(\mathbf{k}' - \mathbf{k}) \cdot \mathbf{l}} \right| n_Q \right\rangle \right. \\ &\quad \left. + \left\langle n_Q + 1 \left| (\mathbf{k}' - \mathbf{k}) \sqrt{\frac{\hbar}{2mN}} \sum_l e^{-i(\mathbf{k}' - \mathbf{k}) \cdot \mathbf{l}} \sum_{\mathbf{q}p} \frac{1}{\sqrt{\omega_{\mathbf{q}p}}} \left[\mathbf{e}_{\mathbf{q}p}^* e^{-i\mathbf{q} \cdot \mathbf{l}} a_{\mathbf{q}p} - \mathbf{e}_{\mathbf{q}p} e^{i\mathbf{q} \cdot \mathbf{l}} a_{\mathbf{q}p}^+ \right] n_Q \right\rangle \right\} \end{aligned} \quad (33)$$

Of the matrix, just the element having a_Q^+ , which is creating phonon \mathbf{q}, p survives, and then:

$$\langle f | W | i \rangle = -\frac{w(\mathbf{k}' - \mathbf{k})}{\varepsilon(\mathbf{k}' - \mathbf{k})} \sqrt{\frac{\hbar}{2mN}} \frac{\mathbf{e}_{\mathbf{q}p} \cdot (\mathbf{k}' - \mathbf{k})}{\sqrt{\omega_{\mathbf{q}p}}} \sum_l e^{-i(\mathbf{k}' - \mathbf{k}) \cdot \mathbf{l}} e^{i\mathbf{q} \cdot \mathbf{l}} \langle n_Q + 1 | a_{\mathbf{q}p}^+ | n_Q \rangle \quad (34)$$

Since $\sum_l e^{-i(\mathbf{k}' - \mathbf{k} + \mathbf{q}) \cdot \mathbf{l}} = N \delta_{\mathbf{k}' - \mathbf{k} + \mathbf{q}, \mathbf{g}}$ and $\langle n_Q + 1 | a_{\mathbf{q}p}^+ | n_Q \rangle = \sqrt{n_Q + 1}$, we have:

$$\langle f | W | i \rangle = -\frac{w(\mathbf{k}' - \mathbf{k})}{\varepsilon(\mathbf{k}' - \mathbf{k})} N \sqrt{\frac{\hbar}{2mN}} \frac{\mathbf{e}_{qp} \cdot (\mathbf{k}' - \mathbf{k})}{\sqrt{\omega_{qp}}} \sqrt{n_Q + 1} \quad (35)$$

Of course, we have the generalized conservation of momentum $\mathbf{k}' - \mathbf{k} + \mathbf{q} = \mathbf{g}$. Therefore, the probability for the unit of time is:

$$\begin{aligned} & \frac{2\pi}{\hbar} |\langle f | W | i \rangle|^2 \delta(E_f - E_i) \\ &= \frac{2\pi}{\hbar} \left[\frac{w(\mathbf{k}' - \mathbf{k})}{\varepsilon(\mathbf{k}' - \mathbf{k})} \right]^2 \frac{\hbar N}{2m} \frac{[\mathbf{e}_{qp} \cdot (\mathbf{k}' - \mathbf{k})]^2}{\omega_{qp}} (n_Q + 1) \delta(\varepsilon_{k'} + \hbar\omega_{qp} - \varepsilon_k) \end{aligned} \quad (36)$$

The conservation of energy is represented by $\delta(E_f - E_i)$. Eq.36 is the intrinsic probability that an electron can move from \mathbf{k} to \mathbf{k}' . This probability is conditioned by the fact that \mathbf{k} state is occupied and \mathbf{k}' is empty, due to the Pauli exclusion principle. The true probability is then (36) multiplied by $f_k(1 - f_{k'})$. Therefore we have:

$$P_k^{k'Q} = \frac{2\pi}{\hbar} \left[\frac{w(\mathbf{k}' - \mathbf{k})}{\varepsilon(\mathbf{k}' - \mathbf{k})} \right]^2 \frac{\hbar N}{2m} \frac{[\mathbf{e}_{qp} \cdot (\mathbf{k}' - \mathbf{k})]^2}{\omega_{qp}} f_k (1 - f_{k'}) (n_Q + 1) \delta(\varepsilon_{k'} + \hbar\omega_Q - \varepsilon_k) \quad (37)$$

This is in agreement to (25) if we have:

$$\mathfrak{R}(\mathbf{k}' - \mathbf{k}) = \frac{\pi N}{m} \left[\frac{w(\mathbf{k}' - \mathbf{k})}{\varepsilon(\mathbf{k}' - \mathbf{k})} \right]^2 \quad (38)$$

In the Boltzmann equation we have also to consider the other scattering mechanism shown in the Figure 3. In this case we have to consider $\langle n_Q - 1 | a_Q | n_Q \rangle$ and generalized conservation $\mathbf{k} + \mathbf{q} = \mathbf{k}' + \mathbf{g}$. In this manner, it is straightforward to obtain $P_{kQ}^{k'}$.

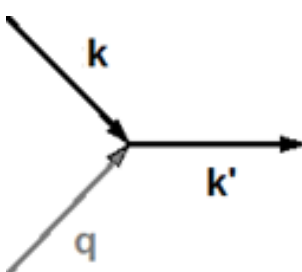


Figure 3: The other scattering electron-phonon process.

Thermal conductivity As given in [28], the thermal current of electrons is the following:

$$\mathbf{U} = \frac{2}{\Omega} \sum_k f_k \mathbf{v}_k (\varepsilon_k - \varepsilon_F) \quad (39)$$

In (39), we find the velocity and energy of electrons. We have also the chemical potential, that we will consider as ε_F . We can follow the same approach used for the phonons so that:

$$\mathbf{U} = \frac{2}{\Omega} \sum_k \mathbf{v}_k (\varepsilon_k - \varepsilon_F) \frac{\partial f_k^0}{\partial \varepsilon_k} \Phi_k \quad (40)$$

In the approach we have shown here, the equilibrium distribution of electrons f^0 is a spherical symmetric function. Then, for the evaluation of the thermal electronic conductivity we can use spherical coordinates k, α, θ . The electronic thermal conductivity is given by [9,28]:

$$\kappa = -\lambda \int_0^\infty \bar{k}^2 d\bar{k} \int_0^\pi \sin(\alpha) d\alpha \int_0^{2\pi} d\theta (\bar{k}^2 - 1) \bar{k} \cos(\alpha) f_k^0 (1 - f_k^0) \phi(\bar{k}, \alpha, \theta) \quad (41)$$

In (41), a reduced momentum \bar{k} and the dimensionless deviation function ϕ had been used so that the dimensional factor turns out to be [29]:

$$\lambda = \frac{k_F^9 \hbar^8 V}{64\pi^2 m_e^5 k_B T^2 e^4 h_l^2} \sqrt{\frac{3mU_o}{2}} \quad (42)$$

In (42), parameter U_o is linked to the potential used for calculating the lattice thermal conductivity [1, 2].

In a future paper we will explain how to solve iteratively the coupled equations (21'') and (24''). Once the deviation functions of phononic and electronic distributions have been obtained the thermal phononic and the electronic thermal conductivities can be calculated from (16) and (41).

References

- [1] Omini, M., & Sparavigna, A. (1996). Beyond the isotropic-model approximation in the theory of thermal conductivity. *Physical Review B*, 53(14), 9064-9073. DOI: 10.1103/physrevb.53.9064
- [2] Omini, M., & Sparavigna, A. (1997). Heat transport in dielectric solids with diamond structure. *Nuovo Cimento D Serie*, 19, 1537.
- [3] Omini, M., & Sparavigna, A. (1995). An iterative approach to the phonon Boltzmann equation in the theory of thermal conductivity. *Physica B: Condensed Matter*, 212(2), 101-112. DOI: 10.1016/0921-4526(95)00016-3

[4] Omini, M., & Sparavigna, A. (1997). Effect of phonon scattering by isotope impurities on the thermal conductivity of dielectric solids. *Physica B: Condensed Matter*, 233(2), 230-240. DOI: 10.1016/s0921-4526(97)00296-2

[5] Sparavigna, A. C. (2016). The Boltzmann equation of phonon thermal transport solved in the relaxation time approximation – I – Theory. *Mechanics, Materials Science & Engineering Journal*, (3), 1-13. DOI: 10.13140/RG.2.1.1001.1923

[6] Sparavigna, A. C. (2016). The Boltzmann equation of phonon thermal transport solved in the relaxation time approximation – II – Data analysis. *Mechanics, Materials Science & Engineering Journal*, 2016(3), 1-10. DOI: 10.13140/RG.2.1.2026.4724

[7] Srivastava, G. P. (1990). *The physics of phonons*. CRC Press.

[8] Kittel, C., & Fong, C. Y. (1963). *Quantum theory of solids* (Vol. 33). New York: Wiley.

[9] Ziman, J. M. (1960). *Electrons and phonons: the theory of transport phenomena in solids*. Oxford University Press.

[10] Srivastava, S. K., & March, N. H. (Eds.). (1995). *Condensed Matter - Disordered Solids*. World Scientific.

[11] Peierls, R. (1935). Quelques propriétés typiques des corps solides. In *Annales de l'institut Henri Poincaré*, 5(3), 177-222.

[12] Klemens, P. G. (1951). The thermal conductivity of dielectric solids at low temperatures (theoretical). In *Proceedings of the Royal Society of London A: Mathematical, Physical and Engineering Sciences*, 208(1092), 108-133. DOI: 10.1098/rspa.1951.0147

[13] Klemens, P. G. (1958). Thermal conductivity and lattice vibrational modes. *Solid State Physics*, 7, 1-98. DOI: 10.1016/s0081-1947(08)60551-2

[14] Callaway, J. (1959). Model for lattice thermal conductivity at low temperatures. *Physical Review*, 113(4), 1046-1051. DOI: 10.1103/physrev.113.1046

[15] Krumhansl, J. A. (1965). Thermal conductivity of insulating crystals in the presence of normal processes. *Proceedings of the Physical Society*, 85(5), 921-9130. DOI: 10.1088/0370-1328/85/5/310

[16] Srivastava, G. P. (1976). Calculation of lattice thermal conductivity of Ge from 4 to 900 K. *Philosophical Magazine*, 34(5), 795-809. DOI: 10.1080/14786437608222052

[17] Srivastava, G. P. (1980). Phonon conductivity of insulators and semiconductors. *Journal of Physics and Chemistry of Solids*, 41(4), 357-368. DOI: 10.1016/0038-1098(80)90461-5

[18] Parrott, J. E. (1971). Generalization of the Callaway thermal conductivity equation. *Physica Status Solidi (b)*, 48(2), K159-K161. DOI: 10.1002/pssb.2220480266

[19] Guyer, R. A., & Krumhansl, J. A. (1966). Solution of the linearized phonon Boltzmann equation. *Physical Review*, 148(2), 766-778. DOI: 10.1103/physrev.148.766

[20] Srivastava, G. P. (1980). Phonon conductivity of insulators and semiconductors. *Journal of Physics and Chemistry of Solids*, 41(4), 357-368. DOI: 10.1016/0038-1098(80)90461-5

[21] Omini, M., & Sparavigna, A. (1993). Thermal conductivity of rare gas crystals the role of three-phonon processes. *Philosophical Magazine B*, 68(5), 767-785. DOI: 10.1080/13642819308220158

[22] Jancel, R. (2013). *Foundations of classical and quantum statistical mechanics: International Series of Monographs in Natural Philosophy* (Vol. 19). Elsevier.

[23] Gurevich, V. L. V. (1986). *Transport in phonon systems*. Amsterdam, North-Holland.

[24] Mizutani, U. (2001). *Introduction to the Electron Theory of Metals*, Cambridge University Press.

[25] Barbero, D., & Omini, M. (1984). Vacancy formation volume of sodium, aluminium and argon. *Il Nuovo Cimento D*, 3(3), 533-560. DOI: 10.1007/bf02457768

[26] Omini, M. (1994). Phonon-phonon interaction and phonon drag in potassium at low temperatures. *Philosophical Magazine B: Physics of Condensed Matter*, 69(6), 1197-1215. DOI: 10.1080/01418639408240189

[27] Sparavigna, A. C. *Appunti di un seminario del Professor Omini sullo pseudopotenziale* (unpublished).

[28] Ziman, J. M. (1975). *I principi della teoria dei solidi*. Tamburini Editore.

[29] Ponasso, L. & Sparavigna, A. (2001). Determinazione del trasporto termico nei metalli con approccio iterativo all'equazione di Boltzmann. In: *LXXXVII Congresso Nazionale Società Italiana di fisica*, Milano, Milano, 24-29 Settembre 2001. Page 71.

Dynamical Analyses of Piston Machines Used in Oil Industry

V.I. Bakhshaliy^{1, a}

1 – Professor, Dr., Azerbaijan Technical University, Baku, Azerbaijan

a – v.bakhshali@aztu.edu.az



DOI 10.13140/RG.2.1.1837.4644

Keywords: dynamics, mechanical oscillations, stresses, durability, piston machine.

ABSTRACT. The investigation of a complex problems with taking into account of a friction, oscillation and impact processes in mechanisms of piston machines, does possible the all-round decision of the problem of increase of their reliability and durability. In this work, based on the dynamic analysis of the crank-piston mechanisms the method for definition of the parameters of longitudinal vibration of a connecting rod of piston machines is developed. The dangerous sections of a "floating" connecting rod are determined.

Introduction. The problem of increasing durability and reliability of units of machine parts on longevity criterion at the simultaneous reduce of their metal capacity is urgent. For the parts of Piston Machine traditionally applied in engineering practice calculations of durability and reliability are insufficient and illegal.

Movement of systems under the influence of external forces is the basis of mechanical oscillations in the machines. Mechanical oscillations can cause significant harm, as they form the direct threat to the durability of extremely responsible constructions to which the piston machines refer. Mechanical oscillations can disturb normal conditions of the exploitation of machines. The main part of the damages in the machines and their details take place because of appearance of oscillations in them. Oscillations are raised periodically or by sudden applied forces. Under the influence of periodically variable forces and moments parts or units of piston machines make elastic oscillations, which become especially strong in the zone of resonances where frequencies of disturbed forces or moments coincide with the frequencies of the system oscillations. The forces influencing on details of crank piston mechanisms (CPM) of piston machines are variables (on direction and on value). That's why probability of appearance of resonance regimes of piston machines increases with the raise of quickness of machines.

As a result of improvement of work indices of PM the character of oscillations is complicated and their loading on the parts is increased.

Calculations of oscillations of CPM parts have great significance in projecting and exploitation of PM. Reduction of oscillations in the parts and units provides high quality of work of PM.

Oscillation processes mainly take place in the crankshafts, piston rods and connecting rods of KP piston machines. Besides it oscillations of the fundament and vibration of gas flow along the pipeline can also cause considerable harm to the work of machines.

For calculation PM parts on strength and durability first we consider the problem of longitudinal and cross oscillation movements of elements of above mentioned details of PM.

Oscillation control becomes inalienable condition for providing of high quality piston machines. It is carried out for designing and exploitation of PM [1, 2, 3, 4]. In practice reduction of oscillations in the parts and units of machines takes place as a result of as natural and artificial damping. The first is achieved as a result of internal friction in material and units of construction and external

friction as a result of interaction of oscillating parts and units with external medium; the second at the expense of use of antivibrations, dampers. The task consists of theoretical and experimental determination of frequencies and forms of their oscillations, in creation of possibility of amplitude reduce in the resonances, in the choice of effective control measures with them in working range of frequency of machine rotation, and also in the analyses of possible estimation methods of level of oscillations danger [5, 6, 7].

Analyses of the mechanical motion of the connecting rod of PM. Connecting rod is one of heavy-loaded elements of PM. In horizontal machines the length of the connecting rod is $L = (4.5 \div 5)r$, where r - is the radius of the crankshaft. Reducing L the length or height of PM decreases, but pressure on crosshead shoe or side surface of the piston increases. In selecting of construction and material of connecting rod, necessity of reduce of its mass in connection with necessary strength and rigidity should be considered. Connecting rods having forked crosshead are often used in vertical machines. Forked connecting rod is more complicated when it is produced, but in combination with corresponding crosshead of open-type it allows to draw near rod to the crosshead pin and reduce the height of PM. Usually in practice for achieving liquidous friction diametric clearance in the shell of crankshaft of the connecting rod is formed in the range $(0,0007 - 0,12)d$ and in bushing of crosshead $(0,0010 - 0,0018)d$, where d - is internal diameter corresponding the shell and bushing. However, investigations show that providing of liquidous friction in the shown kinematic pairs is practically impossible [8, 9, 10, 11].

When calculating the strength and durability oscillation movements of the connecting rod of PM are considered. As it is known there are clearances filled with lubricating oil between crosshead pin, crank pin and corresponding shells of connecting rod. Besides it movement of the connecting rod is determined by the totality of many factors. Due to the movement of the connecting rod as regards to cross head pin and crank pin becomes uncontrolled. This connecting rod conditionally is called "floating" [8].

Let's consider oscillating movement of "floating" connecting rod. Movement of this connecting rod is determined by the forces influencing on all mechanism links considering clearances. Such movement of the connecting rod is kinematically uncontrolled. One of the main tasks of the calculation of the connecting rod of piston machines used in transport, oil, heat energetic industry is providing of its durability in the exploitation condition. Thus, the investigation of the problems of oscillation of connecting rod is very important for its calculation of durability [12, 13, 14, 15, 16].

Analysis of cross oscillations of "floating" connecting rod. In Fig. 1 the scheme of crank-crosshead mechanism consisting of crank OA , connecting rod BC , crosshead O' , piston E and its rod $O'E$, where clearances ($AB = e_1$, $O'C = e_2$) are shown in the increased scale. All forces applied on connecting rod are also shown in this figure.

The task about cross oscillation of "floating" connecting rod will be solved in the following assumption. Let's suppose that mass in the connecting rod and stiffness of its rod are equally distributed between the heads and crank rotates equally with angular velocity $\omega = \varphi/t$ (φ - is the turning angle of crankshaft).

As it is known the following forces influence on movement of the connecting rod: 1) normal and tangent component forces influencing crank pin on connecting rod shell N_A , F_A ; 2) normal and tangent component forces crosshead pin influencing on connecting rod shell N_O , F_O^{fr} ; 3) gravity force of the connecting rod P ; 4) component of unit inertia forces of connecting rod elements q_x^{in} , q_y^{in} (coordinate axis x and y are shown in the figure).

Accept the coordinate system $B\xi\eta$, where axis $B\xi$ is directed perpendicularly to the connecting rod and the axis $B\eta$ - along the connected rod.

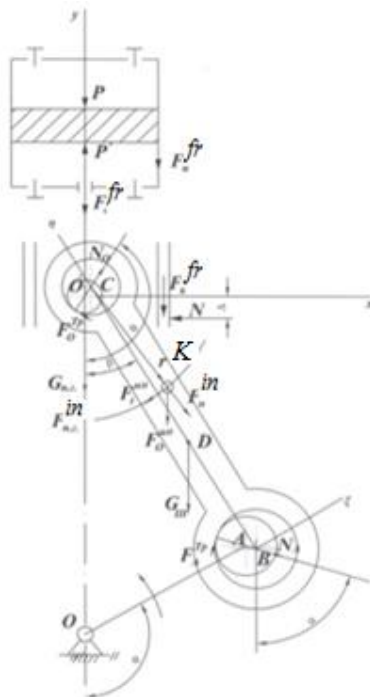


Fig.1. Crank-piston mechanism with acting forces on it.

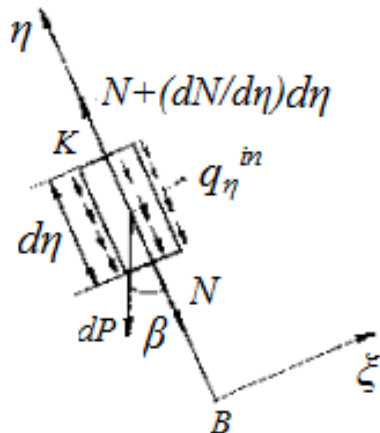


Fig. 2. Element of connecting rod.

Let's isolate element of connecting rod K with length $d\eta$ with abscissa η and consider its cross movement relatively to cross head pin (Fig.2). Forces influence on this element: N and $N + (dN/d\eta)d\eta$ – forces influencing correspondingly of lower and upper parts of connecting rod on element K ; $dP = m_0gd\eta$ is the gravity force of element (m_0 - is the unit mass of the length of connecting rod, g – gravity acceleration of free fall); q_η^{in} intensity of the inertia force of the element in cross direction of connecting rod.

The force N on the basis of Hook's law is:

$$N = EF \frac{\partial u}{\partial \eta} \quad (1)$$

where u is the cross displacement of the considered element K of connecting rod during the oscillations of its balanced condition relatively to the centre of shell B , $u = u(\eta, t)$;

F – is the square of its cross, which are accepted as constant quantities.

Equation of motion of system is (Fig. 2):

$$m_0 d\eta \frac{\partial^2 u}{\partial t^2} = -N + N + \frac{\partial N}{\partial \eta} d\eta - q_\eta^{in} - m_0 g d\eta \cos \beta$$

Or

$$\frac{\partial^2 u}{\partial t^2} = \frac{1}{m_0} \frac{\partial N}{\partial \eta} - \frac{1}{m_0} q_\eta^{in} - g \cos \beta, \quad (2)$$

where β is the turn angle of connecting rod around the center of shell B ;

m_0 is the unit mass of the length of connecting rod, $m_0 = \rho F$,

ρ is the density of connecting rod material.

Considering dependence (1) the following comes out of equation (2):

$$c^2 \frac{\partial^2 u}{\partial \eta^2} - \frac{\partial^2 u}{\partial t^2} = \frac{1}{\rho F} q_\eta^{uh} + g \cos \beta \quad (3)$$

where $c = \sqrt{E/\rho}$ is a velocity of sound spreading in the connecting rod material;

E – is a modulus of elasticity.

Substituting values of parameters in the right member of equation (3) and having spread out this function into a Fourier series, we will receive the differential equation of a longitudinal motion of a rod in relation to a neck of a crank shaft and a finger of piston.

$$c^2 \frac{\partial^2 u}{\partial \eta^2} - \frac{\partial^2 u}{\partial t^2} = \alpha_0 + \sum (a_i \cos i\omega t + b_i \sin i\omega t) \quad (4)$$

Number quantities of coefficients a_0, a_i, b_i are located in concrete values of the given function

$$\left(\frac{1}{\rho F} q_\eta^{uh} + g \cos \beta \right).$$

For solving the differential equation (4) let's join it boundary conditions:

when $\eta=0$, $EF \frac{\partial u}{\partial \eta} = N_{A\eta} = -N_A \cos(\alpha - \beta) + F_A^{in} \sin(\alpha - \beta)$

when $\eta=L$,

$$EF \frac{\partial u}{\partial \eta} = N_{O\eta} = -N_O \cos(\theta - \beta) + F_O^{in} \sin(\theta - \beta), \quad (5)$$

where $N_{A\eta}$ and $N_{O\eta}$ – are accordingly longitudinal forces of action of a neck of a crank and a finger of piston on a connecting rod in the beginning (point A) and the end (point O) of this rod; L – length of a rod;

α and θ – corners, between normal forces \bar{N}_A and \bar{N}_O with a vertical axis (-y) which are defined from the dynamic equation of equilibrium of CPM.

Having spread out the functions $N_{A\eta}$ and $N_{O\eta}$ into a Fourier series, we obtain:

$$\begin{aligned} N_{A\eta} &= A_O^{cr} + \sum (A_i^{cr} \cos i\omega t + B_i^{cr} \sin i\omega t) \\ N_{O\eta} &= A_O^P + \sum (A_i^P \cos i\omega t + B_i^P \sin i\omega t) \end{aligned} \quad (6)$$

Numerical values of factors A_o^{cr} , A_i^{cr} , B_i^{cr} , A_o^P , B_i^P are determined on concrete values of forces $N_{A\eta}$ and $N_{O\eta}$.

The solution of the differential equation (4) with taking into account the boundary conditions (5) and expressions (6) is found in a following form:

$$\begin{aligned} u(\eta, t) &= \sum \left[\left(\frac{A_i^{cr} \cos kL - A_i^P}{kEF \sin kL} \cos k\eta + \frac{A_i^{cr}}{kEF} \sin k\eta + \frac{a_i}{k^2 c^2} \right) \cos i\omega t + \right. \\ &\quad \left. + \left(\frac{B_i^{cr} \cos kL - B_i^P}{kEF \sin kL} \cos k\eta + \frac{B_i^{cr}}{kEF} \sin k\eta + \frac{b_i}{k^2 c^2} \right) \sin i\omega t \right] \end{aligned} \quad (7)$$

where $k = \frac{i\omega}{c}$.

The expression (7) describes relative cross oscillatory movement of “floating” connecting rod. It should be mentioned that for practical use in (6) it is enough to keep some numbers of series, that's to say $i = 1, 2$.

Differentiating (7) after some reduction we get the amplitude of the normal stress of relative cross deformation of connecting rod ($i=1$):

$$\sigma_a = E \frac{\partial u}{\partial \eta} = \sqrt{\left(\frac{A_i^{cr} \cos kL + A_i^P}{EF \sin kL} \sin k\eta + \frac{A_i^{cr}}{EF} \cos k\eta \right)^2 + \left(\frac{B_i^{cr} \sin kL + B_i^P}{EF \sin kL} \sin k\eta + \frac{B_i^{cr}}{EF} \cos k\eta \right)^2}$$

The results of calculations of normal stresses in different sections of connecting rod by this expression for piston compressor 505VP20/18 are given in the Table 1.

Table 1. The results of calculations of normal stresses in different sections.

η	L/8	L/4	3L/8	L/2	5L/8	3L/4
σ , N/m ²	$2,41 \cdot 10^7$	$2,32 \cdot 10^7$	$2,02 \cdot 10^7$	$1,99 \cdot 10^7$	$1,84 \cdot 10^7$	$1,62 \cdot 10^7$

Thus the methods of account to the durability of connecting rod of piston machines has been worked out.

Summary. Researches show that dangerous sections of a connecting rod in which there are the greatest normal pressure, those sections which are more close to a neck of the neck of crank shaft.

References

- [1] Rangwala A.S. Reciprocating Machinery Dynamics, New Age International Publishers, Delhi, 2006
- [2] Davitashvili N., Bakhshaliyev V. Dynamics of Crank - Piston Mechanisms. Springer Publisher, 242 p., 2016
- [3] Lioung R.T., Proppe C. Application of a Cohesive Zone Model for the Investigation of the Dynamic Behavior of a Rotating Shaft with a Transverse Crack. Proc. 8th IFTOMM International Conference on Rotor dynamics 12.-15.09, Seoul, Korea, 2010
- [4] Yanovsky Yu.G., Zgaevskii V.E. Mechanical properties of high elastic polymer matrix composites filled with rigid particles: Nanoscale consideration of the interfacial problem. Composite Interfaces, v.11, N3, pp. 245-261, 2004
- [5] Vakhrouchev A.V. Computer simulation of nanoparticles formation, moving, interaction and self-organization. Journal of Physics: Conference Series. V. 61. pp. 26-30, 2007
- [6] Galin L.A. Contact problems of the theory of elasticity and viscoelasticity. Moscow, "Science" publishing house, 304 pp. 2004 (in Russian)
- [7] Bakhshaliyev V.I. The Problem of Mathematical Simulation of Rolling Friction, Journal of Friction and Wear, 2009, Vol. 30, No. 5, © Allerton Press, Springer, Inc., pp. 305–308, 2009
- [8] Bakhshaliyev V.I. Mechanics of Piston Machines. - Lambert Academic Publishing, Germany, 312 p., 2011
- [9] Plastinin P.I. Piston compressors. Colos publisher, Moscow, 711p., 2008 (in Russian)
- [10] Goryacheva I.G., Dobychin M.N., Soldatenkov I.A., Bogdanov V.M., Zakharov S.M. Simulation of Wheel/Rail Contact and Wear in Curved Track, Proceeding of International Heavy Haul Association Conference "Wheel-Rail Interface", Vol.1, pp. 215-220, 1999

- [11] Popov V.L. Contact Mechanics and Friction. Physical principles and applications. Springer-Verlag, Berlin, Heidelberg, 2010
- [12] Bakhshaliyev V.I. Analysis of the accuracy of the crank-slider mechanism of piston machines with clearances. J. Machinery manufacture and reliability, No.3, pp. 1-4, Allerton Press, 2004
- [13] Galakhov M.A, Usov P.P. Differential and integral equations of the mathematical theory of a friction - Moscow, “Nauka” publishing house, 152 p., 2006 (in Russian)
- [14] Davitashvili N. Mgebrishvili N. etc. Dynamic investigation of hinged mechanisms by taking into account wear and clearances in kinematics pears. Inter. S. J. “Problems of Applied Mechanics”. Tbilisi, N 4(25), pp. 47-57, 2006
- [15] Hetzler H. On the influence of contact mechanics on friction induced flutter instability. In Proc. in Applied Mathematics and Mechanics (PAMM), Volume 9, Number 1, p. 275-276, 2009
- [16] Boyaci A., Seemann W., Proppe C. Nonlinear stability analysis of rotor-bearing systems. In Proc. in Applied Mathematics and Mechanics (PAMM), Volume 9, Number 1, p. 279-280, 2009

V I I . E n v i r o n m e n t a l S a f e t y
M M S E J o u r n a l V o l . 5



Study of Ground Treatment on Improvement of Pile Foundation Response in Liquefiable Soils

Chen Yulong ^{1, a}

1 – Department of Civil Engineering, The University of Tokyo, Tokyo 113-8656, Japan

a – 673054399@qq.com



DOI [10.13140/RG.2.1.2504.0140](https://doi.org/10.13140/RG.2.1.2504.0140)

Keywords: liquefaction, pile, ground treatment, retrofitting countermeasures.

ABSTRACT. In light of the disastrous the 2011 Tohoku Pacific Earthquake, the government of Japan has conducted studies to revise the seismic design code, and elevated peak ground accelerations have been adopted. Consequently, revisions on existing design to comply with the updated code are required for public projects that are still undergoing. The design safety needs to be reassessed, and implementation of strengthening measures is required if deemed necessary. For liquefaction countermeasures, ground treatment techniques that could increase the density of soils are often the preferable alternatives. The treatment usually increases the in-situ SPT-N or CPT-q_c values, which in turn would increase the resistance of soil against liquefaction. For many public infrastructures in Japan supported by bored piles embedded partly or entirely in sandy soils, reevaluation of design safety against soil liquefaction would be required. In an assessment of possible retrofitting countermeasures for an infrastructure foundation, ground treatment has been considered. In this case study, effect of ground treatment on response of piles in liquefiable soils was investigated with numerical analyses using FLAC. Results provide insights into this ground treatment effect and useful information for consideration in future design or decision making.

Introduction. The 2011 Great East Japan Earthquake, with a magnitude of $M_w=9.0$, occurred in the Pacific Ocean about 130 km off the northeast coast of Japan's main island on March 11, 2011. The hypocentral region of this quake was about 500 km in length and 200 km in width. The quake was followed by a huge tsunami that destroyed many cities and killed and injured many people along the Pacific Coast. The numbers of dead and missing persons as of July 11, 2012 were 15867 and 2909, respectively. The tsunami broke the emergency cooling system of a nuclear power plant in Fukushima Prefecture, and large areas of Japan have been plagued by radiation and a shortage of electricity ever since. In the geotechnical field, many houses and lifelines were damaged by soil liquefaction, landslides occurred, dams failed and river dikes settled not only in the Tohoku district of northeastern Japan, but also in the Kanto district, which surrounds Tokyo. Liquefaction occurred over a wide area of reclaimed lands along Tokyo Bay, although the epicentral distance was very large, about 380–400 km.

During the 2011 off the Pacific Coast of Tohoku Earthquake, soil liquefaction caused extensive damage to residential lands and houses, as well as to infrastructures, such as roads, rivers, ports, and water supply/sewage systems, over a wide area along the Pacific Coast in Tohoku and in Kanto, including the Tokyo Bay area. Due to the large fault zone, the duration of the strong shaking was extremely long. According to Tokimatsu et al. [1], liquefaction induced damages in Urayasu City such as sand piping on ground surfaces and significant ground subsidence resulting in buildings settlement, tilt, and lateral movement from 3cm to 45cm, 2° to 3°, and 1 cm to 20cm, respectively, were recorded.

Most of the foundations of major infrastructures located on eastern Japan are composed of pile foundations. Because the surface soils in this area are primarily alluvial with characteristics of composition, dense/loose extents and ground water levels prone to liquefaction during earthquake, it is obvious that a pile foundation situated in this area is subject to high risk of failure when

liquefaction occurs. The consequences may cause collapse of the superstructure. To avoid the damage of pile foundation and associated superstructure situated at the liquefaction-prone soil layers, prevention measure should be implemented in planning, design and construction, while one of the methods that have been widely applied in practice is ground treatment.

This paper presents a potential to approach determine and evaluate the range of ground treatment in practice and the verification of the effectiveness of ground treatment with the behavior of the pile foundation.

Methodology. The causes of liquefaction in sandy soils can be grouped into two categories: internal and external. The internal factors include soil density, fine contents, permeability, etc., while the external factors are related to the scales and durations of earthquakes. Liquefaction countermeasures can be developed in accordance with these two aspects and specific characteristics of local ground condition. Most of the current practices use SPT-N value (i.e. [2], [3], [4]) or CPT- q_c value (i.e. [5], [6]) as baselines for evaluating the liquefaction potential. These baselines reflect the loose or dense extent and fine content of the ground soils of interest in which the denser the subsoil, the greater the values of these baseline factors and the lower the liquefaction potential. In gravel soils, liquefaction is in essence a function of void size and the properties of material filled-in rather than the above baseline factors. Thus, the direct use of the SPT-N value or the CPT- q_c value in evaluating the liquefaction potential of gravelly soils is inappropriate.

During liquefaction, the lateral resistance of the pile decreases and may result in significant lateral deformation. In some cases, buckling failure may also occur. To minimize the lateral resistance reduction and lateral deformation of pile foundations in such a way that the risk of buckling failure can be controlled or avoided, the ground treatment methods, such as low pressure grouting, high pressure grouting, compaction grouting and dynamic compaction, are usually adopted in practice. The liquefaction potential can be reduced by increasing the densification extent or shear strength of the soils.

While the liquefaction of sandy soils occurs during an earthquake, the lateral earth pressure acting on the pile foundation decreases significantly as the effective stress reduces to zero, and the pile foundation will reach the maximum lateral deformation. With the dissipation of the excess pore pressure, the effective stress will recover and the soil will regain its shear strength. Nevertheless, this strength will not be the same as the one before the liquefaction. This recovered strength is generally termed the residual strength and can be estimated by using the reduction factor [7]. Results of centrifuge tests indicated that the liquefied fine sand has a residual strength of about 10 percent of the initial p - y curve resistance, and other soil types with less liquefaction potentials are expected to have higher residual strength values [8].

Finn (2015) [9] used centrifuge tests to develop a dimensionless degradation parameter Cu , which was a multiplier to reduce the load p on p - y curves developed for piles in sand under static conditions to account for excess pore water pressure effects. As can be seen in [9], Cu can be lower than 0.1 for high values of excess pore water pressure ratio. This implies that the residual p - y resistance can be less than 10 percent of the initial resistance during liquefaction.

Turner (2016) [10] applied centrifuge model tests to develop the multiplier used for reducing the load p of static p - y curves for a single pile and to account for the effect of relative density on liquefaction potential. It shows that the values of the multiplier are generally between 0.1 and 0.2 for fine sand at a relative density of about 35 percent, and between 0.25 and 0.35 for a relative density of about 55 percent, respectively.

To estimate the lateral deformation of the pile foundation during liquefaction, the strength parameters of the liquefied soil are subject to reduction because of the residual strength of the liquefied soil. The extent of the ground improvement can also be determined in such a manner. Assuming that the soils do not liquefy after appropriate ground improvement, the lateral

deformation of the pile subjected to the same magnitude of earthquake should also be reduced. The amount of reduction depends on the strength of the improved soils.

Researches on the effects of ground treatment types, sizes, and locations showed that there were associated results for embankment. Zekri et al. (2015) [11] studied and reported the effects of improved ground sizes and locations on the performance of a section of the Highway I-57 bridge abutment. As shown from the results, the effect of the treatment size and location of an embankment underlain by a liquefiable soil layer indicate that a 24-m-wide treatment zone was most effective when it was located beneath the sloping portion of the embankment, as the treated zone location moves outward from beneath the sloping portion, predicted lateral displacement become progressively larger.

The impact of different treatment types on the performance of an embankment is illustrated by centrifuge test results from Huang and Wen (2015) [12] and summarized in Adalier et al. (1998) [13]. Adalier et al. (1998) [13] made several observations on the effectiveness of the various ground treatment methods on improving the performance of the embankment. If the intent of the ground improvement is to minimize lateral displacement and vertical settlement of the embankment, Adalier et al. (1998) [13] suggests that the available methods in order to decrease effectiveness are: (1) sheet piles with tie rods, (2) densification or gravel buttresses, and (3) cement-treated blocks, the latter the less effective. Cooke and Mitchell (1999) [14] showed that the reduction of liquefaction-induced ground deformations to acceptable levels may require more than one improvement type, and a particular type of improvement may be effective for only one target reduction (i.e. acceleration, deformation, or pore water pressure) but less effective in improving others.

The effect of the width of a densified sand zone on settlement of a supported shallow foundation structure was investigated using shaking table tests [15]. Results showed that for a given structure width, the increment of ratio of treatment zone width to structure width resulted in a decrease in the structure settlement ratio (measured settlement of structure divided by the liquefiable sand layer thickness).

The effect of treatment depth on response of a footing supported on a densified sand zone within a liquefiable sand deposit was investigated using centrifuge tests [16]. The results showed that the magnitude of footing settlement could be reduced by increasing depth of treatment beneath the footing, however with the adverse effect of increasing the peak footing acceleration.

Centrifuge model and field case history information was not available on the performance of deep foundations situated in improved ground zones during earthquake loading and liquefaction. Further research was needed on the performance of deep foundations in liquefiable soil deposits and the benefits of using ground improvement to reduce the risk of damage on deep foundations, particularly in areas prone to lateral spreading [14].

The objective of this paper is to determine the range and effect of ground treatment for existing pile foundations situated in treated soils with liquefaction potential for retrofitting countermeasure. Results of the study can be used as a reference for decision-making or design practice. The computation software used for this study is the FLAC 2D (version 4.0), developed by Itasca Inc., USA. Because the behavior of pile foundation studied herein is in essence a result of a complicated soil-structure interaction and the deformation of interest depends on applied earthquake force and ground condition, the following assumptions were made for that the physical realities can be described with appropriate simplification:

- 1) During the earthquake, the pile foundation is subject to the same applied force before and after the soil liquefaction.
- 2) The residual strength of the liquefied soil is a constant and independent of time.
- 3) The displacements of the pile and the surrounding soils are continuous and compatible.

4) The soils are homogeneous and isotropic, linear elastic, and perfectly plastic before and after liquefaction, and after ground treatment.

Results. A realistic pile foundation located in eastern Japan was studied in this paper. The on-site soils consist primarily of silty sand (SM) and silty clay (CL). The simplified soil profile and parameters are listed in Table 1. The peak ground acceleration (PGA) is 0.34g, and the groundwater table is about 0.1 m below the ground surface.

Table 1. Summary of soil parameters used for the case study

Depth(m)	Thick(m)	USCS Classification	SPT-N	γ (kg/m ³)	s_u (kg/m ²)	ϕ' (°)	E (GPa)	ν	Reduction factor
10.1	10.1	SM	10	2020		31.0	17.10	0.3	1/3
20.6	10.5	SM	19	1970		31.5	33.66	0.3	2/3
23.6	3.0	CL	15	1900	7300		14.60	0.495	1
29.6	6.0	CL	11	1920	8600		17.20	0.495	1
49.1	19.5	CL	18	1880	10600		21.20	0.495	1
56.6	7.5	SM	27	2000		30.5	48.96	0.3	1
61.1	4.5	SM	64	2180		32.5	114.66	0.3	1
72.6	11.5	SM	49	2050		31.0	88.02	0.3	1

The results of liquefaction hazard assessment using “Assessment of Liquefaction Potential” [4] and “Evaluation of Liquefaction Index” [17] showed that the sandy soil layers within 20.6m from ground surface had low to medium liquefaction potential, and the associated reduction factors were respectively 0.33 and 0.67, referred to Akin et al. (2011)[4]. During liquefaction, the maximum lateral displacement of 2.2cm at top of foundation piles is expected, and the shearing stresses exceed the shearing resistance of pile.

In the analysis, high pressure jet grouting is assumed as the retrofitting measure of ground treatment, and the allowable lateral displacement of foundation piles is 1.66cm in the original design requirement of pile to avoid shearing failure during liquefaction in the surrounding soils of improved ground.

The original analysis and design for the pile group were performed using the Group software (version 3.0), developed by Ensoft Inc., USA. For the case study, we used the FLAC software instead to estimate range of ground treatment, and the displacement compatible principle was used in the analysis to bridge over the commercial softwares, FLAC and Group, for the analysis of pile foundation and effectiveness of ground improvement. Using FLAC, we simulate and determine the range of treated zone by changing the soil parameters in local treated region while satisfying the same displacement between pile head and pile cap analyzed by Group and FLAC, respectively.

The analysis procedure is illustrated as follows:

- 1) Using maximum lateral displacement as the control factor, the simulation was completed when the displacements of pile cap and pile head obtained from FLAC and Group, respectively, are identical.
- 2) The activity forces applied to soil layers came from parts of pile cap and pile. The pile cap was assumed as a rigid body, so its lateral displacement was same as the pile head. By using the lateral displacement of soils before ground treatment, in the seismic situation, analyzed by Group for checking, the distribution of applied forces on pile foundation used as an initial condition in FLAC was calibrated with the displacement compatible principle of which the associated displacement field of pile foundation must be identical to that obtained from Group analysis.
- 3) By conducting a parametric study for a treated zone based on the consideration of post ground treatment and seismic state, and numerically simulating soil displacements with input forces as

indicated above. Until the simulated lateral displacement is identical to the results obtained from Group, the improvement zone (i.e. zone with soil parameters changed) can be identified.

According to the statements mentioned above, the analytical scheme and the results are described as below:

- 1) Set up the semi-infinite numerical mesh ($X68 \times Y58$), according to soil profiles and characteristics as shown on Table 1, and assign corresponding soil parameters to corresponding soil region, respectively. Mohr-Column model as the failure criterion is considered, and the scale unit is in KMS system (Fig. 1).
- 2) The maximum lateral displacement of pile group obtained from the analysis of Group, prior to ground improvement in seismic conditions, is simplified as the control soil displacement curve (Fig. 2).
- 3) Assuming that the displacement of pile cap (s_{cap}) is equal to the displacement of pile head (s_{pile}) gained from Group, and then the applied forces can be obtained with iteration until the s_{cap} is identical to s_{pile} for this particular case (Fig. 3 and Fig. 4). Results of the computed maximum displacement for pile group (with pile cap) subjected to simulated lateral forces are in agreement with each other between Group and FLAC in the liquefaction without ground treatment state.
- 4) With the applied forces mentioned above, the liquefaction conditions with treated ground, and the treated strength shown as undrained shear strength, s_u , the improvement zone can be obtained by iteration until the maximum lateral displacement is almost identical to that obtained from Group (Fig. 5 and Fig. 6).

The strength reduction from liquefaction generally causes increased lateral displacements. The less allowable lateral displacements of piles are, the larger the range of improvement zone is. Results of the computed maximum lateral displacements of pile group (with pile cap) subjected to simulated lateral forces are in agreement with each other between Group and FLAC in the liquefaction with ground treatment state.

Results of analysis in this case study showed that the treated range was considerably large when the treated strength was equal to 12500 kg/m^2 in improvement zone, with width, $W=15.7\text{m}$, and depth, $D=7\text{m}$. The improvement zone is identified and the displacement vectors of improved zone has upward potential after ground treatment.

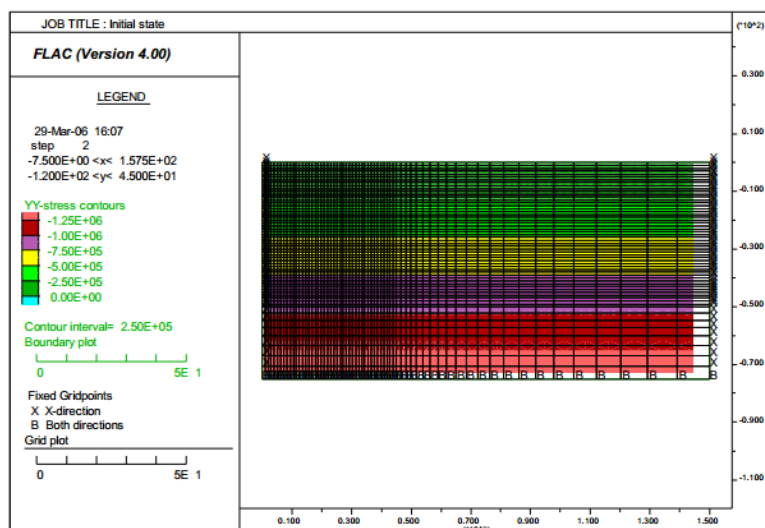


Fig. 1. The initial state of the finite difference mesh generated with FLAC grid

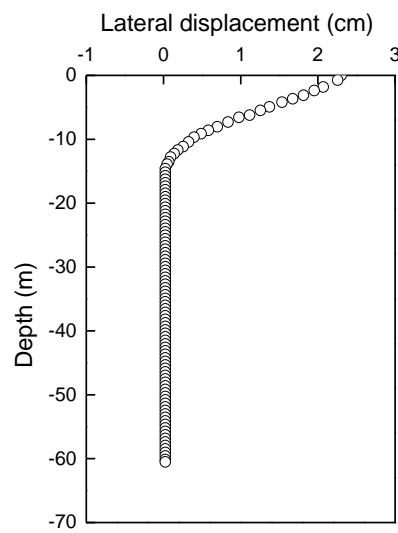


Fig. 2. The maximum lateral displacement of pile group computed by Group.

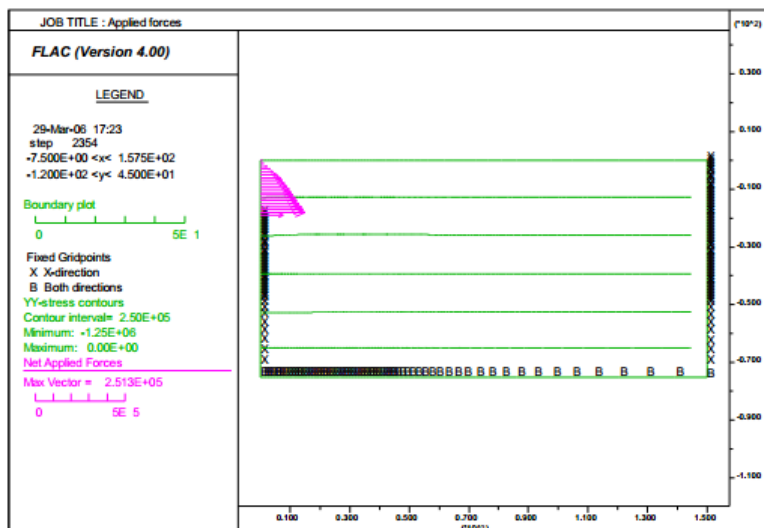


Fig. 3. The applied forces gained to analyze the case being studied (Liquefaction without ground treatment).

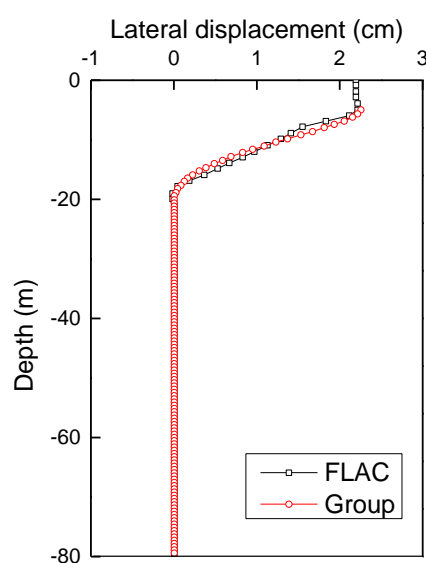


Fig. 4. Maximum displacement for pile group (with pile cap) subjected to simulated lateral forces.

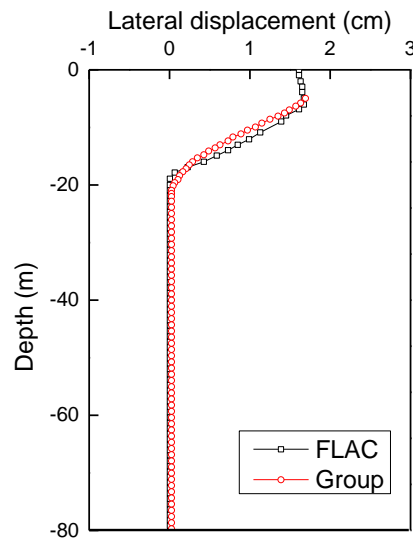


Fig. 5. Maximum lateral displacements of pile group (with pile cap) subjected to simulated lateral forces.

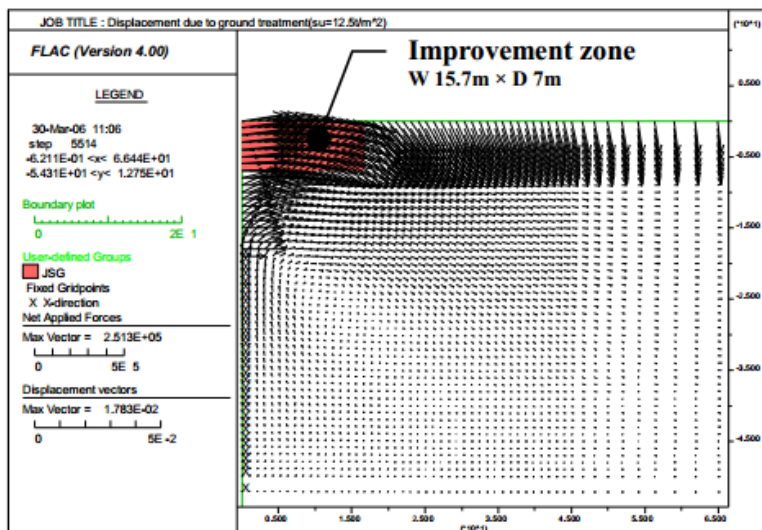


Fig. 6. Improvement zone.

Discussion. The following statements can be concluded from the analysis results stated above:

- 1) When soils were liquefied, the displacement vectors of soils around the pile group exhibited downward movement (Fig.7), which was in agreement with liquefaction phenomenon in practice, where the ground settlements were observed in liquefied soils.
- 2) When soils were subject to lateral forces, the displacements in vertical direction could be developed. With the same treated strength and constant treated width, the vertical displacements of soils around the pile group would change from settlement into dilation with the increasing treated depth gradually, which agreed with real soil behavior in the same situation. In other words, only horizontal displacement would be developed when the treated depth increased to some critical value (Fig. 8). When the treated depth was insufficient, the improvement zone would sink, i.e. the treated effect would not be suitable.
- 3) With the same treated strength and constant treated depth, the horizontal displacement and vertical displacement decrease with the increasing treated width gradually (Fig.9). However, because the strength of soil in the improvement zone was higher than the unimproved liquefied soil

underneath, the soils around the improvement zone still settle and the treated effect would be limited.

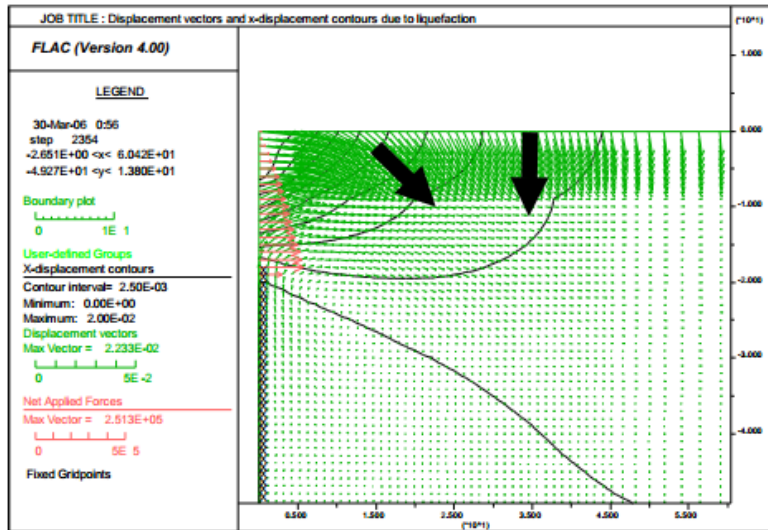


Fig. 7. Liquefaction induced soil settlements associated with downward potential as implied by the displacement vectors.

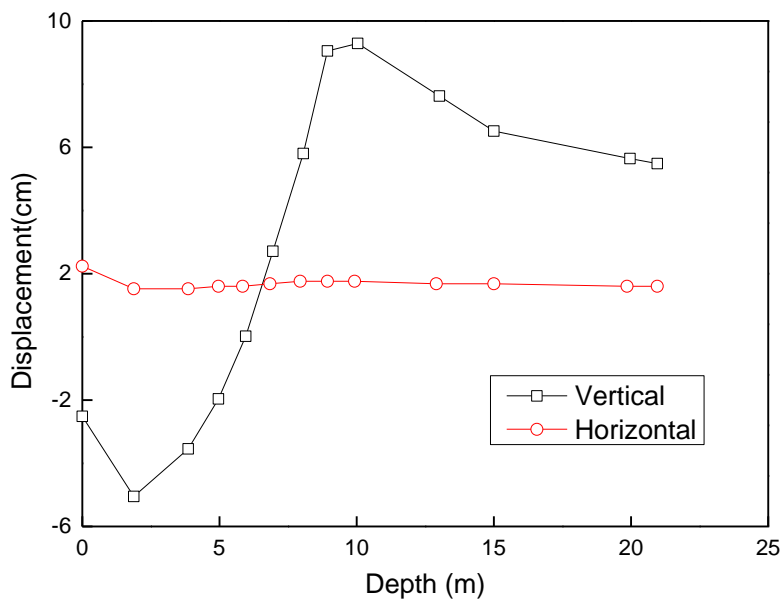


Fig. 8. The computed displacements verse the depth of the improvement zone at a constant treated width of 15.7m.

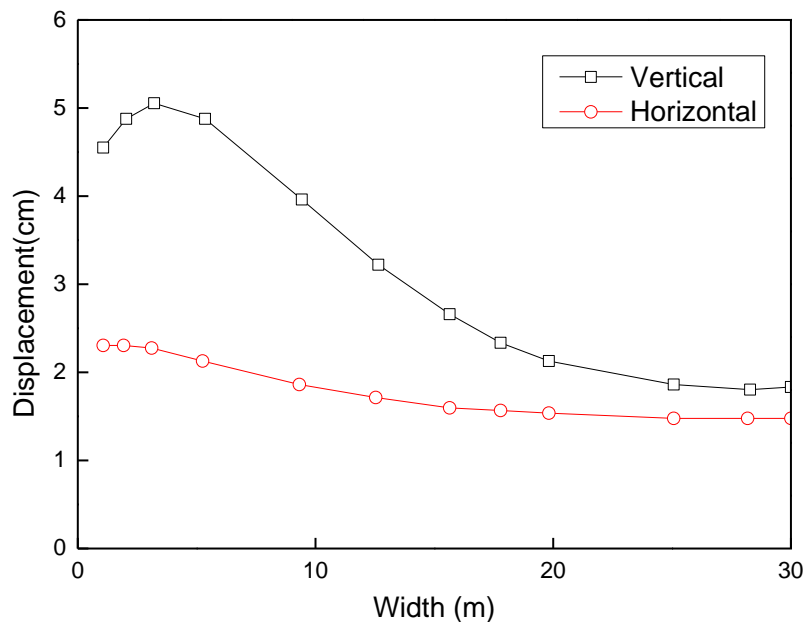


Fig. 9. The computed displacements verse the width of the improvement zone at a constant treated depth of 7m.

Summary. According to the study above, if simply consideration of effect of ground treatment, the suggestion to determine the range of improvement zone is that to assume the treated depth, which not more than depth of liquefiable soils, and then to decide the smallest treated width satisfied with design treated strength and vertical displacement, which not less than zero in the bottom of improvement zone.

If consideration of adopting ground treatment to increase soil shear resistance in order to avoid shear failure of existing piles, the suggestion is that to determine design demands in terms of treated depth and treated strength, then to decide treated width of the improvement zone incorporating with the control of allowable lateral displacement of pile. Besides, it is need to recheck vertical displacement such that it is no less than zero.

Although the effect of ground treatment in resistance of displacement is effective, but the corresponding cost is significant, most of the time the ground treatment countermeasure is not agreed by the client. Unless the other retrofitting measures are not working, the ground treatment would be limited to unformed countermeasure, and it is an inevitable problem in construction practice.

Reference

- [1] Tokimatsu K, Tamura S, Suzuki H, et al. Building damage associated with geotechnical problems in the 2011 Tohoku Pacific Earthquake. *Soils and Foundations*, 2012, 52(5): 956-974.
- [2] Bolton Seed H, Tokimatsu K, Harder L F, et al. Influence of SPT procedures in soil liquefaction resistance evaluations. *Journal of Geotechnical Engineering*, 1985, 111(12): 1425-1445.
- [3] Tokimatsu K, Yoshimi Y. Empirical correlation of soil liquefaction based on SPT N-value and fines content. *Soils and Foundations*, 1983, 23(4): 56-74.
- [4] Akin M K, Kramer S L, Topal T. Empirical correlations of shear wave velocity (Vs) and penetration resistance (SPT-N) for different soils in an earthquake-prone area (Erbaa-Turkey). *Engineering Geology*, 2011, 119(1): 1-17.
- [5] Stark T D, Olson S M. Liquefaction resistance using CPT and field case histories. *Journal of Geotechnical Engineering*, 1995, 121(12): 856-869.

[6] Juang C H, Yuan H, Lee D H, et al. Simplified cone penetration test-based method for evaluating liquefaction resistance of soils. *Journal of geotechnical and geoenvironmental engineering*, 2003, 129(1): 66-80.

[7] Smith R E. *Prefab architecture: A guide to modular design and construction*. John Wiley & Sons, 2011.

[8] Nutt R V. Improved Seismic Design Criteria for California Bridges: Provisional Recommendations. 1996.

[9] Finn W D L. 1st Ishihara Lecture: An overview of the behavior of pile foundations in liquefiable and non-liquefiable soils during earthquake excitation. *Soil Dynamics and Earthquake Engineering*, 2015, 68: 69-77.

[10] Turner B J, Brandenberg S J, Stewart J P. Case Study of Parallel Bridges Affected by Liquefaction and Lateral Spreading. *Journal of Geotechnical and Geoenvironmental Engineering*, 2016: 05016001.

[11] Zekri A, Ghalandarzadeh A, Ghasemi P, et al. Experimental study of remediation measures of anchored sheet pile quay walls using soil compaction. *Ocean Engineering*, 2015, 93: 45-63.

[12] Huang Y, Wen Z. Recent developments of soil improvement methods for seismic liquefaction mitigation. *Natural Hazards*, 2015, 76(3): 1927-1938.

[13] Adalier K, Elgamal A W, Martin G R. Foundation liquefaction countermeasures for earth embankments. *Journal of Geotechnical and Geoenvironmental Engineering*, 1998, 124(6): 500-517.

[14] Cooke H G, Mitchell J K. *Guide to Remedial Measures for Liquefaction Mitigation at Existing Highway Bridge Sites*. Buffalo, New York, 1999.

[15] Hatanaka M, Suzuki Y, Miyaki M, et al. Some factors affecting the settlement of structures due to sand liquefaction in shaking table tests. *Soils and Foundations*, 1987, 27(1): 94-101.

[16] Liu L, Dobry R. Seismic response of shallow foundation on liquefiable sand. *Journal of geotechnical and geoenvironmental engineering*, 1997, 123(6): 557-567.

[17] Iwasaki T, Arakawa T, Tokida K I. Simplified procedures for assessing soil liquefaction during earthquakes. *International Journal of Soil Dynamics and Earthquake Engineering*, 1984, 3(1): 49-58.

Noise-Induced Hearing Loss in Relation With Vibration Disease and Exposure to Vibration Among Employees in Latvia

Kristina Karganova¹, Jelena Reste²

1 – Riga Stradiņš University, Faculty of Medicine, Riga, Latvia

2 – Institute of Occupational Safety and Environmental Health, Riga Stradiņš University, Riga, Latvia



DOI 10.13140/RG.2.1.3178.6480

Keywords: noise-induced hearing loss, occupational noise-induced hearing loss, intensive noise, vibration, effects of vibration, vibration white finger, pneumatic hammer syndrome.

ABSTRACT. Occupational noise-induced hearing loss (ONIHL) is a form of sensorineural hearing loss that is caused by intensive and continuous exposure to noise. It is one of the most frequently encountered occupational diseases worldwide despite numerous available control measures. ONIHL is a preventable disease, however, once the damage to the inner ear structures has occurred no medical intervention can reverse it.

Aim. The purpose of this study was to describe and analyse incidence of registered cases of ONIHL in relation to vibration disease and exposure to vibration among employees in Latvia between 2005 and 2014.

Materials and methods. The data used in the study were acquired from the Latvian State Register of Patients with Occupational Diseases and afterwards analyzed with applicable statistical tests using both Excel and IBM SPSS programmes to compare epidemiological parameters between ONIHL, vibration disease (VD) and exposure to vibration and to identify the association between them.

Results. In total data were obtained about 2302 patients with 2562 cases of occupational ear, nose and throat (ENT) diseases. Out of them ONIHL was registered in 1699 cases (819 cases were ONIHL in combination with VD). Most of the employees with ONIHL and ONIHL simultaneously with VD were males aged 55-64. There was found statistically significant association between ONIHL and VD ($p<0.001$; Cramer's $V=0.42$; $OR=32.08$; 95% confidence interval (95% CI) 19.62–52.45). Statistically significant association was encountered between ONIHL and exposure to vibration as well ($p<0.001$; Cramer's $V=0.46$; $OR=10.97$; 95% CI: 8.63–13.96).

Conclusion. In total ONIHL was the most prevalent occupational ENT disease followed by chronic laryngitis, chronic pharyngitis and allergic rhinitis. Statistically significant association was found between ONIHL and VD, and ONIHL and exposure to vibration. Study revealed that hearing quality of workers employed in manufacturing; transport, storage and communication; construction and agriculture, hunting and forestry industries should be strongly controlled.

Introduction. Occupational noise-induced hearing loss (ONIHL) is a form of sensorineural hearing loss that is caused by intensive and continuous exposure to noise [1]. ONIHL is one of the most prevalent occupational diseases that occurs in a wide variety of industries in both developing and industrialized countries [2, 3]. It has a gradual onset, therefore at the beginning hearing impairment may not be even noticed by an employee until a significant damage and reduction in hearing has occurred [4]. ONIHL is a preventable disease if numerous available control measures are used such as personal hearing protective equipment, isolation of noise source, design and manufacturing of low-noise technologies and many more [2]. However, once the damage to the structures of inner ear has developed no medical intervention can reverse this damage and permanent hearing loss occurs [1]. Additionally, continuous exposure to hazardous noise level may cause vestibular symptoms as well even before noticeable hearing impairment [4].

In general, the labyrinthine injury depends on the noise intensity, duration of the exposure and its pattern. The damage is more significant when the exposure is continuous rather than intermittent even if the overall noise level and exposure time is the same [4]. This may be explained by the fact that in case of intermittent noise exposure, ear has a time to recover from the injury [3]. ONIHL

most frequently represents as symmetrical, bilateral hearing impairment not reaching total loss. The damage develops most rapidly within the first 10-15 years of exposure and thereafter progresses in a much reduced tempo [5]. Early in the course of the disease ONIHL has a characteristic pattern in the audiogram: loss mostly is limited to the 3, 4 and 6 kHz range and recovers at the 8 kHz. The most pronounced loss usually appears as a notch in the audiogram at the 4 kHz [3, 5]. However, it may appear in any of the aforementioned frequencies. The location of the notch is determined by multiple factors such as anatomical characteristics of an ear and frequency of the noise employee is exposed to [3]. If the exposure to the hazardous noise level continues other frequencies get involved as well, however, the most prevalent injury stays at the 3, 4 and 6 kHz [5]. Hearing loss due to hazardous noise level is usually not greater than 75 dB in high frequencies and 40 dB in lower, speech frequencies [1, 3]. Once an employee is removed from the noisy environment or the noise source is isolated the progression of ONIHL stops, but the injury caused so far does not reverse [1].

Recent evidences show that the co-exposure to vibration and co-morbidity with vibration white finger (VWF) increases the risk of the development of ONIHL and its severity [1, 6]. The exact mechanism of the effect of vibration on inner ear structures is not known yet [1]. *Pyykkö et al.* suggested that the effect of vibration on inner ear is due to vibration caused activation of sympathetic nervous system and subsequent vasoconstriction and reduction of blood flow in the labyrinth [7]. Apart from vasoconstrictive effects of vibration, a study by *Sutinen et al.* has shown that vibration has a direct effect on inner ear structures due to transmission of vibration to the temporal bone. Besides it was concluded that temporal bone vibration at higher frequencies resulted in more significant hearing deterioration, despite the fact that vibration at lower frequencies was much better transmitted to the temporal bone and its structures while vibration at high frequencies was heavily attenuated [8]. *Seki et al.* in an experimental study on guinea pigs suggested that relation between hearing loss and vibration might be due to vibration caused effect on blood vessels in the stria vascularis. It was noted that exposure to vibration caused damage to the blood vessels in the stria vascularis that increased their permeability and elicited degenerative changes in the intermediate cells of the stria vascularis [6, 9]. *Zou et al.* detected an increased expression of tumor necrosis factor - alpha (TNF- α) and vascular endothelium growth factor (VEGF) and their receptors in the cochlea of those guinea pigs that were exposed to vibration. None of these factors have been detected in normal cochlea, suggesting their role in the pathogenesis of the vibration caused damage and subsequent repair of the cochlea [10, 11]. Additionally, expression of TNF- α elicits recruitment of inflammatory cells into the cochlea that may cause further damage [12].

Aim. The purpose of this study was to describe and analyse incidence of registered cases of ONIHL in relation to vibration disease and exposure to vibration among employees in Latvia between 2005 and 2014.

Materials and methods. The data used in the study were acquired from the Latvian State Register of Patients with Occupational Diseases. All of the occupational diseases mentioned in the register were coded using International Classification of Diseases 10th edition (ICD-10). None of the names of the patients in the register were mentioned. 1st revision of Statistical classification of economic activities in the European Community (NACE 1) was used to code the economic activities sectors, where patients were employed in. Only those employees whose occupational disease status was confirmed (further in the article patients) were included in the register. The confirmation of occupational diseases included scrupulous diagnostic procedures such as anamnestic data collection, including information about patients work conditions (information about exposure to hazardous work factors, total length of employment and the length of employment under harmful conditions), performance of specific diagnostic tests and exclusion of possible non-work related causative factors. The diagnosis of ONIHL was suspected in patients who complained about deteriorating hearing and tinnitus. During otoscopy no pathologies that could affect hearing were detected. Afterwards the diagnosis was confirmed by pure tone audiometry that depicted symmetrical, bilateral hearing loss of 20 dB or more in air and bone conduction at 0.5-2 kHz frequencies and 65 dB and more at 4 kHz frequencies. The diagnosis of vibration disease (VD) was

established in patients who were daily exposed to vibration and complained about numbness or tingling sensation in extremities, episodes of hand blanching when exposed to cold, intermittent vertigo, tinnitus, sleep disturbance and polyradiculoneuropathy syndrome. The diagnosis was confirmed after positive cold provocation test and neurometry or neurography for the nerves of hands and feet. Exposure to vibration and noise was established from anamnestic data, mandatory occupational health surveillance card and hygienic description of work environment that was performed by inspector of the State Labour Inspectorate of the Republic of Latvia.

The data about patients with occupational ear, nose and throat (ENT) diseases between 2005 and 2014 were obtained. Out of them patients with ONIHL and ONIHL in combination with VD were selected and further analysed. In total data were obtained about 2302 patients with 2562 cases of occupational ENT diseases. Out of them ONIHL was registered in 1699 cases (819 cases were ONIHL in combination with VD) (Fig. 1). In total there were 1423 male patients (61.8%) and 879 female patients (38.2%). The mean age of all patients of both genders with occupational ENT diseases at the moment of diagnosis were 55.94 ± 7.01 years (the range of age 23-80 years) and the mode age was 56: for the male patients 57.15 ± 6.89 years and 59, and for the female patients 53.99 ± 6.75 years and 56, respectively. All the selected patients were divided and further analysed by gender, age and the economic activity sector they were employed in. Afterwards these groups were compared between each other. All the data used in the study were analysed by Excel programme and IBM SPSS using to the specific data parameters applicable tests (Pearson's Chi-squared test, Cramer's V value and odds ratio (OR)).

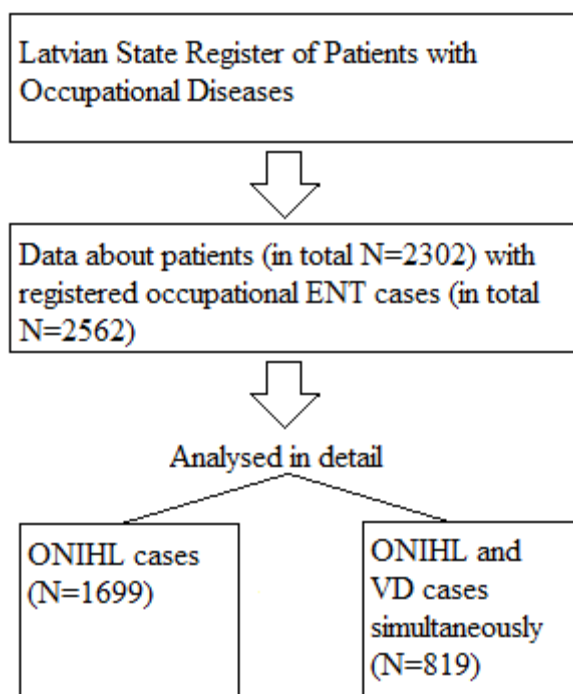


Fig. 1. The selection of data from the Latvian State Register of Patients with Occupational Diseases (ENT – ear, nose and throat diseases; ONIHL – occupational noise-induced hearing loss; VD – vibration disease).

Results. In total between 2005 and 2014 there were registered 1699 cases of ONIHL: 1307 cases in male patients (76.9% from all the registered cases of ONIHL) and 392 cases in female patients (23.1%). It was the most frequently registered occupational ENT disease (66.3% from all the registered cases of ENT diseases), followed by chronic laryngitis, chronic pharyngitis and allergic rhinitis. In total chronic laryngitis was registered in 380 cases (14.8% from all the registered cases

of ENT diseases): 103 cases in male patients (27.1% from all the registered cases of chronic laryngitis) and 277 cases in female patients (72.9%); chronic pharyngitis – 321 cases (12.5%): 73 cases in male patients (22.7%) and 248 cases in female patients (77.3%); and allergic rhinitis – 114 cases (4.4%): 21 case in male patients (18.4%) and 93 cases in female patients (81.6%).

Out of 1699 cases of ONIHL 819 cases were in combination with VD (48.2% from all the registered cases of ONIHL): 793 cases in male patients (96.8% from all the registered cases of ONIHL in combination with VD) and 26 cases in females (3.2%). Pearson's Chi-squared test showed that there is statistically significant association between ONIHL and VD ($p<0.001$). The strength of association between ONIHL and VD was measured by Cramer's V. The strength of association was calculated as strong (Cramer's V=0.42). Odds for patients with confirmed VD to acquire ONIHL was 32.08 times higher (Odds ratio (OR) = 32.08; 95% confidence interval (95% CI): 19.62–52.45).

Majority of patients with registered ONIHL in total had two occupational diseases (OD): ONIHL and another OD (N=887; 52.2% from all the patients with ONIHL). Out of them ONIHL in combination with VD was registered in 727 patients (82.0% from all the patients with two registered OD and one of them being ONIHL) (Table 1).

Table 1. Total number of registered occupational diseases (OD) with one of them being occupational noise-induced hearing loss (ONIHL) in patients between 2005 and 2014

Number of registered occupational diseases in patients with ONIHL	Number of patients	Percentage from all the patients with confirmed ONIHL (%)
Only ONIHL	52	3.1
ONIHL and another OD	887	52.2
ONIHL in combination with VD	727	-
ONIHL in combination with 2 OD	295	17.4
ONIHL in combination with 3 OD	205	12.1
ONIHL in combination with 4 OD	148	8.7
ONIHL in combination with 5 OD	75	4.4
ONIHL in combination with 6 OD	23	1.4
ONIHL in combination with 7 OD	8	0.5
ONIHL in combination with 8 OD	5	0.3
ONIHL in combination with 9 OD	1	0.1

The mean age of patients both males and females with ONIHL at the moment of diagnosis were 56.93 ± 6.61 years and the mode age 56 (the range of age 26-80): in male patients 57.41 ± 6.74 and 59 year and in female patients 55.35 ± 5.90 and 56 years, respectively. Most of the cases of ONIHL were registered in patients aged 55-64 years (N=941; 55.4% from all the registered ONIHL cases) (Table 2).

The mean age of patients both males and females with ONIHL in combination with VD at the moment of diagnosis were 57.97 ± 6.64 years and the mode age 59 (the range of age 34-80): in male patients 57.93 ± 6.66 and 59 year and in female patients 59.15 ± 6.12 and 60 years, respectively. Majority of cases were registered in patients aged 55-64 years (N=474; 57.9% from all the registered cases of ONIHL in combination with VD) (Table 2).

Most of the ONIHL cases were registered in patients employed in the following economic activities sectors (the 1st revision of Statistical classification of economic activities in the European Community (NACE) was used): 1) manufacturing (N=627); 2) transport, storage and communication (N=488); 3) construction (N=175); and 4) agriculture, hunting and forestry (N=149) (Table 3).

Table 2. Number of registered occupational noise-induced hearing loss (ONIHL) and ONIHL in combination with vibration disease (VD) cases and percentage in patients of various age groups in Latvia between 2005 and 2014.

Age	Total number of ONIHL cases	Percentage from all the registered ONIHL cases (%)	Total number registered ONIHL in combination with VD cases	Percentage from all the registered ONIHL in combination with VD cases (%)
<35	5	0.3	1	0.1
35-44	48	2.8	19	2.3
45-54	515	30.3	208	25.4
55-64	941	55.4	474	57.9
65-74	175	10.3	106	12.9
>74	15	0.9	11	1.3

Table 3. Number of registered cases of occupational noise-induced hearing loss (ONIHL) in patients working in various economic activities sectors in Latvia between 2005 and 2014.

Economic activity sector	Total number of cases in the industry	Percentage from all the registered cases of ONIHL (%)	Number of cases in male patients	Percentage from all the registered cases of ONIHL in the industry (%)	Number of cases in female patients	Percentage from all the registered cases of ONIHL in the industry (%)
Manufacturing	627	36.9	314	50.1	313	49.9
Transport, storage and communication	488	28.7	467	95.7	21	4.3
Construction	175	10.3	165	94.3	10	5.7
Agriculture, hunting and forestry	149	8.8	136	91.3	13	8.7
Other:						
<i>Electricity, gas and water supply</i>	57	3.4	51	89.5	6	10.5
<i>Wholesale and retail trade; repair of motor vehicles, motorcycles and personal and household goods</i>	39	2.3	35	89.7	4	10.3
<i>Public administration and defence; compulsory social security</i>	39	2.3	36	92.3	3	7.7
<i>Other community, social and personal service activities</i>	29	1.7	23	79.3	6	20.7
<i>Health and social work</i>	28	1.6	18	64.3	10	35.7
<i>Mining and quarrying</i>	22	1.3	22	100	-	-
<i>Education</i>	22	1.3	12	54.5	10	45.5
<i>Real estate, renting and business activities</i>	14	0.8	14	100	-	-
<i>Fishing</i>	6	0.4	6	100	-	-
<i>Hotels and restaurants</i>	2	0.1	2	100	-	-
<i>Not mentioned</i>	2	0.1	1	50.0	1	50.0
A total of ONIHL cases in 2005-2014	1699		1302	76.6	397	23.4

Co-existence of ONIHL and VD most frequently were registered in patients employed in: 1) transport, storage and communication (N=339); 2) manufacturing (N=117) 3) construction (N=114); and agriculture, hunting and forestry (N=114) sectors (Table 4).

Table 4. Number of registered cases of occupational noise-induced hearing loss (ONIHL) simultaneously with vibration disease (VD) in patients working in various economic activities sectors in Latvia between 2005 and 2014.

Economic activity sector	Total number of cases in the industry	Percentage from all the registered cases of ONIHL (%)	Number of cases in male patients	Percentage from all the registered cases of ONIHL in the industry (%)	Number of cases in female patients	Percentage from all the registered cases of ONIHL in the industry (%)
Transport, storage and communication	339	41.4	331	97.6	8	2.4
Manufacturing	117	14.3	107	91.5	10	8.5
Construction	114	13.9	112	98.2	2	1.8
Agriculture, hunting and forestry	114	13.9	111	97.4	3	2.6
Other:						
<i>Electricity, gas and water supply</i>	28	3.4	28	100	-	-
<i>Public administration and defence; compulsory social security</i>	22	2.7	22	100	-	-
<i>Wholesale and retail trade; repair of motor vehicles, motorcycles and personal and household goods</i>	21	2.6	21	100	-	-
<i>Health and social work</i>	17	2.1	15	88.2	2	11.8
<i>Other community, social and personal service activities</i>	14	1.7	14	100	-	-
<i>Mining and quarrying</i>	12	1.5	12	100	-	-
<i>Real estate, renting and business activities</i>	9	1.1	9	100	-	-
<i>Education</i>	5	0.6	4	80.0	1	20.0
<i>Fishing</i>	5	0.6	5	100	-	-
<i>Hotels and restaurants</i>	1	0.1	1	100	-	-
<i>Not mentioned</i>	1	0.1	1	100	-	-
<u>A total of ONIHL in combination with VD cases in 2005-2014</u>	819		793	96.8	26	3.2

1147 patients with confirmed ONIHL admitted that they were daily exposed to vibration (67.5% from all the patients with registered ONIHL). Out of them 808 patients (70.4% from all the patients with ONIHL who had been daily exposed to vibration) were diagnosed VD as well (Fig. 2). Pearson's Chi-squared test showed that there is statistically significant association between ONIHL and vibration ($p<0.001$). The strength of association between ONIHL and vibration was calculated

as strong (Cramer's V=0.46). Odds for patients who were daily exposed to vibration during work hours to acquire ONIHL was 10.97 times higher (OR=10.97; 95% CI: 8.63–13.96).

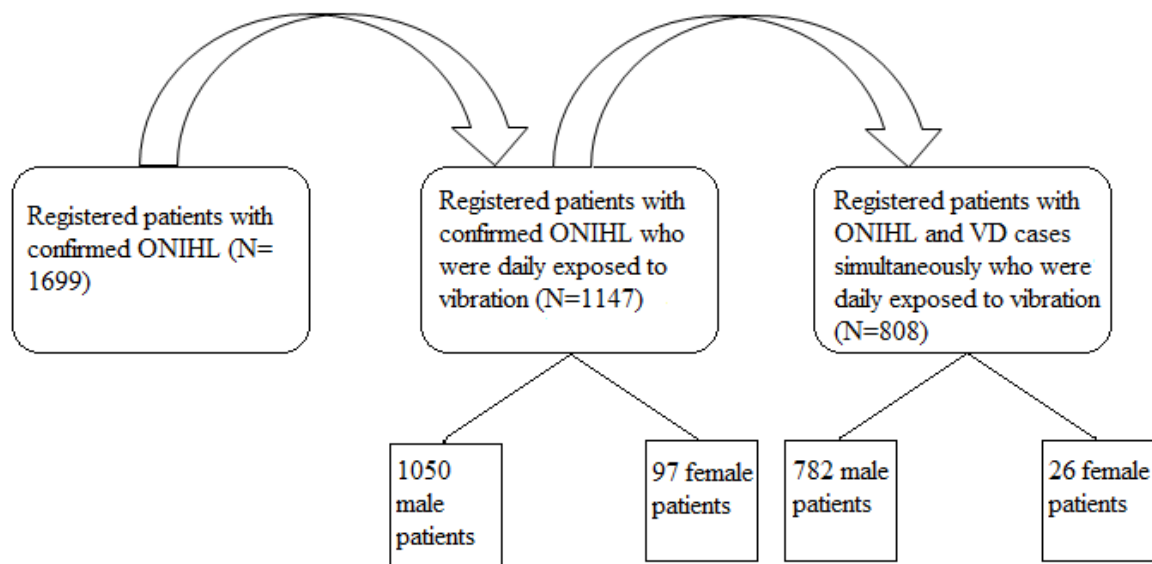


Fig. 2. Number of patients with confirmed occupational noise-induced hearing loss (ONIHL) who were daily exposed to vibration and had simultaneously vibration disease (VD).

Incidence of ONIHL per 100 000 employees in the corresponding year throughout the study period the highest was in male employees rather than in female employees. The highest incidence was detected in 2010 in both genders together and in male and female employees separately: 35.97 per 100 000 employees of both genders together; 55.89 per 100 000 male employees and 18.08 per 100 000 female employees. Incidence of ONIHL in combination with VD per 100 000 employees in the corresponding year throughout the study period the highest was in male employees with a peak in 2010 when 153 cases were registered. However, the incidence of ONIHL in combination with VD in female employees was considerably lower and no peak in incidence were detected. Incidence in female employees during the study period did not rise above 1.35 cases per 100 000 employees that was registered in 2011 and was the highest incidence detected in females. After 2010 when the highest incidence levels were registered for both ONIHL and ONIHL simultaneously with VD incidence decreased. In case of ONIHL the incidence level in the last years has stayed more or less the same, however, incidence level in case of ONIHL with VD slightly increased in 2013 in male employees and afterwards dropped once again.

Table 5. Incidence of registered occupational noise-induced hearing loss (ONIHL) cases and ONIHL cases simultaneously with vibration disease (VD) in employees in Latvia between 2005 and 2014.

Year	2005	2006	2007	2008	2009	2010	2011	2012	2013	2014
<u>Total incidence of ONIHL per 100 000 employees in the corresponding year (absolute number of cases)</u>	12.86 (125)	8.44 (87)	15.04 (159)	16.21 (171)	33.57 (305)	35.97 (306)	19.61 (169)	13.93 (122)	14.43 (129)	14.24 (126)
Incidence of ONIHL per 100 000 <u>male</u> employees in the corresponding year (absolute number of cases)	20.74 (103)	12.94 (68)	23.33 (126)	23.52 (125)	51.03 (222)	55.89 (225)	33.16 (138)	22.19 (95)	24.74 (109)	21.89 (96)
Incidence of ONIHL per 100 000 <u>female</u> employees in the corresponding year (absolute number of cases)	4.63 (22)	3.76 (19)	6.38 (33)	8.79 (46)	17.53 (83)	18.08 (81)	6.96 (31)	6.03 (27)	4.41 (20)	6.72 (30)
<u>Total incidence of ONIHL simultaneously with VD per 100 000 employees in the corresponding year (absolute number of cases)</u>	6.27 (61)	4.07 (42)	6.53 (69)	6.07 (64)	14.75 (134)	18.69 (159)	12.88 (111)	7.54 (66)	8.39 (75)	4.30 (38)
Incidence of ONIHL <u>simultaneously with VD</u> per 100 000 <u>male</u> employees in the corresponding year (absolute number of cases)	11.88 (59)	7.80 (41)	12.78 (69)	11.67 (62)	29.66 (129)	38.00 (153)	25.23 (105)	14.95 (64)	17.02 (75)	8.21 (36)
Incidence of ONIHL <u>simultaneously with VD</u> per 100 000 <u>female</u> employees in the corresponding year (absolute number of cases)	0.42 (2)	0.20 (1)	-	0.38 (2)	1.06 (5)	1.34 (6)	1.35 (6)	0.45 (2)	-	0.45 (2)

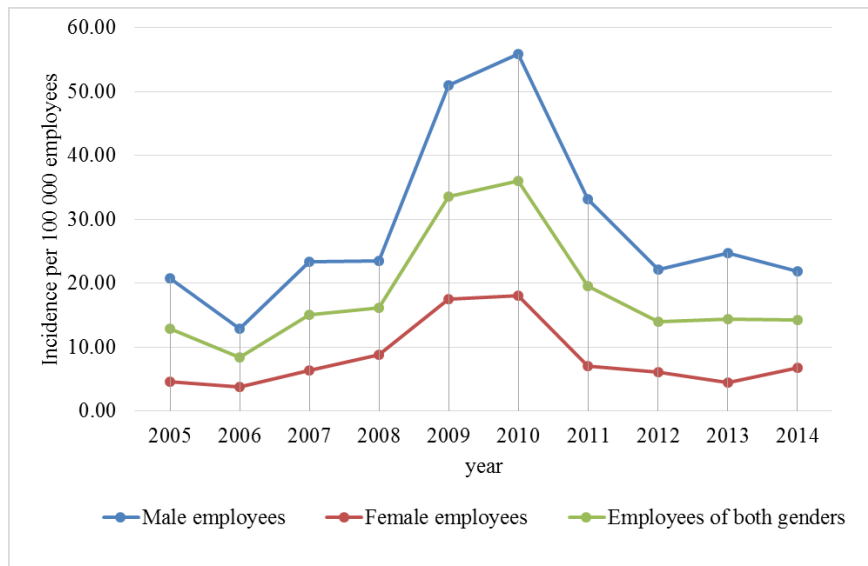


Fig. 3. Incidence of registered occupational noise-induced hearing loss (ONIHL) cases per 100 000 employees in Latvia between 2005 and 2014.

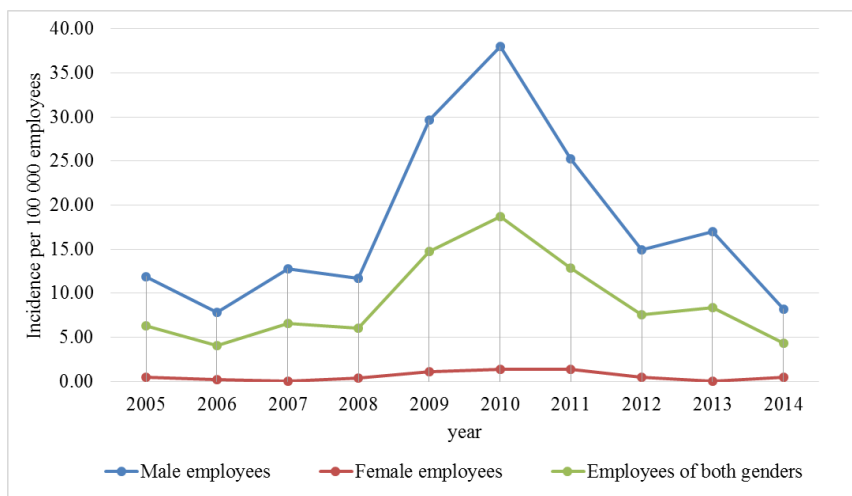


Fig. 4. Incidence of registered occupational noise-induced hearing loss (ONIHL) cases simultaneously with vibration disease (VD) cases per 100 000 employees in Latvia between 2005 and 2014.

Discussion. The Latvian State Register of Patients with Occupational Diseases contains data only about those employees who actively seek medical attention and undergo all the necessary procedures and diagnostic tests to register their disease as work factor or work environment caused a.k.a. occupational. The register does not contain data about all the employees with ONIHL or VD, most probably due to the fact that the onset of these conditions is gradual and imperceptible or the severity of symptoms of both ONIHL and VD is mild and intermittent at the moment before a significant damage has been caused to the structures of inner ear, blood vessels and peripheral nervous system. While symptoms stay mild and appear only occasionally, they might not significantly interfere with a patient's daily routine, activities and work productivity. Due to aforementioned patients usually look for a doctor's appointment only when the symptoms become obvious and severe. Another factor that might prevent patients from looking for a medical help is a possibility of their job loss if they are considered unfit. Due to these factors the true incidence rate

of ONIHL and ONIHL simultaneously with VD among the employees most probably was higher than calculated in the study.

Increase in incidence of ONIHL and ONIHL simultaneously with VD between 2008 and 2010 most probably was due to economic instability in Latvia that began in 2008 and went on for the next couple of years. Due to this considerable number of employees lost their job positions. The number of appointments with occupational physicians by the contrary increased during this period of time. This might be explained by the fact that those employees who lost their jobs actively sought consultation with the occupational physician and were motivated to undergo all the necessary procedures and laboratory, radiological or other tests so that their medical condition provoked by hazardous work environment and factors could be officially registered as occupational disease. Once their condition were officially registered as occupational these former employees were able to claim and receive economic support from the government of Latvia.

Prolonged exposure to noise and intensive noise level is a prevalent hazardous work factor encountered in many economic activities sectors despite numerous preventive methods and regulations [13]. A study by *Tak* and a study by *Tak et al.* revealed that the highest prevalence of ONIHL was found in employees working in mining, manufacturing, construction, transportation, agriculture, forestry and fishing, as well as trucking and repair services [14, 15]. In Latvia the mining industry is not developed, therefore this study showed that most of the employees with registered ONIHL cases came from manufacturing, transportation and storage, construction, as well as agriculture, hunting and forestry industries. These results correspond to the study by *Tak*. The majority of patients were males (76.9% from all the patients with registered cases of ONIHL) possibly due to the fact that the sample of patients had higher proportion of male patients, but also employees of male gender are more prevalent in those industries were ONIHL is most frequently registered in [16; 17]. A study by *Tak et al.* reported that the prevalence of ONIHL was higher in male patients rather than in females as well - 14.0% and 8.5%, respectively [15]. The same study showed that prevalence of ONIHL was the highest in middle aged patients (55-64 years) [15]. This fact corresponds with the results from this study, where in total 55.4% of all the ONIHL cases were registered in patients aged 55-64 years.

Another risk factor that is widely encountered in those industries where employees are exposed to a long-lasting or intensive noise level, is vibration [7]. Daily exposure to vibration from vehicles and machines used during work and hand held vibratory tools are the leading cause of vibration disease [18]. Additionally, continues exposure to vibration is thought to effect inner ear and promote development of ONIHL. It has been previously concluded that employees who had claimed to have episodes of white fingers or had been diagnosed with HAV had an increased risk for the development of ONIHL [6, 7, 19-22]. The results of this study are consistent with the previous ones. *Turkot et al.* concluded that presence of VWF increased the risk for the noise-induced hearing loss (NIHL) 1.34 times (95% CI: 1.21-1.49) [6]. *Petterson et al.* showed that among 133 participants with NIHL 120 participants reported white finger (WF) episodes of them 49 participants daily used hand held tools [19]. Another study by *Petterson et al.* further supports the link between noise, vibration and NIHL concluding that those employees who were co-exposed to noise and vibration have a greater risk for NIHL [7]. Study by *Palmer et al.* demonstrates that in those participants who reported WF episodes NIHL was twice as common, even among those participants who claimed never to be exposed to hand arm vibration (HAV) [6, 20]. An experimental study by *Zhu et al.* supports the hypothesis that combination of exposure of both noise and vibration causes a more significant temporary threshold shift (TTS) than exposure to a noise alone. The study demonstrated that those subjects who were exposed to noise and vibration simultaneously had a higher TTSs at 4 and 6 kHz than those who were exposed to a noise alone. Exposure only to HAV had no effect on TTS, therefore demonstrating that vibration augments the effects caused by noise [21]. A study by *Petterson et al.* has demonstrated similar results [22].

Summary. Absolute majority of registered cases of occupational ENT diseases among employees in Latvia between 2005 and 2014 were ONIHL followed by chronic laryngitis, chronic pharyngitis and allergic rhinitis. Most of the patients with ONIHL and ONIHL simultaneously with VD were males aged 55-64. Statistically significant association was found between ONIHL and VD; and ONIHL and exposure to vibration. These results are consistent with previous studies and literature data. Due to association between hearing loss and VD and exposure to vibration it is of utmost importance to include in ONIHL prevention programmes and campaigns information about vibration and its effect on an employee's health. Moreover, strategies and methods to decrease employees' exposure to vibration or avoid it altogether should be studied and implemented in the daily life.

ONIHL most commonly was registered in those employees who were daily exposed to intensive or continues noise; and noise and vibration simultaneously. The study demonstrates employees of which economic activities sectors are at the highest risk of the development of ONIHL or ONIHL simultaneously with VD and hearing quality of workers of which economic activity sector should be tightly controlled.

The study showed that incidence level of ONIHL and ONIHL simultaneously with VD was higher in male employees and that socioeconomic processes in the country had a significant impact on it. Increase in incidence of ONIHL and ONIHL simultaneously with VD was caused not only due to worsened work environment when socioeconomic stability in Latvia decreased, but also due to increased visit rates with the occupational physician and higher motivation of patients to have their condition recognised as occupational. In such a way patients were able to claim economic support from the Latvian government.

Further studies are necessary to comprehend the exact mechanism by which vibration effects inner ear structures and contributes to the development of ONIHL.

References

- [1] Lalwani, A. K. (Ed.). (2012). *Current Diagnosis & Treatment in Otolaryngology – Head & Neck Surgery* (3rd ed.). New York: McGraw-Hill Medical.
- [2] Rantanen, J. (n.d.). Global strategy on occupational health for all: The way to health at work. Recommendation of the second meeting of the WHO Collaborating Centres in Occupational Health. Retrieved January 8, 2016, from http://www.who.int/occupational_health/globstrategy/en/
- [3] ACOEM Task Force on Occupational Hearing Loss, Kirchner, D. B., Dobie, C. E., Rabinowitz, R. A., Crawford, J., Kopke, R., & Hudson, T. W. (2012, January). Occupational noise-induced hearing loss: ACOEM Task Force on Occupational Hearing Loss. *Journal of Occupational and Environmental Medicine / American College of Occupational and Environmental Medicine*, 54(1), 106-108, doi: 10.1097/JOM.0b013e318242677d
- [4] Pelegrin, A. C., Canuet, L., Rodríguez, A. A., & Morales, M. P. (2015, September/October). Predictive factors of occupational noise-induced hearing loss in Spanish workers: A prospective study. *Noise & Health*, 17(78), 343-349, doi: 10.4103/1463-1741.165064
- [5] Flint, P. W., Haughey, B. H., Lund, V. J., Niparko, J. K., Robbins, K. T., Thomas, J. R., & Lesperance, M. M. (2015). *Cummings Otolaryngology. Head and Neck Surgery* (6th ed.). Philadelphia: Elsevier.
- [6] Turcot, A., Girard, S. A., Courteau, M., Baril, J., & Larocque, R. (2015, April). Noise-induced hearing loss and combined noise and vibration exposure. *Occupational Medicine*, 65(3), 238-244, doi: 10.1093/occmed/kqu214
- [7] Pettersson, H., Burström, L., Hagberg, M., Lundström, R., & Nilsson, T. (2012, July/August). Noise and hand-arm vibration exposure in relation to the risk of hearing loss. *Noise & Health*, 14(59), 159-165, doi: 10.4103/1463-1741.99887

[8] Sutinen, P., Zou, J., Hunter, L. L., Toppila, E., & Pyykkö, I. (2007, February). Vibration-induced hearing loss: Mechanical and physiological aspects. *Otology and Neurotology*, 28(2), 171-177, doi: 10.1097/MAO.0b013e31802e29f2

[9] Seki, M., Miyasaka, H., Edamatsu, H., & Watanabe, K. (2001, February). Changes in permeability of striae vessels following vibration given to auditory ossicle by drill. *The Annals of Otology, Rhinology, and Laryngology*, 110(2), 122-126.

[10] Sutinen P. (2008). *Pathophysiological Effects of Vibration with Inner Ear as a Model Organ*. (Doctoral dissertation). Retrieved May 29, 2016, from <http://wanda.uef.fi/ukuvaitokset/vaitokset/2008/isbn978-951-27-0944-1.pdf>

[11] Zou, J., Pyykkö, I., Sutinen, P., & Toppila, E. (2005, April). Vibration induced hearing loss in guinea pig cochlea: Expression of TNF-alpha and VEGF. *Hearing Research*, 202(1-2), 13-20.

[12] Keithley, E. M., Wang, X., & Barkdull, G. C. (2008, September). Tumor necrosis factor alpha can induce recruitment of inflammatory cells to the cochlea. *Otology and Neurotology*, 29(6), 854-859.

[13] Verbeek, J. H., Kateman, E., Morata, T. C., Dreschler, W. A., & Mischke, C. (2014, March). Interventions to prevent occupational noise-induced hearing loss: A Cochrane systematic review. *International Journal of Audiology*, 53, Suppl. 2, S84-96. Retrieved June 1, 2016, from <http://www.ncbi.nlm.nih.gov/pmc/articles/PMC4678960/>

[14] Tak, S. W. (2009, Summer). Noise, hearing protector use, and hearing loss in American workers. *Update (Council for Accreditation in Occupational Hearing Conservation)*, 21(2), 5-6. Retrieved June 3, 2016, from <http://www.caohc.org/updatearticles/summer09.pdf>

[15] Tak, S. W., & Calvert, G. M. (2008, January). Hearing Difficulty Attributable to Employment by Industry and Occupation: An Analysis of the National Health Interview Survey—United States, 1997 to 2003. *Journal of Occupational and Environmental Medicine*, 50(1), 46-56.

[16] Latvijas Statistikas Datu Bāze. (1996-2009). *NBG08. Nodarbinātie pēc ekonomiskās darbības veidiem un dzimuma (NACE 1.1 red.)*, 1996.-2009.g. Retrieved from http://data.csb.gov.lv/pxweb/lv/Sociala/Sociala__ikgad__nodarb/NB0080.px/table/tableViewLayout1/?rxid=cdcb978c-22b0-416a-aacc-aa650d3e2ce0

[17] Latvijas Statistikas Datu Bāze. (2009-2015). *NBG081. Nodarbinātie pēc saimnieciskās darbības veida un dzimuma (NACE 2.red.)*. Retrieved from http://data.csb.gov.lv/pxweb/lv/Sociala/Sociala__ikgad__nodarb/NB0081.px/table/tableViewLayout1/?rxid=cdcb978c-22b0-416a-aacc-aa650d3e2ce0

[18] Eglīte, M. (2012). *Darba medicīna* (2nd ed.). Rīga: Rīgas Stradiņa universitāte.

[19] Pettersson, H., Burström, L., & Nilsson, T. (2014, March/April). Raynaud's phenomenon among men and women with noise-induced hearing loss in relation to vibration exposure. *Noise & Health*, 16(69), 89-94.

[20] Palmer, K. T., Griffin, M. J., Syddall, H. E., Pannett, B., Cooper, C., & Coggon, D. (2002, September). Raynaud's phenomenon, vibration induced white finger, and difficulties in hearing. *Occupational and Environmental Medicine*, 59(9), 640-642.

[21] Zhu, S., Sakakibara, H., & Yamada, S. (1997). Combined effects of hand-arm vibration and noise on temporary threshold shifts of hearing in healthy subjects. *International Archives of Occupational and Environmental Health*, 69(6), 433-436.

[22] Pettersson, H., Burström, L., & Nilsson, T. (2011, December). The effect on the temporary threshold shift in hearing acuity from combined exposure to authentic noise and hand-arm vibration. *International Archives of Occupational and Environmental Health*, 84(8), 951-957, doi: 10.1007/s00420-011-0635-6

I X . E c o n o m i c s & M a n a g e m e n t
M M S E J o u r n a l V o l . 5



ANFIS and Multi Linear Regression to Estimate the LTLF for the Kingdom of Bahrain

Mohamed Y. Al-Hamad^{1, a}, Isa S. Qamber^{2, b}

1 – Client Interface Executive, GCC Interconnection Authority, Dammam, KSA

2 – University of Bahrain, Department of Electrical and Electronics Engineering, Kingdom of Bahrain

a – mhamad@gccia.com.sa

b – iqamber@uob.edu.bh



DOI [10.13140/RG.2.1.3552.1524](https://doi.org/10.13140/RG.2.1.3552.1524)

Keywords: ANFIS, GDP, MATLAB, Bahrain, LTEL.

ABSTRACT. In the present study, Multiple Linear Regression Method and Adaptive Neuro-Fuzzy Inference System (ANFIS) are designed for output estimated Long Term Estimated Load for the Kingdom of Bahrain. Three variables used as inputs, which are Present Peak Load, Gross Domestic Product (GDP) and Population versus years. Obtaining the estimated Peak Loads calculated using the multi linear regression and ANFIS. The MATLAB Simulink 7.10 package used to obtain the estimated peak load for the Kingdom of Bahrain. The models obtained using the multi linear regression and Neuro-Fuzzy techniques. Bahrain Population and GDP used in the Multiple Linear Regression Model. Different GDP growth scenario based on development in the country used and taken in consideration. The results used for the Peak Demand will compared with actual peaks data. The average percentage of error for each model calculated based on data used to generate the model, where the less average error model presented and recommended for the long-term load forecast for the peak load demand.

Introduction. For the electricity sector decision makers, the energy trading and facility expansion are required. The electricity demand pattern is a multifaceted due to the different types of loads, weather conditions, and socio-economic factors. Therefore, finding an appropriate peak load-forecasting model for Bahrain Peak Demand of the electricity network is an important task for a network planning and power trading which interconnected to another five national networks through Gulf Cooperation Council Interconnection Authority (GCCIA) grid. This will help to plan for a reliable and economical operated network.

Electricity becomes in the picture in Arabian Peninsula's when the oil discovered at Bahrain. The first electricity generating plant in Bahrain became operational in 1930. The growth in electricity demand increased since that time based on area where government was planning to develop and based on budget and availability of electricity generated. The electrical system security comes to the surface after the electricity blackout found on August 2004. Therefore, as part of development for Gulf Cooperation Council GCC Countries, the GCC electrical sectors decided to interconnect their networks based on number of studies [1]. Such studies used to be the bases to build the GCC states to receive the benefits of having the interconnection. The benefits of the interconnection summarized in the reduction of operating costs, sharing of operating and installed capacity reserves [2]. Since that time, Bahrain Electricity Network was interconnected to the largest transmission lines project in the region, which is connect the six countries (Kingdom of Saudi Arabia, Kuwait, Bahrain, Qatar, United Arab Emirates and Oman as shown in Fig. (1). The interconnection which was commissioned in 2009 opens the doors to plan for utilizing the interconnection in energy trading between GCC countries [3].

Research Objective. The present study presents a pragmatic methodology used as a guide to construct Electric Power Peak Load Forecasting Model for Kingdom of Bahrain. There are many exogenous variables for the long-term load forecasting (LTLF) – like weather conditions, industrial development, Population Growth and social events in the country. For more simplicity, the Model using the main variables, which effect on the peak load demand and selected for the proposed Model. Therefore, Bahrain Population and Gross Domestic Product (GDP) selected as the variable elements in the Multiple Linear Regression Model and there will be a need to study the previous period deeply for Bahrain.



Fig. 1. Geographical Layout of the GCC Interconnection.

1. Load Forecasting Types. Electric Power Load Forecasting (EPLF) is an essential process in the planning of electricity utilities and the operation of their power systems. Perfect estimation for load forecasting will show the way to significant economic saving in operating and maintenance costs. Number of studies were carried out long time ago and the peak load for Kingdom of Bahrain modulated to forecast the peak load demand for the upcoming year [4]. These types of studies are helping in increasing the reliability of power supply and delivery system, which help to correct the decisions for future development.

Electric Peak load demand is the highest recorded demand and supplied by generators. It recorded for different time horizon, which is hourly, daily, weekly, monthly, and yearly periods. EPLF has very different characteristics compared to a different type of energy commodity. This type of energy should consumed as soon as it was generating. Therefore, Electricity Load Forecasting for the peak load that made for various purposes classified into three categories. These three categories, which are the short-term, the medium-term and the long-term forecasts. These classifications based on range of the forecasted period.

Regularly, the target of Short-Term Load Forecast (STLF) [5] is used to predict the load up to one week. It used for daily power system operation. Part of this classification is the very short-term load forecast (VSTLF) which is used for less than one day forecast and used to meet the load demand during the day in energy market [6,7].

The Medium-Term Load Forecast (MTLF) used to predict the load from one week to one year. The target of this type of forecasting is to enables electricity utilities and trading companies to estimate the load demand for less than one year and greater than STLF period. The MTLF helps the electricity sector's companies to negotiate the contracts with other companies and to schedule the operations and maintenance [8].

The Long-Term Load Forecast (LTLF) is used to predict the load for more than one year [9], where it is usually used for period of 20 years [5], and 25 to 30 years for some cases. The target of this type of forecasting is to plan for the install capacity to build it in future for the expected load demand based on the projects and the master plan of the country. For example, the LTLF helps the

country in allocating and involving the independent power companies to participate in bidding in building power generation or to plan purchasing electrical energy for long period to manage the energy demand in more economic and reliable way.

ANFIS is used in many research to identify the LTLF for the peak load demand [4, 10], where both used ANFIS for the Long-term load forecasting. Qamber forecast the Kingdom of Bahrain peak load using Neuro-Fuzzy, this paper considered as continuation for Qamber paper where another methodology used, new updated data and the results compared with the ANFIS modelling. Chen use collaborative fuzzy-neural approach for long-term load forecast. Adaptive neural fuzzy inference system had used to obtain long term forecasting results and the results compared to mathematical methods to show validity and error levels [11], where the partial consensus fuzzy intersection and radial basis function network (PCFI-RBF) approach is used.

2. Load Forecasting Data. Weather conditions are the most significant factors that considered as a significant influence on the forecasting during the year. Generally, the weather condition is repeating its behaviour every year. The weather temperature varied during the period of the day, week, month and year, where the temperature is always in range of forty Degree Celsius during the peak time at Bahrain. The same thing is implementing for humidity, wet bulb, wind direction, wind speed, weather pressure, etc. Therefore, these weather condition factors usually used for STLF and MTLF [12].

The models and methods applied for the LTLF is different from the other two forecasting categories because it depends on different input data. The factors affect in the load demand are including numerous of element from weather conditions, over seasonal effects, and socio-economic factors. The socio-economic becomes the available data, which used as selected data and used as input available at forecast the LTLF.

The LTLF for peak load demand had used to estimate the future expected peak load to avoid spending money in capacity in case of overestimated peak load forecasted that did not utilized for long period and causes negative economic impact in the efficient use of national resources. In addition, underestimated peak load forecasted may lead to a shortage in energy available, which may causes a load shedding for the load supplying domestic or industrial area in case.

In the developing countries like GCC countries, their peak load growth in electricity are mainly based on variables such as economic growth, population, and efficiency standards, coupled with other factors inherent in the mathematical development of forecasting models making accurate projection difficult [13,14].

The following elements are the main factors that affecting in the for peak load forecasted [15]:

1. The gross domestic product (GDP)
2. The population (POP)
3. The GDP per capita (GDP/CAP)
4. The multiplication of electricity consumption by population (EP)
5. The power system losses (LOSS)
6. The load factor (LF)
7. The cost of one kilowatt-hour (the average rate per unit sale; R/S) (mill/kWh).

3. Forecasting Process Methods and Model. There are number of methods could be used to model the long-term peak load of electricity network. Each method has advantages and disadvantages. The method chosen should be suitable for the target and data used for the study. There are many methods could be used for LTLF, where the most famous methods used are the Least Squares Regression Method, the simple linear regression, the multiple linear regressions, the quadratic

regression, the exponential regression, the intelligent methods including Fuzzy logic, Artificial Neural Network and Artificial Neural-Fuzzy method.

Going back to the elements, which could be considered in the model for peak load forecasting, the social behaviour can be presented by the first four factors. These factors may vary from country to country. The last three factors interlinked with the electric power system characteristics, load demand and consumption.

The multiple linear regression technique used the given elements affecting the LTLF are presented in equation (1). This equation could be simplified by neglecting the last three factors, because the losses and load factor could be considered as a fixed component, where the cost of energy fixed in Kingdom of Bahrain. The peak-load demand could be formulated as a function of country dependency factors, which are the first four factors. The formula could be written as follows [16]:

$$P_L = P_0 + P_1 \cdot (GDP) + P_2 \cdot (POP) + P_3 \cdot (EP) + P_4 \cdot (GDP/CAP), \quad (1)$$

where GDP – the gross domestic product,

POP – the population;

EP – the multiplication of electricity consumption by population GDP/CAP : The GDP per capita.

To have more focus on the elements that may affect the forecasted peak load demand, it needed to look into the behaviour of each element. Then we will be focusing on the elements that have the same behaviour of the peak load growth. Therefore, it needed to explore Bahrain data to decide on the element to use for load forecasting.

Bahrain Peak load demand.

The shape of the peak load demand is a very important item for any type of load demand forecast. Generally, Bahrain Peak load demand has continuously increased during the last 12 years where the average growth found 6.3% [16]. Figure (2) pointing out the Bahrain peak load demand in the last 12 years which shows a growth of around 6% during the years before 2012 with high growth records during 2006, 2007 and 2010, where it reaches after that 10.8% of growth rate. The growth in the Bahrain peak load dropped to 0.3% in 2012 where it increased after that in the next year to 1.3%. The growth in the peak load returned to its normal rate in year 2014 where the growth recorded was 7.5% at the peak load 3152MW. The other parameter shall be similar to peak load demand growth pattern presented in Figure (2).

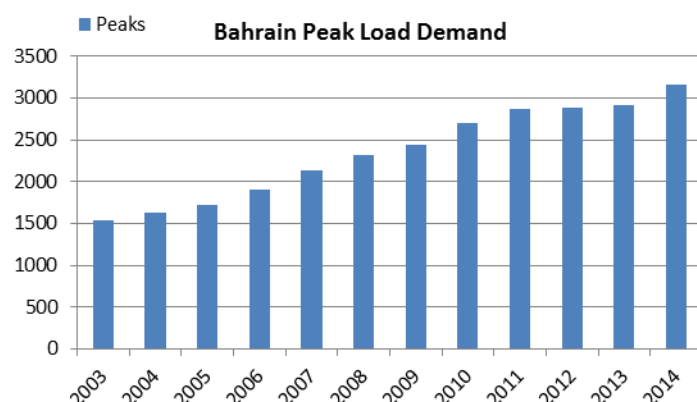


Fig. 2. Bahrain peak load demand during the last 12 years, Source: www.cio.gov.bh

Bahrain Gross Domestic Product (GDP).

The GCC countries have almost similar Gross Domestic Product (GDP), which is a market value of all officially recognized final products and services produced by country in defend period. Figure (3) presents Bahrain GDP in the last 12 years, where the recorded growth illustrates three periods of growths, which faced a drop in growth at years 2009 and 2012. The average growth in GDP before 2009 found about 15.1%, where it dropped to 11.1% during the years 2010 and 2011. More drop in the growth of the GDP recorded after 2011, where it found 5.2% averagely. Therefore, the GDP has similar growth pattern to the peak load demand and expected to have major impact on the peak load forecasting.

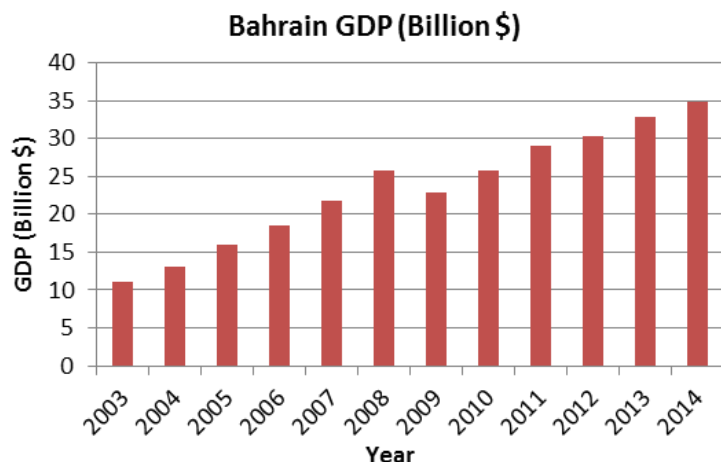


Fig. 3. Bahrain GDP at last 12 years. Source: <http://www.tradingeconomics.com>, World Bank.

Bahrain Population.

The Population growth rates in GCC countries have been increases last decades very sharply. Besides, number of people living in the

GCC countries to cover the shortage in workers in the region also increases dramatically. The population of Kingdom of Bahrain is as shown in Table (1) has high number of non-Bahraini nationality. The population of non-Bahraini nationality is 51.07% in 2011. The data shows increases in both populations of Bahraini and non-Bahraini quantities since 1992.

Figure (4) illustrates the population for Kingdom of Bahrain where it shows the continuity of population growth even after economical problem that the country faced. The average growth in Bahrain population before 2010 was about 7% yearly, where it dropped to 3.2% after 2011. Therefore, the population has similar growth pattern to the peak load demand and expected to have major impact on the peak load forecasting.

Table 1. The population of Kingdom of Bahrain.

Year	Population / Type							
	Total الجملة			Non Bahraini غير بحريني			Bahraini بحريني	
	كلا النوعين	ذات	ذكور	كلا النوعين	ذات	ذكور	كلا النوعين	ذات
	Both sexes	Females	Males	Both sexes	Females	Males	Both sexes	Females
1992	516,458	217,559	298,899	188,232	55,265	132,967	328,226	162,294
1993	530,225	223,637	306,588	193,974	57,359	136,615	336,251	166,278
1994	544,366	229,892	314,474	199,887	59,521	140,366	344,479	170,371
1995	558,879	236,324	322,555	205,979	61,752	144,227	352,900	174,572
1996	573,792	242,937	330,855	212,262	64,055	148,207	361,530	178,882
1997	589,115	249,743	339,372	218,738	66,431	152,307	370,377	183,312
1998	604,842	256,742	348,100	225,407	68,884	156,523	379,435	187,858
1999	620,989	263,933	357,056	232,275	71,409	160,866	388,714	192,524
2000	637,582	271,335	366,247	239,361	74,017	165,344	398,221	197,318
2001	661,317	274,605	386,712	251,698	71,895	179,803	409,619	202,710
2002	710,554	292,358	418,196	283,307	80,924	202,383	427,246	211,433
2003	764,519	311,619	452,900	318,888	91,087	227,800	445,632	220,532
2004	823,744	332,549	491,195	358,936	102,527	256,409	464,808	230,022
2005	888,824	355,323	533,501	404,013	115,403	288,610	484,810	239,920
2006	960,425	380,141	580,285	454,752	129,896	324,856	505,673	250,245
2007	1,039,297	407,223	632,074	511,864	146,209	365,654	527,433	261,013
2008	1,103,496	426,906	676,590	561,909	158,931	402,978	541,587	267,975
2009	1,178,415	446,418	731,997	620,404	170,418	449,986	558,011	276,000
2010	1,228,543	464,186	764,357	657,856	181,951	475,905	570,687	282,235
2011	1,195,020	453,537	741,483	610,332	164,727	445,605	584,688	288,810
2012								295,878

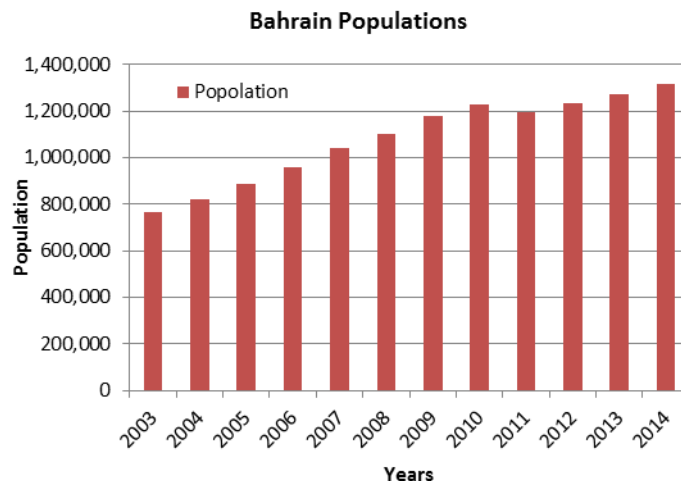


Fig. 4. Bahrain Population at last 12 years. Source: www.cio.gov.bh

Bahrain GDP per capita

The GDP per capita calculated by dividing the country's gross domestic product, which adjusted by inflation and the total population. Bahrain GDP per capita from 2006 to 2014 illustrated in Figure (5). The GDP per capita was decreasing from year 2006 to 2012. Its behaviour where changed after 2012, where it was found increasing rapidly in the last two years. The behaviour of Bahrain GDP per capita is not similar to the behaviour of peak load demand. Therefore, this element will be ignored because of mismatching behaviour with peak load demand.

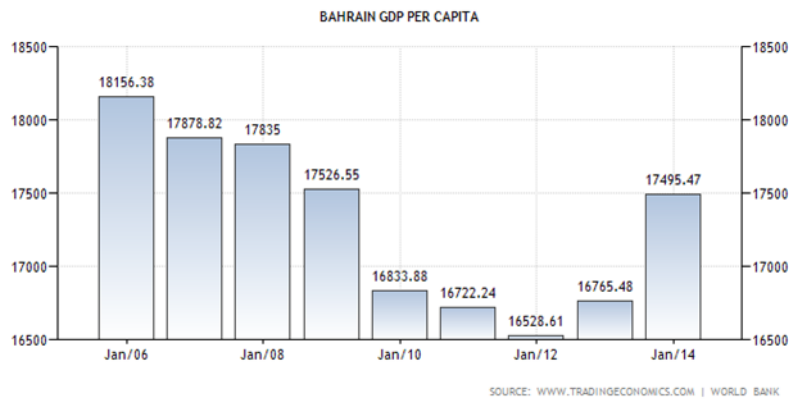


Fig. 5. Bahrain GDP per capita [1].

Electricity consumption by population.

This element neglected because the population element already chosen for the equation and the forecasted peak load demand directly related to the electricity consumption. Therefore, it is the same element required to be identify in the forecasted element. Therefore, these elements will eliminated from the given equation, which will be able to identify the forecasted peak load demand.

Peak Load Forecast Model.

Finally, the main elements as shown in Figure (6) can used to identify the forecasted load demand. These elements are the population and the GDP, which can formulated in equation (2) as follows:

$$P_L = P_0 + P_1 \cdot (GDP) + P_2 \cdot (POP). \quad (2)$$

Figure (6) illustrates the relation between the GDP and Population with Power System Peak Load, where both behaviours are similar to the peak load demand.

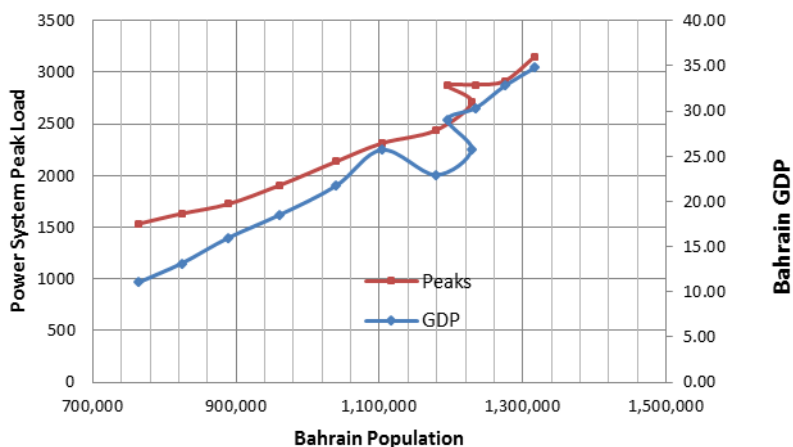


Fig. 6. Relation between GDP and Population with Peak Load Demand.

4. Results generated from this study. To find the coefficients of equation (2), the historical data of both GDP and population used for forecasting peak load demand. The curve fitting technique used to determine the coefficient found in equation (2). The result of curve fitting in equation (2) for the model is as follows:

$$P_0 = -156.2, P_1 = 35.27, \text{ and } P_2 = 0.001549.$$

The result of subletting these coefficients in equation (2) presented in Table (2). Results of peak load forecasting are very close to the actual peaks recorded. The average error calculated for this type and presented in Table (2) that shows errors less than 2%. The level of error presented is acceptable error level.

Table 2. Results of peak load forecasting and error recorded

Year	Peaks (MW)	Calculated Peak using Model (MW)	Errors
2012	2880	2827	-1.82%
2013	2917	2975	1.99%
2014	3152	3110	-1.34%

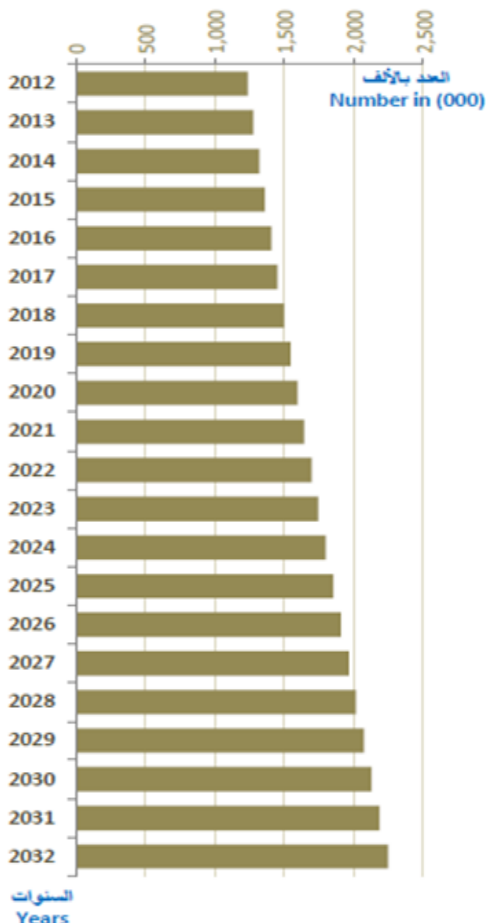


Fig. 7. Mid-Year Population Projections for Bahrain. Source: www.cio.gov.bh

5. Forecasted Peak Load Demand using the Model.

The forecasted peak load demand can be calculated for the future years if we have the forecasted population and forecasted GDP of Kingdom of Bahrain. Mid-Year Population Projections for the Kingdom of Bahrain (2012 - 2032) was collected from central information organization which is presented in Figure (7). Three scenarios estimate for Bahrain GDP, which represents high growth, normal growth and low growth for Bahrain GDP. These scenarios will cover different trends of GDP growths. These scenarios will give more visibility for the decision maker to account for the risk of economy growth in the future forecasting of the peak load demand. The results of calculating the forecasted peak load demand illustrated in Figure (8).

6. ANFIS for Estimated Peak Load Demand. Figure (9) illustrates the four layers connection for three inputs and one output. These four layers represent the Neuro-Fuzzy model, which will be used to represent the developed estimated peak load model in this study. It is clear that the results obtained automatically through training of data performed in ANFIS (Adaptive Neuro-Fuzzy Inference System). Figure (10) shows the proposed model using the Neuro-Fuzzy, where the proposed model is three inputs and one output model. The three inputs are the year, population and GDP. The output is the peak load for the Kingdom of Bahrain. Therefore, the three inputs used as follows:

1. Input 1: **Year.**

2. Input 2: **Population.**

3. Input 3: **GDP.**

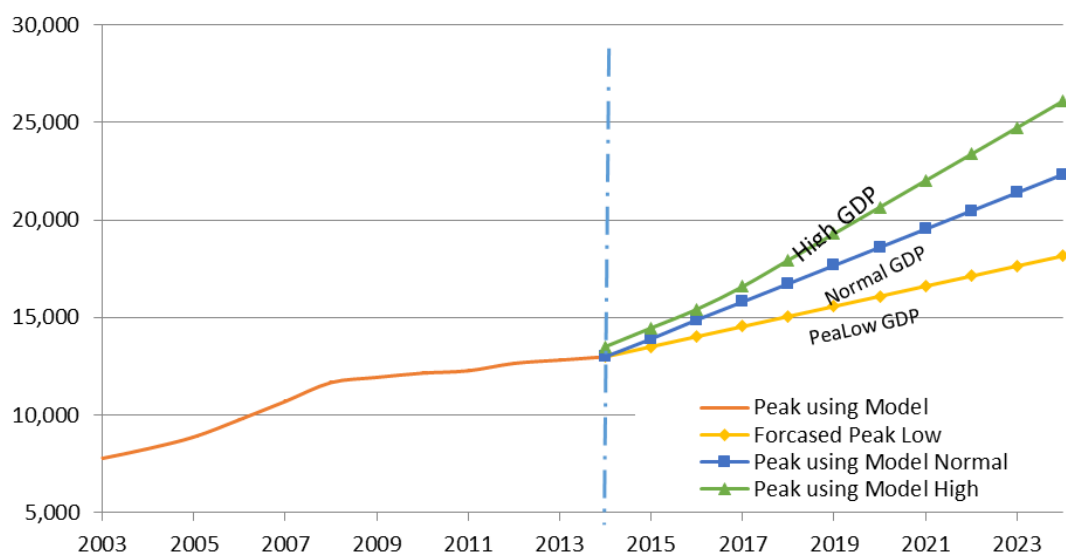


Fig. 8. Bahrain three scenarios of load forecast for 2014 – 2024.

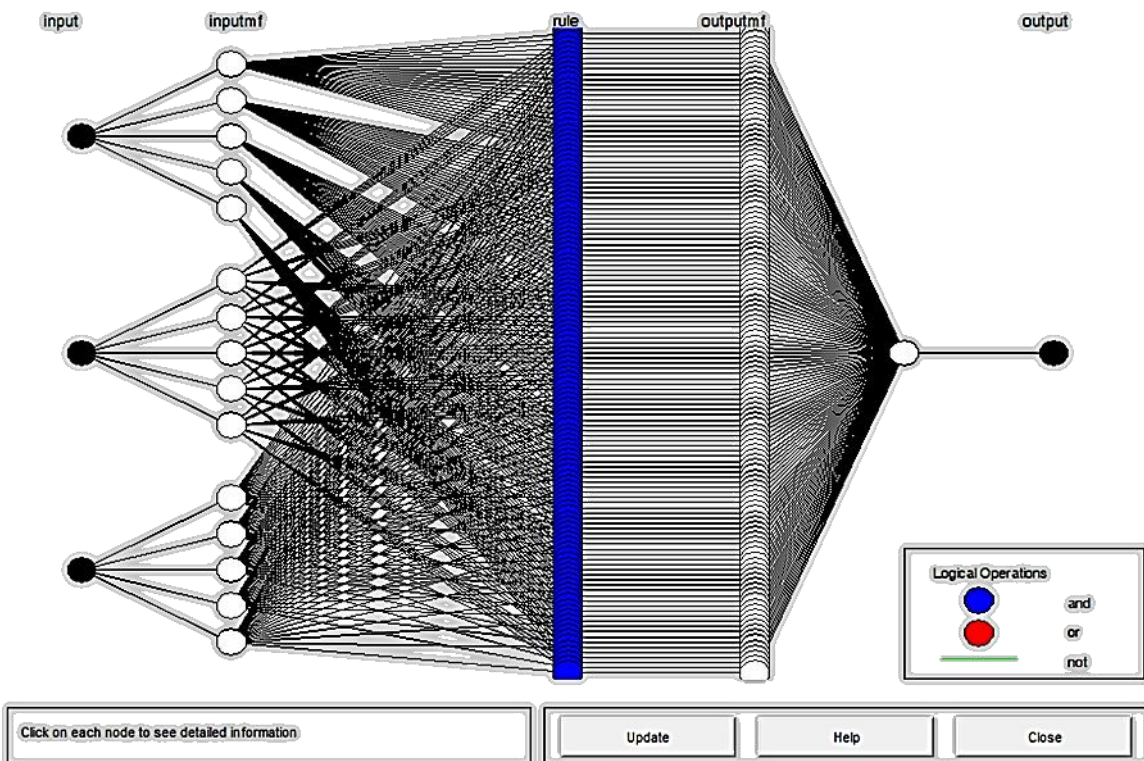


Fig. 9. ANFIS Structure in Matlab with three Inputs and One Output.

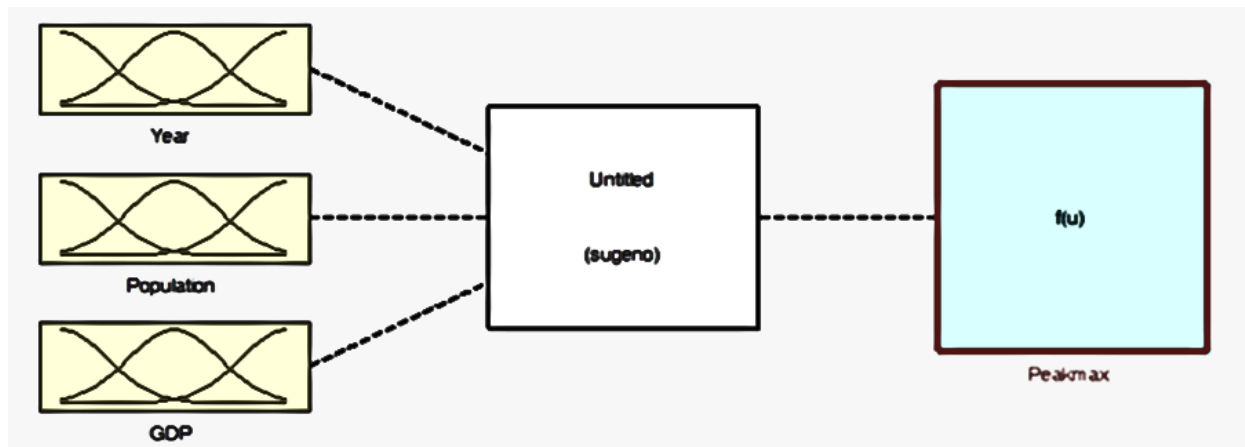


Fig. 10. Artificial Neuro-Fuzzy Logic Model Using Long Term Load Forecasting.

Figure (11) illustrates the actual data collected and presented for member states peak demand, where the estimated peak load demand for the coming years generated by Neuro-Fuzzy model. The output of the given model presents the Neuro-Fuzzy model average results error, which is equal to 0.53% and it is less than the multi regression method, which is almost about 2%. The final membership functions for each input variable as shown in Figure (12-a). It shows the range of the years from 2003 until 2014. Figures (12-b), (12c) and (12-d) show the membership functions used for population, year and GDP, respectively.



Fig. 11. Actual Data Used Versus Output of the Neuro-Fuzzy Model.



Fig. 12 (a). Membership Function Used in the Neuro-Fuzzy Logic Model for Long Term Load Forecasting.

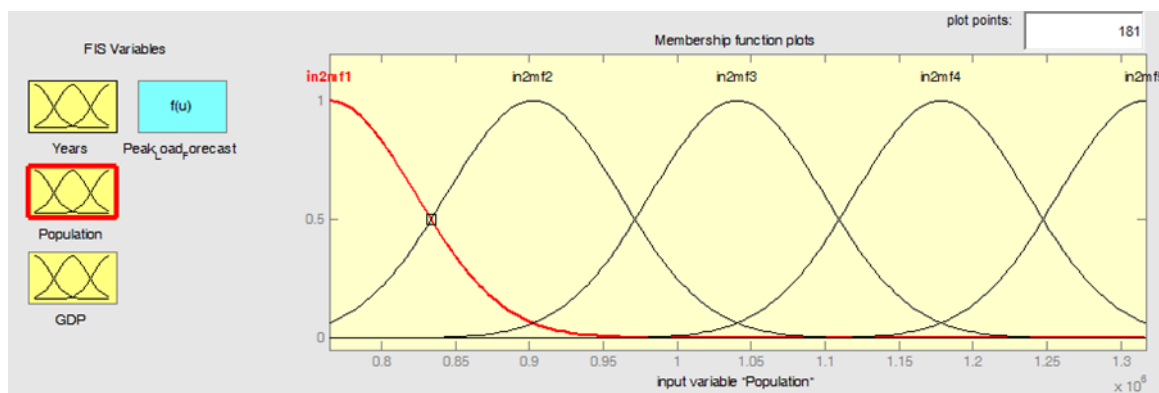


Fig. 12 (b). Membership Function Used for the Population.

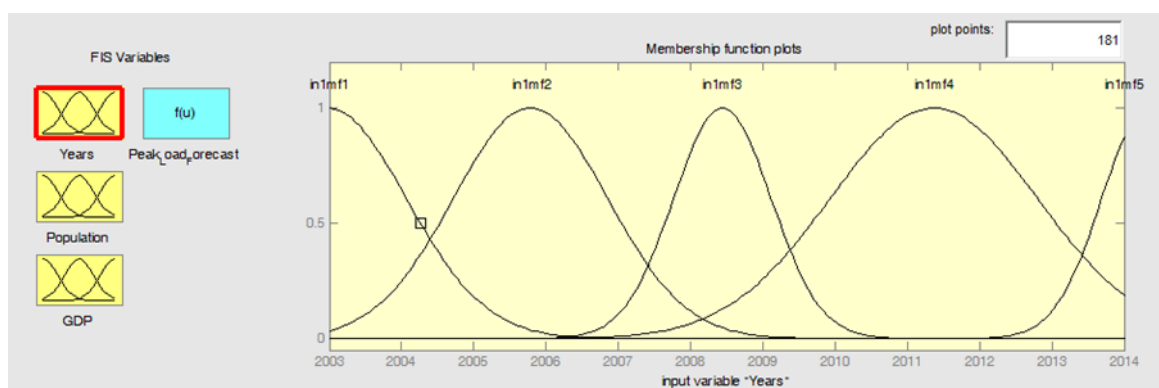


Fig. 12 (c). Membership Function Used for the Year.

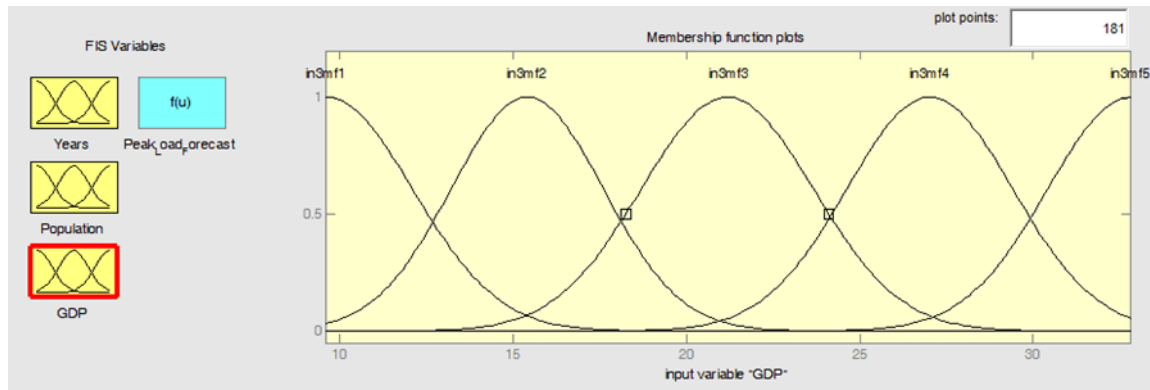


Fig. 12 (d). Membership Function Used for the GDP.

The input-output surface of the model presented in Figure (13). This means that the number of membership functions chosen as three inputs, where the surface view between the inputs and the output illustrated in Figure (13). The input-output shown is a non-linear surface and illustrates how the model will respond to varying values of year.

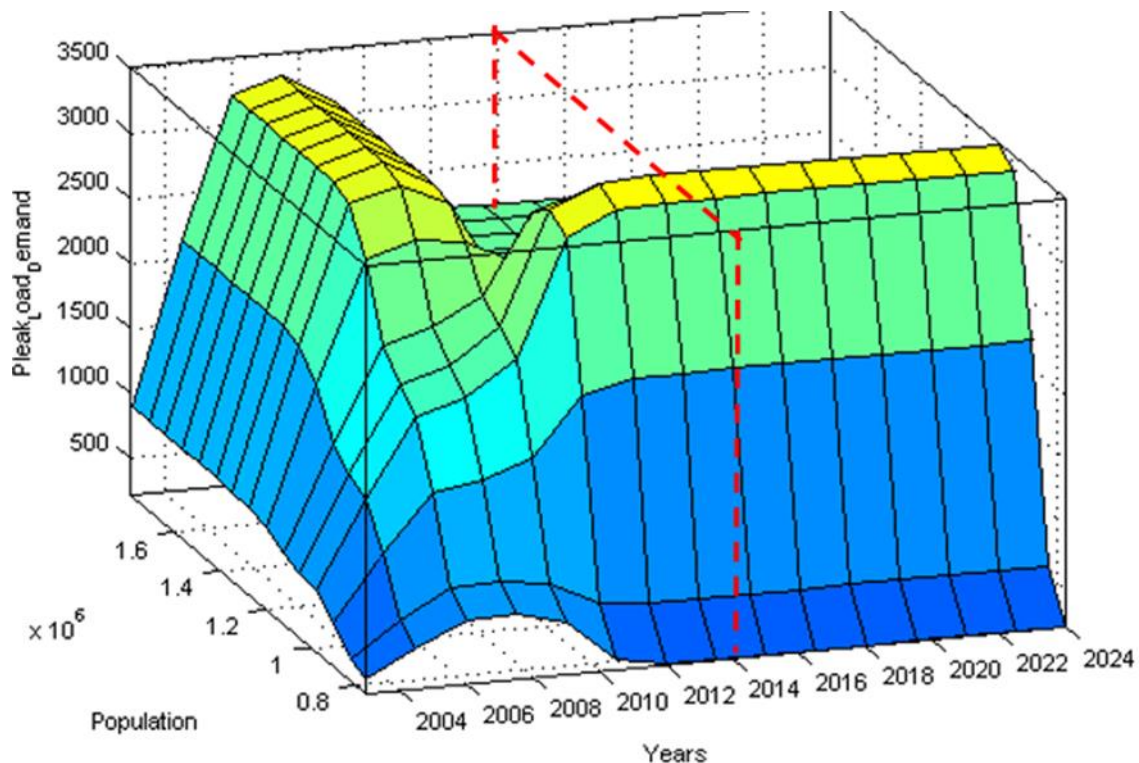


Fig. 13. Surface Sketch for the Output of the Neuro-Fuzzy Model.

Input 1: Year, Input 2: Population, Output: Peak Load (MW).

Summary. It is known, that the Peak load forecasting is one of the important tasks for decision makers in proposing the planning for periodical operations, energy trading and facility expansion in the electricity sector. Peak load demand forecasting is central and integral processes for this purpose.

The multiple linear regression and Neuro-Fuzzy applied in the present paper to model the peak load for the Kingdom of Bahrain. Both techniques applied, where the average percentage errors

calculated from the results obtained and found to be close to 2% and 0.53% in multi linear regression and Neuro-Fuzzy, respectively. The obtained results demonstrate clearly that the obtained models effectively help in finding the estimated future loads and the Neuro-Fuzzy is the more accurate technique compared with the Multi Linear Regression requested by energy traders and decision makers. In addition, the present study indicates the high ability of Neuro-Fuzzy modelling the maximum load. The system does not require a large number of sample data. The models present the Electrical long term peak load demand forecasting using both the Neuro-Fuzzy and Multiple Linear Regression method, which both have an acceptable error percentage.

The results present the peak load forecasted, taken in consideration the different expected growth in the GDP of the country. This type of forecasting will give more visibility for the decision makers and energy traders to take the correct decision for planning of the periodical operations, energy trading and facility expansion in the electricity sector.

References.

- [1] GCC Electrical Interconnection Grid – Market Study Report 2004 – GIC / SNC Lavalin Int. / White & Case LLP, March 2004.
- [2] Ahmed A. AL-Ebrahim (2005) “Towards Creating Competitive Electricity Markets in the Middle East” – 23rd Arab Engineering Conference – Bahrain – March 2005.
- [3] Nayef S. Al-Haddad, & Mohamed Y. Al-Hamad, “Power trading through the Interconnector: Initiation of a local GCC Power market and overcoming challenges”, 21-24 April, session 215, LISBON 2013.
- [4] Isa S. Qamber, M. Al-Hamad, and A. Al-Jamea, "Kingdom of Bahrain Load Forecasting Using Neuro-Fuzzy", Second IEEE-GCC Conference and Exhibition, 23-25 November, 2004, Manama, Kingdom of Bahrain.
- [5] E. Kyriakides, M. Polycarpou (2007) “Short term electric load forecasting” A tutorial. In: Chen, K., Wang, L. (Eds.), Trends in Neural Computation, Studies in Computational Intelligence, vol. 35. Springer, P. 391-418 (Chapter 16).
- [6] J. Yang, Power system short-term load forecasting. PhD Thesis, 2006, TU Darmstadt.
- [7] H. Heiko, M. Silja, Stefan Pickl. (2009) “Electric load forecasting methods- tools for decision making”, ELSEVIER, European Journal of Operational Research, 199, P. 902-907. doi:10.1016/j.ejor.2009.01.062
- [8] E. Gonzalez-Romera, M. A. Jaramillo-Moran, D. Carmona-Fernandez (2006) “Monthly electric energy demand forecasting based on trend extraction”. IEEE Transactions on Power Systems 21 (4), P. 1946–1953. doi:10.1109/TPWRS.2006.883666
- [9] E. A. Feinberg, D. Genethliou. Load forecasting. In: Chow, J.H., Wu, F.F., Momoh, J.J. (Eds.) (2005) “Applied Mathematics for Restructered Electric Power Systems” Optimization, Control and Computational Intelligence, Power Electronics and Power Systems. Springer, US, P. 269–285.
- [10] Toly Chen, Yu-Cheng Wang (2012) “Long-term load forecasting by a collaborative fuzzy-neural approach”, International Journal of Electrical Power & Energy Systems, Volume 43, Issue 1, December 2012, P. 454–464. doi:10.1016/j.ijepes.2012.05.072
- [11] Bayram Akdemir and Nurettin Çetinkaya (2012) “Long-term load forecasting based on adaptive neural fuzzy inference system using real energy data”, Energy Procedia, 2011 2nd International Conference on Advances in Energy Engineering (ICAEE), Volume 14, P. 794–799.
- [12] Soliman A. Soliman, Ahmad M. Al-Kandari (2010) “Electrical Load Forecasting: Modeling and Model Construction”, Chapter 3 “Load Modeling for Short-Term”, Elsevier Inc., P. 79-97.

[13] H.L. Willis, L.A. Finley, M.J. Buri (1995) “Forecasting electric demand of distribution system in rural and sparsely populated regions”, IEEE Trans. Power Syst. 10 (4), P. 2008–2013. doi:10.1109/59.477100

[14] P.H. Henault, R.B. Eastvedt, J. Peschon, L.P. Hajdu (1970) “Power system long term planning in the presence of uncertainty”, IEEE Trans. Power Apparatus Syst. PAS-89, P. 156–164. doi: 10.1109/TPAS.1970.292684

[15] Soliman A. Soliman, Ahmad M. Al-Kandari (2010) “Electrical Load Forecasting: Modeling and Model Construction”, Chapter 9 “Load Modeling for Long-Term”, Elsevier Inc., P. 353-407.

[16] Central Information Organization, website address www.cio.gov.bh, Kingdom of Bahrain.

Taxation of Public Owned Land for Real Estate Reconstruction in Kiev, Ukraine

M.A. Malashevskyy¹, I.M. Ciobanu^{2,a}

1 – candidate of technical sciences, associate professor, Head of the Land Management, Geoinformation and Cadastre department of the Institute of Advanced Education Kyiv National University of Construction and Architecture, Kyiv, Ukraine

2 – candidate of technical sciences, associate professor of the Land Management, Geoinformation and Cadastre department of the Institute of Advanced Education Kyiv National University of Construction and Architecture, Kyiv, Ukraine

a jdoroshenko@ukr.net



DOI 10.13140/RG.2.1.1209.6243

Keywords: land tax, rent of land, reconstruction, real property.

ABSTRACT. Researched of plots and fences used during the reconstruction of real estate in the city Kiev and proposed taxation on public owned land for a period of reconstruction of the real estate. On the base of these calculations, demonstrate the feasibility of such a land taxation.

Problem definition. Public lands should ensure the proper functioning of settlements. The current Land Code of Ukraine [1] does not explicitly state the total used land. However, according to the norms we talk about “objects for public purposes” (Article 38) and lands of public use in settlements (squares, streets, driveways, roads, embankments, beaches, parks, squares, avenues, cemeteries, places of disposal and waste management, and etc.) (Article 83). A characteristic feature of the total land use is its free nature of use for the personal needs of the entire population. The operation of this land is carried out by an unlimited range of subjects that are not related to each by reciprocal rights and obligations, in accordance with established procedure. Typically, they are owned either by state or municipal authorities and cannot be transferred to private ownership. On these lands, the construction of permanent buildings and premises that comply with the purpose of these lands, as well as temporary premises, without prejudice to the land with special destination. Ukrainian law provides the possibility of limiting the right to use these lands (particularly during construction or other works) by closing driveways, streets etc. But this requires a decision issued by an authorized state body or local administration authority. Improvement of these lands is performed by municipal authorities of local councils and their subordinate organizations and institutions. They are also responsible for the proper operation of these lands [2].

According to the current legislation of Ukraine [1, 3] public land is exempt from land fee, but today there are cases where reconstruction of the existing building or facility occurs without registration of ownership or land use, and hence, without the development of land use documentation even though this land is occupied, especially by fence and no land tax for their use is charged.

Funds obtained from land tax payment for the use of land during the period of reconstruction of houses will contribute to filling local budgets and an effective management of land in the respective region.

The main material. When for allocation of a land plot for property construction special documentation for land management is elaborated, which clearly indicates the limits of the construction site and, if necessary, establishes a temporary rent for the land during the construction

period. Therefore, for this land, a land fee will be charged. Under Article 274 [3] the tax for land plots, provided after a normative financial estimation, shall be equal to 1% of the normative monetary value. For the estimation of the monetary value of land, the coefficient of functional land use - which reflects the relative profitability of economic activities – shall be applied. In respect of land occupied for the current building works and the land set aside for future building works, this ratio is 0.5 [4].

There are many cases when the reconstruction of the existing building or facility occurs without the registration of ownership or use of land, and hence, without the elaboration of land use documentation, even when the land for public use is fenced for a long period which may create an inconvenience for safe and regular movement of the city community.

In Kiev and in Ukraine in general, the issue of reconstruction is very current, as a large number of houses both residential and non-residential need reconstruction. Kiev is growing and developing, so the construction works, of course, do not stand still – new comfortable residential areas, providing housing for the population are built and operated. There is also the old city where many buildings are cultural heritage, which need special care and reconstruction works. Also in Kiev, there are neighbourhoods of old buildings, which, due to financial problems cannot be demolished therefore they also should be reconstructed to ensure comfort and safety for the population.

In addition, according to [5] the requirements of technical standards and maintenance regulations, as well as deadlines of cyclicity of reconstruction works of the housing stock in the next 20-25 years, 5.3 thousand buildings with the total surface of more than 20 million m² need reconstruction. Out of this number, 4 thousand of very old buildings with the total surface of 11.8 million m² are planned for reconstruction, including 5 floors buildings from the first period of industrial housing construction – with the surface of 4.0 million m².

If during the period 2001-2010 (Table 1) historical buildings - mainly houses and five floor houses – were reconstructed, in the period 2011-2020, according to [5,6] reconstruction works (reorganization) will be performed for nine-storey buildings, especially panel houses built in the 70s. During the reorganization works of 5-9-16 floors panel houses in the period 2011-2020, some mandatory activities related to the development of energy efficiency in the housing stock have also been planned.

Table 1. The volume of long-term forecast of housing reconstruction in Kiev, Ukraine.

	Total	2001-2010	2011-2020
Is subject for reconstruction (thousand m ² /%), total including:	11816,3/100	2685,6/100	9130,7/100
- 5-floors buildings	4005,0/34	1511,7/56	2493,3/27
- other buildings	7811,3/66	1173,9/44	6637,4/73

If to make an estimation of the number of reconstructed objects or those that shall be reconstructed (Fig.1), as well as the surface of the public land that is occupied or could be occupied, without paying any land tax, it becomes obvious that the city budget is losing a lot of money. Therefore, it makes sense to examine this issue in detail.

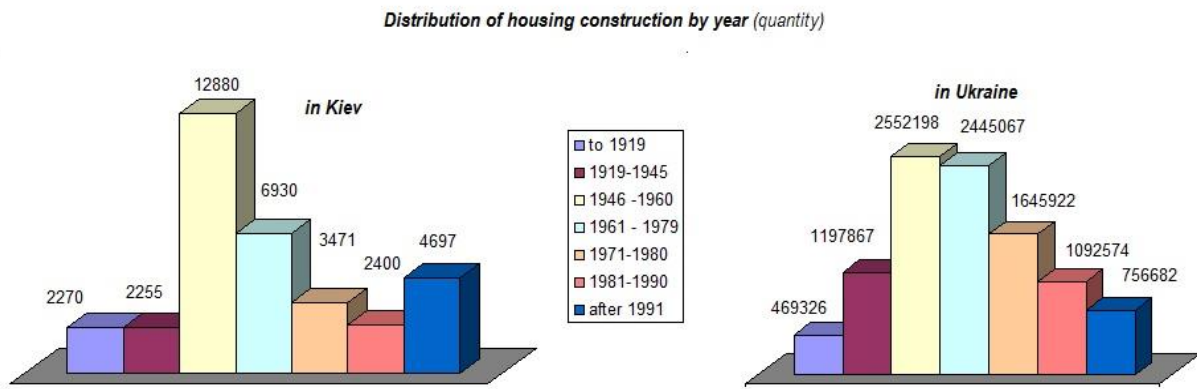


Fig. 1. Distribution of housing in Ukraine and in Kiev by year of construction [5].

Reconstruction of buildings and structures may be necessary when changing the functionality of use for the existing buildings, when they are modernized or restored. The reconstruction works on buildings and structures may include changing the configuration and size of the existing facilities, construction of new facilities. Therefore, it will always be current issue in the development of the city.

Also in accordance with [7] for any works aimed to change the appearance of the facade is mandatory to establish a temporary fence. The main purpose of all protection fences is to prevent the penetration of people on the protected territory, so that they do not cause harm to their health or property, which is located behind the fence. These constructions provide protection, as well as keeping people to a safe distance from the place where the works are held. All of fence constructions shall be adjusted for ease of installation, long life and reliability.

According to [9], fences which are used in the reconstruction of real estate can be classified as follows (Fig. 2).

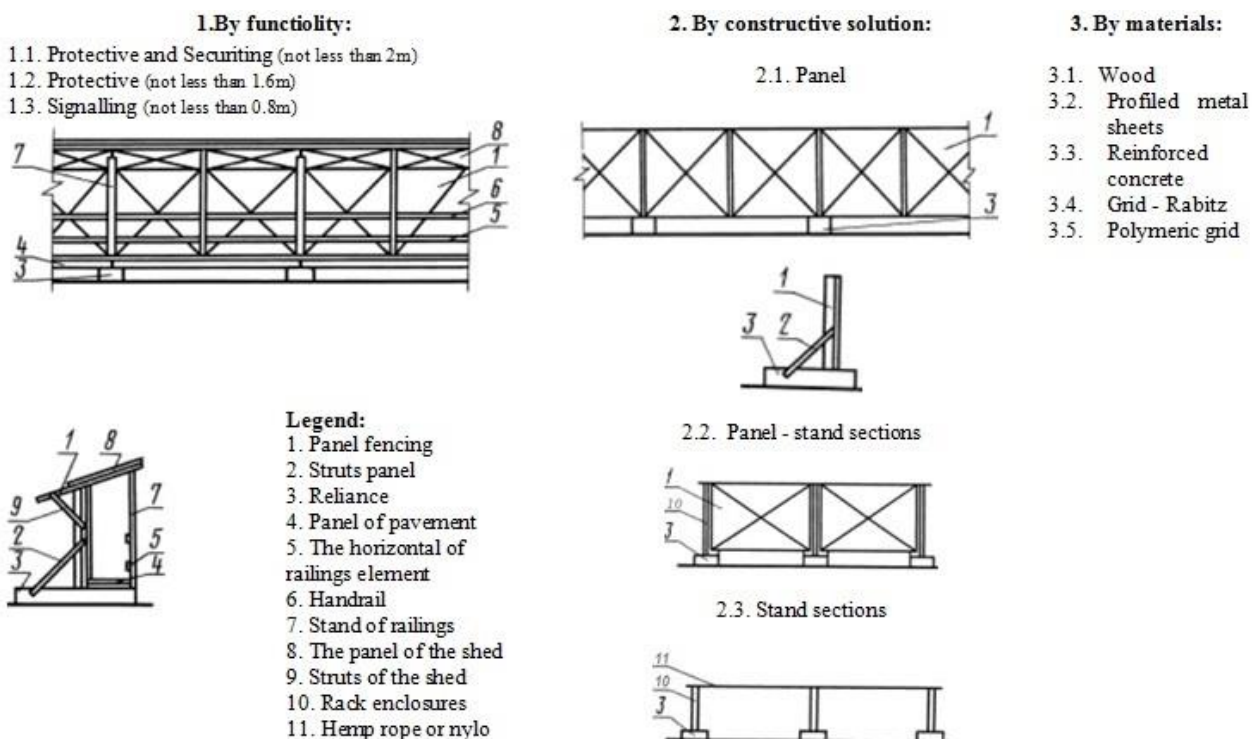


Fig. 2. Types of fences, which are used in the reconstruction of real estate.

By examining the examples of the use of temporary fencing for reconstruction of buildings in Kiev, it was established that (Fig. 3) for reconstruction works of buildings – as fences – functionality purposes protective security fences are used, which have selected elements, panels for constructive solution made of:

- profiled metal sheets, on the 10 Upper Val street;
- wood, on 8/12 Kostiantynivska street and 4 Kontraktova square;
- profiled metal sheets and plastic netting fence, on 21/20 Vladimir street.



№1 Upper Val Street, 10



№2 Kostiantynivska Street, 8/12



№3 Kontraktova square, 4



№4 The Vladimir Street 21/20

Fig. 3. Photo-fixation of temporary fencing for reconstruction in Kiev, Ukraine.

We investigate the reconstruction of the Central Department Store (CDS) in Kiev, which is located the land from 2 B. Khmelnytsky street, in the Shevchenko district of Kiev, which represent part of the old city. This is one of two buildings in the Khreshchatyk ensemble, which survived in its original form after the Second World War. As a result of the reconstruction, the total store area will be doubled - up to 45.000 m² and an underground parking for 200 cars will be added. This can be achieved through the use of the courtyard and underground space. The facade of the building, built in 1939, will remain unchanged. Behind the historic facade of the Central Department Store a new building of the department store will be constructed.

According to the data of automatic system of "Cadastre" software package the owner of the building is a legal entity – the company "Esta Holding". The land with an area of 4.721 m² is privately owned. The object of research is situated in the area where a large numbers of people is constantly moving, thus, for safety purposes (Fig. 4) a fence has been established.

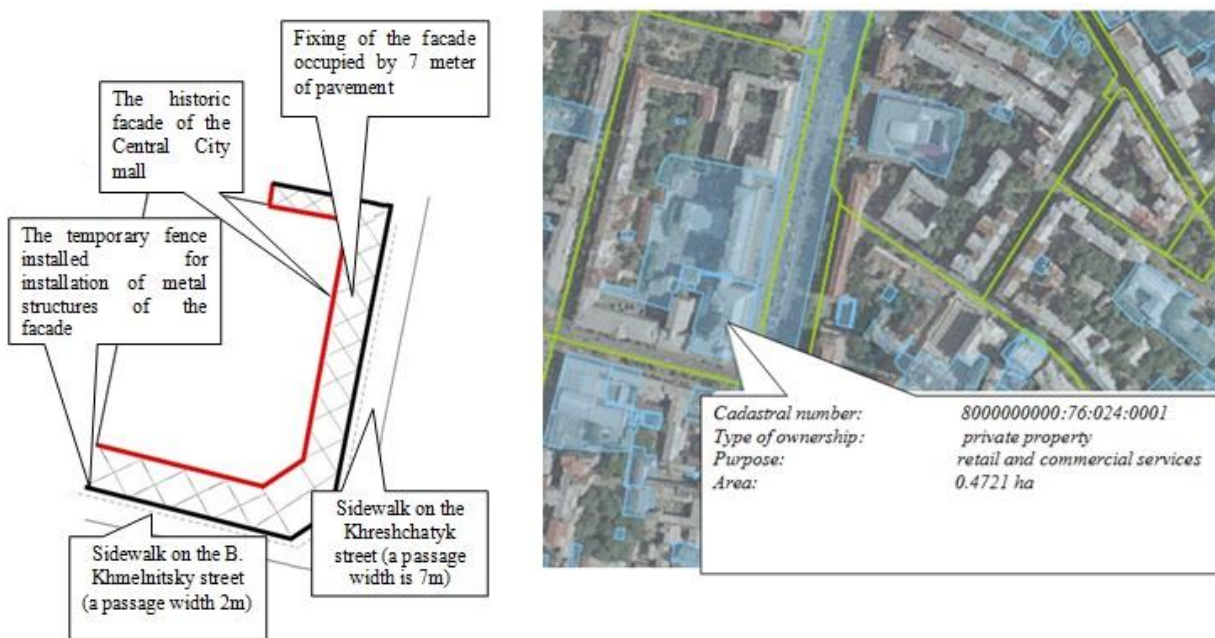


Fig. 4. Plot of land on 2 B. Khmelnytsky street, Kiev, Ukraine [8].

In fact, the fence occupied a territory of public use, which is not regulated by any approved documents hence the territory has no status. Performing some estimative measurements of the territory of public use, which was fenced for the period of reconstruction, we found that the area has 945 m^2 . Estimation of the normative monetary value of this land (Table 2).

Table 2. The calculation of regulatory monetary value of a land plot.

Indexes	Basis	Value
Land area	Contract of lease of land (draft)	945 m^2
Economic-planning zone		the zone № 61
The base cost of 1 m^2 of land	[10] (Appendix 2)	2341.81 UAH/m^2
Factor for functional use of land	The procedure of regulatory monetary value of agricultural land and the settlements	0.50
Local factors in the location a land plot within the economic-planning zones	<p>[10] (Appendix 4)</p> <ul style="list-style-type: none"> - in the zone pedestrian accessibility of community centers - in the zone highways of high city forming value - in the zone walking of high-speed urban and external passenger transport - without centralized gas supply - within the protected area 	<p>1.20</p> <p>1.20</p> <p>1.15</p> <p>0.95</p> <p>1.20</p>
Synthesis local rate	$1.20 \times 1.20 \times 1.15 \times 0.95 \times 1.20$	1.89
Coefficient of indexing monetary valuation	<p>Tax Code of Ukraine, art. 289. Letter of the State Agency of Land Resources of Ukraine on 10.01.08</p> <p>Letter of the State Committee of Ukraine of 09.01.2009</p> <p>Letter of the State Committee of Ukraine of 11.01.2010</p> <p>Letter of the State Tax Service of Ukraine of 19.01.2011</p> <p>Letter of the State Tax Service of Ukraine of 20.01.2012</p> <p>Letter of the State Tax Service of Ukraine of 21.01.2013</p> <p>Letter of the State Agency of Land Resources of Ukraine of 01.10.2014</p>	<p>1.028</p> <p>1.152</p> <p>1.059</p> <p>1</p> <p>1</p> <p>1</p> <p>1</p>
Regulatory monetary valuation	$945 \times 2341.81 \times 0.50 \times 1.5 \times 1.028 \times 1.152 \times 1.059 \times 1 \times 1 \times 1 \times 1$	2081547.3 UAH
Land tax	Land tax (if the lease) is 3% of the normative assessment	62446.419 UAH

Thus, in accordance with the calculation, the normative monetary evaluation of the land of public use amounts to 2,081,547.3 UAH, and the land tax – 62,446.419 UAH. Since the reconstruction of the Central Department Store lasts already for 4 years, it is subject to a 3% land lease of the normative monetary value which amounts to 2,997,428.112 UAH, which is exactly the amount of budget loss in Kiev.

Also, exploring the territory of the economic-planning zones no 61, which according to [10] is located in the Shevchenko District of Kiev, including the following streets: Khreshchatyk, Volodymyrska, Prorizna, Tereshchenkivska, B. Khmelnitsky, T. Shevchenko boulevard, Pushkinska street, 4 objects under reconstruction were identified (Fig. 5). We analyzed them in detail and calculated the land tax for that part of the public land that is actually occupied by a temporary fence.

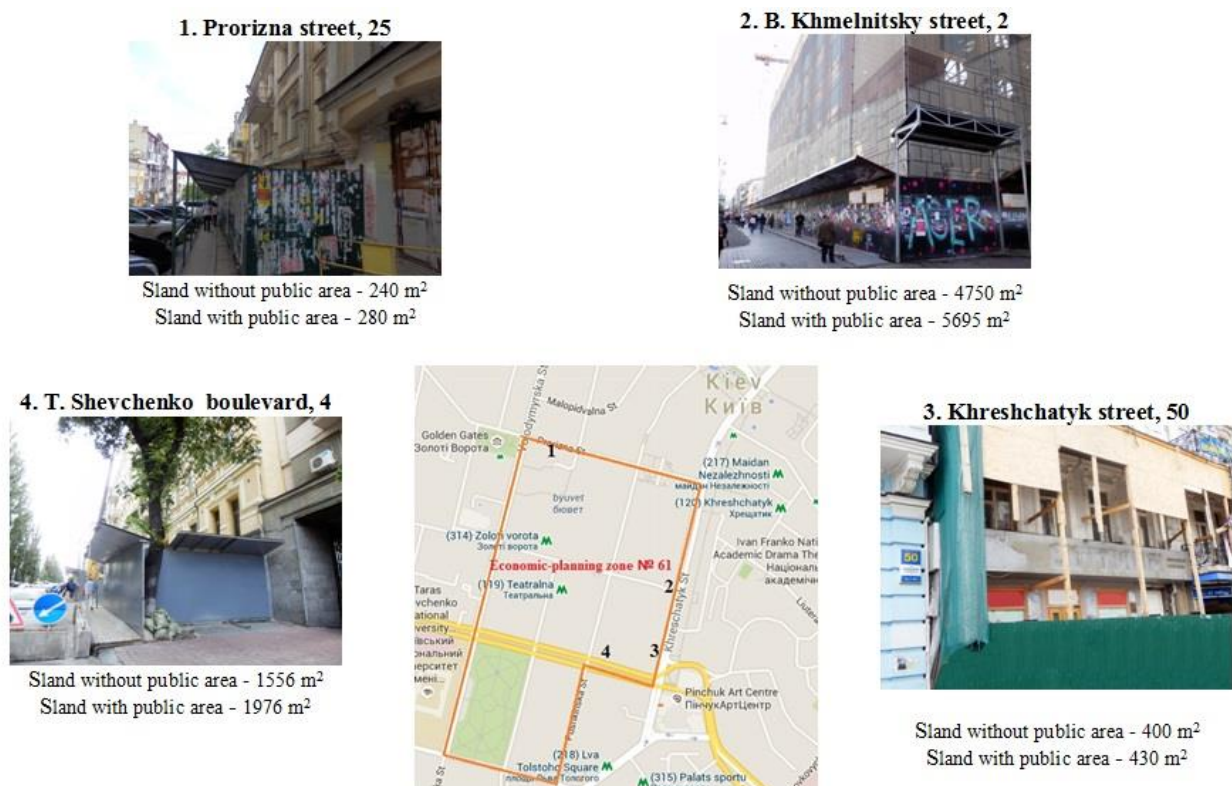


Fig. 5. Photo-fixation of objects for reconstruction in the economic-planning zone №61 Kiev, Ukraine.

Table 3. The calculation of land tax for the occupied land for real estate reconstruction.

Indexes	Value			
Address the objects for reconstruction	Prorizna street, 25	B. Khmelnitsky street, 2	Khreshchatyk street, 50	T. Shevchenko boulevard, 4
Area [8] m ²	240	4750	400	1556
Area of land public use occupied fence for a period of reconstruction m ²	40	945	30	420
Economic-planning zone	the zone № 61			
The base cost of 1 m ² of land	2341.81 UAH/m ²			
Factor for functional use of land	0.50			

Local factors in the location a land plot within the economic-planning zones	<ul style="list-style-type: none"> - in the zone pedestrian accessibility of community centers = 1.20; - in the zone highways of high cityforming value = 1.20; - in the zone walking of high-speed urban and external passenger transport = 1.15; - without centralized gas supply = 0.95; - within the protected area = 1.20; 			
Synthesis local rate	$1.20 \times 1.20 \times 1.15 \times 0.95 \times 1.20 = 1.89$			
Coefficient of indexing monetary valuation	Tax Code of Ukraine, art. 289. Letter of the State Agency of Land Resources of Ukraine on 10.01.08 (1.028); Letter of the State Committee of Ukraine of 09.01.2009 (1.152); Letter of the State Committee of Ukraine of 11.01.2010 (1.059); Letter of the State Tax Service of Ukraine of 19.01.2011 (1); Letter of the State Tax Service of Ukraine of 20.01.2012 (1); Letter of the State Tax Service of Ukraine of 21.01.2013 (1); Letter of the State Agency of Land Resources of Ukraine of 01.10.2014 (1); $1.028 \times 1.152 \times 1.059 \times 1 \times 1 \times 1 \times 1$			
Normative monetary evaluation, UAH	88107.822	2081547.294	66080,8665	925132,131
Land tax, UAH / Month	2643,234	62446,419	1982,426	27753,964
Land tax, UAH / Year	31718,815	749357,02	23789,112	333047,567
The total amount of land tax for the year, UAH	1 137 912,519			

It seems that only for few objects under reconstruction the city loses every year about 1,140,000.00 UAH. At city level, these revenues in the local budget will be several times higher.

Summary. Thus, on the base of these calculations proved as examples, we can demonstrate the feasibility of land taxation, occupied for the period of reconstruction of real estate.

References

- [1] Land Code of Ukraine (2002). Verkhovna Rada of Ukraine; Supreme Council of Ukraine (VVR), 2002, № 3-4, art. 27. Available at: <http://zakon4.rada.gov.ua/laws/show/2768-14>
- [2] Y.S. Shemshuchenko and others, 1998. The juridical Encyclopedia in 6, K. "Ukr. Encycl." Available at: http://leksika.com.ua/17711216/legal/zemli_zagalnogo_koristuvannya
- [3] Tax Code of Ukraine (2012). Verkhovna Rada of Ukraine; Supreme Council of Ukraine (VVR), 2012, № 2755-VI. Available at: <http://zakon4.rada.gov.ua/laws/show/2755-17>
- [4] The order on the normative monetary value of agricultural land and human settlements (2006). Order of the State Committee of Ukraine, Ministry of Agrarian Policy of Ukraine, the Ministry of Construction of Ukraine, the Ukrainian Academy of Agrarian Sciences. (Official Bulletin of Ukraine), 2006, № 15, p.154. Available at: <http://zakon3.rada.gov.ua/laws/show/z0388-06>
- [5] On the approval of the General Plan of Kiev and its planning projects for the suburban until 2020 (2002). Decision of Kiev city council 2002 № 370/1804. Available at: http://kmr.ligazakon.ua/SITE2/1_docki2.nsf/alldocWWW/56E1D135DED9D0B0C22573C00053FC_A6?OpenDocument
- [6] Worleyparsons, ENSI, Local Development Institute, Institute of Housing Estimated study on the "Impact of new legislation on the construction industry and housing sector" (2012), p. 86. Available at: http://www.teplydim.com.ua/uk/news/view/350/otsnochne_dosldjenna_vpliv_novogo_zakonodavstva_na_budvelnu_galuz_ta_jitloviyi_sektor#
- [7] On approval of the maintenance, repair, reconstruction, restoration of facades of buildings in the city of Kiev (2003). Decision of Kiev city council 2003, № 220/1094. Available at:

http://kmr.ligazakon.ua/SITE2/l_docki2.nsf/alldocWWW/59F485FD766981AAC22573C000530E70

[8] Public cadastral map of Ukraine (2013) Available at: <http://map.land.gov.ua/kadrova-karta>

[9] Fences for inventory construction sites and sites of construction and installation works (1978), Specifications , GOST 23407-78, Moscow

[10] On approval of the technical documentation on the normative monetary estimation of land in Kiev and Procedure of estimation (2007) Decision of Kiev city council 2007 № 43/1877. Available at: http://search.ligazakon.ua/l_doc2.nsf/link1/MR071188.html

The Benchmark Survey Methods of the Lecturers and Chairs Work in the Higher Educational Establishments, with Using the Cumulative Ranking Index

Protsiv I.V.^{1, a}, Shevchenko O.V.^{2, b}, Protsiv V.V.³

1 – Research fellow, Economics and National Economy Management Department, Oles Honchar Dniproperetrovsk National University

2 – Ph.D. in Economics, assistant professor, chair of the International Tourism, Zaporizhzhya National Technical University

3 – Professor, Head of the Mining Engineering Technology Department, National Mining University, Ukraine

a – 4327313@gmail.com

b – cheva-lena1979@mail.ru



DOI **10.13140/RG.2.2.1002.41242**

Keywords: ranking, higher educational establishments.

ABSTRACT. Approaches to ranking of the higher educational establishments' staff and its chairs with a "Cumulative Ranking Index" and "Average Weighted Placement" methods. The method of ranking "by the integrated index rating" is quite difficult to calculate, so can be used by only using specialized computer programs in fairly large groups (up to 1000 subjects), for example among the faculty. Such an approach encourages teachers to hard work at the same time in many ways, so it is better to use the method with "In sum places" and additional calculation "for the weighted average place".

Introduction. The quality rating of the teaching staff is afforded by normative documents [1, 2, 3]. The most thorough, comprehensive, profound and balanced is "Cumulative Ranking Index" method of ranking that allows to weigh the efficiency of the individual employees including the whole chairs, and to calculate a relative index of subject ranking against the average university level. It also helps to calculate the contribution of each subject into the general university result being the most correct summing up of ranking, however allows the possibility of win (obtaining the highest placements in ranking) in consequence of unnaturally high results in one or more indices, such as publication of 10 books by one lecturer in a reporting period (semester).

Aim. To develop the methodology for the calculation of lecturers and chairs of the higher education establishments ranking by rating index, and to connect results with other counting methods.

Analysis. Certainly, using the "total of placements" method there would be only top position by one or two indices, that wouldn't significantly decrease the total of employee placements and wouldn't give him the medal place at university. And most likely, such person couldn't have good results at any other indices, because of lack of time for another work.

That is why summing up with using every methods above will rate the employees (subdivisions) differently, and for more objectivity, there is a sense to do one more step of rating - by average placement using two methods, means by "average weighted placement". Such approach gives a possibility to respect others, who work productive for all the rating indices, and those who concentrated on just a few of them reaching the highest achievements. In symbolic model description below using such conventional signs:

K_{ϕ} – number of university departments;

K_{ki} – number of chairs on i -department;

K_{kij} – number of employees working on j -chair of i -department;

$K_{\Pi i}$ – number of indices that allows the i -department to act in rating;

$K_{\Pi ij}$ – number of indices that allows j -chair of i -department to act in rating;

$K_{\Pi ijt}$ – number of indices that allows the employees of j -chair of i -department to act in rating;

C_{ij} – total of established post deals on j -chair of i -department;

C_{ijt} – total of established post deals (in general by university) of t -employee, who work in j -chair of i -department;

Π_{kij} – numerical value of k -index in j -chair of i -department;

Π_{kijt} – numerical value of k -index that has t -employee working on j -chair of i -department;

I_{kij} – coefficient of j – chair of i -department coefficient by k -index;

I_{kijt} – coefficient of t -employee who works on j - chair of i -department;

k_k – weight number (factor) by k -index in university;

k_{nk} – correction factor for the work priorities of departments by k -index in university;

k_{ck} – correction factor for the work priorities of employees by k -index in university;

K_{kij} – positioning factor of j - chair on i -department by k -index;

K_{ki} – positioning factor of j -chair by k - index;

P_{kij} – cumulative ranking index (CRI) of j - chair on i -department by k -index;

P_{ij} – CRI of j -chair on i -department at university;

P_i – CRI of i -department by university;

P_{ijt} – CRI of t -employee, who works on j -chair of i -department at university;

h – inferior index shows the method by which the rating place of subject could be found, 1 – “by total of placements”, 2 – “by cumulative ranking indices”, 3 – “by average weighted placement”; adding to the last inferior index, as for example M_{ijt1} – placement of t -employee, who works on j -chair of i -department, is analyzed by “total of placements”.

M_{kij1} – placement of j -chair of i - department by k -index, is analyzed by “total of placements”;

M_{ki1} – placement of i - department by k -index, is analyzed by “total of placements”;

M_{kijt1} – placement of t -employee of i -department by k -index, is analyzed by “total of placements”;

M_{ijh} – placement of j -chair of i - department at university;

M_{ih} – placement of i – department at university;

M_{ijth} – placement of t -employee of i -department at university;

Generally, this method uses for ranking as of subdivisions, so employees, though there is a sense to consider it separately for each of them.

The method of chair ranking and departments (subdivisions) by “cumulative ranking index”. To reduce the working results of each chair by k - index, means to find the numerator that belongs to each employee who works full hours (on j -chair of i - department), uses the “Coefficient” term. It estimates like

$$I_{kij} = \frac{\Pi_{kij}}{C_{ij}} \quad (1)$$

For the i -department “Coefficient” estimates like total of numbers by k - index of all its’ chairs.

$$I_{ki} = \frac{\sum_{j=1}^{K_{ki}} \Pi_{kij}}{\sum_{j=1}^{K_{ki}} C_{ij}} \quad (2)$$

The mid “Coefficient” by k -index at university equals

$$I_k = \frac{\sum_{j=1}^{K_{ki}} \sum_{i=1}^{K_{\phi}} \Pi_{kij}}{\sum_{j=1}^{K_{ki}} \sum_{i=1}^{K_{\phi}} C_{ij}} \quad (3)$$

Farther, uses “Weight coefficient” term by k -index that is reciprocal to mid “Coefficient” by this index at university, like

$$k_k = \frac{1}{I_k} . \quad (4)$$

Now, calculate the positioning factor of j -chair on i -department by k -index as multiplication applicable to Coefficient, Weight Coefficient and correction factor for the work priorities

$$K_{kij} = I_{kij} k_k k_{nk} . \quad (5)$$

Then find the cumulative ranking index (CRI) of j -chair on i -department as a quotient of positioning factor total’s cleavage (by which the chair ranks) and the number of indices.

$$P_{ij} = \frac{\sum_{k=1}^{K_{\Pi ij}} K_{kij}}{K_{\Pi ij}}.$$

After, use calculated cumulative ranking indices of j -chair on i -department to ranging, means each chair gets a placement M_{ij2} that it has among the others in universities. The more P_{ij} – the higher placement has chair while ranging by index. Among the multitude of cumulative ranking indices P , the first place will get those chair, the index of which is corresponding to highest lower limit inf P .

The last need is ranking the departments. Calculate the positioning factor of i -department by k -index, as product of corresponding Coefficient, Weight Coefficient and correction factor for the work priorities

$$K_{ki} = I_{ki} k_k k_{nk} \quad (6)$$

Then, find the cumulative ranking index (CRI) of i - department as a quotient of positioning factor total's cleavage (by which the chairs of this department are ranking) and the number of indices.

$$P_i = \frac{\sum_{k=1}^{K_{\Pi i}} K_{ki}}{K_{\Pi i}}$$

Do the ranking by calculated cumulative ranking indices of i -department, namely each department gets a placement M_{i2} that it has among the others in universities. The more P_{ki} – the higher placement has department while ranging by index. Among the multitude of cumulative ranking indices P , the first place will get those chair, the index of which is corresponding to highest low limit inf P .

To find the number of indices in which department takes a part, use the next formula:

$$K_{\Pi i} = \frac{\sum_{j=1}^{K_{ki}} K_{\Pi ij}}{K_{ki}} \quad (7)$$

The employee ranking method by “cumulative ranking indices”. To reduce the working results of each employee by k - index, means to find the numerator that belongs to each t -employee who works on j -chair of i - department full hours a day, there are used the “Coefficient” term. It estimates like

$$I_{kijt} = \frac{\Pi_{kijt}}{C_{ijt}}. \quad (8)$$

The mid “Coefficient” by k -index at university equals:

$$I_k = \frac{\sum_{t=1}^{K_{kj}} \sum_{j=1}^{K_{ki}} \sum_{i=1}^{K_{\phi}} \Pi_{kijt}}{\sum_{t=1}^{K_{kj}} \sum_{j=1}^{K_{ki}} \sum_{i=1}^{K_{\phi}} C_{ijt}} \quad (9)$$

Farther, use “Weight coefficient” term by k -index that is reciprocal to mid “Coefficient” by this index at university, like

$$k_k = \frac{1}{I_k}. \quad (10)$$

Now, calculate the positioning factor for t -employee of j -chair on i -department by k -index as multiplication applicable to Coefficient, Weight Coefficient and correction factor for the work priorities.

$$K_{kijt} = I_{kijt} k_k k_{ck} \quad (11)$$

Find the cumulate ranking index (CRI) for t -employee of j -chair on i -department as a quotient of positioning factor total's cleavage (by which the employees of chair are ranking) and the number of indices.

$$P_{ijt} = \frac{\sum_{k=1}^{K_{\Pi_{ij}}} K_{kijt}}{K_{\Pi_{ijt}}} \quad (12)$$

Later, rating is going based on calculated cumulate ranking indices for t -employee of j -chair on i -department, namely, it helps to find placement at university for each employee M_{ijt2} . The more P_{ijt} – the higher placement has chair while ranging by index. Among the multitude of cumulative ranking indices P , the first place will get those employee, the index of which is corresponding to highest low limit inf P .

Then, make ranking by “average weighted placement”. Firstly, find the arithmetic mean value, calculated for each rating subject “by total of placements” (make this calculation previously) and by “cumulative ranking indices”. For j -chair of i - department it is

$$M_{ij3} = \frac{\sum_{h=1}^2 M_{ijh}}{2}, \quad (13)$$

For i -department it is

$$M_{j3} = \frac{\sum_{h=1}^2 M_{ih}}{2} \quad (14)$$

For t -employee of j -chair on i - department;

$$M_{ijt3} = \frac{\sum_{h=1}^2 M_{ijth}}{2} \quad (15)$$

Ranking of subjects by “average weighted placement” happens according to the succeeded results – the highest place gets those who has the lowest average weighted placement. Means, in multiply of placements M the first one will get subject with the lowest average weighted placement that corresponds to the smallest least upper bound sup M .

Using the methods above it's possible to summarizing the ranking of subjects by categories (in this case there are seven as for employees, so for chairs and departments too). For this purpose used the summation of numerical indices and coefficients by categories and all calculations make as for conventional indices.

Summary. Subject ranking method by “Cumulative ranking indices” is quite difficult to calculate so it can be used with a help by specialized computer programs at sufficiently large groups (up to 1000 subjects), for example among the lecturers of university. Such approach doesn't encourage lecturers to work hard at the same time by many indicators, so it is better to use with “total of placements” method and with additional calculation by “average weighted placement”.

References

- [1] The Law of Ukraine “On Higher Education” 01.07.2014 y. Supreme Council. – 2014. – № 37, 38. – P. 2004.
- [2] Standards and Recommendations for Ensuring Quality in the European Higher Education Area. – K. : Lenvit, 2006. – 35 p.
- [3] Decree of Cabinet of Ministers in Ukraine about “Approval of National Qualifications” № 1341 from 23 November 2011 y. – Kyiv.

Mechanics, Materials Science & Engineering Journal ©

ISSN 2412-5954

Powered by Magnolithe GmbH
See more at: <http://mmse.xyz>

